

AD-A053 322

AEROSPACE CORP EL SEGUNDO CALIF ENGINEERING SCIENCE --ETC F/G 22/3
HIGH ALTITUDE ATTITUDE DETERMINATION STUDY.(U)

MAR 78 R T UYEMINAMI, M V DIXON, T A FUHRMAN F04701-77-C-0078

UNCLASSIFIED

TR-0078(3526)-1

SAMSO-TR-78-70

NL

1 of 3
AD
A053322



AD A053322

REPORT SAMSO-TR-78-70

②
5C

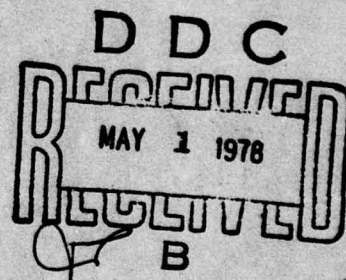
High Altitude Attitude Determination Study

AD No. ~~1~~
DDC FILE COPY

Engineering Science Operations
The Aerospace Corporation
El Segundo, Calif. 90245

31 March 1978

APPROVED FOR PUBLIC RELEASE;
DISTRIBUTION UNLIMITED



THE AEROSPACE CORPORATION

Prepared for
SPACE AND MISSILE SYSTEMS ORGANIZATION
AIR FORCE SYSTEMS COMMAND
Los Angeles Air Force Station
P.O. Box 92960, Worldway Postal Center
Los Angeles, Calif. 90009

This report was submitted by The Aerospace Corporation, El Segundo, CA 90245, under Contract F04701-77-C-0078 with the Space and Missile Systems Organization/YCD, Los Angeles Air Force Station, P.O. Box 92960, Worldway Postal Center, Los Angeles, CA 90009. It was reviewed and approved for The Aerospace Corporation by D. J. Griep, Engineering Science Operations and G. W. Anderson, Development Operations. Capt. Jack Roberts, SAMSO/YCD, was the project engineer.

This report has been reviewed by the Information Office (OI) and is releasable to the National Technical Information Service (NTIS). At NTIS, it will be available to the general public, including foreign nations.

This technical report has been reviewed and is approved for publication. Publication of this report does not constitute Air Force approval of the report's findings or conclusions. It is published only for the exchange and stimulation of ideas.



Jack Roberts, Capt, USAF



Robert Bowman, Lt Col, USAF

FOR THE COMMANDER



UNCLASSIFIED

SECURITY CLASSIFICATION OF THIS PAGE (When Data Entered)

REPORT DOCUMENTATION PAGE		READ INSTRUCTIONS BEFORE COMPLETING FORM
1. REPORT NUMBER 18 SAMS0-TR-78-70	2. GOVT ACCESSION NO.	3. RECIPIENT'S CATALOG NUMBER
4. TITLE (and Subtitle) 6 HIGH ALTITUDE ATTITUDE DETERMINATION STUDY.	5. TYPE OF REPORT & PERIOD COVERED 9 Final report	
7. AUTHOR(s) 10 Richard T. Uyeminami, Martin V. Dixon, Thomas A. Fuhrman, Stuart M. Melzer, J. E. Potter	6. PERFORMING ORG. REPORT NUMBER 14 TR-0078(3526)-14	8. CONTRACT OR GRANT NUMBER(s) 15 F04701-77-C-0078
9. PERFORMING ORGANIZATION NAME AND ADDRESS The Aerospace Corporation El Segundo, California 90245	10. PROGRAM ELEMENT, PROJECT, TASK AREA & WORK UNIT NUMBERS	
11. CONTROLLING OFFICE NAME AND ADDRESS Space and Missile Systems Organization P.O. Box 92960, Worldway Postal Center Los Angeles, California 90009	12. REPORT DATE 11 31 Mar 1978	13. NUMBER OF PAGES 276 12 265 p.
14. MONITORING AGENCY NAME & ADDRESS (if different from Controlling Office)	15. SECURITY CLASS. (of this report) Unclassified	
15a. DECLASSIFICATION/DOWNGRADING SCHEDULE		
16. DISTRIBUTION STATEMENT (of this Report) Approved for public release; distribution unlimited.		
17. DISTRIBUTION STATEMENT (of the abstract entered in Block 20, if different from Report)		
18. SUPPLEMENTARY NOTES		
19. KEY WORDS (Continue on reverse side if necessary and identify by block number) Attitude estimation Attitude reference system Attitude control Attitude processing Estimation filter		
20. ABSTRACT (Continue on reverse side if necessary and identify by block number) Results are presented of various hardware and software studies to determine the attitude of satellites in high altitude (greater than 500 nmi) orbits. A technology survey was conducted to determine the state of the art in attitude reference systems and sensors. Six attitude reference system conceptual designs are hypothesized and parametric performance analyses conducted to determine their performance capabilities. Performance sensitivities for various sensor and filter combinations are		

DD FORM 1473
(FACSIMILE)

UNCLASSIFIED

SECURITY CLASSIFICATION OF THIS PAGE (When Data Entered)

404 068

bb

UNCLASSIFIED

SECURITY CLASSIFICATION OF THIS PAGE(When Data Entered)

19. KEY WORDS (Continued)

20. ABSTRACT (Continued)

presented, and possible areas for technology improvements are suggested.

↑

UNCLASSIFIED

SECURITY CLASSIFICATION OF THIS PAGE(When Data Entered)

PREFACE

This report is the result of the combined efforts of several members of the Technical Staff of The Aerospace Corporation. The areas of study and the corresponding contributors are listed below.

Attitude and Rate Sensors

Conceptual Designs and Analysis

Implications for Technology
Development

Contributor

T. A. Fuhrman

M. V. Dixon

R. T. Uyeminami

S. M. Melzer

R. T. Uyeminami

J. E. Potter

T. A. Fuhrman

ACCESSION for	
NTIS	White Section <input checked="" type="checkbox"/>
DDC	Buff Section <input type="checkbox"/>
UNAN' / INCLD	<input type="checkbox"/>
JUS' / CATION	
BY	
DISTRIBUTION/AVAILABILITY CODES	
Dist. AVAIL. and/or SPECIAL	
A	

DDC
RECEIVED
MAY 1 1978
B

CONTENTS

I.	INTRODUCTION	7
A.	Background and Motivation	7
B.	High Altitude Attitude Determination Study (HAADS) Scope	8
II.	SUMMARY	9
III.	CONCEPTUAL DESIGNS	13
A.	Study Methodology	13
1.	Measurement Devices	13
2.	Attitude Estimation Method	15
3.	Performance Analysis Method	23
B.	Assumptions and Baseline Parameters	26
C.	Attitude Reference System Conceptual Designs	32
D.	Covariance Analysis Steady-State Results	47
1.	Double Integrator Performance	53
2.	Triple Integrator Performance	56
3.	Oscillator Performance	61
E.	Convergence Performance of Conceptual Designs	69
1.	Signal Processing Effects on System Convergence	70
2.	Estimation Filter Transient Response	71
F.	Analytical Performance Results	80
1.	Spacecraft Attitude Estimation Filter Response	81
2.	Kalman Filter Performance with Measurements at Random Points in Time	99
3.	Single Integrator Performance	102
4.	Optimization of Sensor Configurations	111

CONTENTS (Continued)

IV.	IMPLICATIONS FOR TECHNOLOGY DEVELOPMENT.	123
A.	Conceptual Design Performance Trade-Offs and Sensitivities	123
1.	Continuous System Trade-Offs and Sensitivities	124
2.	Discrete System Trade-Offs and Sensitivities.	129
B.	Conceptual Design Performance with Current Technology Sensors	138
C.	Attitude Reference Technology Development	142
APPENDIX A.	Attitude Estimator Equations	A-1
APPENDIX B.	Normalization of Equations	B-1
APPENDIX C.	Normalized Conceptual Design Dynamics	C-1
APPENDIX D.	Power Spectral Density Estimates.	D-1
APPENDIX E.	Kalman Filter Methods.	E-1
APPENDIX F.	Derivation of Upper and Lower Performance Bounds for Random Measurement Filter.	F-1
APPENDIX G.	Kalman Filter Equations for Measurements at Random Points in Time and Numerical Examples	G-1
APPENDIX H.	Equations for the Single Integrator System	H-1
APPENDIX I.	Methods for Sensor Optimization	I-1
GLOSSARY.	G1-1

TABLES

3-1.	Study Assumptions	26
3-2.	Attitude Reference System Conceptual Designs	33
3-3.	Characterization of Conceptual Designs	45
3-4.	Example System	50
4-1.	Current Technology Sensors	140
D-1.	Summary of the rms Noise Levels for the Gyros	D-4
G-1.	Error Covariance Expected Value Bounds for the First-Order Filter	G-13
G-2.	Error Covariance Expected Value Bounds for the Second-Order Filter	G-17

FIGURES

3-1.	Minimum Variance Estimator	19
3-2.	System A Dynamics (Local Vertical, Three-Axis Stable Configuration)	36
3-3.	System B Dynamics (Local Vertical, Yaw-Spin Configuration)	38
3-4.	System C Dynamics (Local Vertical, Momentum-Biased Configuration)	39
3-5.	System D Dynamics (Inertially Stable Configuration)	41
3-6.	System E Dynamics (Inertially Stable Momentum-Biased Configuration)	42
3-7.	System F Dynamics (Dual-Spin or Spinner Configuration)	44
3-8.	Discrete Attitude /Continuous Rate System Transient Response.	51
3-9.	Double Integrator Performance, $E(\theta^2)_{MAX}$	54
3-10.	Double Integrator Performance, $E(\omega^2)_{MAX}$	55
3-11.	Triple Integrator Performance, $E(\theta^2)_{MAX}$	58
3-12.	Triple Integrator Performance, $E(\omega^2)_{MAX}$	59
3-13.	Oscillator Performance, $E(\theta^2)_{MAX}$, $\eta = 0.01$	63
3-14.	Oscillator Performance, $E(\omega^2)_{MAX}$, $\eta = 0.01$	64
3-15.	Oscillator Performance, $E(\theta^2)_{MAX}$, $\eta = 0.10$	65
3-16.	Oscillator Performance, $E(\omega^2)_{MAX}$, $\eta = 0.10$	66
3-17.	Continuous System Normalized Transient Response	74
3-18.	Transient Response, $T' = 0.5$	76
3-19.	Transient Response, $T' = 2$	77
3-20.	Transient Response, $T' = 10$	78
3-21.	Attitude and Rate Filter for Continuous Attitude Measurements	83
3-22.	Bode Diagram of Transfer Function from Angle Measurements z_θ to Rate Estimates $\hat{\omega}$	85
3-23.	Steady-State Angle Errors for Sampled-Data Filter.	93
3-24.	Steady-State Rate Errors for Sampled Data Filter	94
3-25.	Comparison of Single and Double Integrator Performance	106
3-26.	Random Update Single Integrator Average Performance.	110
3-27.	Nonredundant Sensor Configurations ($m = n = 2$)	116
3-28.	Redundant Sensor Configurations ($m = 3, n = 2$)	118
3-29.	Nonunique Redundant Sensor Orientations	120

FIGURES (Continued)

4-1.	Continuous Attitude Double Integrator	126
4-2.	Continuous Attitude and Rate Double Integrator	128
4-3.	Discrete Attitude Double Integrator	132
4-4.	Discrete Attitude/Continuous Rate Double Integrator System	133
4-5.	Star Density versus Visual Magnitude, Total Sphere	136
4-6.	Number of Stars per Revolution versus Sensor Field of View	137
4-7.	System Performance versus Sensor Parameters for Discrete Attitude Continuous Rate System	139
A-1.	Minimum Variance Estimator	A-8
A-2.	Star Sensor Measurement Geometry	A-17
C-1.	System A Dynamics (Local Vertical, Three-Axis Stable Configuration)	C-2
C-2.	System B Dynamics (Local Vertical, Yaw-Spin Configuration) . .	C-4
C-3.	System C Dynamics (Local Vertical, Momentum-Biased Configuration)	C-6
C-4.	System D Dynamics (Inertially Stable Configuration)	C-8
C-5.	System E Dynamics (Inertially Stable Momentum-Biased Configuration)	C-10
C-6.	System F Dynamics (Dual-Spin or Spinner Configuration)	C-12
D-1.	Linearized Power Spectral Densities for Preprototype and Prototype Versions of the TGG Developed by CSDL	D-5
D-2.	Linearized Power Spectral Densities for the Honeywell GG 334 (Data were Derived by Honeywell, CSDL, and The Aerospace Corporation)	D-6
D-3.	Linearized Power Spectral Density for the Northrop GI-T1-B Gyro (The Data were Taken with the Gyro OA Up)	D-7
D-4.	Linearized Power Spectral Density for the 25 IRIG Mod 3 Gyro (The Data were Taken with the Gyro OA Up)	D-8
D-5.	Linearized Power Spectral Density for the Northrop GI-K7G Gyro (The Data were Taken with the Gyro OA Up)	D-9

I. INTRODUCTION

A. BACKGROUND AND MOTIVATION

Knowledge of satellite attitude with respect to some reference coordinate system is a basic requirement for the successful accomplishment of most present and future space missions. The accuracy with which this knowledge must be obtained depends upon specific mission requirements and objectives.

The collection of sensors and electronic components used to provide this attitude knowledge can be called the attitude reference system. In many applications, usually requiring low accuracy, this system is an integral part of the satellite attitude control system. Such systems maintain a desired attitude of the satellite axes with respect to some reference (earth, sun, etc.) by automatically nulling attitude errors, measured by sensors, through control devices such as thrusters or control moment gyros (CMGs). The attitude knowledge is implicit in the satellite's orientation and is limited in accuracy by the sensor noise, control system errors, and control deadbands.

In more sophisticated applications requiring highly accurate attitude determination, the attitude reference system may be considered as a separate entity from the control system. Such systems usually consist of sensors and an estimation filter that explicitly calculates an estimate of satellite attitude. The estimate may then be available for use by other onboard systems such as the mission sensor package, the attitude control system, and, possibly, a navigation system. The accuracies of these systems are limited by the estimation errors, which are functions of sensor noise and the estimation method.

As the complexity of satellite missions increases, it is presumed that greater performance demands in terms of steady-state accuracy, convergence

time, and reliability will be placed upon the attitude reference systems. Undoubtedly, this presumed demand for greater performance will be accompanied by requirements for decreasing reference system size, weight, and power. In anticipation of these demands, efforts should be undertaken to improve the state of the art in attitude reference technology. However, before such efforts are initiated, specific technology areas, whose improvement will yield the greatest payoff in terms of system performance, should be identified. It is the objective of the High Altitude Attitude Determination Study (HAADS) to identify these technology areas, investigate the reference system performance trade-offs and sensitivities, and recommend technology development effort goals and guidelines.

B. HIGH ALTITUDE ATTITUDE DETERMINATION STUDY
(HAADS) SCOPE

The study is focused on attitude reference system technology for satellite missions operating at orbital altitude of 500 nmi and beyond. Reference systems are considered for inertially stable as well as local vertical satellite vehicles with control philosophies including three-axis and momentum-biased stabilizations. Performance analyses are conducted for reference systems using continuous or discrete attitude sensors of varying qualities and for systems with or without continuous rate sensors of varying qualities. The attitude estimation software for all reference systems considered in this study is based upon the minimum variance unbiased estimator (Kalman filter) equations. In general, this estimation approach yields the best performance in terms of estimation accuracy.

Although an attempt has been made to maintain generality in the selection and characterization of attitude reference system configurations, certain simplifying assumptions were necessary to produce practical results within the manpower constraint of this effort. These assumptions inevitably limit the scope and depth of the study. However, it is felt that the reference systems chosen for analysis represent the major types of designs that will satisfy the attitude requirements of future satellite missions.

II. SUMMARY

A summary of the findings and conclusions resulting from the HAADS study is presented in this section. High altitude in this study refers to satellite operation at orbital altitudes greater than 500 nmi.

Six conceptual designs of attitude reference systems that have the potential to satisfy probable future mission performance requirements were identified. The six designs defined correspond to the six vehicle orbital configurations:

- a. Local Vertical, Three-Axis Stable
- b. Local Vertical, Yaw-Spin
- c. Local Vertical, Momentum-Biased
- d. Inertially Stable
- e. Inertially Stable, Momentum-Biased
- f. Dual-Spin or Spinner

The measurement devices for these designs include various combinations of mappers, trackers, and gyros. Mappers are defined to be sensors that obtain attitude measurements on a discrete time basis, and trackers are continuous measurement attitude sensors. The attitude estimation filters for all conceptual designs are based on the Kalman filter and generate minimum variance estimates of satellite attitude and rate. The approach used to determine the performance capabilities of the designs is a covariance analysis method involving both computer-generated and analytical solutions for the attitude and rate estimation error statistics of the conceptual designs.

Results from a covariance analysis indicate that the estimation errors of the six conceptual designs can be predicted by examining the performance of two types of filters, identified in this report as the double integrator filter and the oscillator filter. The double integrator filter performance is representative of the performance of conceptual designs for all nonmomentum-biased configurations, whereas the oscillator filter may be used to predict

the performance of conceptual designs for momentum-biased, dual-spin, or spinning configurations. A third filter type, the triple integrator, is included in the covariance analysis to investigate the performance of systems with gyros that exhibit a low frequency drift characteristic described by a random walk. Normalized steady-state and transient performance curves are presented for these three filter types as a function of sensor quality, update interval, and disturbance environment. The following performance conclusions were drawn as a result of these simulations:

- a. The effects of attitude estimation filter transient response upon system convergence time are negligible compared to the sensor signal processing effects (i.e., effects due to false updates).
- b. Rate measurement error in the form of a random-walk gyro drift degrades performance to a point approaching that of a system with no rate measurements for bias driving levels of 10 percent of the disturbance acceleration level or greater.
- c. The performance of a system with cross-axis coupling in the dynamic model (oscillator filter) is virtually the same as that of a system with no cross-coupling (double integrator) for cross-coupling levels up to 10 percent.

In addition to the computer simulations, steady-state solutions for the estimation errors of the discrete and continuous double integrator as well as the mixed discrete attitude continuous rate single integrator [space precision attitude reference system (SPARS) type] filters were analytically derived. These solutions show that there is a negligible difference between the performance of the suboptimal (single integrator) and the optimal (double integrator) filters for mixed systems with low noise gyros. The advantage of the single integrator is that its performance sensitivities are available analytically whereas those for the mixed double integrator system must be determined by computer simulation.

The findings and conclusions summarized thus far are based on the assumption of a uniform update rate or constant time intervals between updates for the discrete and mixed discrete attitude/continuous rate measurement

systems. The performance of discrete and mixed systems with random update times described by a Poisson sequence was investigated. Performance bounds describing the upper and lower limits of the mean steady-state estimation error variance were derived as a function of the average update interval for the random update systems. A comparison of these bounds with the performance curves for the uniform update system shows that the upper bound is identical to the maximum value of the error variance of the uniform update system for average Poisson update rates equivalent to the uniform update rate. Hence, the performance of the discrete or mixed system with uniform update intervals represents a fairly good approximation to the average performance of the random update system.

Goals and guidelines were identified to direct the attitude reference technology development effort to meet the performance requirements of future high altitude missions. To satisfy this objective, the performance results described above were used to identify performance versus system and sensor noise parameter trade-offs and sensitivities. These trade-offs and sensitivities were used, in turn, to define the technology development directions with the potential for the greatest payoff in terms of system performance. Design goals were suggested based on an assessment of current sensor technology. The following technology development conclusions and recommendations are made as a result of these system level performance considerations:

- a. For mapper systems on dual-spin or spinning configurations, the largest improvement in system performance is obtained by decreasing the attitude measurement error at each discrete update. A suggested goal for this error is 1 arc sec, 1 sigma.
- b. For mapper and gyro systems on local vertical configurations, the greatest benefit in terms of performance is gained by minimizing the update interval and/or improving the quality of the gyro. A suggested goal for the gyro drift rate in terms of the area under its rate noise autocorrelation function is $r_{\delta\omega} = 10^{-16} \text{ rad}^2/\text{sec}$.
- c. Performance improvements for tracker systems must be obtained by decreasing the trackers attitude measurement error. A suggested goal is 1 arc-sec, 1 sigma.

III. CONCEPTUAL DESIGNS

A. STUDY METHODOLOGY

A need for attitude reference systems capable of sub-arc-sec steady-state performance at high altitudes has been postulated. To meet this stringent requirement, several reference system conceptual designs have been investigated. The method chosen to investigate their performance is through a covariance analysis of each conceptual design for various levels of sensor measurement noise, spacecraft disturbance acceleration, and attitude measurement frequency. The results are presented in terms of parametric performance curves that identify performance trade-offs and sensitivities which can be used to define areas of technology development needed to satisfy future attitude reference requirements. The following material is a discussion of the basic types of sensors considered, the attitude estimation filter used in all conceptual designs, and the covariance analysis method.

1. MEASUREMENT DEVICES

The two basic types of measurement devices considered in this study are attitude sensors and rate sensors. Attitude sensors provide angular measurements of the satellite axes with respect to some reference object (such as stars, planets, and landmarks) while rate sensors measure the angular rate of change of the satellite axes with respect to a reference coordinate frame such as inertial space.

Depending upon the desired accuracy, attitude reference systems operating on attitude sensor measurements alone may be sufficient to satisfy mission requirements. However, for missions requiring sub-arc-sec performance, reference systems with both attitude and rate sensors are considered to maximize performance capabilities of the conceptual designs. Reference systems with rate sensors alone are not

considered because, unless the rate measurements are perfect, the errors in the estimated attitude will increase without bound.

The attitude sensors considered in this study are divided into two generic categories, namely, trackers and mappers. A sensor that has the capability of continuously following or tracking some reference object is defined to be a tracker. Examples of trackers include gimbaled and servoed mirror-type sensors that follow the motion of a reference object by physically rotating the sensor line-of-sight (LOS) with respect to the vehicle reference axes as well as strapped-down imaging sensors that follow the reference object electronically.

A mapper is defined herein to be a sensor that obtains attitude measurements on a discrete time basis by scanning the sensor LOS across some reference object or objects. Mapper examples include strapped-down slit-type sensors, such as the SPARS star sensor, which depend upon vehicle motion for scanning, as well as rotating reticle-type sensors that generate their own scanning.

In some instances, the mission sensor may be used as either a mapper or a tracker to provide attitude information. This mode of operation is particularly desirable from the standpoint of minimizing system errors resulting from misalignments by eliminating the need for precision attitude alignment transfer from the reference system to the mission sensor. The degree to which mission sensor information may be used for attitude measurements is, obviously, a function of the design and method of operation of the mission sensor. Such investigations are more properly conducted during the systems definition studies for each individual mission and, therefore, will not be pursued in this study. Rather, the attitude information assumed to be available for systems defined by this study will be categorized only by their continuous (trackers) or discrete (mappers) nature and the degree of measurement error or noise contained in their output. No specification will be made as to whether the source of the measurement is a dedicated attitude sensor or the mission

sensor. Further, no differentiation will be made between single or 2-degree-of-freedom attitude sensors. It will be assumed only that attitude information is available for each axis about which an attitude estimate is desired. This information may be generated by single-degree instruments, 2-degree instruments, or various combinations of both.

Rate measurements for all conceptual designs in this task are assumed to be provided by strapped-down rate gyros. The rate gyro is the only physical device available that directly measures inertial angular velocity accurately. Sensors that derive rate information by time differencing attitude measurements are not true rate sensors. For example, a hypothetical stellar rate sensor that attempts to measure the difference in the angular position of a star against time is, in effect, differentiating noisy position data. The accuracy of the rate measurement from such an instrument would be considerably worse than the estimated rate generated by an optimal filter operating on direct attitude measurement data. The performance of alternate reference systems where only attitude sensor information is available is also analyzed in this report.

2. ATTITUDE ESTIMATION METHOD

If perfect and continuous attitude measurement were available from the attitude sensors, filtering would obviously be unnecessary. However, since both attitude and rate sensors are imperfect physical devices, their measurements are corrupted by noise. Thus, some form of filtering is needed to minimize attitude errors due to measurement noise. Attitude must also be estimated between the discrete measurements of a mapper system. The filtering method selected should minimize the growth of estimation errors between discrete measurements caused by the presence of random disturbance torques acting on the spacecraft.

The filtering philosophy for all conceptual designs in this report is to generate estimates of attitude and attitude rate using a Kalman filter. This

filter generates minimum variance estimates. That is, the estimates of attitude and rate are such that the mean-squared error in the estimates is minimized where the error is taken to be the difference between the estimated and actual values of attitude and rate.

For most attitude reference applications, the approach described is reasonable in that it minimizes any attitude error component as well as the volume of the total error ellipsoid of the reference system. Most of the filters investigated are fully optimal in the sense that both attitude and rate will be optimally estimated. The performance of a sub-optimal filter that only estimates attitude in an optimal manner is briefly investigated and compared with the fully optimal system performance.

The Kalman filter used in an attitude reference system application requires a linearized mathematical model of the rotational dynamics of the actual satellite. This model is obtained by deriving a set of linearized vector differential equations describing the deviations or perturbations in satellite angular velocity and attitude from a nominal trajectory as the result of random disturbance angular accelerations acting on the satellite. The nominal trajectory is taken to be the angular velocity and attitude of the satellite with no random disturbance accelerations. It may be the result of control torques applied to the spacecraft or the natural untorqued vehicle motion. The detailed derivation of the Kalman filter used for all conceptual designs in this section is presented in the appendices of this report. Only a brief description of the Kalman filter is presented in this section.

Representing the nominal angular velocity by the vector $\underline{\omega}_0$, the perturbed angular velocity is defined by

$$\delta \underline{\omega} = \underline{\omega} - \underline{\omega}_0 \quad (\text{III-1})$$

where $\underline{\omega}$ is the actual angular velocity of the satellite. The nominal attitude can be represented by the Euler angle set $\underline{\xi}_0$, which relates the nominal body attitude to the initial body attitude. Defining a set of

infinitesimal rotations (quasi-coordinated rotations) by the vector $\underline{\theta}$, the perturbation in body attitude is given by the equation

$$\underline{\theta} = G^{-1}(\underline{\xi}_0)[\underline{\xi} - \underline{\xi}_0] \quad (\text{III-2})$$

where $\underline{\xi}$ is the Euler angle set describing the actual body attitude and $G(\underline{\xi}_0)$ represents a nonorthogonal matrix transformation relating the body angular velocity to the time rate of change in the Euler angles. Then the perturbation differential equations constituting the mathematical model implemented in the filter are

$$\delta \dot{\underline{\omega}} = F(\underline{\omega}_0, \underline{h}_\omega) \delta \underline{\omega} + \underline{a} \quad (\text{III-3})$$

$$\dot{\underline{\theta}} = -(\underline{\omega}_0 \times) \underline{\theta} + \delta \underline{\omega} \quad (\text{III-4})$$

where the matrix function $F(\underline{\omega}_0, \underline{h}_\omega)$ depends on the nominal rotational dynamics, including the presence of angular momentum \underline{h}_ω resulting from any onboard momentum wheels, and the vector \underline{a} represents the disturbance accelerations acting on the satellite. The cross-product matrix in Eq. (III-4) is defined as

$$(\underline{\omega}_0 \times) = \begin{pmatrix} 0 & -\omega_{z0} & \omega_{y0} \\ \omega_{z0} & 0 & -\omega_{x0} \\ -\omega_{y0} & \omega_{x0} & 0 \end{pmatrix}$$

The derivation of Eqs. (III-3) and (III-4) may be found in Appendix A.

Thus, Eqs. (III-3) and (III-4) represent the dynamic model of the actual satellite's attitude and rate perturbations from the nominal trajectory. Defining

the state vector $\underline{x} = (\underline{\theta}, \delta \underline{\omega})$, these equations can be represented by the state equation

$$\dot{\underline{x}} = \begin{pmatrix} \dot{\underline{\theta}} \\ \delta \dot{\underline{\omega}} \end{pmatrix} = A \underline{x} + \underline{w} \quad (\text{III-5})$$

where

$$A = \left(\begin{array}{c|c} -(\underline{\omega}_0 \underline{x}) & I \\ \hline 0 & F(\underline{\omega}_0, \underline{h}_w) \end{array} \right); \quad \underline{w} = \begin{pmatrix} 0 \\ \underline{a} \end{pmatrix} \quad (\text{III-6})$$

The objective of the attitude estimation filter, implemented in all conceptual designs investigated in this study, is to generate best estimates of the actual state \underline{x} , using attitude and rate measurement information supplied by onboard sensors. In the case of continuous attitude and rate measurements (i.e., systems that have trackers and rate gyros), the block diagram of the minimum variance estimator (Kalman filter) used to generate these estimates is shown in Figure 3-1. Referring to the block diagram, the actual state is measured by the sensors that produce the measurement vector $\underline{z} = (\underline{z}_\theta, \underline{z}_\omega)$. These measurements are not perfect in that they are corrupted by sensor noise, i.e., $\underline{n} = (\underline{n}_\theta, \underline{n}_\omega)$, and may be affected by the sensor measurement geometry matrix H . These imperfect measurements are inputs to the filter that generates the best estimate $\hat{\underline{x}} = (\hat{\underline{\theta}}, \delta \hat{\underline{\omega}})$ of the actual state.

The portion of the filter that is enclosed by the dashed outline in Figure 1 is the dynamic model of the actual system. The output $\hat{\underline{x}}$ is used to generate an expected measurement $\hat{\underline{z}}$. The difference between the actual measurement \underline{z} and the expected measurement is multiplied by a time-varying gain K , and the result is used to drive the dynamic model to follow the actual system. The matrix K is the Kalman gain and is calculated by the equation

$$K = P H^T R^{-1} \quad (\text{III-7})$$

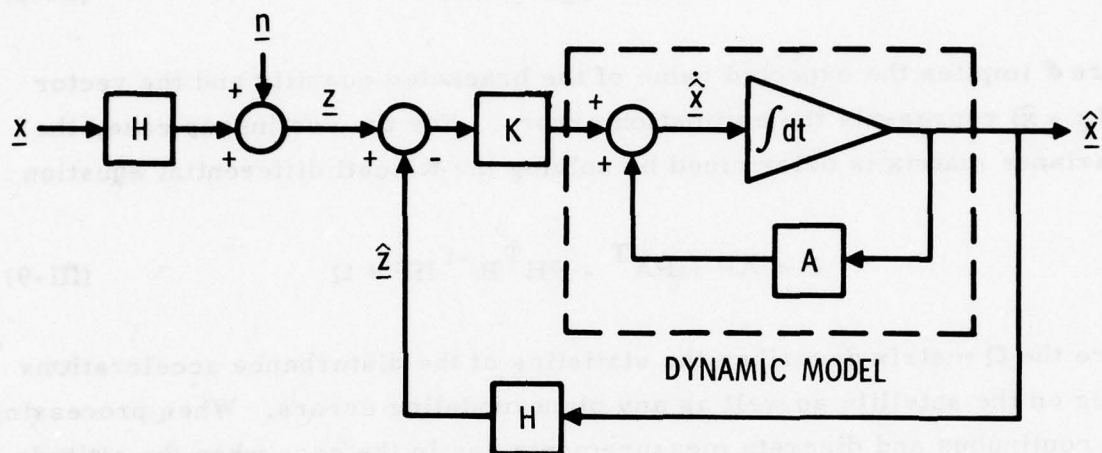


Figure 3-1. Minimum Variance Estimator

where R describes the statistics of the sensor noise, H describes the measurement geometry, and the matrix P is the time-varying system covariance matrix defined by

$$P(t) = \mathcal{E}[\underline{e}(t) \underline{e}^T(t)] \quad (\text{III-8})$$

where \mathcal{E} implies the expected value of the bracketed quantity and the vector $\underline{e} = (\underline{x} - \hat{\underline{x}})$ represents the estimation errors. For the continuous case, the covariance matrix is determined by solving the Riccati differential equation

$$\dot{P} = AP + PA^T - PH^T R^{-1} HP + Q \quad (\text{III-9})$$

where the Q matrix describes the statistics of the disturbance accelerations acting on the satellite as well as any plant modeling errors. When processing both continuous and discrete measurements, as in the case when the attitude sensors are mappers and the rate sensors are continuous rate gyros, the continuous filter illustrated in Figure 1 is used between discrete measurements. The information gained from the discrete measurement at time t_i is used to improve the estimate by calculating a discrete Kalman gain matrix, which is then used to weight the discrete information. This weighted information is added to the last estimate prior to the discrete measurement to update the estimate. The discrete Kalman gain matrix is calculated using the equation

$$K' = P_i H'^T R'^{-1}$$

where H' and R' describe the discrete measurement geometry and noise statistics of the discrete sensor and P_i is the updated system covariance matrix at time t_i . The equation used to update the system covariance matrix is

$$P_i = M_i - M_i H'^T (H' M_i H'^T + R')^{-1} H' M_i' \quad (\text{III-10})$$

where M_1 is the covariance matrix just prior to the measurement at time t_1 . Between discrete updates, the continuous Riccati equation (V-9) is used to propagate the covariance matrix.

Having defined the basic equations of the attitude estimation filter, the matrices R, Q, and H must be formed to implement the filter. As previously mentioned, the R and Q matrices describe the sensor noise and disturbance acceleration statistics respectively. Assuming the sensor noise and acceleration to be "white" gaussian sequences, their autocorrelation functions are impulses. In actuality, the sensor noise and disturbance acceleration are not perfectly white, but in most cases they can be adequately approximated by band-limited white noise. In such cases, the approximate white noise autocorrelation function is an impulse with height equal to the area under the actual autocorrelation function. Defining the area under the attitude sensor noise autocorrelation function by the parameter r_θ and the area under the rate sensor noise autocorrelation function by $r_{\delta\omega}$, the matrix R can be defined as

$$R = \begin{pmatrix} r_\theta I & 0 \\ 0 & r_{\delta\omega} I \end{pmatrix} \quad (\text{III-11})$$

where I is the identity matrix. This form assumes that the attitude sensors as well as the rate sensors used in the system are of equal quality. Assuming that the statistics of the disturbance acceleration affecting each vehicle axis are equal, the Q matrix is defined by

$$Q = \begin{pmatrix} 0 & 0 \\ 0 & qI \end{pmatrix} \quad (\text{III-12})$$

where the parameter q is equal to the area under the acceleration autocorrelation function. The units of r_θ and $r_{\delta\omega}$ are $(\text{rad}^2 \cdot \text{sec})$ and $(\text{rad}^2/\text{sec})$ respectively while the units of q are $(\text{rad}^2/\text{sec}^3)$.

Note that although Eqs. (III-11) and (III-12) assume equal quality sensors as well as equal disturbance acceleration statistics on each axis of the satellite, the performance analysis results presented in the latter part of Section III are not constrained by this assumption. It will be shown that the individual axis performance for most attitude reference system configurations envisioned for future missions is unaffected by the performances of the other axes; i. e., little or no cross-axis coupling exists and each axis can be treated independently. Hence, the equal quality assumption is used only as a convenience in deriving the filter performance equations and should not be considered as a constraint on this study. Additionally, the effects of rate measurement noise sources other than white noise will be investigated. In particular, the effect of gyro bias upon system performance will be explored on a limited basis.

The sensor measurement geometries for each conceptual design must be determined from the physical orientation of the sensor axes with respect to the vehicle reference axes. This geometry is represented by the H matrix which acts as a sensitivity matrix relating the changes in the system states $\underline{\theta}$ and $\underline{\dot{\omega}}$ to changes in the attitude and rate measurements \underline{z}_θ and \underline{z}_ω . The H matrix may be partitioned to represent the attitude sensor measurement matrix H_θ and the rate sensor measurement matrix H_ω by the equation

$$H = \left(\begin{array}{c|c} H_\theta & 0 \\ \hline 0 & H_\omega \end{array} \right) \quad (\text{III-13})$$

For the types of sensors considered in this study, these matrices are given by

$$H_\theta = - \left(\begin{array}{ccc} 1 & 0 & 0 \\ 0 & 1 & 0 \end{array} \right) C_B^S \left(\begin{array}{c} B_0 \\ \underline{u} \\ x \end{array} \right) \quad (\text{III-14})$$

and

$$H_{\omega} = I \quad (\text{III-15})$$

where C_B^S is a direction cosine matrix that transforms a vector from the vehicle reference coordinate system to the sensor reference coordinate system and \underline{u}^{B_0} is a unit vector along the sensor LOS to a reference object (star, planet, etc.) resolved in the nominal or unperturbed vehicle reference coordinate system. The derivation of Eqs. (III-14) and (III-15) is presented in Appendix A.

3. PERFORMANCE ANALYSIS METHOD

The analysis method used in this study to determine the conceptual design performance capabilities is the covariance analysis. This method was selected because the objective is to analyze the capabilities of attitude reference systems for a broad range of possible future missions rather than the detailed design of a particular system. The method permits the evaluation of system performance in terms of rms estimation errors without the necessity of simulating the Kalman filter and detailed truth model of the actual vehicle dynamics. The accuracy of the covariance analysis is usually sufficient for mission planning purposes where rough sizing is required of sensor errors and system parameters, such as average update intervals for the discrete case. It is not a substitute for the detailed system and truth model simulations that are necessary to define the design parameters of an actual system for a particular mission.

The covariance analysis method calls for the propagation of the attitude estimation filter covariance matrix $P(t)$ from its initial value, set to the a priori uncertainties in the system states \underline{x} , to the steady-state value. Since the elements of $P(t)$ contain the statistics of the estimation errors $\underline{e} = (\underline{x} - \hat{\underline{x}})$ in the form of the mean-squared estimation errors (from Eq. [III-8]), the square root of the diagonal elements of P at steady-state

yields the rms attitude and rate estimation accuracies in each axis and, therefore, the system steady-state performance.

The method of propagation of the covariance matrix depends on whether the system is continuous or discrete, i.e., whether the attitude and rate measurements are available on a continuous or discrete time basis. If both attitude and rate measurements are continuous, the Riccati differential equation (III-9) is used by integrating $P(t)$ from $t = 0$ to steady state. For mixed systems where attitude measurements are discrete and rate measurements are continuous, Eqs. (III-9) and III-10) are used together. The Riccati equation is integrated up to the time of a discrete measurement and then reinitialized using the update equation so that the covariance matrix is updated with information regarding the discrete sensor noise at the time of the measurement. The integration is then restarted and continues to the next discrete measurement time when the update process is repeated. Steady state is reached when the system disturbances, represented by the Q matrix in Eq. (III-9), increase the covariance matrix between discrete measurements by the same amount that the discrete measurements decrease the covariance matrix, in other words, when $P_{i+1} = P_i$ or, equivalently, $M_{i+1} = M_i$ in Eq. (III-10).

For systems with pure discrete measurements, the same propagation procedure can be used as that employed in the case of the mixed system. However, the Riccati equation is altered by deleting the term that contains the continuous measurement error information. This is accomplished in the covariance analysis for this study by setting the continuous sensor noise or measurement uncertainty to a large number, thereby rendering the continuous measurements useless.

A covariance analysis computer program capable of propagating the continuous, mixed, and discrete case covariance matrices was generated for the CDC-7600 computer. The coding was accomplished in The Aerospace Corporation simulation language called the Eclectic Simulation Program (ESP). ESP was chosen because of its capability to process discontinuities automatically such as discrete measurement updates, even when these updates

may occur in a random sequence, and the availability of various subroutine packages for convenient data output. The resultant covariance analysis program is the primary tool used in the performance analysis presented in Paragraph D of this section.

The program has been designed to accommodate a maximum of nine state variables and may be further expanded with minor modifications to the coding. In general, nine state variables are required to evaluate the three-axis performance of a system with cross-axis coupling in the vehicle dynamics model and gyro biases. This case is discussed under the heading of Triple Integrator Performance in Paragraph D. 2 of this section. Also implemented in the program is the capability to generate random discrete updates based on a Poisson distribution of update times. However, this option was not used in this study for the reasons stated in Paragraph B of this section. The implications of random update times on discrete system performance are discussed in Paragraph F of this section.

B. ASSUMPTIONS AND BASELINE PARAMETERS

Because of the large number of variables required to fully analyze the three-axis performance of a single conceptual design, it was found necessary to make certain simplifying assumptions before a practical performance analysis involving several conceptual designs covering a broad range of missions could be conducted. These assumptions are listed in Table 3-1. They fall into two general categories, assumptions on the modeling of the sensors and assumptions on the satellite dynamics model.

Table 3-1. Study Assumptions

A. Sensor Model

1. All attitude measurements are valid, i.e., no misidentifications.
2. All attitude sensor measurement errors are uncorrelated between measurements.
3. The rate sensor measurement errors consist of either pure random uncorrelated errors or uncorrelated errors plus a random-walk bias error.
4. The interval between discrete measurements is constant. However, performance bounds for the random (Poisson) update system were derived.
5. Any misalignments between the sensors and the vehicle reference coordinate frame are either precalibrated or combined with the sensor errors.

B. Satellite Dynamics Model

1. On momentum-biased satellites, inertias along axes normal to the bias are equal.
2. Any momentum bias maintains a fixed orientation with respect to the vehicle reference axes.
3. In the nominal case, any net spacecraft momentum is not precessed with respect to inertial space.
4. Random white disturbance torques act on the satellite.

Referring to Table 3-1, Assumption A-1 requires all attitude measurements to be valid. The basis for this assumption is that, for practical attitude sensor designs, there exists a finite probability of obtaining false attitude measurements which are either generated by noise sources internal or external to the sensor (electronic noise, detector background noise, and stray reflections) or the result of misidentification of reference objects (i.e., star field ambiguities). Detection and signal processing electronics are usually included in the sensor design to minimize the probability of false measurements. The effect of false measurements on system performance must be assessed by detailed analysis and simulation of the sensor electronics and detection algorithms. Such modeling efforts would be highly sensor and mission dependent and will be avoided in this study by assuming that the probability of false measurements is zero for all attitude reference systems analyzed. Further discussion of the false measurement problem is included in Paragraph E of this section where convergence performance is described.

Assumptions A-2 and A-3 of Table 3-1 result in white noise models for the measurement errors. In addition, the rate measurement error can include a bias that is modeled as an integral of white noise or a random-walk error source.

Assumption A-4 simplifies the determination of steady-state performance and the comparison of conceptual design performance. Without the constant or uniform update interval assumption, a Monte Carlo analysis would generally be required to obtain the average steady-state performance for any one conceptual design. Different random attitude measurement sequences would have to be generated and the time profiles of the system covariance matrix determined for each sequence. Then, covariance matrix statistics must be generated by ensemble averaging over a large sample of covariance profiles, with attendant difficulties in determining the number of members in the ensemble that constitute a statistically meaningful sample. An alternate analysis technique, which generates bounds on these statistics without recourse to Monte Carlo methods, is discussed in Paragraph F. The uniform update assumption will be used, however, for the bulk of the performance analysis conducted in this study.

The last assumption (A-5) affecting the sensors eliminates the modeling of errors due to sensor misalignments. Generally, these errors vary slowly with time as a result of the fact that their major cause is thermal cycling with orbital frequency. The effect of these errors on system performance is similar to a slowly varying bias on the estimation error. The usual design approach employed to minimize misalignment errors is to mount the sensors on an extremely rigid structure as well as possibly employing some active means of temperature control to minimize thermal gradients and transients. As a result, the accurate modeling of misalignment errors would require a detailed structural and thermal analysis of each conceptual design. The alternative to modeling these errors is to assume that they have been precalibrated or are included in the random components of the sensor noise.

The first assumption (B-1) affecting the dynamics model results in an axis of inertial symmetry for momentum-biased satellite configurations. The axis of symmetry is assumed to be along the momentum-biased direction, and such a configuration results in symmetric cross-axis coupling on the dynamics of a momentum-biased vehicle. This is usually the case in spinning or dual-spin satellite configurations. Configurations with momentum bias due to onboard momentum wheels may not be symmetric; however, it will be shown that unequal cross-axis inertias for such configurations have negligible effect on system performance.

Assumption B-2 excludes dynamic configurations where the momentum bias varies with respect to the vehicle reference axes (e.g., satellite with CMGs) since their performance would be a function of the time profile of the momentum bias. Assumption B-3 eliminates configurations requiring precession of the momentum bias. Such precession requires the expenditure of control fuel and is usually avoided in long duration missions. Finally, Assumption B-4 indicates that the disturbance torques acting on the satellite are random. These torques are the result of unmodeled disturbances that act to perturb the nominal attitude of the satellite.

It is felt that these assumptions are not overly restrictive and the resulting analyses are sufficient to illustrate the attitude reference performance capabilities of conceptual designs that satisfy the requirements of most future satellite missions. Moreover, the number of parameters, which have a key influence upon the performance of the conceptual designs, are reduced by these assumptions to a manageable set. In addition to the simplifications introduced by the assumptions, a further reduction can be attained in the number of variables that must be specified to conduct the performance analyses. This is accomplished by defining nondimensional groupings of noise parameters as well as by rescaling the simulation time. With this normalization procedure, the key variables in the covariance analysis are reduced to a set of baseline parameters with scaling equations to reflect the normalized performance results back to attitude and rate estimation accuracies.

The normalization procedure involves a transformation of the covariance matrix P of the form

$$E = SPS^T \quad (\text{III-16})$$

where the scaling matrix S is a function of the normalized baseline parameters and, in some cases, the vehicle dynamics parameters. The actual form of S varies with the conceptual design and is defined for each design in paragraph C of this section. Using the foregoing transformation and defining a nondimensional time scale by the equation

$$\tau = \Omega_0 t \quad (\text{III-17})$$

the normalized Riccati differential equation for continuous rate measurements and discrete attitude measurements takes the form

$$\frac{dE}{d\tau} = \tilde{A} E + E \tilde{A}^T - \frac{1}{r'} E I_{22} E + \alpha I_{22} \quad (\text{III-18})$$

where

$$I_{22} = \begin{pmatrix} 0 & 0 \\ 0 & I \end{pmatrix}$$

and I is the identity matrix, \tilde{A} is the normalized dynamics matrix, r'_ω is the baseline parameter including sensor noise statistics, and α is an arbitrary scaling constant introduced to improve the numerical stability of the Riccati equation. The normalized discrete covariance update equation (III-10) takes the form

$$E_i = N_i - N_i \tilde{H}^T (\tilde{H} N_i \tilde{H}^T + R')^{-1} \tilde{H} N_i \quad (\text{III-19})$$

where \tilde{H} is the normalized discrete measurement geometry matrix, N_i is the value of the normalized covariance matrix just prior to the discrete update, and E_i is the updated value of the normalized covariance matrix. The procedures to propagate the normalized covariance are the same as those defined in paragraph III.A for the regular covariance matrix. However, the update interval for the discrete case becomes nondimensional as the result of the rescaling of time, and is defined by

$$T' = \Omega_0 T \quad (\text{III-20})$$

where T is the actual update interval in seconds and Ω_0 is a scaling factor with dimension (1/sec).

Thus, the baseline parameters for the covariance analysis have been reduced from four (i.e., r_ω , T , r_θ , and q) to only two (r'_ω and T'). A third parameter, identified as β , will be introduced in the discussion of the triple integrator in paragraph III.D to include the effects of random gyro bias. A fourth parameter, namely, η , will also be introduced to include the gyroscopic effects in momentum-biased satellite configurations. The scaling

equations relating these baseline parameters to measurement noise, disturbance acceleration statistics, and time are

$$\Omega_0 \equiv \left(\frac{q}{r'_\theta \alpha} \right)^{1/3} \quad (\text{III-21})$$

$$r'_\omega \equiv \frac{r_{\delta\omega}}{r'_\theta \Omega_0} \quad (\text{III-22})$$

where α is an arbitrary scaling constant, q and $r_{\delta\omega}$ are the white noise equivalent areas under the actual autocorrelation functions of the disturbance acceleration and rate measurement noise respectively, and r'_θ is the discrete form of attitude sensor measurement noise. The actual covariance matrix is obtained by performing the inverse transformation on Eq. (III-16). The scaling equations for β and η are discussed in Paragraph D of this report.

The derivation of the normalized Riccati equation (III-18) and update equation (III-19) for the mixed continuous/discrete system is presented in Appendix B. These equations form the basis for the covariance analysis conducted in this study. The performance of pure discrete systems, operating with discrete attitude sensors only, was analyzed by setting the parameter r'_ω defined by Eq. (III-22) to a large value. This effectively removes the continuous sensor information term in Eq. (III-18) and reduces the mixed system to a discrete system. Moreover, the simplified case of a system with uncoupled double integrator dynamics can be solved analytically. These results are presented in Paragraph F of this report.

C. ATTITUDE REFERENCE SYSTEM CONCEPTUAL DESIGNS

Attitude reference system conceptual designs that have the performance potential to satisfy the reference requirements of future high altitude missions are described in the following discussion. The configurations of the conceptual designs are highly dependent upon the orbital configuration and attitude control philosophies envisioned for future high altitude satellite missions. Six orbital configurations have been defined together with their probable attitude control philosophies. These configurations were used along with the measurement and filtering philosophies discussed previously to define six attitude reference system conceptual designs. These designs are identified as systems A through F in the first column of Table 3-1. The orbital configuration corresponding to each system is presented in the second column, and the nature of the sensors used in conjunction with each system is identified in the remaining columns. The assumptions governing the attitude and rate sensors, which are discussed in Paragraph B of this section and are listed in Table 3-1, were used in determining the sensors for each system. Although gyro measurements are indicated for each system, the subsequent analyses will also consider the system performance capabilities with no rate information.

System A of Table 3-2 (three-axis, local vertical stable systems) can be implemented with either two mappers or two trackers. The former configuration would correspond to a SPARS-type system if the mappers were body-fixed, slit-type instruments. The performance of such a configuration for high altitude missions usually suffers from a relatively slow measurement rate since the mappers are dependent upon orbital rate for their scanning. The alternate configuration with two trackers eliminates this problem. The trade-off between these two configurations was investigated in this study. Similar reasoning may be used to select the attitude sensor configurations for system C as the dynamics of this system (local vertical momentum-biased) are similar to those of the local vertical, three-axis stabilized configuration with the exception of cross-axis coupling introduced by the momentum bias.

Table 3-2. Attitude Reference System Conceptual Designs

System	On-Orbit Configuration	Attitude Sensors		Rate Sensors	
		Type	Quantity	Type	Quantity
A	Local Vertical Three-Axis Stable	Two-Dimen., Mapper	2	One-Dimen., Gyro	3
		Two-Dimen., Tracker ^a	2		
B	Local Vertical Yaw Spin	Two-Dimen., Mapper	1	One-Dimen., Gyro	3
C	Local Vertical Momentum-Biased	Two-Dimen., Mapper	2	One-Dimen., Gyro	3
		Two-Dimen., Tracker ^a	2		
D	Inertially Stable	Two-Dimen., Tracker	2	One-Dimen., Gyro	3
E	Inertially Stable Momentum-Biased	Two-Dimen., Tracker	2	One-Dimen., Gyro	3
F	Dual-Spin or Spinner	Two-Dimen., Mapper	1	One-Dimen., Gyro	3

^aAlternate sensors.

Body-fixed, slit-type mappers are the logical choice of attitude sensors for systems B and F where part of the body is spinning. By placing the sensor optical or boresight axis normal to the body spin axis, the spinning motion of the body can be used to scan the mappers.

Inertially stable systems D and E require the use of trackers or mappers that generate their own scanning for attitude measurements. Under nominal (undisturbed) conditions, these systems have no angular motion with respect to inertial space. Trackers were selected for these systems to provide continuous attitude information.

Having defined the conceptual design configurations, the system dynamics for each design must be derived to implement the covariance analysis. In the discussion in Paragraph A of this section, the dynamics modeled in the attitude estimation filter are represented by the A matrix in the state equation (III-5) and are defined by Eq. (III-6). For the covariance analysis, this matrix must be used in the Ricatti differential equation to propagate the system covariance. Since the normalized form of the Ricatti equation (III-18) is used in this study, the dynamics matrix for each conceptual design must be rescaled using the equation

$$\tilde{A} = \frac{1}{\Omega_0} (\dot{S}S^{-1} + SAS^{-1})$$

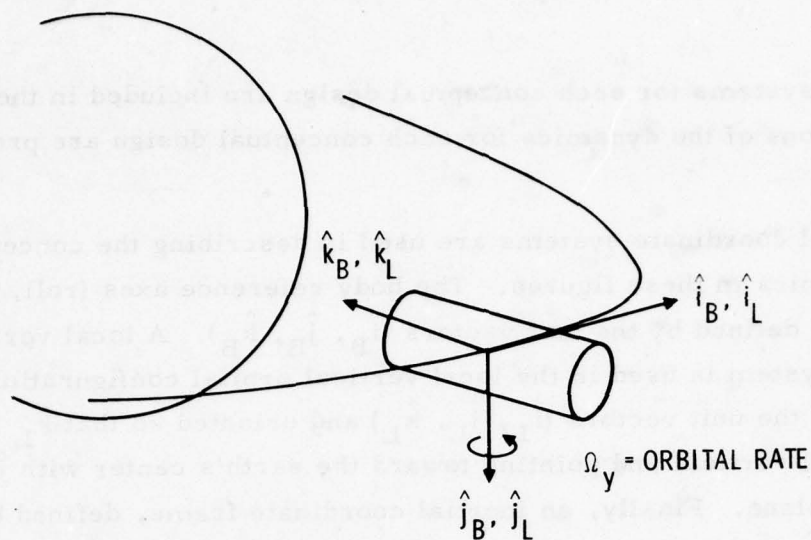
where S is the scaling matrix for each conceptual design and Ω_0 is a scaling frequency defined by Eq. (III-21). The purpose of this normalization is to reduce the number of dynamic variables by introducing dimensionless ratios of angular velocities, moments of inertia, and angular momenta. These ratios are derived using the vehicle dynamics assumptions in Table 3-1 and represent a set of baseline parameters in addition to r'_m and T' defined in Paragraph B. These additional parameters, along with the normalized dynamics matrix \tilde{A} and the scaling matrix S, are presented for each conceptual design in Figures 3-2 through 3-7. The orbital configuration and reference

coordinates systems for each conceptual design are included in these figures. The derivations of the dynamics for each conceptual design are presented in Appendix B.

Several coordinate systems are used in describing the conceptual design dynamics in these figures. The body reference axes (roll, pitch, and yaw) are defined by the unit vectors $(\hat{i}_B, \hat{j}_B, \hat{k}_B)$. A local vertical coordinate system is used in the local vertical orbital configurations, and is defined by the unit vectors $(\hat{i}_L, \hat{j}_L, \hat{k}_L)$ and oriented so that \hat{k}_L is aligned with the local vertical and pointing toward the earth's center with \hat{j}_L normal to the orbit plane. Finally, an inertial coordinate frame, defined by the unit vectors $(\hat{i}_I, \hat{j}_I, \hat{k}_I)$ and maintaining a fixed orientation with respect to inertial space, is used in the inertial and dual-spin orbital configurations.

Figure 3-2 is an illustration of the dynamics of system A and represents the attitude reference system conceptual design for a three-axis stabilized, local vertical oriented vehicle. The dynamics matrix \tilde{A} indicates a cross-axis coupling between the roll and yaw channels through the parameters ρ and k . This effect is due to quarter-orbit coupling as well as inertial coupling between axes. It is a very weak effect since ρ is the ratio of orbital rate Ω_y to steady-state continuous filter bandwidth Ω_0 defined by the scaling equation (III-21) of Paragraph B. For the lowest altitude mission considered under this study (500 nmi altitude) and the worst-case disturbance environment, which is the result of aerodynamic disturbance torques ($q = 10^{-12} \text{ rad}^2/\text{sec}^3$), this ratio is on the order of 10^{-3} . At synchronous altitude, for the same disturbance level, the ratio is on the order of 10^{-4} . Moreover, the inertia parameter k is in all practical cases less than 1, which further diminishes the strength of the cross coupling. Thus, the attitude dynamics for this system behave primarily as if all the axes were identical and independent. Therefore, the three-axis performance of this system can be approximated by the performance of a single-axis system with the dynamics matrix

$$\tilde{A} = \begin{pmatrix} 0 & 1 \\ 0 & 0 \end{pmatrix}$$



DYNAMIC CHARACTERISTICS:

1. BODY REFERENCE AXES ALIGNED WITH LOCAL VERTICAL AXES
2. ORBIT RATE Ω_y ABOUT PITCH AXIS

SCALING MATRIX:

$$S = \frac{1}{\sqrt{r'_\theta}} \left(\begin{array}{c|c} 1 & 0 \\ \hline 0 & \frac{1}{\Omega_0} \end{array} \right)$$

NORMALIZED DYNAMICS:

$$\tilde{A} = \left(\begin{array}{ccc|ccc} 0 & 0 & -\rho & & & \\ 0 & 0 & 0 & & 1 & \\ \rho & 0 & 0 & & & \\ \hline & & & 0 & 0 & k\rho \\ 0 & & & 0 & 0 & 0 \\ & & & 0 & 0 & 0 \end{array} \right)$$

DYNAMIC PARAMETERS:

$$k = 1 - J_z/J_x$$

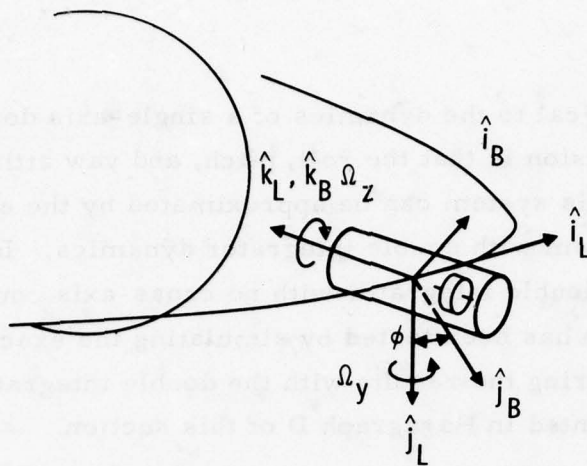
$$\rho = \Omega_y/\Omega_0$$

Figure 3-2. System A Dynamics (Local Vertical, Three-Axis Stable Configuration)

This matrix is identical to the dynamics of a single-axis double integrator system. The conclusion is that the roll, pitch, and yaw attitude and rate estimation errors for this system can be approximated by the estimation errors of a single-axis system with double integrator dynamics. In fact, the pitch channel is an exact double integrator with no cross-axis coupling. The validity of this conclusion has been tested by simulating the exact dynamics of system A and comparing the results with the double integrator system. This comparison is presented in Paragraph D of this section.

Figure 3-3 is an illustration of the dynamics of the conceptual design for a local vertical, yaw-spin-type vehicle. The scaling matrix used to normalize the dynamics contains the rotation matrix $Z(\phi)$, which transforms the dynamic equations for this system from the body reference coordinate system to the local vertical coordinate system. The details of this transformation are discussed in Appendix C. This change of coordinates simplifies the dynamic equations by transforming them from differential equations with sinusoidal coefficients to time-invariant differential equations. The resulting normalized matrix \tilde{A} is identical to that of the previous system. Thus, system B may be simulated by the double integrator-type system.

The dynamics for system C, which is the conceptual design for a local vertical momentum-biased vehicle, are illustrated in Figure 3-4. The normalized dynamics matrix for this system indicates a cross coupling between the roll and yaw axes as a result of the momentum wheel as well as quarter-orbit coupling. Unlike systems A and B, this cross coupling may not be negligible since the magnitude of the wheel momentum h_w can be large for greater stiffness between the roll and yaw axes. In this case, only the pitch axis acts as a pure double integrator system, and the yaw and roll axes behave as oscillatory systems. This can be seen by deriving the state transition matrix for the normalized angular velocities $\delta\tilde{\omega}$. The state equation



DYNAMIC CHARACTERISTICS:

1. ORBITAL RATE Ω_y ABOUT \hat{j}_L - AXIS
2. BODY SPIN Ω_z ABOUT YAW AXIS
3. MOMENTUM WHEEL ALONG YAW TO CANCEL SPIN MOMENTUM

SCALING MATRIX:

$$S = \frac{1}{\sqrt{r'_\theta}} \begin{pmatrix} z(\phi) & 0 \\ 0 & \frac{1}{\Omega_0} z(\phi) \end{pmatrix}$$

WHERE

$$z(\phi) = \begin{pmatrix} \cos \phi & -\sin \phi & 0 \\ \sin \phi & \cos \phi & 0 \\ 0 & 0 & 1 \end{pmatrix}, \quad \phi = \Omega_z t$$

NORMALIZED DYNAMICS:

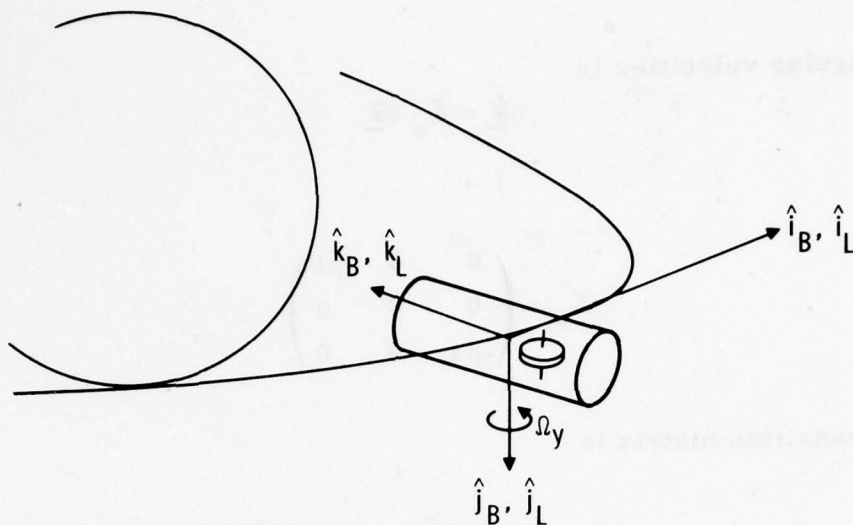
$$\tilde{A} = \left(\begin{array}{ccc|ccc} 0 & 0 & -\rho & & & \\ 0 & 0 & 0 & & & \\ \hline \rho & 0 & 0 & 0 & 0 & k\rho \\ & 0 & & 0 & 0 & 0 \end{array} \right)$$

DYNAMIC PARAMETERS:

$$k = 1 - J_z/J_x$$

$$\rho = \Omega_y/\Omega_0$$

Figure 3-3. System B Dynamics (Local Vertical, Yaw-Spin Configuration)



DYNAMIC CHARACTERISTICS:

1. BODY REFERENCE AXES ALIGNED WITH LOCAL VERTICAL AXES
2. ORBIT RATE Ω_y ABOUT PITCH AXIS
3. MOMENTUM WHEEL ALONG PITCH AXIS WITH BIAS h_w

SCALING MATRIX:

$$S = \frac{1}{\sqrt{r'_\theta}} \left(\begin{array}{c|c} 1 & 0 \\ \hline 0 & \frac{1}{\Omega_0} \end{array} \right)$$

NORMALIZED DYNAMICS:

$$\tilde{A} = \left(\begin{array}{ccc|ccc} 0 & 0 & -\rho & & & \\ 0 & 0 & 0 & & 1 & \\ \rho & 0 & 0 & & & \\ \hline & 0 & & 0 & 0 & \rho b \\ & & & 0 & 0 & 0 \\ & & & -\rho a & 0 & 0 \end{array} \right)$$

DYNAMIC PARAMETERS:

$$\rho = \Omega_y / \Omega_0$$

$$a = h_w / (J_z \Omega_y)$$

$$b = k + h_w / (J_x \Omega_y)$$

$$k = 1 - J_z / J_x$$

Figure 3-4. System C Dynamics (Local Vertical, Momentum-Biased Configuration)

for these angular velocities is

$$\delta \dot{\underline{\omega}} = \tilde{A}_{\omega} \delta \underline{\omega}$$

where

$$\tilde{A}_{\omega} = \begin{pmatrix} 0 & 0 & \rho b \\ 0 & 0 & 0 \\ -\rho a & 0 & 0 \end{pmatrix}$$

The state transition matrix is

$$\Phi(t, t_0) = \mathcal{L}^{-1} \left[(sI - \tilde{A}_{\omega})^{-1} \right]$$

where \mathcal{L}^{-1} indicates the inverse Laplace transform of the bracketed quantity. Evaluating $(sI - \tilde{A}_{\omega})^{-1}$ and performing the inverse transform results in

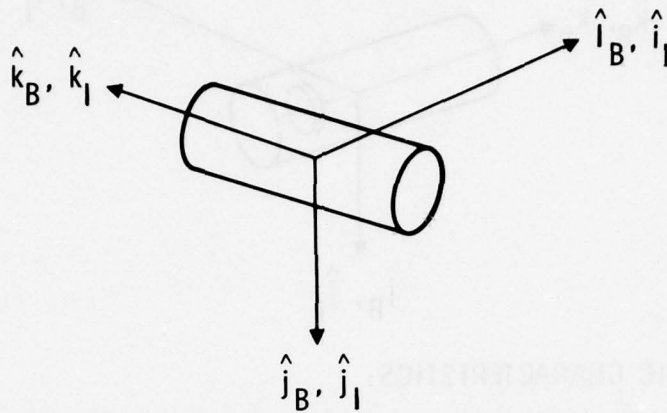
$$\Phi(t, t_0) = \begin{pmatrix} \cos \omega_c (t - t_0) & 0 & \frac{1}{\rho a} \sin \omega_c (t - t_0) \\ 0 & 1 & 0 \\ -\frac{1}{\rho b} \sin \omega_c (t - t_0) & 0 & \cos \omega_c (t - t_0) \end{pmatrix}$$

Thus the normalized angular velocities in the roll and yaw axes are sinusoidal functions of time exhibiting an oscillatory behavior with a frequency equal to

$$\omega_c = \rho \sqrt{ab}$$

Systems with this form of behavior are termed oscillator-type systems in this report, and they represent the second general class of systems in addition to the double integrator-type systems that characterize the dynamics of the conceptual designs.

Figures 3-5 and 3-6 are illustrations of the dynamics of the conceptual designs for inertially stable and inertially stable with momentum bias



DYNAMIC CHARACTERISTICS:

1. BODY REFERENCE AXES ALIGNED WITH INERTIAL AXES
2. ZERO NOMINAL ANGULAR VELOCITY

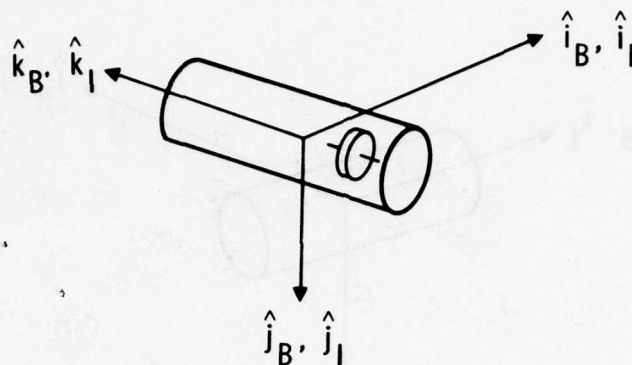
SCALING MATRIX:

$$S = \frac{1}{\sqrt{r_\theta} \Omega_0} \left(\begin{array}{c|c} 1 & 0 \\ \hline 0 & \frac{1}{\Omega_0} \end{array} \right)$$

NORMALIZED DYNAMICS:

$$\tilde{A} = \left(\begin{array}{c|c} 0 & 1 \\ \hline 0 & 0 \end{array} \right)$$

Figure 3-5. System D Dynamics (Inertially Stable Configuration)



DYNAMIC CHARACTERISTICS:

1. BODY REFERENCE AXES ALIGNED WITH INERTIAL AXES
2. ZERO NOMINAL ANGULAR VELOCITY
3. MOMENTUM WHEEL ALONG ROLL WITH BIAS h_w

SCALING MATRIX:

$$S = \frac{1}{\sqrt{r_\theta} \Omega_0} \left(\begin{array}{c|cc} 1 & & 0 \\ \hline 0 & 1/\Omega_0 & 1 \end{array} \right)$$

NORMALIZED DYNAMICS:

$$\tilde{A} = \left(\begin{array}{c|ccc} 0 & & & 1 \\ \hline & 0 & 0 & c \\ 0 & 0 & 0 & 0 \\ & -d & 0 & 0 \end{array} \right)$$

DYNAMIC PARAMETERS:

$$c = h_w / (J_x \Omega_0)$$

$$d = h_w / (J_z \Omega_0)$$

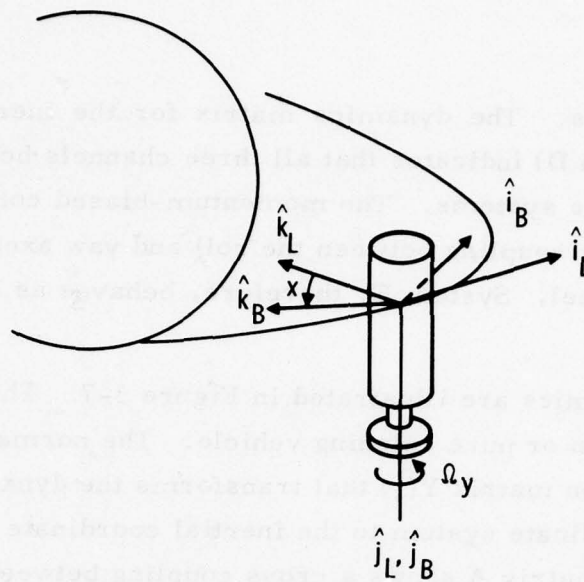
Figure 3-6. System E Dynamics (Inertially Stable Momentum-Biased Configuration)

vehicle configurations. The dynamics matrix for the inertially stable configuration (system D) indicates that all three channels behave as pure double integrator-type systems. The momentum-biased configuration (system E) shows a cross coupling between the roll and yaw axes as the result of the momentum wheel. System E, therefore, behaves as an oscillator-type system.

System F dynamics are illustrated in Figure 3-7. This system is designed for a dual-spin or pure spinning vehicle. The normalization matrix S contains the rotation matrix $Y(\gamma)$ that transforms the dynamics from the body reference coordinate system to the inertial coordinate system. The resulting dynamics matrix A shows a cross coupling between the inertial \hat{i}_I -axis and \hat{k}_I -axis through the parameter $\rho(1 - k)$. Unlike system A, this cross coupling may not be negligible since the ratio ρ is a function of the body spin rate as well as orbital angular velocity. In general, this coupling is strong enough to classify system F as an oscillator-type system.

In summary, the dynamics of the six basic attitude reference system conceptual designs presented in this section can be characterized in terms of double integrator-type dynamics and oscillator-type dynamics. The conceptual systems with their characteristic dynamics are identified in Table 3. This characterization greatly simplifies the performance analysis by reducing the number of dynamic configurations that must be simulated in the covariance analysis program. Coupled with the reduction in variables through the normalization procedure, this simplification permits the performance analysis of all six conceptual designs with only two sets of normalized parametric performance curves representing the performance capabilities of the two general classes of systems (double integrator and oscillator) with varying baseline parameters. These curves are presented in Paragraph D.

A third class of systems, the triple integrator, was included in the covariance analysis in addition to the double integrator and oscillator systems. The triple integrator system includes the effects of gyro biases on



DYNAMIC CHARACTERISTICS:

1. ORBIT RATE ABOUT PITCH AXIS
2. BODY SPIN ABOUT PITCH AXIS
3. TOTAL PITCH RATE IS Ω_y

SCALING MATRIX:

$$S = \frac{1}{\sqrt{r'_\theta}} \begin{pmatrix} Y(\gamma) & 0 \\ 0 & \frac{1}{\Omega_0} Y(\gamma) \end{pmatrix}$$

WHERE

$$Y(\gamma) = \begin{pmatrix} \cos \gamma & 0 & \sin \gamma \\ 0 & 1 & 0 \\ -\sin \gamma & 0 & \cos \gamma \end{pmatrix}; \gamma = \Omega_y t$$

NORMALIZED DYNAMICS:

$$\tilde{A} = \begin{pmatrix} 0 & 1 & 0 & 0 \\ 0 & 0 & 0 & 0 \\ 0 & 0 & 0 & 0 \\ -\rho(1-k) & 0 & 0 & 0 \end{pmatrix}$$

DYNAMIC PARAMETERS:

$$\rho = \Omega_y / \Omega_0$$

$$k = 1 - J_y / J_x$$

Figure 3-7. System F Dynamics (Dual-Spin or Spinner Configuration)

Table 3-3. Characterization of Conceptual Designs

System	On-Orbit Configuration	Characteristic Dynamics
A	Local Vertical Three-Axis Stable	Double Integrator
B	Local Vertical DSP	Double Integrator
C	Local Vertical Momentum-Biased	Oscillator
D	Inertially Stable	Double Integrator
E	Inertially Stable Momentum-Biased	Oscillator
F	Dual-Spin or Spinner	Oscillator

the estimation error through the addition of three bias states to the system dynamics matrix A of the double integrator system. These states represent the low frequency drift behavior of each of the three rate gyros implemented in the conceptual designs. The states affect the system performance by introducing a correlated source of measurement noise in the rate sensor in addition to the assumed white noise. The model used to represent the behavior of these gyro biases is a random walk produced by integration of white noise. Further details on the triple integrator system are presented in Sec-Appendix C.

The motivation for adding the triple integrator system to the covariance analysis is to determine the effects of gyro bias upon the performance of the conceptual designs. Estimation errors due to gyro biases would not be evident in the performance of the double integrator system unless a detailed simulation of this system, complete with a truth model reflecting gyro biases, was conducted. The covariance analysis of the triple integrator

D. COVARIANCE ANALYSIS STEADY-STATE RESULTS

The covariance analysis program was run with the normalized forms of the Ricatti and covariance update equations (III-18) and (III-19) to investigate the performance of the double integrator, triple integrator, and oscillator systems. Although these equations represent a mixed continuous rate/discrete attitude system, the performances of the totally continuous system and the totally discrete attitude update system were also investigated with the program by varying the update rate and the measurement noise parameters. As previously indicated, the performance of the mixed system approaches that of the continuous system as the update rate is increased. Further, as the rate measurement noise is increased, the mixed system performance approaches that of a system operating on discrete attitude information alone.

The performance parameters of interest in the covariance analysis are the steady-state estimation errors and transient responses for each of the three major classes of systems (double integrator, triple integrator, and oscillator). The steady-state performance for these systems is presented in the following discussion. Transient performance is discussed in Paragraph E. Steady-state results are presented as normalized curves of the maximum value of the mean-squared attitude estimation error $E(\theta^2)$ and the mean-squared rate estimation error $E(\omega^2)$ versus the normalized update interval T' for each class of system. The baseline parameter r'_ω , representing the quality of the sensors and defined by Eq. (III-22), was parametrically varied on the performance curves for each system. Additional baseline parameters were varied for the triple integrator and oscillator systems and are discussed with their respective steady-state curves below.

Due to the normalization, the steady-state curves present performance versus update intervals for many combinations of attitude and rate sensors. The equations for interpreting these curves have been discussed in Paragraph B, but will be repeated here for reference. The rms attitude error,

identified in this report as θ_{rms} , is obtained from the normalized mean-squared attitude estimation error using the equation

$$\theta_{\text{rms}} = \left[r'_{\theta} E(\theta^2) \right]^{1/2} \quad (\text{III-23})$$

where r'_{θ} represents the discrete attitude sensor measurement noise in (rad^2) and $E(\theta^2)$ is taken from the curves. The rms rate error, identified herein as ω_{rms} , is obtained using the equation

$$\omega_{\text{rms}} = \left[r'_{\theta} \Omega_0 E(\omega^2) \right]^{1/2} \quad (\text{III-24})$$

where Ω_0 is a scaling frequency defined by the equation

$$\Omega_0 = \left(\frac{q}{r'_{\theta} \alpha} \right)^{1/3} \quad (\text{III-25})$$

where α is an arbitrary scaling constant and q is the white noise equivalent area under the autocorrelation function of the disturbance acceleration. The normalized update interval T' is converted to regular time by the equation

$$T = \frac{1}{\Omega_0} T' \quad (\text{III-26})$$

and, for completeness, the baseline parameter r'_{ω} , which is parametrically varied on each curve, is defined by the equation

$$r'_{\omega} = \frac{r_{\delta\omega}}{r'_{\theta} \Omega_0} \quad (\text{III-27})$$

where $r_{\delta\omega}$ represents the rate sensor measurement noise in $(\text{rad}^2/\text{sec})$.

To illustrate the use of these curves, an example system with star mappers and rate gyros is introduced. If the rms measurement uncertainty resulting from the star sensor noise in this example system is on the order of 2 arc sec ($\approx 10^{-5}$ rad), the discrete attitude sensor noise parameter r'_{θ} is approximately 10^{-10} (rad^2). Assuming that the rms rate error would increase because of the effects of disturbance accelerations at 2×10^{-4} arc sec/sec ($\approx 10^{-9}$ rad/sec) each second with no measurements, then the acceleration noise parameter would be on the order of $q = 10^{-18}$ ($\text{rad}^2/\text{sec}^3$). Let the scaling parameter α be equal to 10^{-2} . Then, using Eq. (III-24), the scaling frequency is $\Omega_0 = 10^{-2}$ (1/sec) so that the normalized time is 100 times faster than real time in Eq. (III-25) for this example. Let the rms rate measurement uncertainty resulting from rate gyro noise be on the order of 0.06 deg/hr ($\approx 3 \times 10^{-7}$ rad/sec) and fully correlated for 1/2 sec. Then the rate sensor noise parameter $r_{\delta\omega}$ is approximately equal to 10^{-13} (rad^2/sec). The resulting measurement noise parameter r'_{ω} from Eq. (III-26) is equal to one-tenth. The pertinent parameters for this example system are summarized in Table 3-4. The values listed are used to illustrate the method of obtaining system performance information from the normalized curves shown in Figures 3-9 through 3-16 for each of the three classes of systems. These values represent a system with SPARS-quality instruments mounted on a moderately sized vehicle (inertias on the order of 10^3 slug-ft²) and perturbed by typical disturbance accelerations (10^{-6} ft-lb disturbance torques).

Table 3-4. Example System

Parameter	Description	Value
q	Acceleration Noise	$10^{-18} \text{ (rad}^2/\text{sec}^3)$
r'_{θ}	Attitude Sensor Noise	$10^{-10} \text{ (rad}^2)$
$r'_{\delta\omega}$	Rate Sensor Noise	$10^{-13} \text{ (rad}^2/\text{sec})$
α	Scaling Constant	10^{-2}
Ω_0	Scaling Frequency	$10^{-2} \text{ (sec}^{-1})$
r'_{ω}	Measurement Noise	10^{-1}

In addition to the scaling considerations just mentioned, it should be noted that only curves for the maximum values of the normalized mean-squared attitude and rate estimation errors $E(\theta^2)$ and $E(\omega^2)$ are presented in this section. "Maximum" refers to the peak errors of a uniformly updated mixed or discrete filter. Referring to Figure 3-8, which illustrates a typical mixed system time history generated by the covariance analysis program, it can be seen that the steady-state normalized mean-squared attitude error behaves as a sawtooth waveform between fixed maximum and minimum levels. The discontinuities occur whenever a discrete attitude update is processed. Between updates, the mean-squared error grows as the result of the presence of disturbance accelerations. This growth is inhibited in varying degrees (depending upon the gyro quality) by the continuous rate information available from rate gyros in the mixed system. Since the uniform update assumption is used in all the covariance runs for this study, the attitude updates or discontinuities occur at regular intervals as illustrated in Figure 3-8. The maximum or peak mean-squared estimation error that would be of interest for this particular run is the value $E(\theta^2)_{\text{MAX}}$ just prior to an update after the filter has reached steady state. The minimum

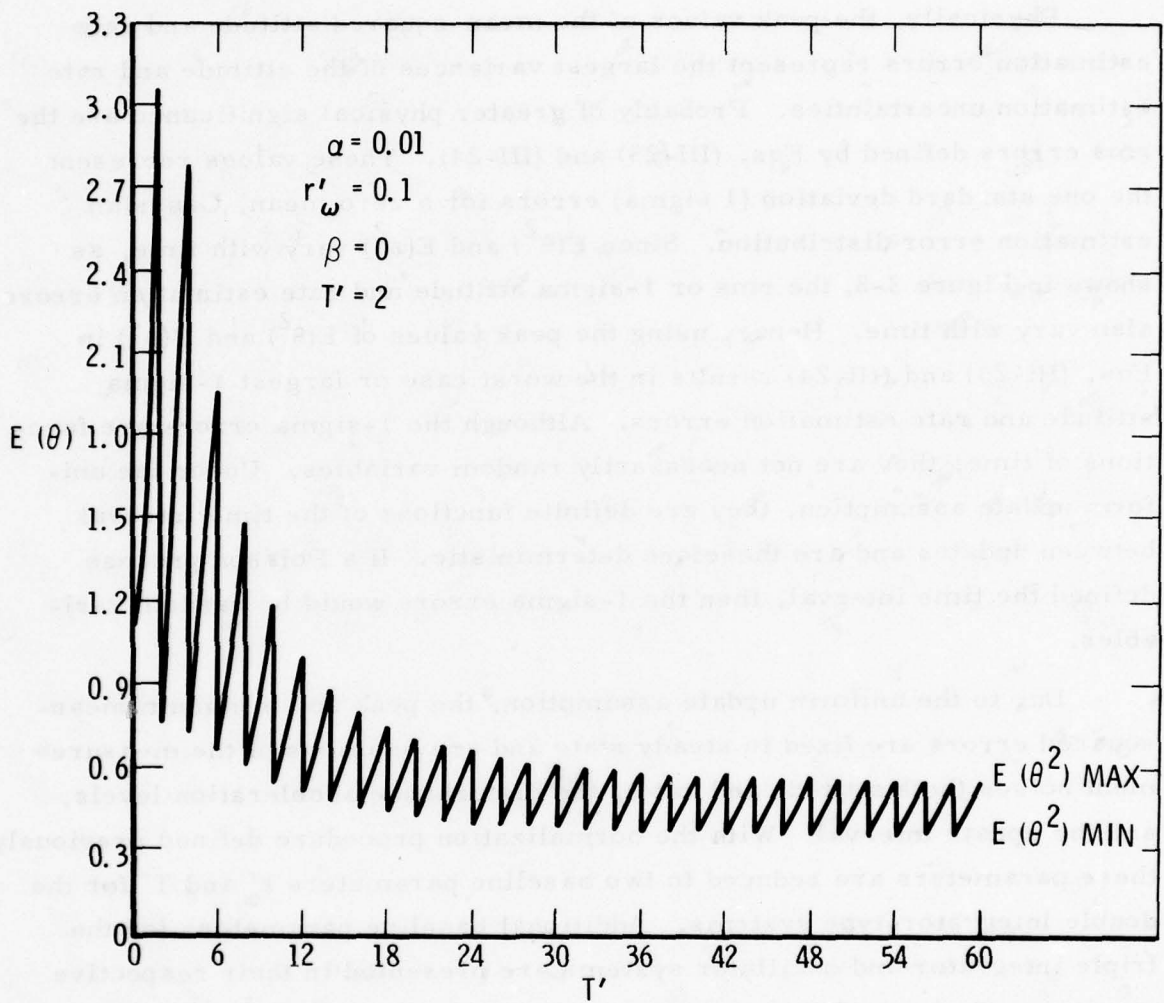


Figure 3-8. Discrete Attitude/Continuous Rate System Transient Response

value is also illustrated in Figure 3-8.

Physically, the peak values of the mean-squared attitude and rate estimation errors represent the largest variances of the attitude and rate estimation uncertainties. Probably of greater physical significance are the rms errors defined by Eqs. (III-23) and (III-24). These values represent the one standard deviation (1 sigma) errors for a zero mean, Gaussian estimation error distribution. Since $E(\theta^2)$ and $E(\omega^2)$ vary with time, as shown in Figure 3-8, the rms or 1-sigma attitude and rate estimation errors also vary with time. Hence, using the peak values of $E(\theta^2)$ and $E(\omega^2)$ in Eqs. (III-23) and (III-24) results in the worst case or largest 1-sigma attitude and rate estimation errors. Although the 1-sigma errors are functions of time, they are not necessarily random variables. Under the uniform update assumption, they are definite functions of the time interval between updates and are therefore deterministic. If a Poisson process defined the time interval, then the 1-sigma errors would be random variables.

Due to the uniform update assumption, the peak and minimum mean-squared errors are fixed in steady state and are functions of the measurement noises (both attitude and rate), the disturbance acceleration levels, and the update interval. With the normalization procedure defined previously, these parameters are reduced to two baseline parameters r'_ω and T' for the double integrator-type systems. Additional baseline parameters for the triple integrator and oscillator systems are presented in their respective sections. Each steady-state performance curve presented in the following discussion was generated by running the covariance simulation program from initialization to steady state for at least ten values of T' . This procedure was repeated for various r'_ω values, thereby generating performance curves for several ratios of sensor quality. The resultant curves

(Figures 3-9 through 3-16) were overlayed to show system performance versus the normalized update interval T' for various r'_ω values on a single plot for each system type.

1. DOUBLE INTEGRATOR PERFORMANCE

The normalized steady-state performance of a mixed continuous rate/discrete attitude system with double integrator-type dynamics is presented in Figures 3-9 and 3-10. Figure 3-9 is a normalized curve of the maximum steady-state mean-squared attitude estimation error $E(\theta^2)$ as a function of the update interval T' for each axis of a double integrator-type system with uniform updates. The sensor parameter r'_ω is varied from 10^6 , which represents a totally discrete attitude system, to 10^{-3} , which represents a mixed system with fairly high quality gyros. As expected, the variance of the error $E(\theta^2)$ increases with increasing update intervals. However, systems with higher quality gyros (smaller r'_ω) experience less performance degradation with increasing intervals because of the availability of continuous low noise rate measurements that inhibit error growth between discrete attitude updates. This is more evident when the rms attitude error is examined. Using the example system parameters from Table 3-4, the normalized time T' for an update interval of 100 sec is 1. From Figure 3-9, for $T' = 1$ and $r'_\omega = 10^6$, the normalized variance $E(\theta^2)$ is approximately equal to 0.6. Using Eq. (III-23), the rms error is $\theta_{\text{rms}} = 7.75 \times 10^{-6}$ rad, which is equivalent to an attitude error of 1.6 arc sec for the discrete system. However, for the mixed system with $r'_\omega = 0.1$, the variance at the same update interval is approximately equal to 0.25. Using Eq. (III-23) and converting the result to arc sec yields an attitude error of about 1.03 arc sec. Thus, the difference in performance between the totally discrete and the mixed systems with SPARS-quality sensors is approximately 0.6 arc sec for an update interval of 100 sec between star sightings. The equivalent performance at an interval of 1000 sec is 7.1 arc sec and 2.6 arc sec for the discrete and mixed systems respectively. The performance difference in this case is 4.5 arc sec, indicating that the presence of rate

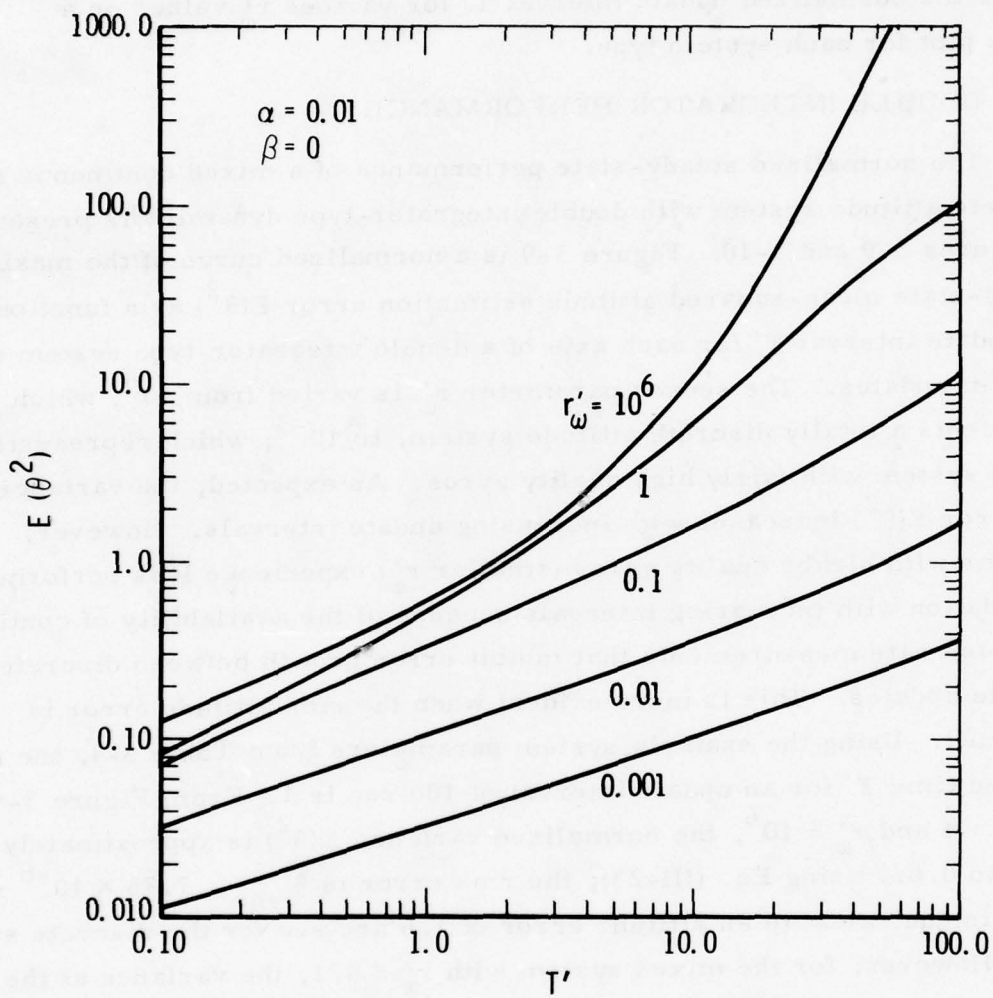


Figure 3-9. Double Integrator Performance, $E(\theta^2)_{MAX}$

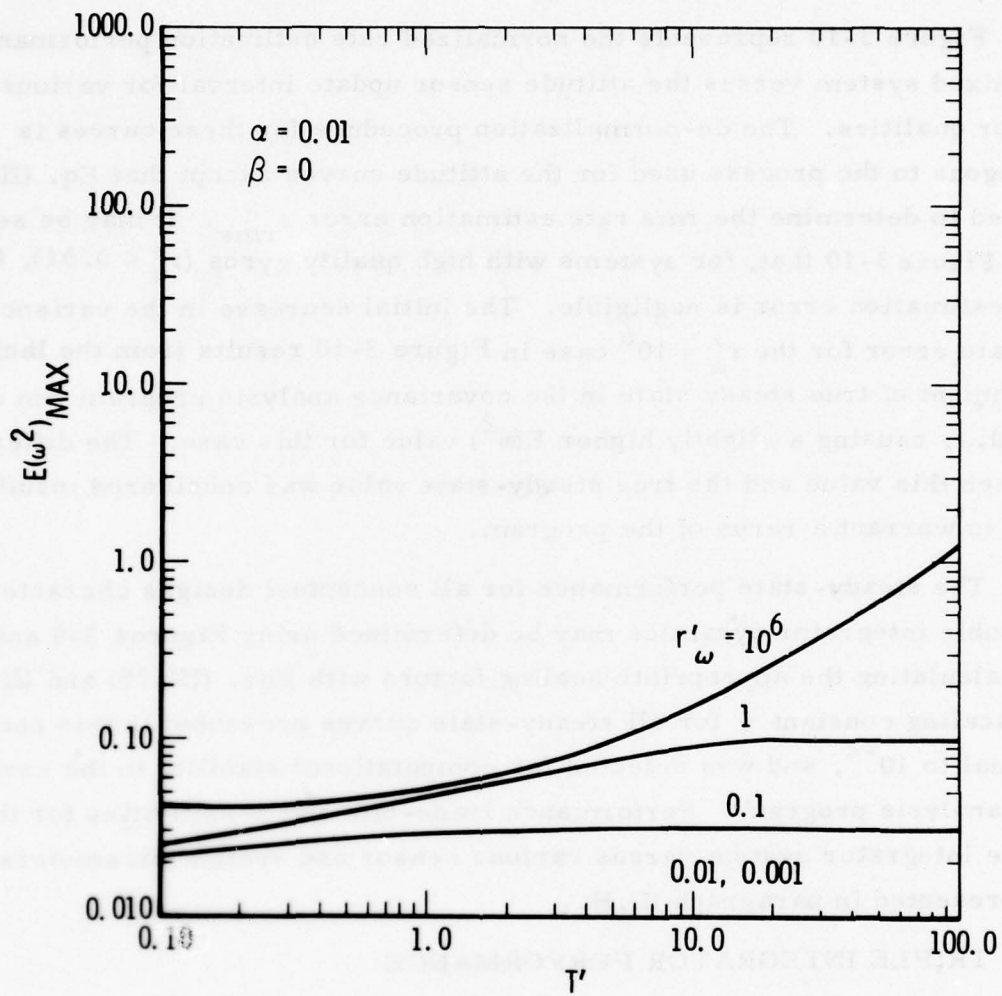


Figure 3-10. Double Integrator Performance, $E(\omega^2)_{MAX}$

information decreases the effects of disturbance accelerations upon system performance between star sightings.

Figure 3-10 represents the normalized rate estimation performance of the mixed system versus the attitude sensor update interval for various sensor qualities. The de-normalization procedure for these curves is analogous to the process used for the attitude curves except that Eq. (III-24) is used to determine the rms rate estimation error ω_{rms} . It may be seen from Figure 3-10 that, for systems with high quality gyros ($r'_\omega < 0.01$), the rate estimation error is negligible. The initial decrease in the variance of the rate error for the $r'_\omega = 10^6$ case in Figure 3-10 results from the lack of attainment of true steady state in the covariance analysis program run at $T' = 0.1$, causing a slightly higher $E(\omega^2)$ value for this case. The difference between this value and the true steady-state value was considered insufficient to warrant a rerun of the program.

The steady-state performance for all conceptual designs characterized by double integrator dynamics may be determined using Figures 3-9 and 3-10 and calculating the appropriate scaling factors with Eqs. (III-25) and (III-26). The scaling constant α for all steady-state curves presented in this section is equal to 10^{-2} , and was selected for computational stability in the covariance analysis program. Performance trade-offs and sensitivities for the double integrator system versus various sensor and system parameters are presented in paragraph III.H.

2. TRIPLE INTEGRATOR PERFORMANCE

As was indicated in paragraph III.C, a covariance analysis was conducted on the triple integrator system to investigate the effects of gyro bias upon the steady-state system performance. The bias model used was a random walk produced at the output of an integrator whose input is white noise. Thus, the state equation representing the gyro biases is

$$\dot{\underline{b}} = \underline{q}_b \quad (\text{III-28})$$

where the vector \underline{b} contains the bias components along each of the three measurement axes and \underline{q}_b represents the white noise input driving the bias. Equation (III-28) represents a third state equation to be integrated in addition to the state equations for $\underline{\delta\omega}$ and θ (Eqs. [III-3] and [III-4]) within the dynamic model, hence the name triple integrator for systems including gyro biases.

The triple integrator adds a new baseline parameter β to the covariance analysis. This parameter determines the level of white noise driving the bias and is defined by the equation

$$\beta = \frac{q_b}{q} \alpha \quad (\text{III-29})$$

where α is the scaling constant and q is the white noise equivalent of the disturbance acceleration. Thus, the normalized parameter β represents a ratio between the white noise driving the gyro bias and the equivalent white disturbance acceleration noise driving the vehicle dynamics. All other baseline parameters and scaling equations for the triple integrator are identical to those for the double integrator.

The covariance analysis program was run with triple integrator dynamics to obtain steady-state performance data similar to the curves obtained for the double integrator. These data are presented in Figures 3-11 and 3-12. The normalized variance of the attitude estimation error $E(\theta^2)$ is presented in Figure 3-11 as a function of the normalized update interval T with varying sensor qualities r'_w . Figure 3-12 is an illustration of the normalized variance of the rate estimation error $E(\omega^2)$ as a function of the same parameters. De-normalization of these curves is identical to the procedure used for the double integrator curves. The value of $\beta = 0.001$, selected for the triple integrator, results in a noise level, driving the gyro bias, of one-tenth the magnitude of the disturbance acceleration noise. Using the

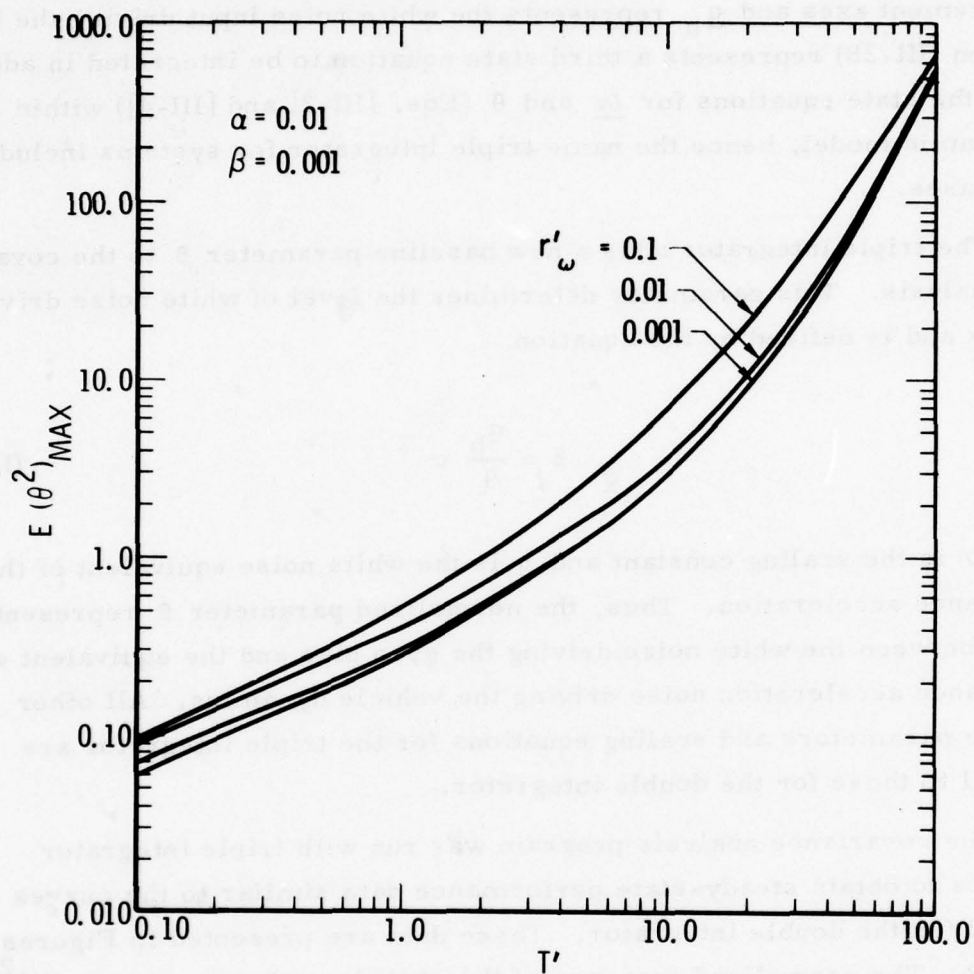


Figure 3-11. Triple Integrator Performance, $E(\theta^2)_{MAX}$

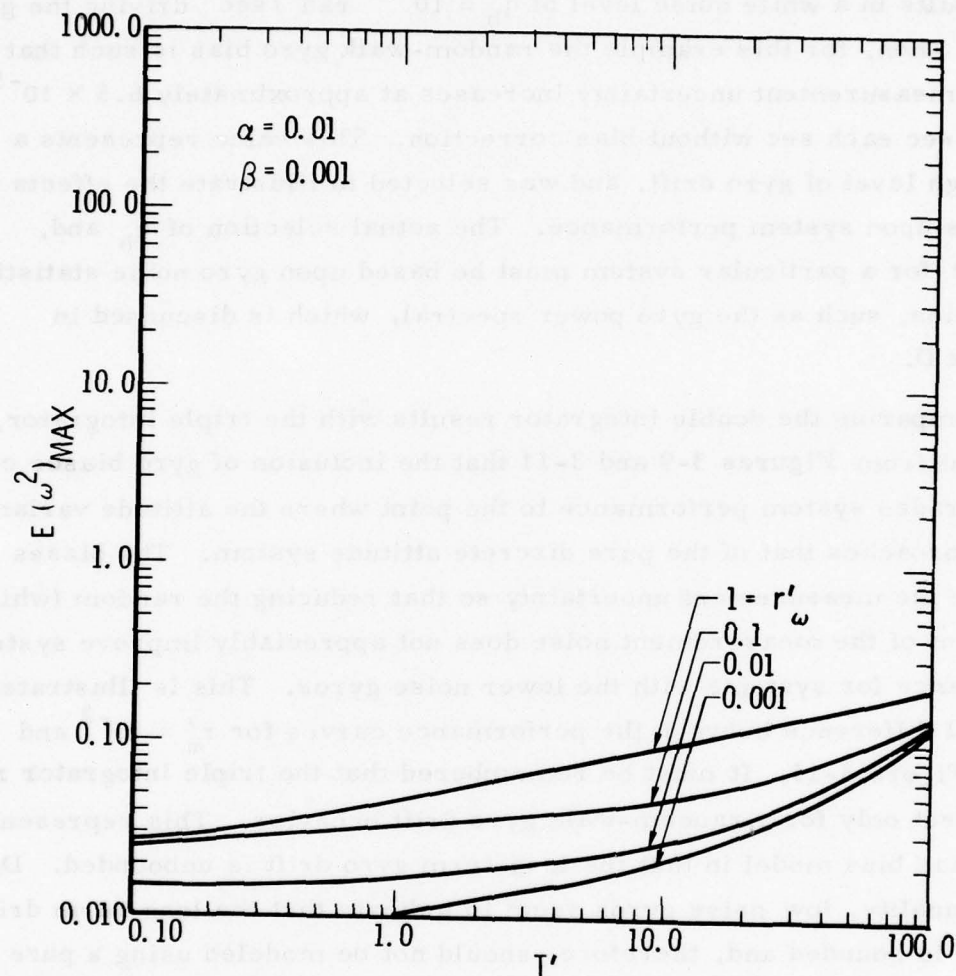


Figure 3-12. Triple Integrator Performance, $E(\omega^2)_{MAX}$

example system parameter values of Table 3-4 in Eq. (III-29), this value of β results in a white noise level of $q_b = 10^{-19} \text{ rad}^2/\text{sec}^3$ driving the gyro biases. Then, for this example the random-walk gyro bias is such that the rate measurement uncertainty increases at approximately 6.5×10^{-5} arc sec/sec each sec without bias correction. This value represents a fairly high level of gyro drift, and was selected to illustrate the effects of gyro bias upon system performance. The actual selection of q_b and, hence, β for a particular system must be based upon gyro noise statistical information, such as the gyro power spectral, which is discussed in Appendix D.

Comparing the double integrator results with the triple integrator, it is evident from Figures 3-9 and 3-11 that the inclusion of gyro biases considerably degrades system performance to the point where the attitude variance $E(\theta^2)$ approaches that of the pure discrete attitude system. The biases dominate the measurement uncertainty so that reducing the random (white) component of the measurement noise does not appreciably improve system performance for systems with the lower noise gyros. This is illustrated by the small difference between the performance curves for $r_w' = 10^{-2}$ and 10^{-3} in Figure 3-11. It must be remembered that the triple integrator results are correct only for a random-walk gyro drift behavior. This represents a worst-case bias model in that the long-term gyro drift is unbounded. Data on high quality, low noise gyros seem to indicate that the long-term drift behavior is bounded and, therefore, should not be modeled using a pure random walk. Other drift models were not considered in this analysis due to time constraints; however, recommendations concerning gyro noise modeling and testing are included in Section IV. In general, the triple integrator results indicate that measurement noise sources other than white noise can drastically affect system performance and should not be neglected in any detailed performance analysis.

In particular, gyros exhibiting low frequency drift behavior in the form of a random walk with driving noise levels on the order of one-tenth the

disturbance acceleration noise are of little benefit to the mixed system. The performance of a system with these gyros is, for all practical purposes, equal to the performance of a double integrator system with mappers and no rate information.

3. OSCILLATOR PERFORMANCE

As indicated in Table 3-3, three of the six basic conceptual designs can be characterized as having oscillator-type dynamics. In particular, their normalized dynamics matrices \tilde{A} are defined in Figures 3-4, 3-6, and 3-7. To evaluate the performance of these systems, a single generalized oscillator system was used in lieu of three different oscillator dynamics models. The dynamics matrix of the generalized oscillator system used in the covariance analysis is

$$\tilde{A} = \left(\begin{array}{ccc|c} 0 & 0 & -\eta & \\ 0 & 0 & 0 & I \\ \eta & 0 & 0 & \\ \hline & 0 & & 0 \end{array} \right) \quad (\text{III-30})$$

The primary difference between the generalized matrix of Eq. (III-30) and the dynamics matrices of Figures 3-4, 3-6, and 3-7 lies in the fact that cross-axis coupling is contained solely in the kinematics or attitude geometry of the generalized system. The dynamics matrices of the oscillator-type conceptual designs contain cross-axis coupling in the dynamics or angular velocity states as well as possible coupling in the kinematics as the result of quarter-orbit effects. The generalized oscillator (Eq. [III-30]) is derived from the conceptual design oscillator cases by a transformation from the body reference frame to a nonnutational reference frame. This coordinate transformation places all cross-coupling effects solely in the attitude states

or kinematics, and results obtained in this nonnutational frame are equally as valid as those obtained in the body reference frame.

The only restrictive assumption used in conjunction with the covariance analysis of the generalized oscillator system is that the cross-axis coupling is symmetric and represented by the normalized dimensionless parameter η as indicated in Eq. (III-30). This assumption permits the description of the cross coupling by one variable instead of two and thus reduces the number of computer runs necessary to determine oscillator performance. It is equivalent to the assumption that the inertias along the principal axis normal to a momentum bias are equal.

The covariance analysis of the general oscillator system was run for two levels of cross-axis coupling ($\eta = 0.1$ and 0.01), representing a strongly cross-coupled system as a result of momentum due to small onboard wheels. These results are presented in Figures 3-13 through 3-16. Maximum values of $E(\theta^2)$ and $E(\omega^2)$ for the strongly coupled oscillator system versus T' and at three values of r'_ω are shown in Figures 3-13 and 3-14. Similar results for the weakly coupled system are illustrated in Figures 3-15 and 3-16. The baseline parameter definitions and de-normalization procedures are the same as those used in the double integrator analysis. Although the oscillator is a cross-coupled system, the performance results given here are in terms of single-axis curves. From the generalized oscillator dynamics matrix (Eq. [III-20]), it is evident that the y-axis is uncoupled and behaves like a pure double integrator. Also, since the cross coupling between the x and the z-axes is symmetric, their estimation errors behave similarly with time and, therefore, the steady-state performance of these axes is identical. Hence, the oscillator performance data contained in Figures 3-14 through 3-16 apply to each of the two coupled axes. The third axis performance can be obtained directly from the double integrator curves shown in Figures 3-9 and 3-10.

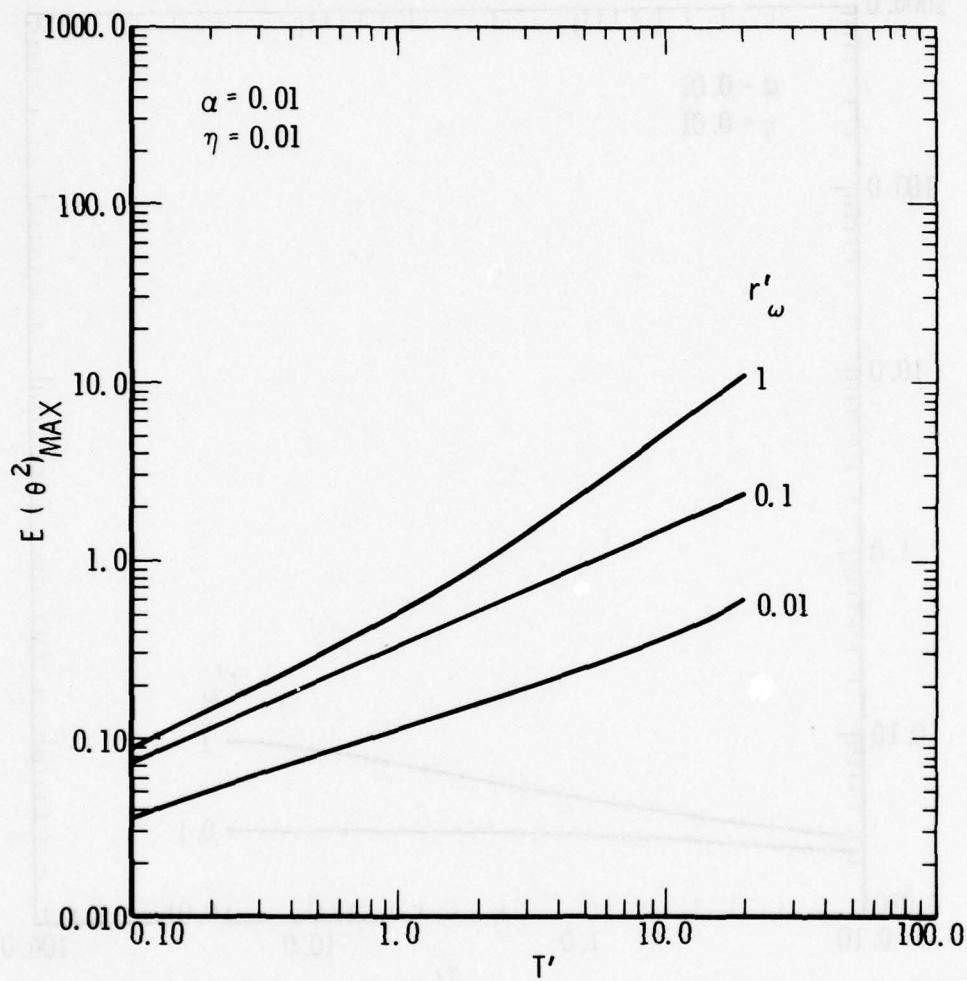


Figure 3-13. Oscillator Performance, $E(\theta^2)_{MAX}$, $\eta = 0.01$

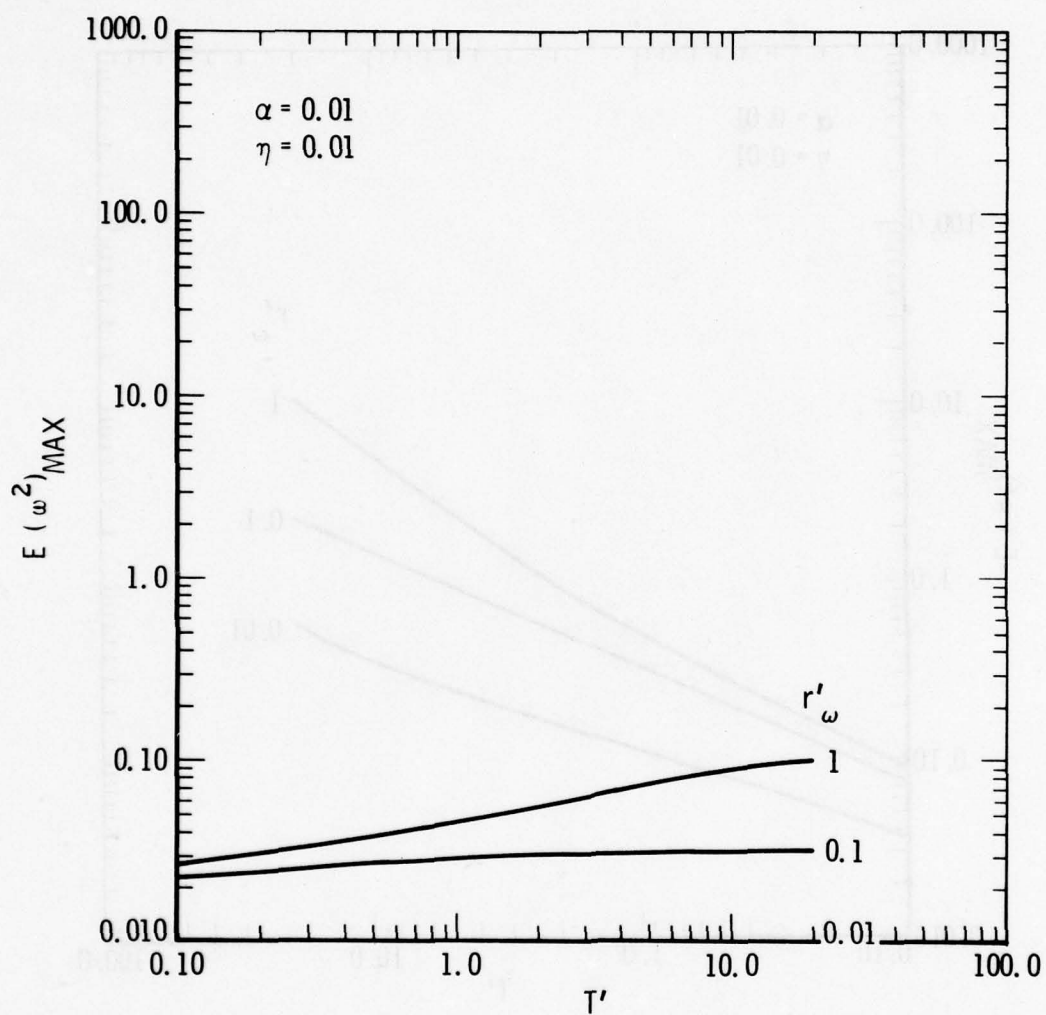


Figure 3-14. Oscillator Performance, $E(\omega^2)_{MAX}$, $\eta = 0.01$

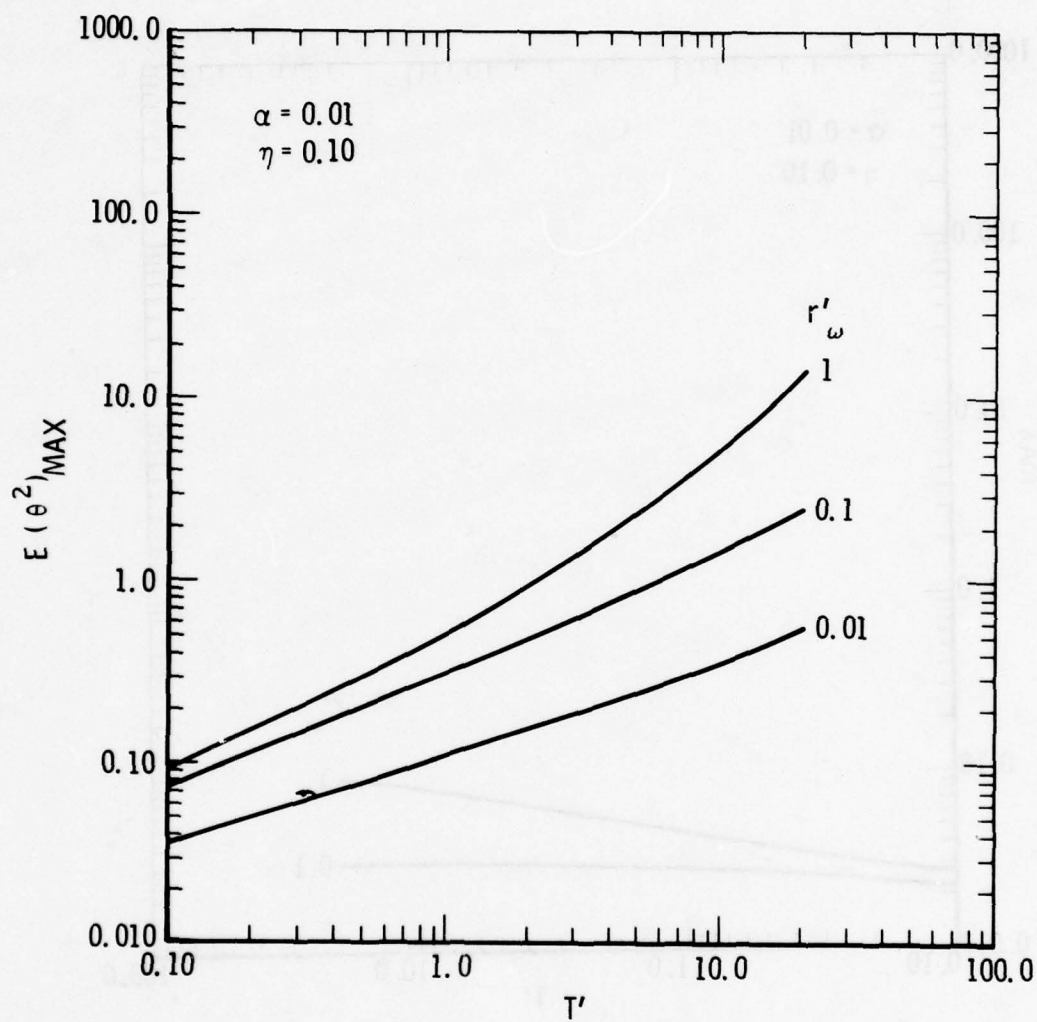


Figure 3-15. Oscillator Performance, $E(\theta^2)_{MAX}$, $\eta = 0.10$

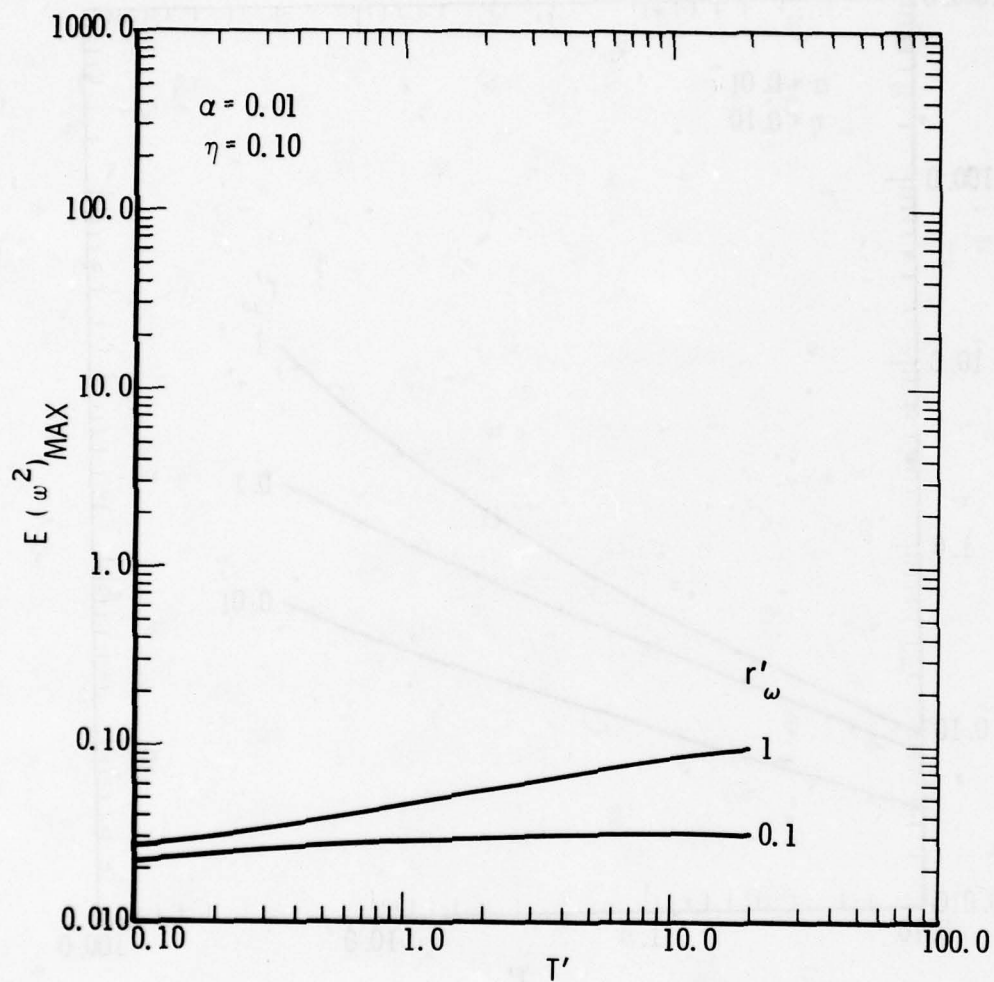


Figure 3-16. Oscillator Performance, $E(\omega^2)_{MAX}$, $\eta = 0.10$

Comparison of the $E(\theta^2)$ curves for the weakly coupled oscillator (Figure 3-13) with those for the double integrator (Figure 3-9) shows virtually no difference in performance. Thus, for cross-axis coupling ratios of $\eta = 0.01$ or less, the steady-state performance of oscillator-type systems can be determined from the double integrator curves. Comparison of the strongly coupled oscillator performance (Figure 3-15) with the double integrator performance curves indicates that, for the poorer quality rate sensor systems, the oscillator system out-performs the double integrator system. However, this performance improvement is the result of the fact that estimation errors between discrete updates in the oscillator system behave in a bounded sinusoidal manner whereas the errors in a double integrator system grow in an unbounded secular fashion between updates. Thus, for the higher update rates (shorter update intervals), the performance advantage of the oscillator-type system over the double integrator system is negligible. As the update interval increases, the performance improvement increases. The performance advantage of the oscillator system also improves as the quality of the rate sensor decreases (i.e., r'_ω increases). This is a result of the Kalman filter's heavier reliance upon the dynamic model as the measurement noise increases.

Although the oscillator is capable of better performance than the double integrator because of the bounding of errors between updates, this performance advantage appears to be small even at fairly large update intervals and cross-coupling levels. Using the example system parameters of Table 3-4, the oscillator normalized performance for a 10-percent cross-coupled ($\eta = 0.1$) system at an update interval of 1000 sec ($T' = 10$ for $\Omega_0 = 10^{-2}$) is approximately $E(\theta^2) = 1.45$ based on the $r'_\omega = 0.1$ curve in Figure 3-15. Using Eq. (III-23) with $r'_\theta = 10^{-10} \text{ (rad)}^2$, the rms attitude estimation error (θ_{rms}) for this example is $1.20 \times 10^{-5} \text{ (rad)}$ or approximately equal to 2.48 arc sec. The double integrator performance for the same update interval and instrument qualities results in a normalized variance

of $E(\theta^2) = 1.60$. Again using Eq. (III-23), the estimation error for this example is $\theta_{\text{rms}} = 1.26 \times 10^{-5}$ or 2.61 arc sec.

Thus the difference in performance between the double integrator and the oscillator is 0.13 arc sec. This is a performance advantage of only 4 percent in favor of the oscillator. Bearing in mind that this advantage diminishes with increasing gyro quality of update rate, it may be concluded that the oscillator performance is essentially the same as that of the double integrator for most applications. The implication of this conclusion is that the dynamic model implemented in the attitude estimation filter for a vehicle with cross-coupled dynamics (i.e., spinning a momentum-biased satellite) need not include cross-axis coupling since the estimator performance is essentially the same with or without cross coupling. However, this conclusion is based on a limited covariance analysis of the oscillator (with 1 and 10-percent cross coupling) and, thus, it cannot be assumed to be valid for all possible reference systems for future satellite missions and configurations. Detailed analyses should be conducted for each particular system before simplifying the estimator dynamic model. However, for the purposes of this technology study as well as any mission planning applications, this conclusion seems reasonable. System performance sensitivities and trade-offs, presented in paragraph III.H, are based primarily upon double integrator results.

E. CONVERGENCE PERFORMANCE OF CONCEPTUAL
DESIGNS

The convergence or response time of an attitude reference system is the time duration from system initialization to the settling of attitude reference errors below the system accuracy requirement. System initialization would occur after orbital injection and probably following station-keeping maneuvers. The convergence behavior is, therefore, the transient response of the reference system.

The transient response of an attitude reference system is a function of the types of algorithms used to process the attitude sensor output signals and the transient response of the attitude estimation filter. The filter transient response can be well defined in terms of sensor noise parameters, initial uncertainties, and update rates. Transient response curves for both the continuous and mixed continuous/discrete filters are presented in paragraph E.2 below. It should be emphasized, however, that attitude estimation filter transient response is often not the dominant influence on the total system transient response and, hence, gives only a limited indication of system convergence time. The star identification problem can be of greater impact on the convergence time in that a false identification during the filter initial transient will result in a bad measurement and considerably delay the convergence.

The attitude sensor signal processing method is the other major influence upon system transient response. Unlike the filter transient response, this influence is difficult to define since detailed sensor and signal processing models are required to describe adequately the transient behavior of each conceptual design. Such modeling is highly mission and sensor dependent and would thus be too restrictive in scope and prohibitive in time to include in this study. However, a brief qualitative discussion of the effects of the signal processing method upon system convergence time is presented in the following subsection.

1. SIGNAL PROCESSING EFFECTS ON SYSTEM CONVERGENCE

The attitude sensor output signal must be processed in some fashion before attitude measurement data can be supplied to the estimation filter. The purpose of this processing is to determine if the sensor output is due to a valid reference object within the sensor field of view (FOV) or if the output is due to background noise including other objects not used for reference purposes. Moreover, if there are multiple candidate reference objects, the output processing must be able to identify the object being viewed. An example of such a detection and identification processing scheme is a star catalog search routine used in conjunction with a star sensor system.

The basic goal of the signal processing scheme is to maximize the probability of rejecting false objects while maintaining a high probability of detecting true reference objects. The latter consideration is particularly important in mapper systems to maintain a high attitude measurement rate. Generally, this goal represents a conflicting trade-off. For example, star sensor systems that have a high probability of rejecting false or misidentified stars usually accept fewer stars than systems with a lower rejection probability. The latter type of system accepts more stars but with a greater risk of accepting a false or misidentified star.

The convergence time for tracker systems is a function of the tracker acquisition time. This is the time required to locate and lock on to a reference object. Using a star tracker example, it is evident that a tracker system that accepts more stars will generally converge faster than one that must search out a relatively few number of acceptable stars. The problem with such a system is the higher probability of locking on to a false or misidentified star. Should this occur, the system may never converge unless some override feature is available. Exercise of this feature would reset the system to start acquisition again.

The same basic considerations apply to a mapper system. However, the detection and identification procedure occurs repeatedly, each time a discrete mapper output signal occurs. Using a star mapper system example, whenever a mapper signal occurs the signal processing scheme must determine if the output is due to a true star being scanned by the FOV. This is usually accomplished by consulting a star catalog that lists the probable stars in the FOV at the time the signal occurred. Assuming that the probability of false or misidentified star rejection is 100 percent, the fastest converging mapper system is obviously the system with the highest measurement rate, and the convergence behavior would be strictly a function of the filter transient response. In reality, the probability of false star rejection will be something less than 100 percent due to measurement and processing uncertainties. The convergence time is then strongly influenced by the possibility of accepting false or misidentified stars. To determine this effect adequately, a detailed simulation including the system truth model must be exercised in a Monte Carlo fashion with randomly occurring false measurements. Convergence time statistics would then be determined based on ensemble averaging with various false measurement occurrence rates and initial conditions. Such an effort cannot be undertaken unless a specific system is defined in detail including sensors, processing electronics, and estimation filter. For the purposes of this study, the effects of the signal processing method upon system convergence have been ignored by assuming that all measurements, whether they are discrete or continuous, are due to true, properly identified reference objects. Given this assumption, the system convergence performance is strictly a function of the attitude estimation filter transient response.

2. ESTIMATION FILTER TRANSIENT RESPONSE

The transient response of the attitude estimation filter used by the conceptual designs in this study is a function of the initial attitude and rate uncertainties as well as sensor noise parameters and, for the mixed filter,

update rate. The effects of sensor noise and update rate upon the filter transient response are presented using a double integrator example system that operates with continuous and mixed continuous/discrete sensors. A normalized set of initial attitude and rate uncertainties was used in generating these transient data. Actual initial conditions must be determined from detailed mission analyses that consider such factors as attitude control deadbands and booster dispersions. These considerations were not included in this study because they are so highly mission dependent.

Referring to the description of the continuous, single-axis double integrator system discussed in Section IV, the normalized Ricatti differential equation can be written as

$$\frac{dE}{d\tau} = AE + EA^T - ER'E + Q' \quad (\text{III-31})$$

where

$$A = \begin{pmatrix} 0 & 1 \\ 0 & 0 \end{pmatrix} \quad Q' = \begin{pmatrix} 0 & 0 \\ 0 & 1 \end{pmatrix} \quad R' = \begin{pmatrix} 1 & 0 \\ 0 & (2\zeta)^2 - 2 \end{pmatrix} \quad (\text{III-32})$$

Equation (III-31) indicates that the transient response of the continuous double integrator system is a function of the initial normalized covariance value $E(t = 0)$ and the normalized parameter

$$\zeta \equiv \frac{1}{2} \sqrt{2 + \frac{1}{r_{\delta w}} \sqrt{r_{\theta} q}} \quad (\text{III-33})$$

The time in Eq. (III-31) has been normalized by the scaling frequency

$$\Omega \equiv \left(\frac{q}{r_\theta} \right)^{1/4} \quad (\text{III-34})$$

The foregoing ζ and Ω parameters can be interpreted for the steady-state Kalman filter as the filter damping ratio and bandwidth, respectively. During transient operation, the filter bandwidth is initially large so that the filter can rapidly converge to an approximate value of the system state. As time progresses, the bandwidth is decreased to provide more smoothing of the signal from high frequency noise. In the steady state, the bandwidth approaches the value defined by Eq. (III-34). The parameter ζ cannot be interpreted as a damping ratio during transient operation. This may be seen from the fact that the minimum value of ζ is $1/\sqrt{2}$, reached when the rate measurement noise $r_{\delta\omega}$ becomes very large ($r_{\delta\omega} \gg r_\theta q$). Moreover, the larger the value of ζ , the faster the filter response becomes. This may be seen from Figure 3-17, which represents an overlay plot of the normalized attitude estimation error variance $E(\theta^2)$ transient response versus normalized time τ for various values of ζ . The normalized initial condition used for the transient responses in Figure 3-17

$$E(t = 0) = \begin{pmatrix} 1 & 0 \\ 0 & 1 \end{pmatrix}$$

Looking at Eq. (III-33), which defines ζ , the larger values of ζ are obtained when the rate measurement uncertainty $r_{\delta\omega}$ becomes very small. Under this circumstance the rate measurement is very accurate, which tends to inhibit growth of the estimation errors to a greater extent than with less accurate rate measurements. The result is faster filter convergence as

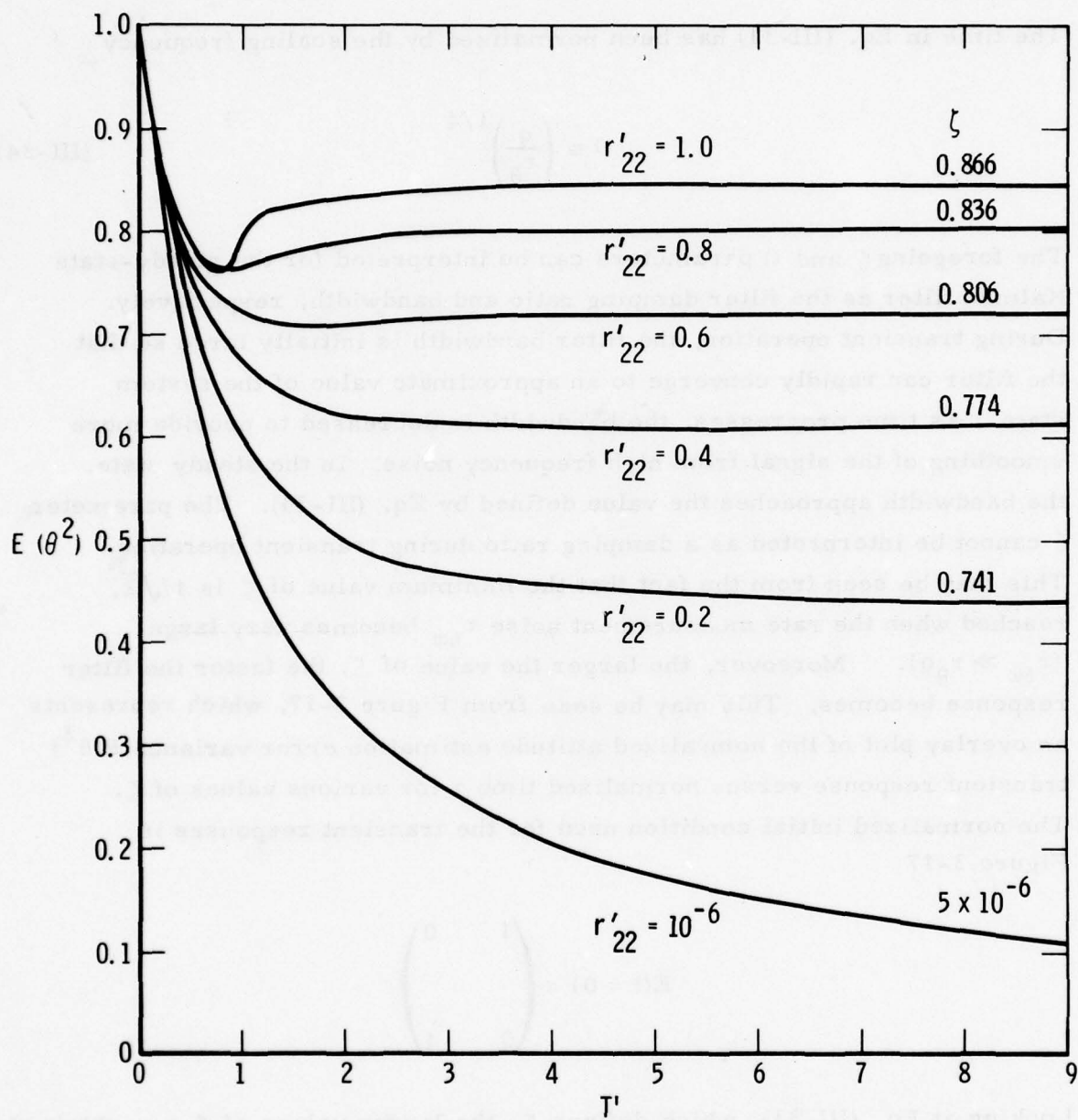


Figure 3-17. Continuous System Normalized Transient Response

can be seen from Figure 3-17. Alternately, the larger the disturbance environment, represented by q , the larger the value of ζ , resulting in faster convergence. This is because large values of q result in large initial system bandwidths Ω , which allow rapid initial convergence to an approximate value of the system state.

Using the parameters listed in Table 15, with a continuous attitude sensor noise r_θ equal to 10^{-10} (rad^2/sec), the appropriate transient response curve for the example system is determined by calculating ζ from Eq. (III-33). This results in a ζ value of 0.725. From Figure 17, the closest response curve is the transient response for ζ of 0.741. Fitting this curve to an exponential results in a time constant of $\tau = 0.8$. From Eq. (III-34), using the example system parameters results in a scaling frequency of $\Omega = 10^{-2}$ (1/sec). Hence, the time constant of the system is

$$T = \frac{1}{\Omega} \tau = 80 \text{ sec}$$

It can be seen that such a system time constant is of negligible concern compared to the continuous sensor acquisition problem mentioned at the beginning of this subsection. Even an order-of-magnitude increase in the filter time constant for the continuous system would have minimal effect upon convergence requirements.

The transient response for a mixed system with continuous rate sensors and discrete attitude sensors operating at three different update intervals is presented in Figures 3-18, 3-19, and 3-20. As in the continuous case, the initial condition used for the normalized attitude error variance $E(\theta^2)$ is unity, and the time is normalized by Eq. (III-26) where the mixed system bandwidth is defined by Eq. (III-25). The scaling factor for the transient response is $\alpha = 10^{-2}$, and the instrument quality used for the three runs is $r'_\omega = 0.1$ in order to match the example system parameters. As in the steady-state case, only the peak variance is indicated.

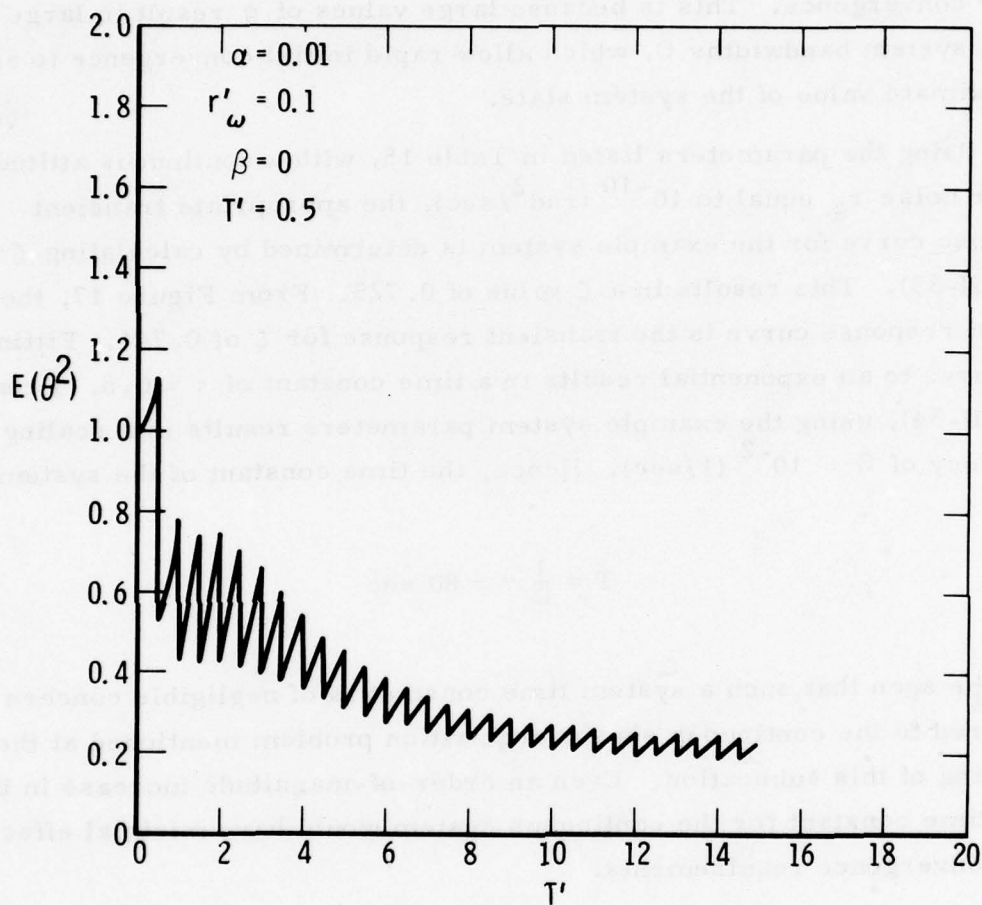


Figure 3-18. Transient Response, $T' = 0.5$

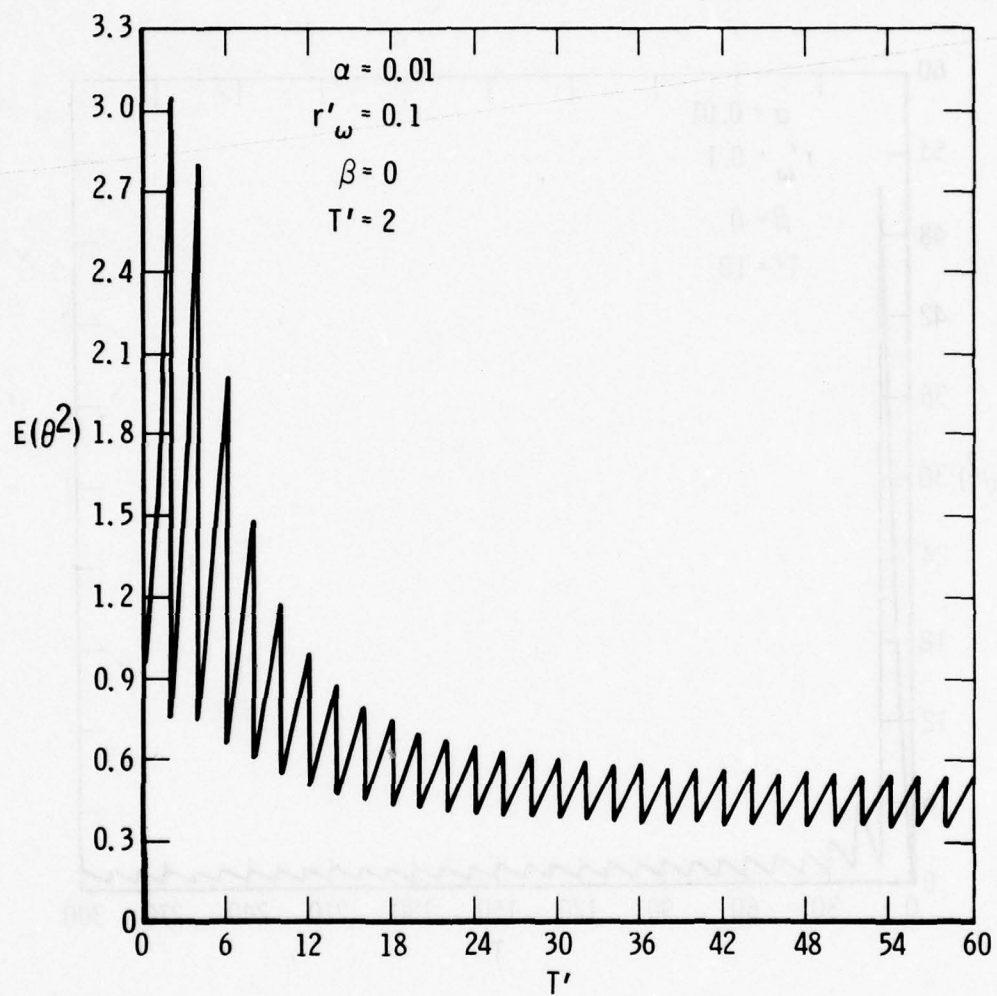


Figure 3-19. Transient Response, $T' = 2$

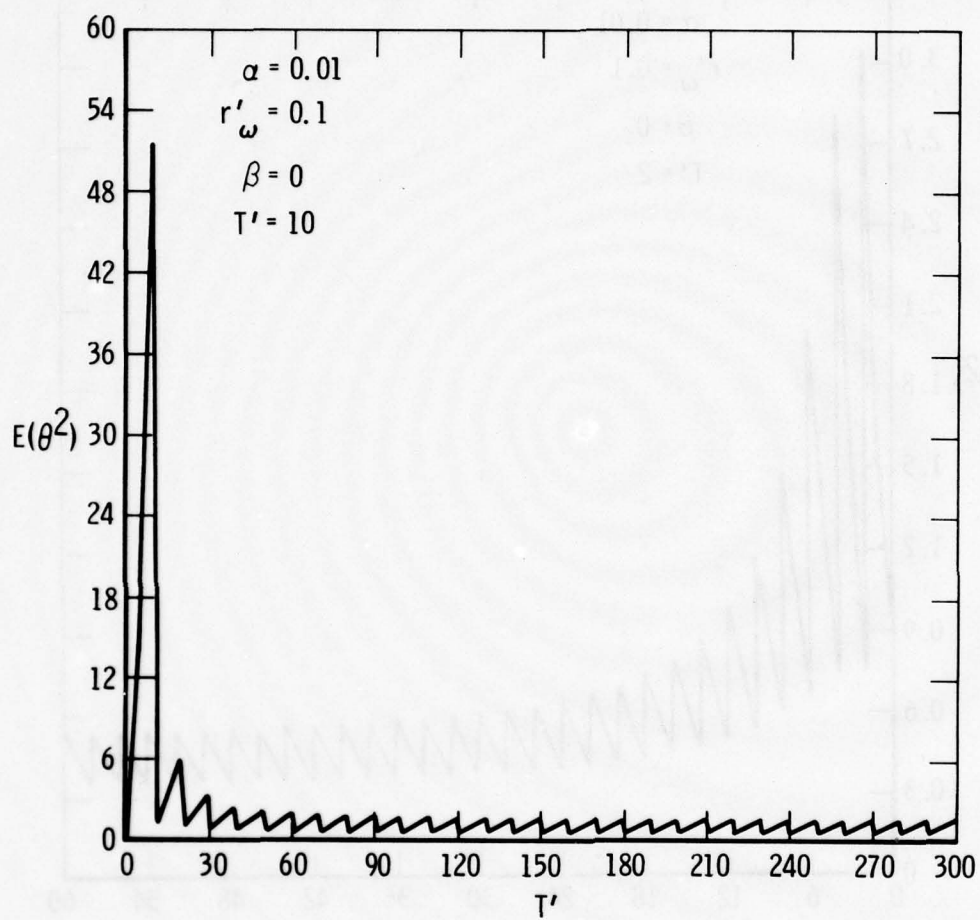


Figure 3-20. Transient Response, $T' = 10$

The mixed system estimation filter transient response is shown in Figure 3-18 for a normalized update interval of $T' = 0.5$. Using the example system scaling frequency of $\Omega_0 = 10^{-2} \text{ (sec)}^{-1}$, the update interval is equal to 50 sec in real time. It can be seen from this figure that the filter has practically reached steady state by the twentieth update ($t' = 10$), which results in a filter convergence time on the order of 15 min. Assuming that all measurements are correct, the filter transient response for this system is well within a convergence time of 1 hr.

Figure 3-19 is an illustration of the transient behavior for a mixed system with an update interval of $T' = 2$, or, for the example system, a time of 200 sec between updates. At 1 hr ($T' = 36$) the system performance has almost reached steady state with a normalized attitude error variance of 0.6. This level of performance is attained after 18 updates. The system could, therefore, be marginal for a 1-hr convergence time requirement, depending on how close the performance must be to steady state at the convergence time limit.

In Figure 3-20, the transient response curve is shown for a system with update intervals of $T' = 10$ or $T = 1000$ sec for the example. Because of the scaling it is difficult to establish the exact nature of the response. However, it appears that the error is still decaying at $T' = 60$ or an equivalent real time of about 1.7 hr. Such a system would obviously not meet a 1-hr convergence time requirement.

Usually, systems calling for fast convergence require high steady-state performance. Such systems, if relying on mappers, require short update intervals to maintain steady-state performance. Thus, systems with average update intervals on the order of 1000 sec will probably not be required to converge within 1 hr.

F. ANALYTICAL PERFORMANCE RESULTS

Thus far, the approach taken in the analysis of the performance of the attitude reference system conceptual designs has been a "brute force" covariance analysis with computer programs to conduct covariance analyses of the three major dynamic system types, i.e., double integrator, triple integrator, and oscillator, identified in Section III.C as most representative of the behavior of the conceptual designs. The somewhat idealized case of uniform update intervals was assumed in the covariance analyses computer simulation. Such an assumption approaches reality for spinning satellite configurations. However, its validity has not yet been established for the local vertical configurations where the update interval may follow a random sequence.

Based upon the foregoing covariance analysis computer program results, the following major performance conclusions have been drawn:

- a. The effects of attitude estimation filter transient response upon system convergence time are negligible compared to the sensor signal processing effects.
- b. Rate gyro bias in the form of a random walk degrades the performance of a mixed system to a point approaching a pure discrete attitude system for bias driving levels of 10 percent of the random disturbance acceleration or greater.
- c. The performance of a system with cross-axis coupling in the dynamic model (oscillator) is virtually the same as that of a system with no cross coupling (double integrator) for cross-coupling levels up to 10 percent.

In addition to these major conclusions, a series of normalized steady-state performance curves was generated that may be used to determine the performance of mixed continuous rate/discrete attitude systems for various sensor qualities and update intervals. The effects of cross coupling may be determined from the oscillator performance curves, and the effects of gyro bias from the triple integrator performance curves.

To improve understanding of the sensitivities illustrated by these normalized performance curves as well as to establish a relationship between

the performance of the uniform update system and the random update system, a series of studies was performed with the intent of deriving analytical performance relations. These efforts, which were based primarily upon the double integrator model, are presented in paragraphs F.1 through F.4.

Paragraph F.1 is a discussion of analytical performance sensitivities to various system and sensor parameters for the double integrator system with continuous attitude and rate measurements or discrete (uniform update interval) attitude measurements only. In Paragraph F.2, an analysis is presented of the effects of random (Poisson) update intervals upon the performance of a mixed system, and analytical performance bounds are derived that may be used to define the average performance of the random update system. The performance of a suboptimal (single integrator) filter similar to the SPARS filter is described in Paragraph F.3, and its performance is compared with the fully optimal (double integrator) filter. In addition, performance comparisons are made of the uniform and random update suboptimal filters. Finally, in Paragraph F.4, a discussion is presented of the effects of measurement geometry on system performance, and two approaches are defined for the determination of optimal sensor configurations.

1. SPACECRAFT ATTITUDE ESTIMATION FILTER RESPONSE

a. Introduction

A description is presented in this subsection of the characteristics of the Kalman filter that estimates attitude angles and rates from continuous and discrete measurements of attitude angles. It is assumed that the spacecraft axial cross coupling is negligible and the attitude angles are simple integrals of the attitude rates. In addition, the vehicle is subject to random disturbance torques and the attitude angle measurements are corrupted by additive random noise.

The dynamic characteristics of the Kalman filter are described using the concepts of filter gain, bandwidth, and damping ratio. Since a Kalman filter is a linear filter, it can be described in terms of a linear (time-varying)

system. In the steady state, it becomes a time-invariant (Wiener) filter. This filter can be described by using linear system analysis techniques including frequency domain methods such as Bode diagrams. Since the order of the filter (the number of poles) is equal to the number of state variables estimated, in this example the filter is second order and may be described by its gains, natural frequency, and damping ratio.

The steady-state performance characteristics of the continuous and discrete angle measurement filters and the continuous angle and rate measurement filters are also presented and compared. Analytical expressions for the maximum, minimum, and average mean-squared angle and rate-estimation errors of the filter are provided and are shown graphically. Sensitivity analyses of the Kalman filter performances are also presented, and trade-offs between the sensor measurement errors and the interval between measurements are discussed.

b. Continuous Angle Measurement Filter Characteristics

Figure 3-21 is an illustration of the Kalman filter when continuous attitude angle measurements z_θ are taken (see Section IV). Physically, these measurements may be obtained from star or landmark tracker data.

In this figure, the filter input is measurement z_θ of angle θ corrupted by additive white noise n , and the filter outputs $\hat{\theta}$ and $\hat{\omega}$ are the best estimates of angle θ and its rate ω . The filter natural frequency Ω and the damping ratio ζ are time varying until the filter reaches steady state so, strictly speaking, the filter model in Figure 3-21 is only applicable in the steady state. However, one can imagine a filter with a time-varying bandwidth (and damping ratio). Initially, when very few measurements have been taken, the bandwidth is wide, thus allowing rapid changes in the output. This wide bandwidth also passes considerable noise so the outputs are also noisy. After many measurements have been processed, the filter output has almost converged to the true rate and angle values so the bandwidth can be decreased,

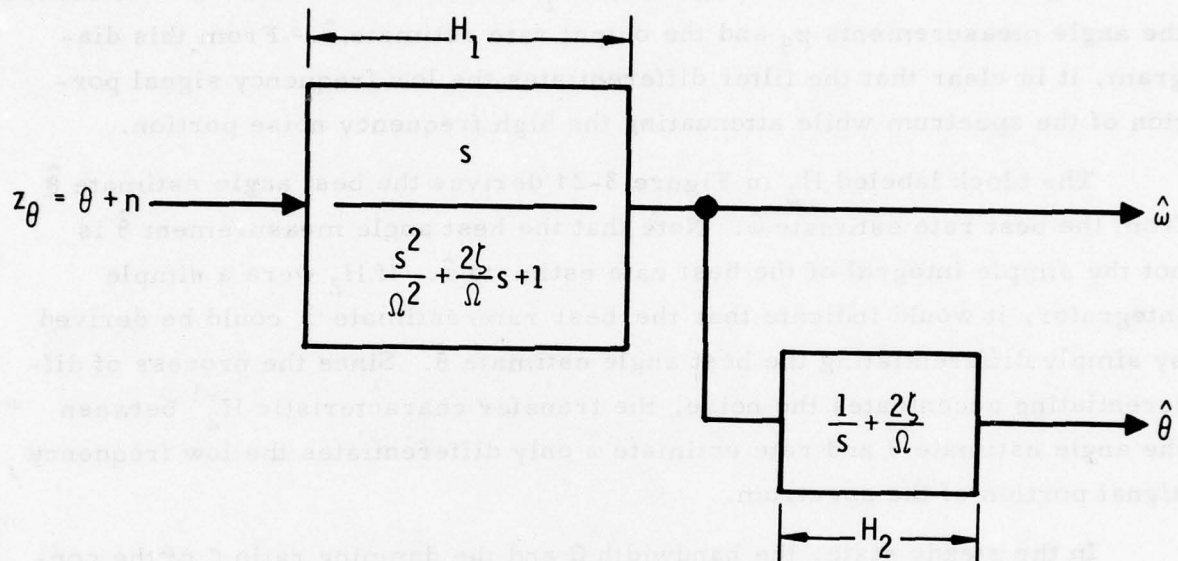


Figure 3-21. Attitude and Rate Filter for Continuous Attitude Measurements

reducing the noise on the outputs. However, the bandwidth cannot be reduced to zero because the random torques acting on the vehicle cause changes in the vehicle rates and angles that the filter must track.

Figure 3-22 is a Bode diagram of H_1 , the transfer characteristic between the angle measurements z_θ and the output rate estimate $\hat{\omega}$. From this diagram, it is clear that the filter differentiates the low frequency signal portion of the spectrum while attenuating the high frequency noise portion.

The block labeled H_2 in Figure 3-21 derives the best angle estimate $\hat{\theta}$ from the best rate estimate $\hat{\omega}$. Note that the best angle measurement $\hat{\theta}$ is not the simple integral of the best rate estimate $\hat{\omega}$. If H_2 were a simple integrator, it would indicate that the best rate estimate $\hat{\omega}$ could be derived by simply differentiating the best angle estimate $\hat{\theta}$. Since the process of differentiating accentuates the noise, the transfer characteristic H_2^{-1} between the angle estimate $\hat{\theta}$ and rate estimate $\hat{\omega}$ only differentiates the low frequency signal portion of the spectrum.

In the steady state, the bandwidth Ω and the damping ratio ζ of the continuous angle measurement filter illustrated in Figure 3-21 are given by

$$\Omega = (q/r)^{1/4} \quad (\text{III-35})$$

$$\zeta = 1/\sqrt{2} \quad (\text{III-36})$$

where q and r represent the heights of the disturbance torque and measurement noise in power spectral densities (PSDs). These PSDs are flat since both the disturbance torques and noise are assumed to be white noise processes. Physically, this implies that their bandwidths are much wider than the filter bandwidth. The bandwidth Ω increases as the disturbance torque level q increases because larger disturbance torque levels cause the true vehicle attitude to change more rapidly. The bandwidth decreases as the measurement noise level r increases, thus reducing the output noise.

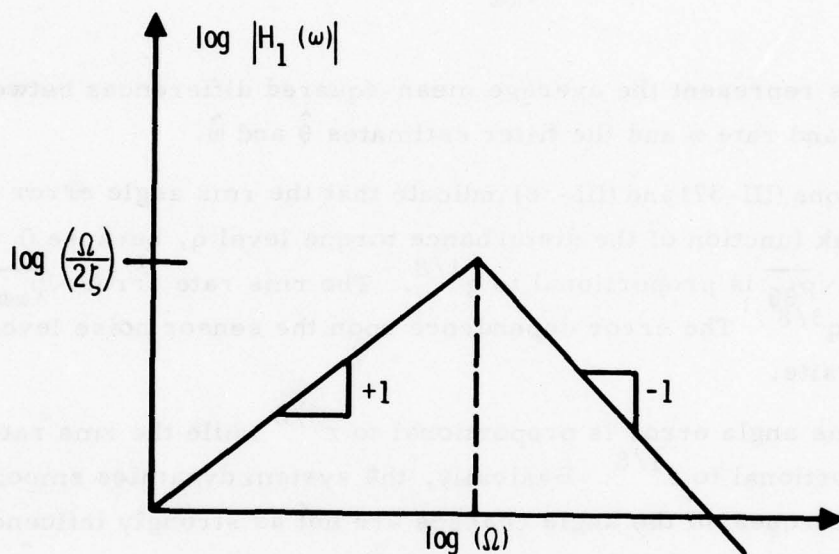


Figure 3-22. Bode Diagram of Transfer Function from Angle Measurements z_θ to Rate Estimates \hat{w}

The steady-state mean-squared angle and rate estimation errors of this continuous filter are given by

$$p_{\theta\theta} = \sqrt{2} r \Omega \quad (\text{III-37})$$

$$p_{\omega\omega} = \sqrt{2} r \Omega^3 \quad (\text{III-38})$$

These errors represent the average mean-squared differences between the true angle θ and rate ω and the filter estimates $\hat{\theta}$ and $\hat{\omega}$.

Equations (III-37) and (III-38) indicate that the rms angle error $\sqrt{p_{\theta\theta}}$ is only a weak function of the disturbance torque level q , because $\Omega = (q/r)^{1/4}$ implies that $\sqrt{p_{\theta\theta}}$ is proportional to $q^{1/8}$. The rms rate error $\sqrt{p_{\omega\omega}}$ is proportional to $q^{3/8}$. The error dependence upon the sensor noise level r is just the opposite.

The rms angle error is proportional to $r^{3/8}$ while the rms rate error is only proportional to $r^{1/8}$. Basically, the system dynamics smooth the disturbance torques so the angle changes are not as strongly influenced by the disturbance torque levels (q) as are the rate changes.

Equations (III-35) through (III-38) not only indicate the sensitivities of the errors to the disturbance torque q and measurement noise r levels, but they also allow the filter to be designed from a bandwidth viewpoint. In most cases, the sensor measurement noise level q can be determined fairly accurately from laboratory test data. However, the disturbance torque level q is generally much more difficult to determine because it represents the orbital (zero g) spacecraft environment, which cannot be simulated accurately prior to launch. Therefore, in these cases where q is difficult to determine, the filter bandwidth Ω can be used to specify the filter. Equations (III-37) and (III-38) then indicate the angle and rate errors that result from a choice of bandwidth. If the desired filter bandwidth produces unacceptable errors, a time-varying bandwidth must be used. For example, if

thrusters are used for attitude control, the filter bandwidth could be increased when a thruster fires to achieve the required filter response time and then decreased to attain the desired estimation error levels.

c. Continuous Angle and Rate Measurement Filter Characteristics

The steady-state performance for a Kalman filter with both continuous angle and rate measurements can be represented in terms of the bandwidth Ω and damping ratio ζ by the relations

$$P_{\theta\theta} = r_{\theta} \Omega \frac{2\zeta}{(2\zeta)^2 - 1} \quad (\text{III-39})$$

$$P_{\omega\omega} = r_{\theta} \Omega^3 \frac{2\zeta}{(2\zeta)^2 - 1} \quad (\text{III-40})$$

where r_{θ} is the angle sensor noise. Equations (III-39) and (III-40) are derived in Volume III of Reference 1. The bandwidth for this system is identical to that defined for the continuous angle filter

$$\Omega = (q/r_{\theta})^{1/4} \quad (\text{III-41})$$

The damping ratio for the continuous angle and rate system is defined by

$$\zeta = \frac{1}{2} \sqrt{2 + \frac{\sqrt{r_{\theta}q}}{4r_{\delta\omega}}} \quad (\text{III-42})$$

where $r_{\delta\omega}$ is the rate sensor noise. Note that, in the case of systems with very noisy rate sensors ($r_{\delta\omega} \gg r_{\theta}q$), the damping ratio approaches $1/\sqrt{2}$ and the angle and rate estimation errors defined by Eqs. (III-39) and (III-40) approach those of the continuous angle filter with no rate measurements (Eqs. [III-41] and [III-42]).

¹J. D. Gilchrist, Final Report on Program STRETCH, TR-0066(5763)-1, The Aerospace Corporation, El Segundo, California (31 July 1970).

Substitution of Eqs. (III-41) and (III-42) into Eqs. (III-39) and (III-40) results in

$$P_{\theta\theta} = (r_{\theta})^{3/4} (q)^{1/4} \sqrt{\frac{2 + \frac{1}{r_{\delta\omega}} \sqrt{r_{\theta}q}}{1 + \frac{1}{r_{\delta\omega}} \sqrt{r_{\theta}q}}} \quad (\text{III-43})$$

$$P_{\omega\omega} = (r_{\theta})^{1/4} (q)^{3/4} \sqrt{\frac{2 + \frac{1}{r_{\delta\omega}} \sqrt{r_{\theta}q}}{1 + \frac{1}{r_{\delta\omega}} \sqrt{r_{\theta}q}}} \quad (\text{III-44})$$

Equations (III-43) and (III-44) indicate the angle and rate estimation error sensitivities to sensor noise and disturbance accelerations. As previously indicated, systems with poor rate sensors ($r_{\delta\omega} \gg r_{\theta}q$) approach the performance of the continuous angle filter. Hence, their sensitivities to r_{θ} and q are the same as those indicated in Paragraph III. F. 1. b. If the rate sensors are very high quality ($r_{\delta\omega} \ll r_{\theta}q$), the ratios on the right sides of Eqs. (III-43) and (III-44) may be approximated by

$$\sqrt{\frac{2 + \frac{1}{r_{\delta\omega}} \sqrt{r_{\theta}q}}{1 + \frac{1}{r_{\delta\omega}} \sqrt{r_{\theta}q}}} \approx (r_{\delta\omega})^{1/2} (r_{\theta}q)^{-1/4}$$

Using this approximation in Eqs. (III-43) and (III-44) results in

$$P_{\theta\theta} \approx (r_{\theta})^{1/2} (r_{\delta\omega})^{1/2} \quad (\text{III-45})$$

$$P_{\omega\omega} \approx (r_{\delta\omega})^{1/2} (q)^{1/2} \quad (\text{III-46})$$

Equation (III-45) indicates that, for systems with low noise rate sensors, the rms angle error $\sqrt{p_{\theta\theta}}$ is proportional to $r_{\theta}^{1/4}$ and $r_{\delta\omega}^{1/4}$. The rms rate error $\sqrt{p_{\omega\omega}}$ is proportional to the fourth root of both $r_{\theta\omega}$ and q . Comparison of these sensitivities with those of the continuous angle filter shows that the presence of high quality continuous rate sensors improves the system capability to track the disturbance accelerations. The result is an rms angle error that is insensitive to q and an rms rate error with sensitivity reduced from $q^{3/8}$ to $q^{1/4}$.

d. Discrete Angle Measurement Filter Characteristics

The continuous angle measurement Kalman filter model in Figure 3-21 can also be used to characterize the behavior of the Kalman filter that results when angle measurements are taken only at discrete times. This situation occurs when strapped-down star mappers are employed. Here, the sighting times are assumed to occur at equal time spacings T . The assumptions that the attitude angles are simple integrals of the vehicle rates and the angle (star) measurements are uniformly spaced are very good for zero-net-momentum spinning spacecraft with strapped-down star mappers such as those suggested for system B in Table 3-2.

The assumption that the attitude angles are simple integrals of the vehicle rates is also good for a spacecraft stabilized to the local vertical. However, for a local vertical stabilized spacecraft such as system A in Table 3-2 with strapped-down star mappers, the assumption that the angle (star) measurements are uniformly spaced is not as realistic as for the spinning spacecraft. For a spacecraft stabilized to the local vertical, a better assumption is that the angle (star) measurements are randomly (Poisson) distributed. When the average random sighting rate λ is large compared with the continuous filter bandwidth Ω (Eq. [III-39]), the estimation errors for the uniformly spaced and randomly spaced measurement cases are almost equal. In fact, the estimation errors for the uniform update filter lie between upper and lower bounds derived for the random filter when

the ratio of Ω/λ is less than approximately 0.9. Unfortunately, actual values for the average estimation errors of a filter with random (Poisson) measurement updates have not yet been obtained.

When the angle measurements occur only at discrete times uniformly spaced T sec apart, the filter model in Figure 3-21 must be modified by including a sampler (and zero-order hold) on the angle measurement input. Also, z -transforms instead of Laplace(s) transforms should be used to characterize its response. However, the sampled data response of the filter can be modeled as a continuous system, providing it is understood that the continuous system response is only applicable at the sampling times. In Appendix E, the z -transform model of the discrete angle measurement filter is derived and its response is characterized by a continuous system model.

The bandwidth Ω' and damping ratio ζ' of the discrete angle measurement filter cannot be expressed in simple terms as can the bandwidth Ω and damping ratio ζ of the continuous angle measurement filter given by Eqs. (III-39) and (III-40). The sampled-data filter bandwidth Ω' and damping ratio ζ' depend not only on the disturbance torque level q and mean-squared angle measurement errors r' , but also on the sampling period T . The complex equations required to derive the sampled-data filter bandwidth Ω' and damping ratio ζ' are presented in Appendix E.

Surprisingly, the damping ratio of the sampled-data filter ζ' and the bandwidth Ω' of the sampled-data filter are almost exactly the same as the damping ratio $\zeta = 1/\sqrt{2}$ and the bandwidth $\Omega = (q/r)^{1/4}$ of the continuous filter, providing the sensor measurements are properly normalized.

The mean-squared measurement error of the sampled-data filter is r' and its units are $(\text{rad})^2$. The measurement parameter r of the continuous filter represents the height of the measurement error PSD or the area under the autocorrelation function of the continuous measurement errors. The units of r are $(\text{rad})^2 \text{ sec}$. If these continuous measurements are perfectly correlated over T sec and uncorrelated thereafter, then

$$r = r' T (\text{rad})^2 \text{ sec} \quad (\text{III-47})$$

where r' is the mean-squared measurement error. Substituting this expression into the equation for the continuous filter bandwidth (Eq. [III-39]) gives

$$\Omega' = (q/r' T)^{1/4} (\text{rad/sec}) \quad (\text{III-48})$$

Here, the prime notation is used to indicate the sampled-data characteristics of the measurement. Multiplying this expression for Ω' by T produces the nondimensional variable

$$\sqrt{y} \equiv \Omega' T = T(q/r' T)^{1/4} \quad (\text{III-49})$$

A discussion of the significance of this grouping of parameters defined by y is given in Appendix E-2.

There may appear to be some ambiguity in that the notation Ω' has been used to denote the grouping of parameters indicated in Eq. (III-44) and it is also used to denote the bandwidth of the sampled-data filter. Numerically, however, the expression for Ω' in Eq. (III-44) and the resulting sampled-data filter bandwidth calculated from the equations in Appendix E-1 of this report are almost identical (within three decimal places) over the entire range of parameters. Similarly, the damping ratio ζ' of the sampled-data filter is almost exactly the same as the damping ratio $\zeta = 1/\sqrt{2}$ of the continuous filter for all ranges of parameters. For values of \sqrt{y} (Eq. [III-45]) less than 1, ζ' and ζ are equal to four decimal places. Their difference increases as \sqrt{y} increases. However, for $\sqrt{y} = 2.3$, the difference is only about 1 percent.

Again, the parameter $\sqrt{y} = \Omega' T$ (Eq. [III-45]) represents (almost exactly) the product of the sampled-data filter bandwidth Ω' and the sampling period T . For good filter performance, this parameter should be small because the filter bandwidth Ω' should be small compared with the information rate $1/T$ in order to smooth the data.

Figures 3-23 and 3-24 are illustrations of the normalized steady-state mean-squared position and rate errors for the sampled-data filter as a function of the parameter $\sqrt{y} = \Omega' T$.

In Figure 3-23,

$$\frac{m_{\theta\theta}}{r'} = \frac{\text{peak mean-squared angle error}}{\text{mean-squared angle measurement error}}$$

$$\frac{\bar{p}_{\theta\theta}}{r'} = \frac{\text{average mean-squared angle error}}{\text{mean-squared angle measurement error}}$$

$$\frac{p_{\theta\theta}}{r'} = \frac{\text{minimum mean-squared angle error}}{\text{mean-squared angle measurement error}}$$

The peak angle errors occur just prior to the measurements, and the minimum angle errors occur immediately after the measurements. The average angle error represents the time (integral) average of the angle error and not simply the average of the peak and minimum errors. The continuous filter angle error, with the continuous measurement error parameter r replaced by $r'T$ (Eq. [III-43]), is also plotted in Figure 3-23. This curve also represents a lower bound for the average error when the measurements are randomly (Poisson) distributed with an average rate of $1/T$.

In comparing the angle error curves in Figure 3-23 it is clear that, for large values of $\sqrt{y} = T\Omega'$, the average angle error ($\bar{p}_{\theta\theta}/r'$) is dominated by the peak angle error ($m_{\theta\theta}/r'$). This implies that the filter response in this region is more dramatically affected by changing the product $\sqrt{y} = T\Omega'$ than by reducing the mean-squared sensor error r' . For example, assume $\sqrt{y} = T\Omega' = 2$. Then, from Figure 3-23, $\bar{p}_{\theta\theta}/r'$ is (approximately) 5.8. Reducing the update interval T by a factor of 2 reduces \sqrt{y} to 1.19, which corresponds to a value of $\bar{p}_{\theta\theta}/r' = 2.2$ (approximately). Therefore, a factor of 2 reduction in the sampling interval T' reduces the average angle errors by a factor

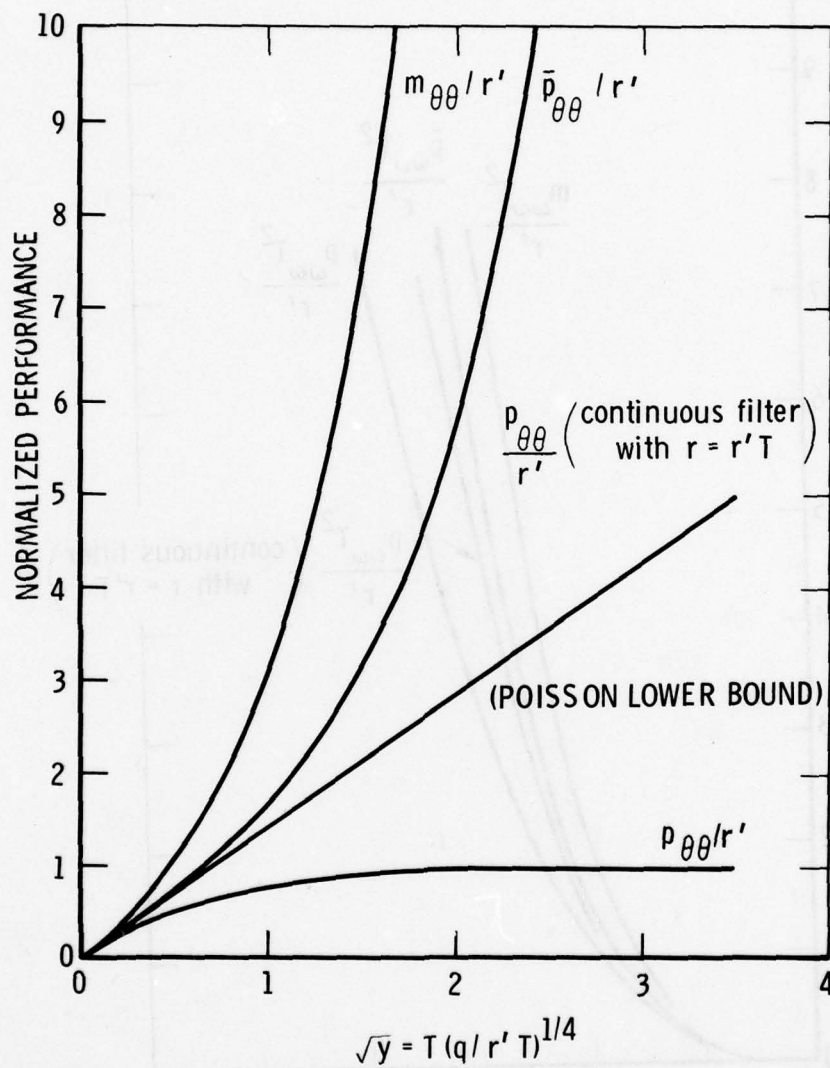


Figure 3-23. Steady-State Angle Errors for Sampled-Data Filter

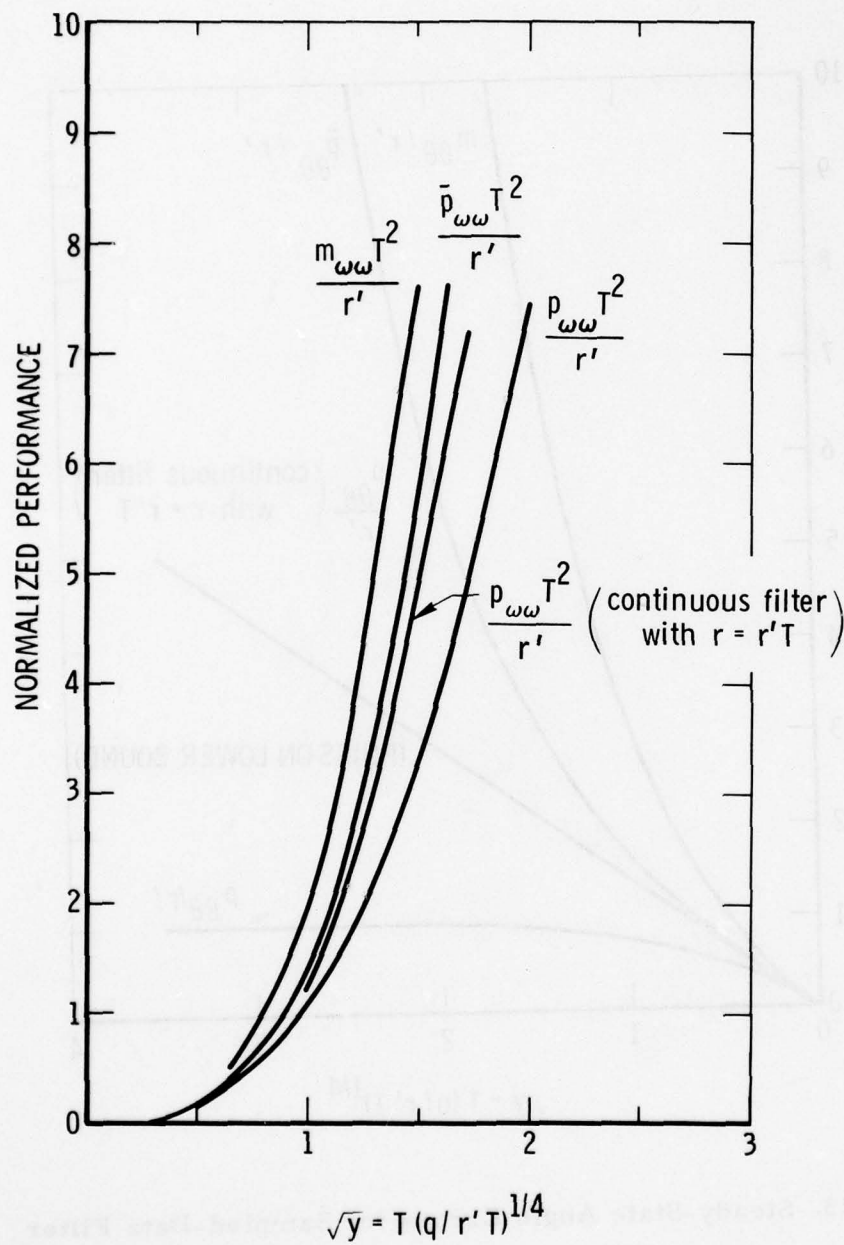


Figure 3-24. Steady-State Rate Errors for Sampled-Data Filter

AD-A053 322

AEROSPACE CORP EL SEGUNDO CALIF ENGINEERING SCIENCE --ETC F/6 22/3
HIGH ALTITUDE ATTITUDE DETERMINATION STUDY.(U)

MAR 78 R T UYEMINAMI, M V DIXON, T A FUHRMAN F04701-77-C-0078
TR-0078(3526)-1 SAMSO-TR-78-70 NL

UNCLASSIFIED

2 OF 3
AD
A053322



of $5.8/2.2 = 2.64$. If the values of \sqrt{y} were larger, the reductions would be more dramatic.

Continuing this example, assume that $\sqrt{y} = 2$ and consider a reduction in the mean-squared sensor errors r' of a factor of 2. This, due to the scaling, increases \sqrt{y} from 2 to 2.38. From Figure 3-21, this new value of \sqrt{y} corresponds to $p_{\theta\theta}/r' = 9.3$. However, since r' has been halved, the resulting angle error is $9.3/2 = 4.65$. Therefore, halving the mean-squared measurement r' error only has reduced the (normalized) mean-squared angle from 5.8 to 4.65 or only about 20 percent.

For large values of $\sqrt{y} = \Omega'T$, by taking the proper limits of the equations in Appendix E-2, it can be shown that

$$\bar{p}_{\theta\theta} \approx k_1 y^2 = k_1 T^3 q; \quad (\Omega'T \gg 1) \quad (\text{III-50})$$

where $k_1 = (3 + 2\sqrt{3})/36 = 0.18$. Therefore, the behavior of $\bar{p}_{\theta\theta}$ for large values of $\sqrt{y} = \Omega'T$ is independent of the sensor accuracy r' and is strongly dependent upon the sampling interval T . The reason for this behavior is that the mean-squared angle error increases as qt^3 between measurements, so even if the angle errors were zero after the measurements (implying perfect sensors, $r' = 0$), the average angle error $\bar{p}_{\theta\theta}$ would be governed by the growth between measurements. This growth rate assumes that no rate sensor data are available. The addition of continuous rate sensors, such as rate gyros, would appreciably decrease this angle error growth rate.

A lower bound for the average mean-squared error when the angle measurements occur at random (Poisson) intervals is equal to $2 T^3 q$ for large values of $\sqrt{y} = \Omega'T$ where $1/T$ is the average measurement rate. The upper bound for the average mean-squared error when the angle measurements occur at random (Poisson) intervals and this lower bound are essentially the same for the values of \sqrt{y} greater than 10. Therefore, for large

values of \sqrt{y} , the average mean-squared angle error for the random (Poisson) measurement intervals is a factor of $2/k_1 = 11.1$ worse than the average mean-squared angle error for uniform measurement intervals.

As \sqrt{y} decreases to zero, the sensitivity of the angle error $\bar{p}_{\theta\theta}$ to the sampling interval T decreases, finally approaching the sensitivity of the continuous filter (with parameter $r = r'T$) given by Eq. (III-41).

$$\bar{p}'_{\theta\theta} = \sqrt{2} r'T\Omega' = \sqrt{2} (r')^{3/4} T^{3/4} (q^{1/4}) ; \quad (\Omega'T \ll 1) \quad (\text{III-51})$$

In this limiting case, $\bar{p}_{\theta\theta}$ has the same dependence upon r' as T . Therefore, only as \sqrt{y} approaches zero does the sensitivity of $\bar{p}_{\theta\theta}$ to sensor measurement errors r' approach the sensitivity of $\bar{p}_{\theta\theta}$ to sampling interval T .

These sensitivities of $\bar{p}_{\theta\theta}$ to sampling period T and sensor errors r' imply that, if the angle sensor can be designed to obtain more measurements ($T_{\text{new}} < T_{\text{old}}$) even if the measurement errors increase ($r'_{\text{new}} > r'_{\text{old}}$), the mean-squared angle error $\bar{p}_{\theta\theta}$ will decrease, providing

$$r'_{\text{new}} T'_{\text{new}} \leq r'_{\text{old}} T'_{\text{old}} \quad (\text{III-52})$$

A more detailed derivation of this result is given in Section IV.

To interpret the consequences of this result on sensor design, consider the design of a star sensor. As the FOV of the sensor increases, the average time between star sightings T decreases while the sensor measurement error r' increases because the wider FOV necessitates decreasing the sensor focal length and magnification. The previous analysis indicates that the mean-squared angle errors $\bar{p}_{\theta\theta}$ will be reduced if the wider FOV decreases the average star-sighting interval (T) as much as (or more than) it increases the mean-squared measurement errors r' .

The graphs in Figures 3-23 and 3-24 also indicate the effects on the steady-state errors of changing the sampled-data filter bandwidth. For example,

assume a star measurement interval of $T = 1$ sec and a bandwidth of $\Omega' = 2$ Hz, which gives $\sqrt{y} = \Omega' T = 2$. If this bandwidth was more than adequate from a control standpoint, any slight reduction in the bandwidth would appreciably decrease the steady-state errors. For example, a 10-percent reduction in the bandwidth Ω' would result in $\sqrt{y} = 1.8$, which corresponds to $\bar{p}_{\theta\theta}/r' = 4.4$ or a reduction in the mean-squared angle error of over 20 percent. Of course, the bandwidth can not be arbitrarily reduced because it must be adequate to track the vehicle attitude changes.

The mean-squared rate errors are shown graphically in Figure 3-24. In this figure,

$$\frac{T^2 m_{\omega\omega}}{r'} = T^2 \times \frac{\text{peak mean-squared rate error}}{\text{mean-squared angle measurement error}}$$

$$\frac{T^2 \bar{p}_{\omega\omega}}{r'} = T^2 \times \frac{\text{average mean-squared rate error}}{\text{mean-squared angle measurement error}}$$

$$\frac{T^2 p_{\omega\omega}}{r'} = T^2 \times \frac{\text{minimum mean-squared rate error}}{\text{mean-squared angle measurement error}}$$

where T is the interval between the angle measurements. Again, the peak rate errors occur just prior to the measurements and the minimum rate errors occur immediately following the angle measurements. The average rate error $\bar{p}_{\omega\omega}$ represents the time (integral) average of the rate error. However, since the mean-squared rate error increases linearly in time, the average rate error $\bar{p}_{\omega\omega}$ is also the average of the peak and minimum rate errors

$$\bar{p}_{\omega\omega} = \frac{m_{\omega\omega} + p_{\omega\omega}}{2} \quad (\text{III-53})$$

This result is derived in Appendix E-2.

The continuous filter rate error with the continuous angle measurement parameter r replaced by $r'T$ (Eq. [III-47]) is also plotted in Figure 3-24. This curve also represents a lower bound for the average mean-squared rate error when the angle measurements occur at randomly (Poisson) distributed times with an average rate of $1/T$. From Figure 3-24 the average sampled-data rate errors $\bar{p}_{\omega\omega}$ are very closely approximated by the continuous filter errors for small values of $\sqrt{y} = \Omega'T$. Therefore, from Eq. (III-42),

$$\bar{p}_{\omega\omega} \approx p_{\omega\omega} = \sqrt{2} r'T (\Omega')^3; \quad (\Omega'T < 1)$$

or

$$\bar{p}_{\omega\omega} \approx \sqrt{2} (r')^{1/4} T^{1/4} q^{3/4}; \quad (\Omega'T < 1) \quad (\text{III-54})$$

This relationship indicates that the average rate errors $\bar{p}_{\omega\omega}$ are equally sensitive to the angle measurement errors r' and sampling interval T and more sensitive to the disturbance torque level q for small values of $\sqrt{y} = \Omega'T$.

For large values of $\sqrt{y} = \Omega'T$, by taking the appropriate limits of the equations in Appendix E-2, it can be shown that

$$\bar{p}_{\omega\omega} \approx k_2 q T; \quad (\Omega'T \gg 1) \quad (\text{III-55})$$

where

$$k_2 = \frac{3 + \sqrt{3}}{6} = 0.79$$

Upper and lower bounds for the average mean-squared rate error when the measurement intervals are randomly (Poisson) distributed converge to $q T$ for large values of $\Omega'T$ where $1/T$ is the average measurement rate. Therefore, over all ranges of $\Omega'T$, the average rate error $\bar{p}_{\omega\omega}$, when the

measurements occur at uniform intervals, closely approximates the average rate error when the measurements occur at random (Poisson) intervals.

From Eqs. (III-54) and (III-55), for all values of $\Omega'T$ the average rate errors are relatively insensitive to the angle measurement errors r' , and for small values of $\Omega'T$, the average rate errors depend primarily upon the disturbance torque level q . For large values of $\Omega'T$, the average mean-squared rate errors are equally dependent upon q and the sampling interval T .

2. KALMAN FILTER PERFORMANCE WITH MEASUREMENTS AT RANDOM POINTS IN TIME

As was indicated in Paragraph III. A in the discussion of the attitude estimation method, the statistics of the estimation error are contained in the system covariance matrix defined by

$$P(t) = \mathcal{E}[\underline{e}(t) \underline{e}^T(t)]$$

where \mathcal{E} implies the expected value of the bracketed quantity and the vector $\underline{e} = (\underline{x} - \hat{\underline{x}})$ represents the estimation errors. It may be shown that the square roots of the diagonal or trace elements of the covariance matrix represent the rms estimation errors for each state and, hence, the 1-sigma performance of the system for zero-mean Gaussian errors.

It was shown in Paragraph III. D that the rms errors for a mixed or purely discrete system with uniformly spaced (in time) attitude updates varies regularly in a sawtooth fashion between fixed upper and lower bounds. The errors are at a minimum or lower bound just after each attitude measurement and grow to a maximum or upper bound just prior to the next attitude measurement. Thus, the 1-sigma performance varies regularly with time between the fixed bounds, which are solely determined by the update interval, sensor qualities, and disturbance environment.

For a mixed or purely discrete system with randomly spaced attitude updates, the 1-sigma performance becomes a random quantity. It no longer varies regularly with time in that the maximum and minimum estimation errors have random levels. Hence, statistical averaging of the 1-sigma

performance or rms estimation errors becomes necessary to characterize the performance of the random update system. Assuming that the time of occurrence of a random update is determined by a Poisson counting process, the matrix differential equation for the propagation of the expected value of the random system covariance matrix may be found (see Appendix G). For a time invariant mixed system, i. e., a system in which the dynamic coefficients and measurement geometries are constants, this equation takes the form

$$\begin{aligned} \frac{d}{dt} \mathcal{E}[P(t, \xi)] &= A \mathcal{E}[P(t, \xi)] + \mathcal{E}[P(t, \xi)] A^T + Q \\ &- \mathcal{E}[P(t, \xi) G^T R_u^{-1} G P(t, \xi)] \\ &- \lambda \mathcal{E}\left[P(t, \xi) H^T \left\{ H P(t, \xi) H^T + R_v \right\}^{-1} H P(t, \xi) \right] \quad (\text{III-56}) \end{aligned}$$

where \mathcal{E} indicates the expectation of the bracketed quantity, G is the continuous measurement geometry matrix, H is the discrete measurement geometry matrix, R_u is the continuous sensor noise, R_v is the discrete sensor noise, and λ is the Poisson average update occurrence rate. The covariance matrix $P(t, \xi)$ for the random Poisson update system is a function of both time t and the particular realization ξ of update sequence. That is, the value of the covariance matrix at any particular time depends upon the particular update time sequence (realization) experienced out of all possible update time sequences.

The solution of Eq. (III-56) is not possible with only a knowledge of the first-order statistics of the covariance matrix represented by the mean or expected value of the covariance matrix $\mathcal{E}[P(t, \xi)]$. Second-order statistics must be known to evaluate the two nonlinear terms on the right side of Eq. (III-56). Simplifying assumptions can be made, however, that allow a solution to Eq. (III-56) based only on a knowledge of the mean covariance value. These assumptions result in bounds upon the mean or average values of the random update system covariance matrix.

In particular, the equations for one upper and two lower bounds were obtained in Appendix G. Abbreviating the upper and lower bounds by

$$\text{Upper bound on } \mathcal{E}[P(t, \xi)] = P_u(t)$$

$$\text{First lower bound on } \mathcal{E}[P(t, \xi)] = P_{L1}(t)$$

$$\text{Second lower bound on } \mathcal{E}[P(t, \xi)] = P_{L2}(t)$$

the differential equations propagating these bounds for time invariant systems are

$$\dot{P}_{L1}(t) = A P_{L1}(t) + P_{L1}(t) A^T + Q - \lambda P_{L1}(t) \quad (\text{III-57})$$

$$\dot{P}_{L2}(t) = A P_{L2}(t) + P_{L2}(t) A^T + Q - \lambda P_{L2}(t) H^T R_v^{-1} H P_{L2}(t) \quad (\text{III-58})$$

$$\begin{aligned} \dot{P}_u(t) = & A P_u(t) + P_u(t) A^T + Q - P_u(t) G^T R_v^{-1} G P_u(t) \\ & - \lambda P_u(t) H^T [H P_u(t) H^T + R_v]^{-1} H P_u(t) \end{aligned} \quad (\text{III-59})$$

The first lower bound (Eq. [III-57]) represents the performance of a purely discrete attitude system with perfect measurements and an average Poisson update rate equal to λ . The second lower bound can be derived assuming imperfect discrete attitude measurements only with an average Poisson event rate of λ . It may be employed as a lower bound for the mixed system as well, providing proper scaling is used for the continuous sensor measurement noise. The upper bound Eq. (III-59) represents the mean performance of the suboptimal system whose filter gains are independent of the particular realization ξ of the time sequence of updates. That is, the filter gains are precalculated

based upon an average expected update rate λ . It can be shown that the mean performance of this suboptimal system is identical to the peak estimation errors of an equivalent uniform update system operating with an update rate equal to the average Poisson rate λ . Thus, the upper bound on the random system average covariance $P_u(t)$ is equal to the peak value of the covariance matrix (identified as the M_i matrix in Eq. (III-52) for the equivalent uniform update system. Hence, the peak estimation error variance curves $E(\theta^2)_{MAX}$ obtained from the covariance analysis of the uniform update systems may be used to determine the upper bound on the average estimation error variance for the random (Poisson) update system. This tends to support the validity of using the uniform update assumption in determining the performance of the conceptual designs for local vertical satellite configurations. Numerical examples of these bounds for both simple and double integrator systems can be found in Appendix G. The single integrator and its performance bounds are discussed in the following subsection.

3. SINGLE INTEGRATOR PERFORMANCE

The single integrator may be thought of as a suboptimal attitude estimator that directly integrates continuous rate measurements between discrete attitude updates. Whenever an attitude update occurs, the measurement is processed optimally to obtain an improved attitude estimate. The SPARS filter is representative of the single integrator type. This filter is suboptimal in the sense that only attitude measurements are optimally processed in obtaining the attitude estimate. Although the rate is measured, it is directly integrated without filtering to propagate the estimate between attitude measurements. In contrast, the double integrator can be considered a fully optimal filter in the sense that both attitude and rate measurements are processed optimally to obtain estimates of both states.

The detailed derivation of the single integrator filter is presented in Appendix H. Only a brief description of this derivation is given in Section III to aid in understanding the performance sensitivities of the system.

A comparison of the single and double integrator systems is made to illustrate the difference in performance between the fully optimal and sub-optimal filters. Finally, the equations defined previously in Paragraph III. F. 2 are used to determine the upper and lower bounds on the average performance of the suboptimal single integrator filter with random (Poisson) update sequences.

a. Comparison of Single and Double Integrator Performance

The measurements for the single integrator system consist of continuous rate measurements from rate gyros

$$z_w = \omega + n_w \quad (\text{III-60})$$

and discrete attitude measurements from mappers

$$z_\theta = \theta + n_\theta \quad (\text{III-61})$$

where n_w and n_θ are white measurement noises, and ω and θ are true rate and attitude respectively. The system covariance for the single integrator filter is

$$p_\theta = \mathcal{E}[(\hat{\theta} - \theta)^2] \quad (\text{III-62})$$

where \mathcal{E} indicates the expected operation and $\hat{\theta}$ is the estimated attitude.

Between discrete attitude measurements, the filter directly integrates the rate measurements to obtain an estimate of attitude. Hence, the state equation for the estimate is

$$\dot{\hat{\theta}} = z_w = \omega + n_w \quad (\text{III-63})$$

The true attitude is represented by

$$\dot{\theta} = \omega \quad (\text{III-64})$$

Integrating Eqs. (III-63) and (III-64) and substituting the results into Eq. (III-62) gives the equation

$$m_{\theta} = p_{\theta} + r_{\omega} t \quad (\text{III-65})$$

where m_{θ} is the system covariance between discrete attitude measurements, p_{θ} is the covariance at the last discrete attitude update, and r_{ω} is the white noise equivalent area under the actual gyro noise autocorrelation function. As is shown by Eq. (V-65), the system covariance grows linearly with time between discrete attitude updates.

At a discrete update time, the attitude measurement defined by Eq. (III-61) is optimally processed, and the system covariance is updated using Eq. (III-52). For this single integrator system, the result from Eq. (V-52) is

$$p_{\theta} = \frac{m_{\theta} r'_{\theta}}{m_{\theta} + r'_{\theta}} \quad (\text{III-66})$$

where r'_{θ} is the discrete attitude sensor measurement noise and the measurement geometry was assumed to be unity. Solving Eqs. (III-65) and (III-66) gives

$$p_{\theta} = \frac{r_{\omega} T}{2} \left(-1 + \sqrt{1 + \frac{4r'_{\theta}}{r_{\omega} T}} \right) \quad (\text{III-67})$$

and

$$m_{\theta} = \frac{r_{\omega} T}{2} \left(1 + \sqrt{1 + \frac{4r'_{\theta}}{r_{\omega} T}} \right) \quad (\text{III-68})$$

where T is the time interval between discrete attitude updates. Equations (III-67) and (III-68) are the desired analytical solutions for the single integrator steady-state performance. Equation (III-67) indicates the lower steady-state limit on the attitude estimation error variance, and Eq. (III-68) indicates the upper limit on the error variance.

Rescaling Eq. (III-68) using the previously defined scaling Eqs. (III-25), (III-26), and (III-27), the maximum variance equation may be rewritten in normalized form. Defining the normalized maximum variance by

$$E(\theta^2)_{\text{MAX}} \triangleq \frac{m_{\theta}}{r'_{\theta}} \quad (\text{III-69})$$

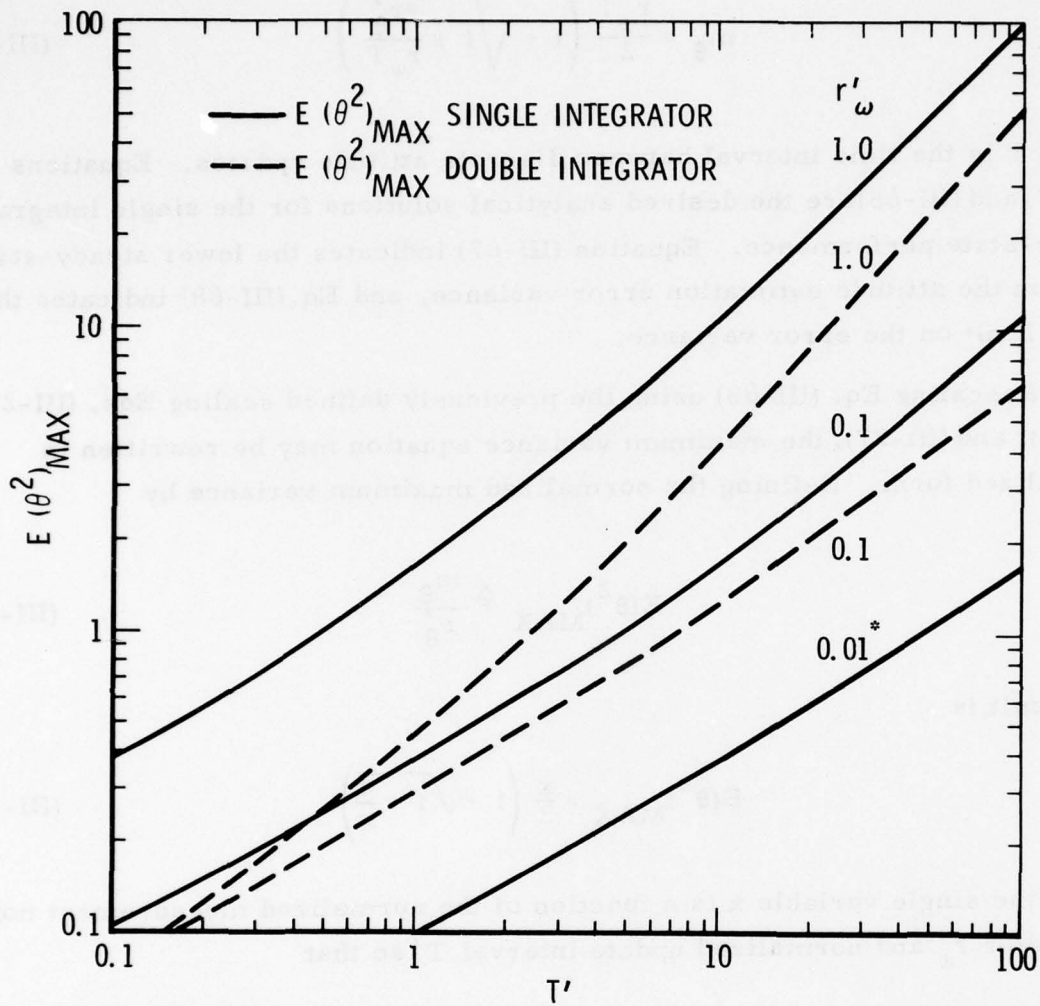
the result is

$$E(\theta^2)_{\text{MAX}} = \frac{x}{2} \left(1 + \sqrt{1 + \frac{4}{x}} \right) \quad (\text{III-70})$$

where the single variable x is a function of the normalized measurement noise parameter r'_{ω} and normalized update interval T' so that

$$x = r'_{\omega} T' \quad (\text{III-71})$$

Thus the steady-state performance of the single integrator system is a function of the product defined by Eq. (III-71). Equation (III-70) is plotted as solid curves for various values of r'_{ω} in Figure 3-25. Also indicated in this illustration are the normalized performance results for the double integrator mixed system from the covariance analysis simulation. These results are presented as dashed curves for the same values of r'_{ω} derived for the single integrator



* Single and double integrator curves coincide for this $r'\omega$ value

Figure 3-25. Comparison of Single and Double Integrator Performance

case. Recalling that the parameter r'_ω is directly proportional to the rate gyro quality (from Eq. [III-27]), it can be seen from Figure 25 that the suboptimal (single integrator) performance is considerably worse for poor gyros ($r'_\omega = 1.0$) than the fully optimal (double integrator) system performance. However, as the quality of the rate measurements improves, the suboptimal system performance approaches that of the fully optimal system until there is virtually no performance difference for systems with $r'_\omega = 0.01$ or less.

To further illustrate the use of Figure 3-25, a numerical example may be worked using the example system parameters given in Table 3-4. To compare the performance difference between the suboptimal and optimal systems for an update interval of 1000 sec, Eq. (III-26) is used with $\Omega_0 = 10^{-2}$ to determine T' . The result is $T' = 10$. Since $r'_\omega = 0.1$ for the example system, the two middle curves must be used to determine performance. Then, for $T' = 10$, the suboptimal system normalized performance is

$$E(\theta^2)_{\text{MAX}} = 1.65$$

and the optimal system performance is

$$E(\theta^2)^*_{\text{MAX}} = 1.22$$

where an asterisk is used to identify the optimal system. De-normalizing using Eq. (III-23) results in

$$\theta_{\text{rms}} = 2.64 \text{ arc sec}$$

and

$$\theta^*_{\text{rms}} = 2.27 \text{ arc sec}$$

for $r'_\theta = 10^{-10} (\text{rad})^2$. The performance difference, therefore, between the optimal and suboptimal example systems is 0.37 arc sec in favor of the

optimal system. It can be seen from this result that the performance advantage of the fully optimal (double integrator) system is small for instruments of Space Attitude Reference System (SPARS) quality or better.

The suboptimal system performance sensitivities may be investigated using Eq. (III-68) and taking partial derivatives of m_θ with respect to r'_θ , r_ω , and T . Thus the sensitivity to the attitude sensor noise variations is

$$\frac{\partial m_\theta}{\partial r'_\theta} = \frac{1}{\sqrt{1 + \frac{4r'_\theta}{r_\omega T}}} \quad (\text{III-72})$$

The sensitivities to update interval variations and rate sensor noise variations are

$$\frac{\partial m_\theta}{\partial T} = \frac{\partial m_\theta}{\partial (r_\omega T)} r_\omega \quad (\text{III-73})$$

and

$$\frac{\partial m_\theta}{\partial r_\omega} = \frac{\partial m_\theta}{\partial (r_\omega T)} T \quad (\text{III-74})$$

where

$$\frac{\partial m_\theta}{\partial (r_\omega T)} = \frac{\left(1 + \sqrt{1 + \frac{4r'_\theta}{r_\omega T}}\right)^2}{4 \sqrt{1 + \frac{4r'_\theta}{r_\omega T}}} \quad (\text{III-75})$$

Equations (III-73) and (III-74) imply that simultaneous variations in the gyro quality and update interval so that the product $r_\omega T$ remains unchanged, results in no changes in m_θ . A comparison of Eqs. (III-72) and (III-75) shows that

$$\frac{\partial m_\theta}{\partial(r_\omega T)} \geq \frac{\partial m_\theta}{\partial r_\theta'} \quad \text{for} \quad \frac{r_\theta'}{r_\omega T} \geq 0 \quad (\text{III-76})$$

Thus the steady-state performance of the suboptimal (single integrator) system is generally more sensitive to changes in the product of gyro noise and update interval ($r_\omega T$) than to changes in the attitude sensor quality. It may be concluded, therefore, that improvements in the ($r_\omega T$) product are more beneficial to system performance than improvements in attitude sensor quality.

b. Single Integrator Random-Update Performance

To illustrate the performance of the suboptimal (single integrator) system when the update interval is determined by a Poisson random process, the equations developed in Paragraph III. F. 2 are used to determine bounds on the mean error covariance at various average update rates. The upper bound was described by Eq. (III-59). The steady-state upper bound value may be obtained by solving this equation with $\dot{P}_u = 0$. Similarly, the steady-state lower bounds may be obtained by solving Eqs. (III-57) and (III-58) for $\dot{P}_{L1} = \dot{P}_{L2} = 0$. Figure 3-26 is an illustration of the variations in these bounds with the average normalized update interval \bar{T}' . The de-normalization relations for this plot are

$$\bar{\theta}_{\text{rms}} = \sqrt{r_\theta' E(\theta^2)} \quad (\text{III-77})$$

and

$$\bar{T}' = \frac{\Omega_0}{\lambda} \quad (\text{III-78})$$

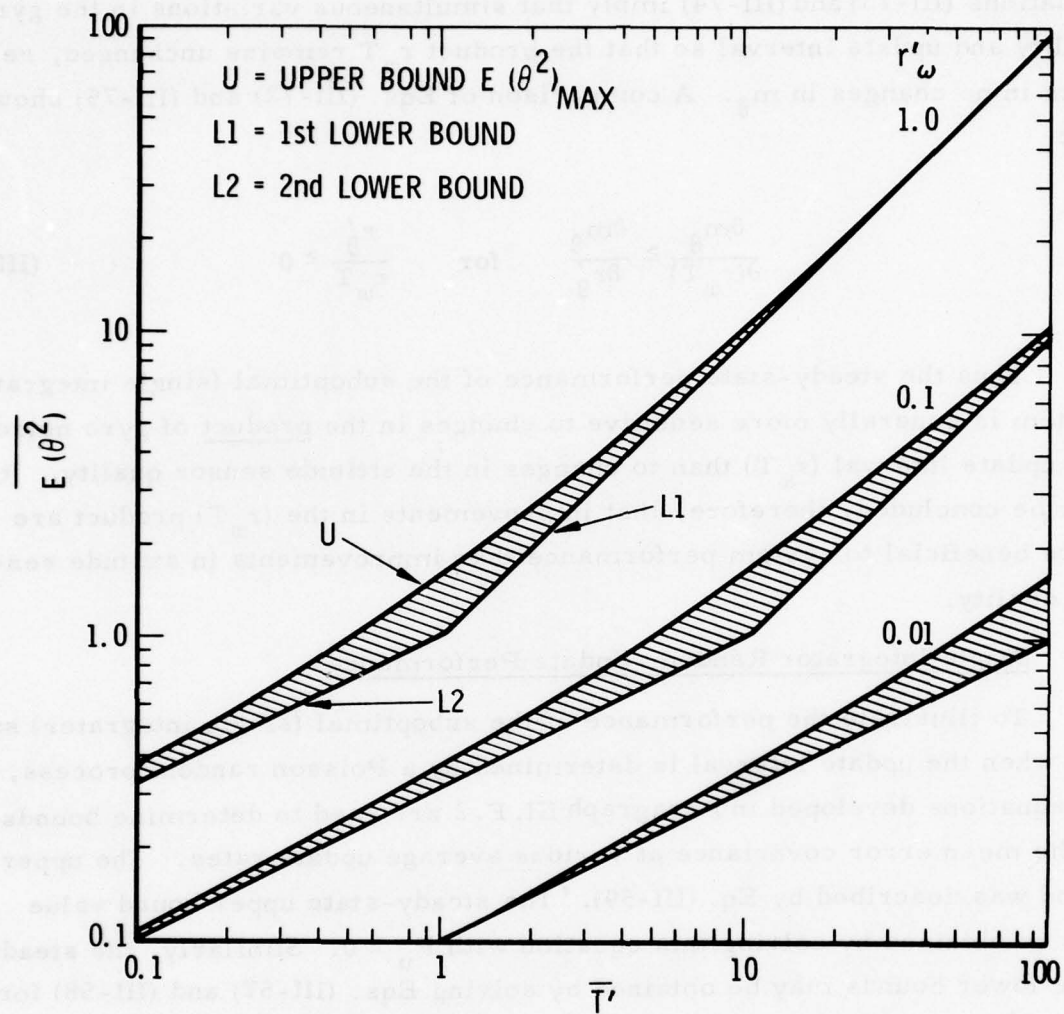


Figure 3-26. Random Update Single Integrator
 Average Performance

where $\bar{\theta}_{rms}$ is the average value of the rms attitude error for the random update single integrator system, λ is the average Poisson update rate with dimensions (1/sec), and r'_θ and Ω_0 are previously defined scaling parameters. The single integrator average performance bounds are shown in Figure 3-26 for three different values of r'_ω in terms of cross-hatched areas. The curves defining the boundaries of these areas are the upper and lower bounds. Thus, the actual average performance for the random update suboptimal system lies within the cross-hatched areas. It can be seen from the figure that the upper and lower bounds are fairly close with the largest differences occurring at \bar{T}' values corresponding to

$$r'_\omega \bar{T}' = 1 \quad (\text{III-79})$$

For \bar{T}' values when the product is less than 1, the second lower bound defined by Eq. (III-58) provides a tighter bound. If the product is greater than 1, the first lower bound defined by Eq. (III-57) should be used. The tightness of these bounds tends to support the validity of using Eqs. (III-57) through (III-59) to define the average random update system performance.

Comparing the solid curves of Figure 3-25 with the upper-bound curves of Figure 3-26, it may be seen that the maximum variance of the uniform update system $E(\theta^2)_{MAX}$ is the same as the upper bound on the average performance of the random update system (the curves labeled "u"). This is true for the double integrator as well as the single integrator system as explained in Paragraph V. F. 3.

4. OPTIMIZATION OF SENSOR CONFIGURATIONS

Thus far in this study, the effects of measurement geometry upon system performance have not been discussed. The easiest approach to this aspect of system performance is through the information matrix J . It is defined by the equation

$$J \triangleq H^T R^{-1} H \quad (\text{III-80})$$

where H is the measurement geometry matrix and R is the measurement noise matrix. The significance of the J matrix lies in the equation

$$P^{-1} = M^{-1} + J \quad (\text{III-81})$$

which shows that the J matrix contains all the information necessary to update the system covariance matrix (M) before a discrete measurement to produce the latest system covariance (P) immediately after the measurement. Equation (III-81) is an alternate expression for the discrete covariance update equation (III-52), and can be derived by using a standard matrix inversion formula on Eq. (III-52). It may be seen from Eq. (III-81) that maximizing the information matrix results in maximizing P^{-1} and, hence, minimizing the variance of the estimation error. An obvious approach to maximizing J is to minimize the measurement noise matrix R , i.e., to use better quality sensors. When this is not possible, the J matrix may still be maximized through the proper selection of the measurement geometry matrix H by optimizing the sensor configurations.

The relationship between the J matrix and the actual sensor configuration can be seen from the case of a multiple-slit attitude sensor (such as the SPARS star sensor) by rewriting Eq. (III-80) in the form

$$J = H^T R^{-1} H = \sum_{i=1}^m \frac{1}{r_i} \underline{h}_i \underline{h}_i^T \quad (\text{III-82})$$

where m is the number of slits in the sensor, r_i is the measurement noise of the i^{th} slit, and \underline{h}_i is a unit vector normal to the i^{th} slit and lying in the focal plane of the sensor. Equation (III-82) assumes that: the measurement noise matrix R is diagonal (i.e., noise is uncorrelated between slits); a reference object transiting the sensor FOV crosses all slits; and the time interval between slit crossings for a transit of the FOV is negligible. If there is

more than one sensor, the total system information matrix would be the sum of the individual sensor information matrices.

Equation (III-82) may be used directly to determine the relative performance between the axes of an attitude reference system given a particular sensor configuration. This may be accomplished by determining the slit normal directions (\underline{h}_i) for each sensor in its own coordinate system and calculating the information matrix, using Eq. (III-82), for each sensor. These J matrices are then transformed into body reference coordinates and summed to form the total system information matrix. The resulting information weighting on each axis (i. e., the relative values of the diagonal elements of the J matrix) can be used to define an effective measurement noise for each axis. When used with the normalized performance curves in Paragraph III. D, these effective measurement noise values will determine the relative performance between each axis of the particular system.

With the relationship between the sensor configuration and measurement matrix identified, optimization of the sensor configuration can be discussed. In many applications, the orientation of sensors used for estimating the state variables of a system is not rigidly specified by hardware constraints, but may be chosen to minimize (in some sense) the estimation errors. Occasionally, additional sensors may be employed if necessary for redundancy or if their use will appreciably reduce the estimation errors.

In the remainder of this section, techniques for optimally orienting sensors are described and illustrated with simple examples. Improvements that will result from using optimally oriented redundant sensors are also presented (See Appendix I for the derivation of these results).

In many estimation applications, it is desirable when possible to choose the sensor orientations to minimize the worst case measurement errors. In the discussion that follows, a description of the sensor orientations and the

performance that results from using this criterion are given along with some illustrative examples and applications to spacecraft attitude estimation. Techniques for extending this criterion are also discussed.

a. Optimal Sensor Orientations

Minimizing the worst case measurement errors is a reasonable policy when measurement accuracies on all axes are equally important. However, when the accuracies are not equally important the numerical procedures outlined can be used to calculate the sensor configurations that give the desired mix of measurement accuracies. Applying the criterion of minimizing the worst case measurement errors produces the sensor orientations and performances described in the following discussion.

(1) Nonredundant Sensor Orientations and Performance

If there are no redundant sensors, the sensor measurement axes are oriented so that they are orthogonal even if the sensor accuracies are not all equal. In this configuration, the measurement errors along each axis are equal to the individual sensor errors.

(2) Redundant Sensor Orientations

If there are redundant sensors, the sensor axes are skewed according to their accuracies. A numerical procedure for calculating the optimal sensor configurations is provided in Paragraph III. F. 4. d, page 3-109. In the optimal redundant sensor configuration, two cases arise.

- a. If any one sensor is not as accurate as $1/\sqrt{n}$ times the rss accuracy of all sensors when n is the number of axes (dimensions) measured, then the measurement accuracy in all directions is the same and equal to $1/\sqrt{n}$ times the rss accuracy of all instruments combined.
- b. If one (or more) sensor(s) is more accurate than $1/\sqrt{n}$ times the rss accuracy of all sensors, orient these superior sensors orthogonally to each other and skew the remaining sensors over the remaining l directions (dimensions). The measurement accuracies along the axes containing the superior sensors are

equal to the individual sensor accuracies. The measurement accuracy in all other directions is the same and equal to $1/\sqrt{l}$ times the rss accuracy of all the remaining instruments combined where l is the number of axes measured with the remaining instruments.

The combined accuracy of an optimally oriented set of sensors is unique. However, there may be more than one optimal sensor configuration that produces this maximum performance.

b. Optimal Sensor Orientation and Performance Examples

Some different optimal sensor configurations and their performance for the cases of nonredundant and redundant sensors are illustrated in the following simple examples.

(1) Nonredundant Sensor Orientation Examples

Perhaps the simplest example of nonredundant sensors is the case of three gyros measuring the three-dimensional vehicle rates. In this example, the optimal gyro configuration is one where all three gyro axes are orthogonal even if the instruments are not of the same quality.

It is intuitively appealing that, if there are just enough sensors to measure each direction separately and the sensors are of equal quality, the sensor axes should be orthogonal. However, it is not obvious that the sensor axes should still be orthogonal when the sensors are not of equal quality. Why this is true is shown in Figure 3-27.

Vectors \underline{j}_1 and \underline{j}_2 in Figures 3-27(a) and (b) represent the directions of the sensor measurement axes, and the lengths of \underline{j}_1 and \underline{j}_2 are proportional to the sensor measurement accuracies. Here, the instrument associated with \underline{j}_2 is more accurate than that corresponding to \underline{j}_1 . The measurement accuracy in any direction \underline{v} is proportional to the rss of the vector dot products of \underline{v} with \underline{j}_1 and \underline{j}_2 (i.e., $\sqrt{(\underline{v} \times \underline{j}_1)^2 + (\underline{v} \times \underline{j}_2)^2}$).

The two instrument axes in Figure 3-27(a) are orthogonal, and the poorest measurement accuracy occurs along the x-axis and is equal to the magnitude

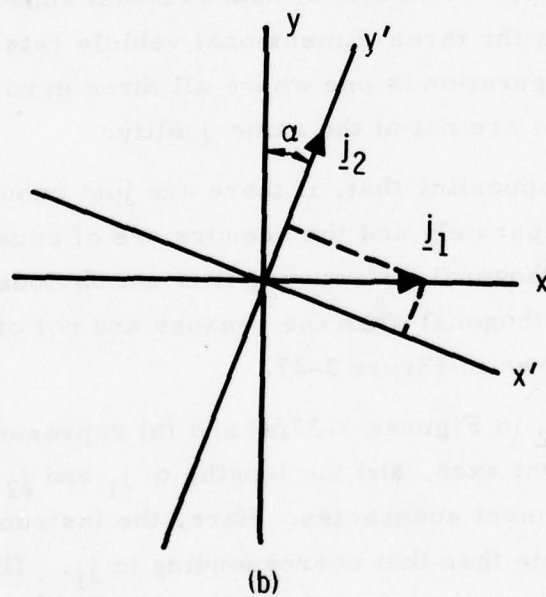
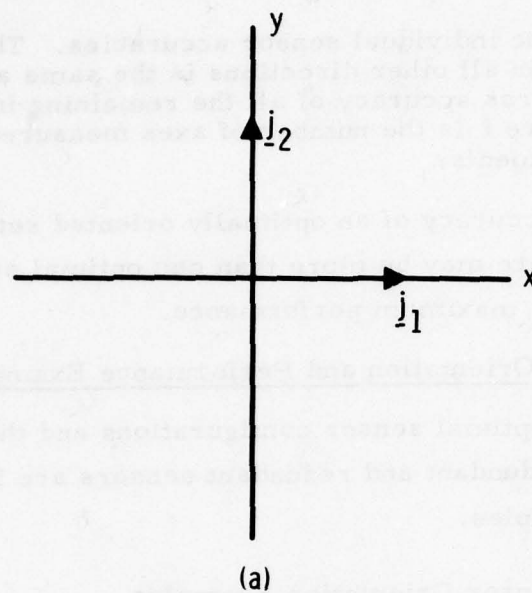


Figure 3-27. Nonredundant Sensor Configurations ($m = n = 2$)

\underline{j}_1 , $|\underline{j}_1|$. In Figure 3-27(b), the most accurate instrument is canted by angle α in an attempt to increase the measurement accuracy along the x-axis. In this case, however, the smallest measurement accuracy occurs in the x' -axis direction and is equal to $|\underline{j}_1| \cos \alpha$, which represents less accuracy than the worst case of Figure 3-27(a). Therefore, even though all instruments are not of equal quality, if there are not redundant sensors the worst case errors are minimized by orienting the sensor measurement axes orthogonally.

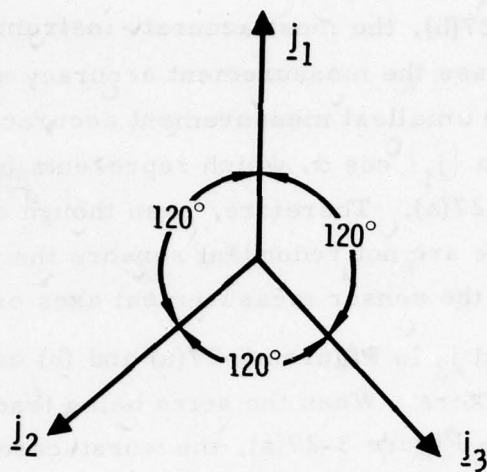
The vectors \underline{j}_1 and \underline{j}_2 in Figures 3-27(a) and (b) could represent the LOS vectors of two star trackers. When the stars being tracked are at right angles, as illustrated in Figure 3-27(a), the worst-case attitude (and rate) estimation uncertainties are minimized.

(2) Redundant Sensor Orientation Examples

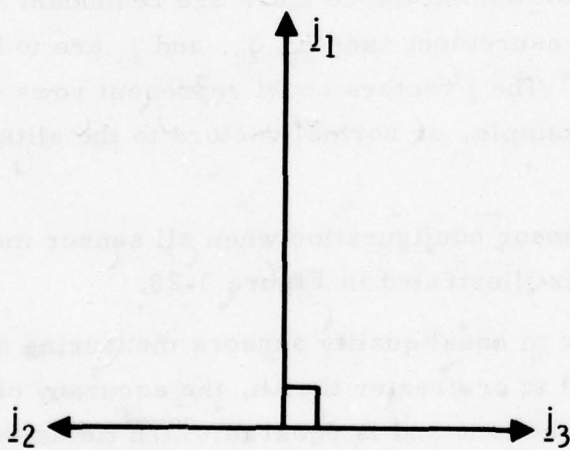
Now consider situations where there are redundant sensors. Assume that three sensor measurement axes \underline{j}_1 , \underline{j}_2 , and \underline{j}_3 are to be oriented to measure two directions. The \underline{j} vectors could represent rows of detectors in a star detector, for example, or normal vectors to the slits of a slit-type star detector.

The optimal sensor configuration when all sensor measurement axes are of equal quality is illustrated in Figure 3-28.

When there are m equal quality sensors measuring n directions (dimensions) and m is equal to or greater than n , the accuracy of the combined set is the same in all directions and is equal to $\sqrt{m/n}$ times the accuracy of a single instrument. The combined accuracy of the $m = 3$ sensors measuring in $n = 2$ directions (in Figure 3-27(a)) is $\sqrt{3/2}$ times the accuracy of a single instrument. Note that two instruments of equal quality measuring in the same direction have only $\sqrt{2}$ times and not twice the accuracy of a single instrument. If the m sensors are not of equal quality, the measurement accuracy of the optimally oriented set is still the same in any direction and equals the $1/\sqrt{n}$ times the rss accuracy of all instruments, providing this combined accuracy does not exceed the accuracy of a single instrument.



(a)



(b)

Figure 3-28. Redundant Sensor Configurations ($m = 3$, $n = 2$)

If the sensors in Figure 3-28(a) are not of equal quality, but the sensor along \underline{j}_1 has $\sqrt{2}$ times the accuracy of either sensor along \underline{j}_2 or \underline{j}_3 , the optimal configuration would appear as illustrated in Figure 3-28(b). Here, the accuracy of the sensor along \underline{j}_1 just equals $1/\sqrt{n} = 1/\sqrt{2}$ times the rss accuracy of all the sensors. These optimal sensor orientations would not change if the accuracy of the instrument along \underline{j}_1 exceeded $1/\sqrt{n}$ times the rss accuracy of all sensors. However, the measurement accuracy of the combined set would no longer be the same in all directions.

(3) Optimal Sensor Orientation Nonuniqueness Example

In general, the combined measurement accuracy of an optimally oriented set of sensors is unique along any axis, except for a rotation of relabeling of axes. However, the optimal sensor orientations are not necessarily unique. For example, consider the set of four equal quality sensors measuring in two dimensions as shown in Figure 3-29. In this figure, instruments along \underline{j}_1 and \underline{j}_2 and those along \underline{j}_3 and \underline{j}_4 are perpendicular. However, the combined set of instruments gives the same optimal measurement accuracy for all values of α .

c. Applications to Spacecraft Attitude Estimation

When this criterion of minimizing the worst case measurement errors is applied to certain examples of spacecraft attitude estimation, the following sensor orientations and performances result.

- a. Configuration 1. This configuration consists of an inertially fixed spacecraft with two equal quality star trackers. For this configuration, the optimal sensor orientation is one where the two stars being tracked are 90 deg apart. This orientation in addition to minimizing the worst case measurement errors also minimizes the worst case attitude and rate estimation uncertainties.
- b. Configuration 2. This configuration consists of spacecraft stabilized to a local vertical frame that contains two body-mounted star sensors. Again, the optimal orientation for these sensors is 90 deg apart and in the orbital plane to maximize the number of star sightings. This sensor

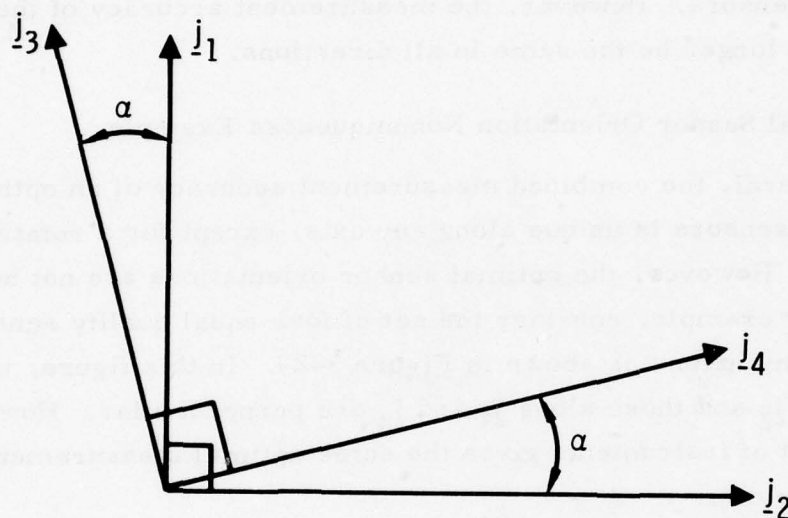


Figure 3-29. Nonunique Redundant Sensor Orientations

orientation minimizes the worst-case measurement errors as well as the worst-case attitude and rate uncertainties.

- c. Configuration 3. This configuration consists of a zero net-momentum spinning spacecraft stabilized with its spin (yaw) axis along the local vertical. The spacecraft contains two equal-quality body-mounted star sensors. The optimal orientation for these star sensors is 90 deg apart in the pitch-roll plane, assuming there are frequent star sightings. This sensor orientation also minimizes the worst-case measurement, attitude, and rate errors.

d. Extension of Optimization Criteria

In the following discussion the numerical techniques are described that are used for calculating the optimal sensor configurations which can be applied to calculate the sensor configurations that minimize some weighing of the estimation uncertainties. Determining these sensor configurations is a two-stage procedure. The first stage consists of an iterative search procedure to determine the measurement accuracies along each axis that are necessary to achieve the desired mix of estimation uncertainties. The second stage uses the numerical procedures outlined in this study to determine the sensor configuration that will achieve the necessary measurement accuracies.

In the first stage, the measurement accuracies are determined that are necessary to provide the desired estimation uncertainties. In general, this requires an iterative search because there is not a simple correspondence between the measurement accuracies on each axis and the resultant estimation uncertainties. When there is appreciable dynamic cross coupling of axes, improving the measurement accuracy along one axis will considerably reduce the uncertainties along other axes. In addition, even if there is no axial cross coupling, improving the measurement accuracy by some factor does not usually reduce the estimation uncertainties by the same amount. Therefore, in general, determining the desired measurement accuracies along each axis involves a search procedure where the estimation uncertainties are calculated for a trial set of measurement accuracies on each axis.

If the resulting estimation uncertainties are not in the desired ratios, improvement perturbations to the original measurement accuracies are calculated, and then the process is repeated for the new accuracies. The new measurement accuracies cannot be arbitrarily chosen since the rss of the measurement accuracies on all axes must equal the rss accuracy of the sensors. This process is considerably simpler, of course, when graphs have been precomputed relating the estimation uncertainties to the measurement accuracies. In such a case, the desired ratios of the measurement accuracies can be determined graphically. Once the measurement accuracies needed to achieve the desired ratios of estimation uncertainties have been determined, the sensor orientations that will produce these accuracies can be calculated from the numerical procedures in Appendix I.

IV. IMPLICATIONS FOR TECHNOLOGY DEVELOPMENT

In this section, the conceptual design performance results derived in Section III are used to define performance trade-off curves and sensitivities to various sensor and system parameters. Current sensor technology is used in conjunction with the trade-off curves to estimate the conceptual design performance capabilities with current technology instruments. The performance sensitivity data is then used to make recommendations on sensor development goals and guidelines.

A. CONCEPTUAL DESIGN PERFORMANCE TRADE-OFFS AND SENSITIVITIES

It was shown in Section III that the six attitude reference system conceptual designs may be modeled using three basic attitude estimation filters (see Table 3-2), namely the double integrator, the triple integrator, and the oscillator. Covariance analysis simulation runs made on these filters indicate that the performance difference between the double integrator and the oscillator systems is negligible for 10-percent cross-axis coupling or less and that the triple integrator performance approaches that of the discrete attitude double integrator for rate gyros exhibiting unbounded low frequency drift behavior of the random-walk type. Thus the performance of a large number of attitude reference systems for future missions may be predicted using the double integrator estimation filter with various combinations of discrete and continuous sensors. Although the double integrator model will not be exact in predicting the performance of oscillator-type systems with cross-axis coupling greater than 10 percent, it will provide a conservative bound on the oscillator performance. This bound is considered sufficient for the purposes of this study where the intent is to define general performance capabilities and trade-offs rather than a detailed attitude reference system design for a particular mission. Hence, the approach taken in the remainder of this subsection is to determine conceptual design performance

trade-offs and sensitivities based on the results of the double integrator filter covariance analyses and simulations.

In addition, performance trade-offs for discrete attitude and mixed discrete attitude and continuous rate systems with random (Poisson) update intervals are determined from the uniform update system performance results. It was shown in Paragraph III. F. 2 that the peak estimation errors for the uniform update system are equal to an upper bound on the average or mean estimation errors for a Poisson update sequence system with average update rate λ equal to the reciprocal of the uniform update interval T . Hence, the uniform update system peak rms errors represent an upper bound on the average rms errors of the random update system.

1. CONTINUOUS SYSTEM TRADE-OFFS AND SENSITIVITIES

Two classes of continuous systems are under consideration here, namely, systems with continuous attitude measurements only (trackers) and systems with both continuous attitude and rate measurements (trackers and rate gyros). These systems are suitable attitude reference system designs for inertially stable and nonspinning local vertical stable satellite configurations.

The steady-state performance of the continuous attitude double integrator system was derived in Section III. F as a function of the tracker noise r_θ and system steady-state bandwidth Ω . The tracker noise parameter represents the area under the actual tracker noise autocorrelation function. Assuming that the tracker output is sampled periodically and the tracker noise is uncorrelated from sample to sample, the noise parameter r_θ is equal to the product of the tracker noise variance and the sampling period. Then the steady-state rms attitude estimation error θ_{rms} for the continuous attitude double integrator system may be written, from Eqs. (III-37) and (III-41), in the form

$$\theta_{rms} = 2^{1/4} (q)^{1/8} T_S^{3/8} (NEA)^{3/4} \quad (IV-1)$$

where the noise equivalent angle (NEA) or tracker noise equivalent angle is taken to be the rms angle measurement error of the instrument and T_S is the sampling period. Equation (IV-1) shows that tracker accuracy or NEA has the greatest influence on the continuous attitude system performance with a three-fourth's power sensitivity. Increasing the sampling rate or decreasing the period T_S has much less influence due to the three-eighth's power sensitivity. As indicated in Section III. F, the system performance is only weakly influenced by the disturbance level q .

The rms rate estimation error ω_{rms} may be defined in terms of the tracker NEA from Eqs. (III-38) and (III-41) as

$$\omega_{rms} = (2)^{1/4} (q)^{3/8} (T_S)^{1/8} (NEA)^{1/4} \quad (IV-2)$$

The influence of the tracker accuracy and sampling rate on the rate error is much weaker than on the angle error. The disturbance torque level q is of primary influence with a three-eighth's power sensitivity.

Equation (IV-1) has been plotted in Figure 4-1 to illustrate the system attitude error as a function of tracker accuracy or NEA. The sampling period is 0.2 sec, equivalent to a 5-Hz sampling rate which should be sufficient for most satellite applications. The performance curves are plotted for four disturbance levels ranging from a fairly severe level ($q = 10^{-12} \text{ rad}^2/\text{sec}^3$) to a low level of $q = 2.5 \times 10^{-15} \text{ rad}^2/\text{sec}^3$, which can be considered as an average disturbance level equivalent to an rms disturbance torque of approximately $5 \times 10^{-5} \text{ ft-lb}$ acting on a 10^3 slug-ft^2 vehicle. This level will be used as a standard disturbance noise figure for performance comparisons.

It is shown in Figure 4-1 that for the average disturbance level the continuous attitude, or tracker only, double integrator system is theoretically capable of two-tenths to 1 arc sec attitude estimation performance

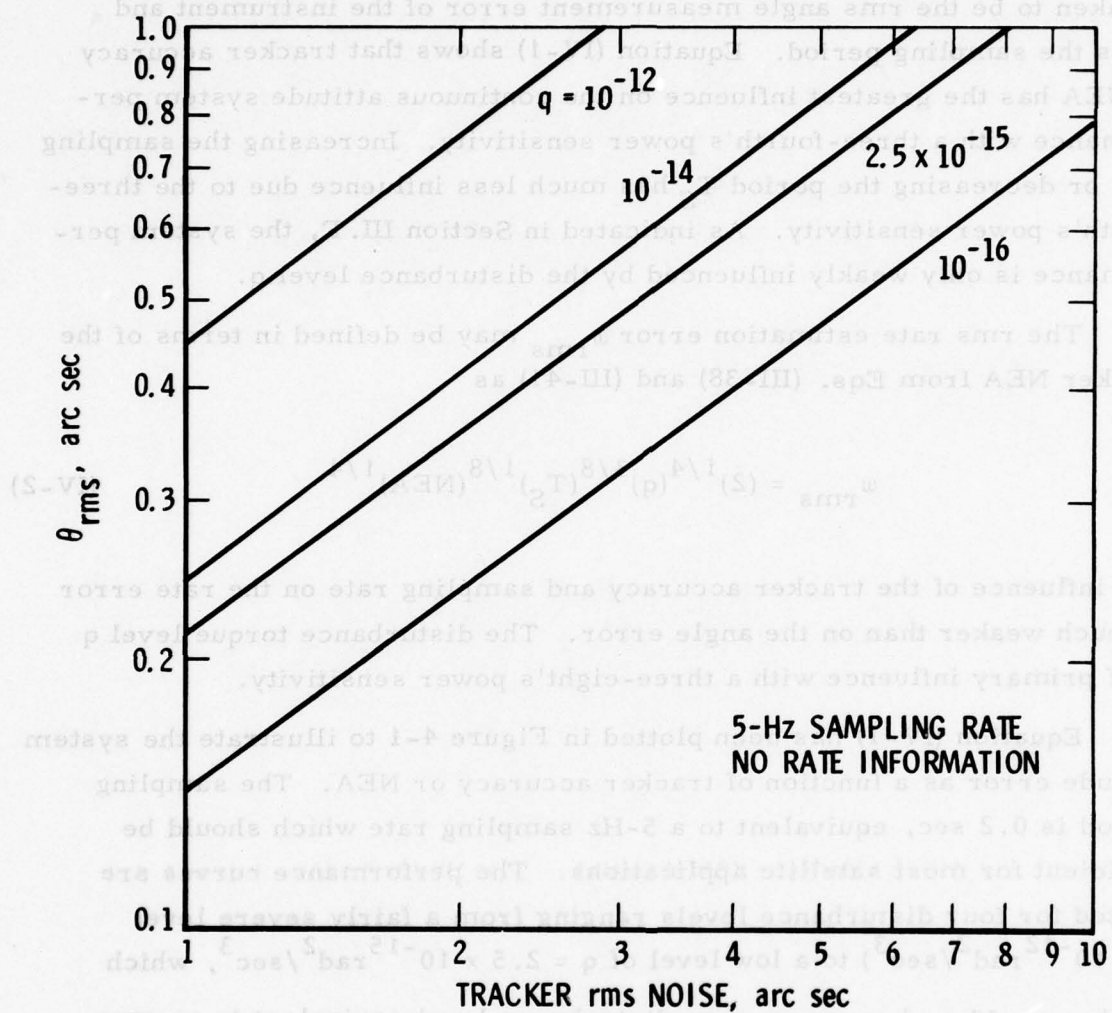


Figure 4-1. Continuous Attitude Double Integrator

with tracker NEAs ranging from 1 to 10 arc-sec. Due to the sensitivities, the most promising area of technology development from the system performance standpoint is to improve tracker accuracy or decrease the tracker noise equivalent angle. This includes decreasing random sensor misalignments as well as sensor noise that contribute to the angle measurement uncertainty.

The addition of continuous rate measurements to the continuous attitude measurement system alters the system performance sensitivities as a function of the rate measurement noise. Recalling the discussion in Section III. F. 1, the steady-state angle and rate estimation error sensitivities are approximately the same as those for the tracker system with poor rate sensors. As the quality of the rate sensors improves, the performance sensitivities from Eqs. (III-45) and (III-46) become

$$\theta_{\text{rms}} \approx (\text{NEA})^{1/2} (T_S)^{1/4} (r_{\delta\omega})^{1/4} \quad (\text{IV-3})$$

$$\omega_{\text{rms}} \approx (r_{\delta\omega})^{1/4} (q)^{1/4} \quad (\text{IV-4})$$

This change in performance sensitivity with changing rate sensor quality can be seen in Figure 4-2 where the steady-state attitude estimation error θ_{rms} is plotted as a function of rate sensor noise $r_{\delta\omega}$. Performance curves for three different tracker NEAs, sampled at 5 Hz, and two disturbance acceleration levels are depicted. It can be seen that the performance of continuous systems with poor quality rate sensors ($r_{\delta\omega} > 10^{-2} \text{ rad}^2/\text{sec}$) is insensitive to changes in $r_{\delta\omega}$. Thus, rate sensors are of no benefit to the system performance unless their quality is better than $r_{\delta\omega} = 10^{-12}$. The sensitivities for systems with poor rate sensors ($r_{\delta\omega} > 10^{-12}$) are the same as those for the tracker system and, hence, their performance is described by Eqs. (IV-1) and (IV-2). Changes in disturbance acceleration level q for these systems influence their performance as shown by the dashed curve segments in Figure 4-2.

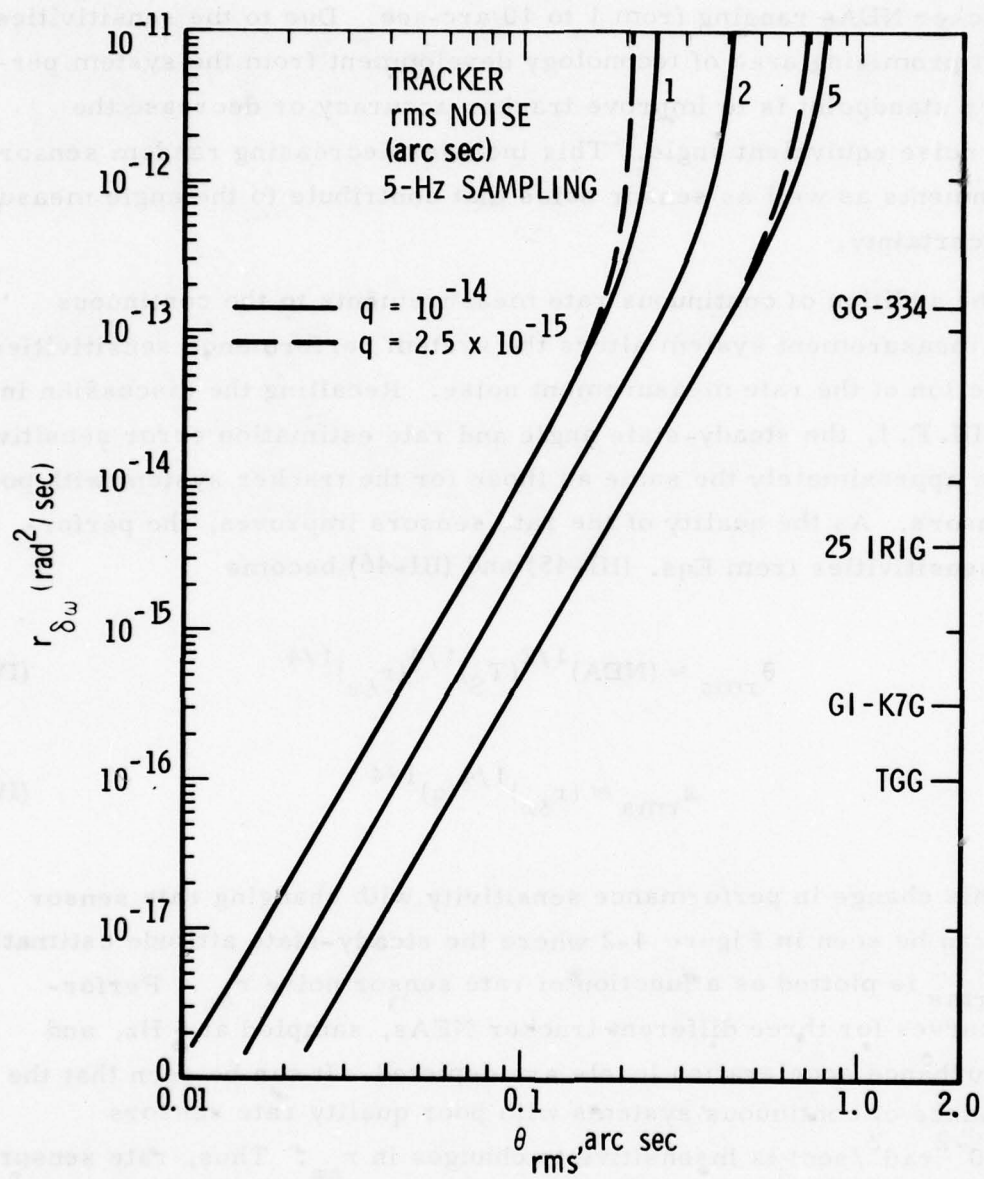


Figure 4-2. Continuous Attitude and Rate Double Integrator

As the rate sensor quality improves, the performance sensitivities shift to those described by Eqs. (IV-3) and (IV-4). It can be seen from the figure that the attitude estimation performance for systems with high quality rate sensors ($r_{\delta\omega} < 10^{-13} \text{ rad}^2/\text{sec}$) is insensitive to disturbance acceleration and exhibits a one-fourth power sensitivity to $r_{\delta\omega}$. It may also be seen from Figure 4-2 that the continuous attitude system when augmented by high quality continuous rate information from low noise gyros is theoretically capable of attitude estimation errors of less than one-tenth of 1 arc-sec. The performance sensitivities (Eqs. [IV-3] and [IV-4]) indicate that, from a performance standpoint, maximum benefit is gained by improving tracker NEA. However, it is shown in Figure 31 that development of rate sensors with noise levels ($r_{\delta\omega}$) on the order of 10^{-15} to 10^{-16} (rad^2/sec) could be an alternative technology effort that would yield large performance improvements.

The physical interpretation of the rate sensor noise $r_{\delta\omega}$ in terms of rate gyro parameters is discussed in Paragraph IV. A. 2 where system performance capabilities with current technology sensors are presented.

2. DISCRETE SYSTEM TRADE-OFFS AND SENSITIVITIES

The discrete systems under consideration in this discussion include systems with discrete attitude measurements (mappers) only and systems with discrete attitude and continuous rate measurements (mappers and gyros). As in the case of the continuous systems, performance sensitivities will be based primarily upon the double integrator filter capabilities. The discrete systems are suitable attitude reference designs for any spinning satellite configuration as well as for nonspinning local vertical configurations where the vehicle pitch rate may be used to scan the mapper.

The steady-state performance of the discrete attitude (mapper only) system was derived in Section III. F. 1 as a function of the product Ω' where Ω' represents the discrete system bandwidth and T represents the uniform

update interval of the mappers. It was shown in Section III. F. 1 that, for small values of the $\Omega'T$ product, the performance sensitivities of the discrete attitude system approach those of the continuous attitude system. The reason for this effect is that small values of the $\Omega'T$ product imply update rates that are much faster than the system bandwidth. Hence, the "discrete" measurements begin to look continuous to the filter, resulting in the same performance sensitivities as those described by Eqs. (IV-1) and (IV-2). Mapper systems mounted on spinning vehicles tend to have low $\Omega'T$ products because of the higher scan rates. The sensitivities indicate that for such systems the technology improvement necessary to increase performance is to decrease the mapper measurement noise or NEA. However, this is not necessarily the case for systems where the $\Omega'T$ product is large. Mapper systems mounted on nonspinning local vertical satellite configurations with low pitch rates due to high orbital attitudes exhibit large $\Omega'T$ products. It was shown in Paragraph III. F. 1 that the average performance for such systems is dominated by the attitude estimation error growth between discrete mapper updates. Hence their performance is strongly influenced by the update interval and the disturbance acceleration level. Furthermore, the average performance sensitivities are such that performance improvements may be gained by decreasing the update interval at the expense of mapper accuracy, provided that

$$(r_{\theta}T)_{\text{NEW}} \leq (r_{\theta}T)_{\text{OLD}} \quad (\text{IV-5})$$

where

$$r_{\theta} \triangleq (\text{NEA})^2$$

Therefore, system performance can be improved by increasing the number of reference sightings per scan of the mapper while allowing the accuracy of each sighting to degrade.

The trade-off between system performance in terms of peak rms attitude error θ_{rms} versus update interval and mapper NEA is presented graphically in Figure 4-3. To generate this plot, the standard disturbance acceleration level of $2.5 \times 10^{-15} \text{ rad}^2/\text{sec}^3$ was used along with the peak normalized error curve ($m_{\theta\theta}/r'$) of Figure 4-3. The performance curves for two different mapper accuracy levels are illustrated. Both curves exhibit an increasing performance sensitivity with increasing update interval. As the interval increases so also does the $\Omega'T$ product, resulting in the increasing sensitivity to T . Referring to Figure 3-3, it can be seen that the 1 arc-sec NEA system exhibits an 8 arc-sec performance capability at an update interval of 100 sec. Decreasing the interval by a factor of 5 to 20 sec yields improved system performance even if the mapper accuracy degrades by the same factor to an NEA of 5 arc sec. Therefore, it may be concluded that, for discrete systems operating with large update intervals, greater performance improvements can be obtained by decreasing the update interval than by increasing the mapper accuracy. The opposite is true for systems operating at high update rates as can be seen from the flattening out of the performance curves in Figure 4-3 with decreasing update interval. Thus, for the fast update systems, it is desirable to improve accuracy rather than to decrease the update interval.

The steady-state performance of discrete attitude double integrator systems augmented with continuous rate measurements (mapper and gyro systems) cannot be derived analytically. Rather, the performance capabilities of this class of system must be determined from the covariance analysis computer simulation curves (see Figure 3-9). These capabilities are presented as attitude error θ_{rms} curves plotted versus update interval for two different rate sensor qualities ($r_{\delta\omega} = 10^{-13}$ and $10^{-16} \text{ rad}^2/\text{sec}$) in Figure 4-4. Comparison of the slopes of the dashed and solid curves in this figure indicate that discrete systems augmented with lower noise rate measurements result in less sensitivity to the update interval. This is a result of the fact that the presence of continuous rate measurements inhibits the attitude error growth between updates. Since

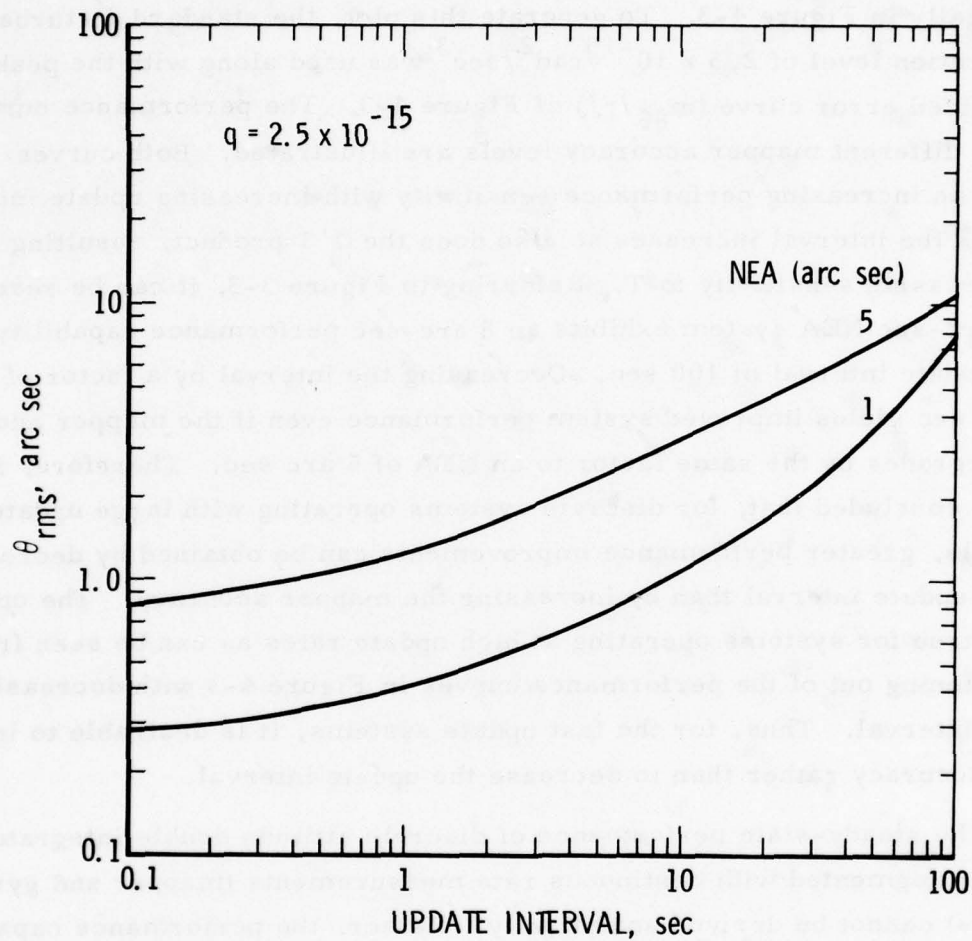


Figure 4-3. Discrete Attitude Double Integrator

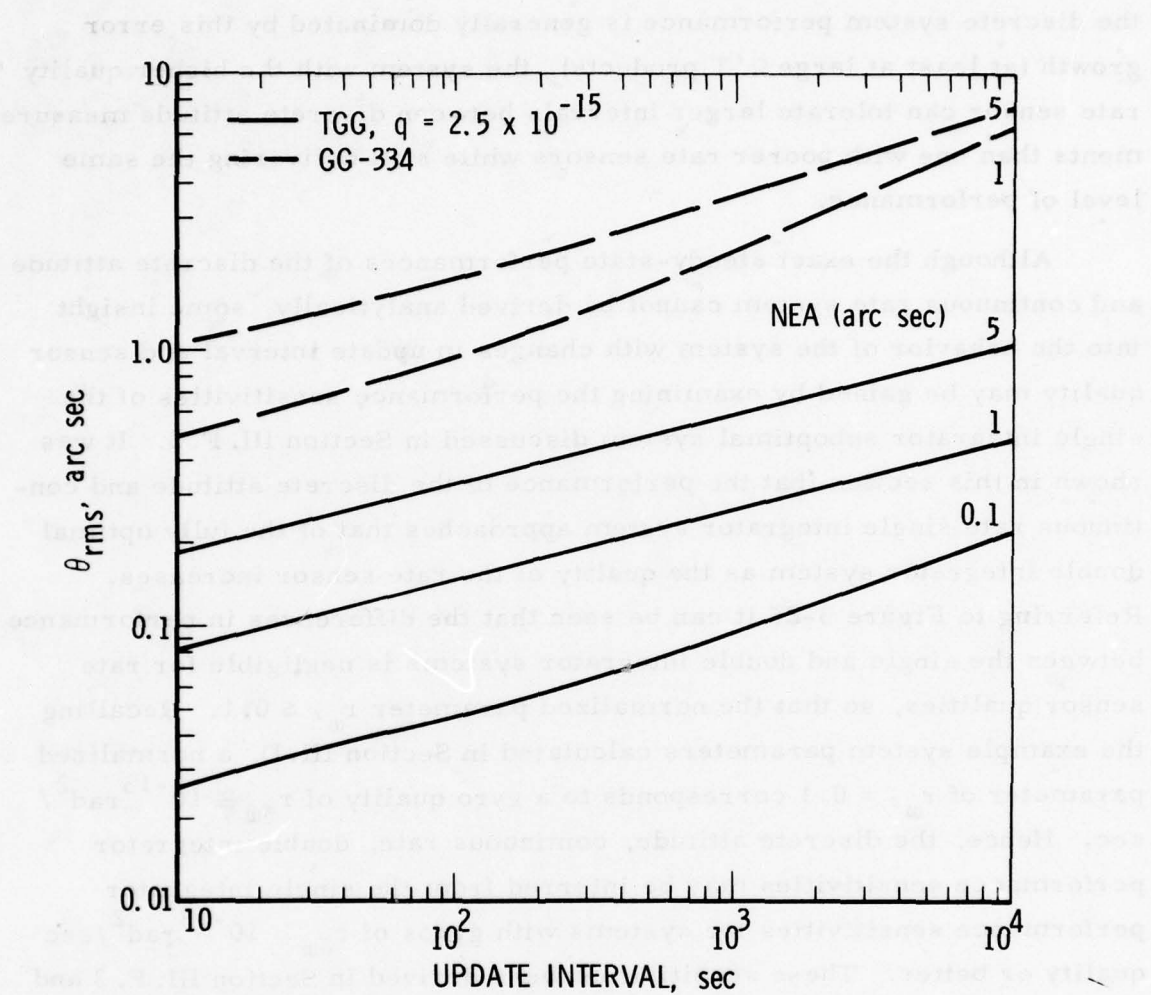


Figure 4-4. Discrete Attitude/Continuous Rate Double Integrator System

the discrete system performance is generally dominated by this error growth (at least at large $\Omega'T$ products), the system with the higher quality rate sensor can tolerate larger intervals between discrete attitude measurements than one with poorer rate sensors while still delivering the same level of performance.

Although the exact steady-state performances of the discrete attitude and continuous rate system cannot be derived analytically, some insight into the behavior of the system with changes in update interval and sensor quality may be gained by examining the performance sensitivities of the single integrator suboptimal system discussed in Section III. F. 3. It was shown in this section that the performance of the discrete attitude and continuous rate single integrator system approaches that of the fully optimal double integrator system as the quality of the rate sensor increases. Referring to Figure 3-25 it can be seen that the differences in performance between the single and double integrator systems is negligible for rate sensor qualities, so that the normalized parameter $r_w \leq 0.1$. Recalling the example system parameters calculated in Section III. D, a normalized parameter of $r_w = 0.1$ corresponds to a gyro quality of $r_{\delta\omega} \cong 10^{-13} \text{ rad}^2/\text{sec}$. Hence, the discrete attitude, continuous rate, double integrator performance sensitivities may be inferred from the single integrator performance sensitivities for systems with gyros of $r_{\delta\omega} = 10^{-13} \text{ rad}^2/\text{sec}$ quality or better. These sensitivities were derived in Section III. F. 3 and are presented as Eqs. (III-72) through (III-75). These equations indicate that there is a direct trade-off between the rate measurement quality $r_{\delta\omega}$ and the update interval T . Consequently, doubling T while halving $r_{\delta\omega}$ results in no change in performance since the product of $r_{\delta\omega}$ and T remains constant. Further, the performance sensitivity to changes in the $r_{\delta\omega} T$ product is greater than to changes in the mapper quality r_θ . Maximum performance improvements, therefore, can be gained by increasing the number of mapper reference sightings per scan (i.e., decreasing T) and/or improving rate sensor quality.

To further illustrate these performance trade-offs, a hypothetical discrete attitude and continuous-rate system is examined in the following discussion. The satellite configuration for this system is a three-axis, stable, local vertical vehicle in synchronous equatorial orbit. Due to the low cross-axis coupling (quarter-orbit kinematic coupling) for such a satellite, the double integrator model can be used to predict system performance. In addition, the attitude reference performance for each axis can be treated independently. Looking at the single-axis performance, assume that the mapper is a strapped-down star sensor with a single slit that sweeps out a swath of angular width γ around the celestial sphere on each orbital revolution. Then, the average time interval between star sightings is equal to the orbital period (24 hr) divided by the number of stars seen by the mapper over one orbit. The number of stars seen by the mapper depends, in turn, upon the area swept by the mapper over the celestial sphere and the sensitivity of the slit. This number can be determined using a star density versus visual magnitude graph such as is shown in Figure 4-5. This graph is based upon a reduction of data contained in the Smithsonian Astrophysical Observatory Star Catalog. The data reduction is described in Volume III of Reference 1, and Figure 4-5 is a duplication of Figure 24 of that document. An approximate analytical relationship between star density and visual magnitude may be obtained by fitting a straight line to the graph in Figure 4-5. Using this relationship and determining the area swept by the mapper as a function of the slit FOV γ , the number of stars seen by the mapper over one revolution may be represented by the equation

$$N = K_1 (10^{K_2 M_v}) \sin (\gamma/2) \quad (\text{IV-6})$$

where the mapper sensitivity is described in terms of the dimmest visual magnitude M_v star that can be seen by the mapper, and the constants K_1 and K_2 are determined from the curve fit to be 3.0024 and 0.5296 respectively. Equation (IV-6) is plotted in Figure 4-6 as a function of various

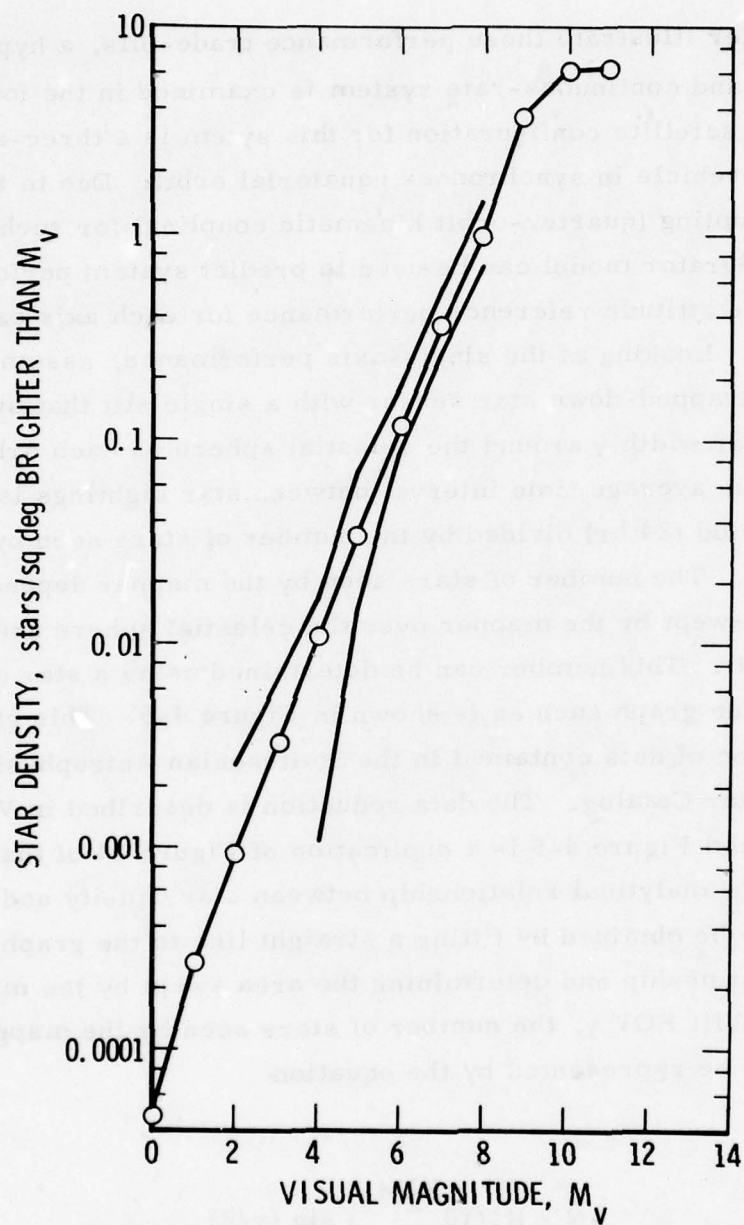


Figure 4-5. Star Density versus Visual Magnitude, Total Sphere

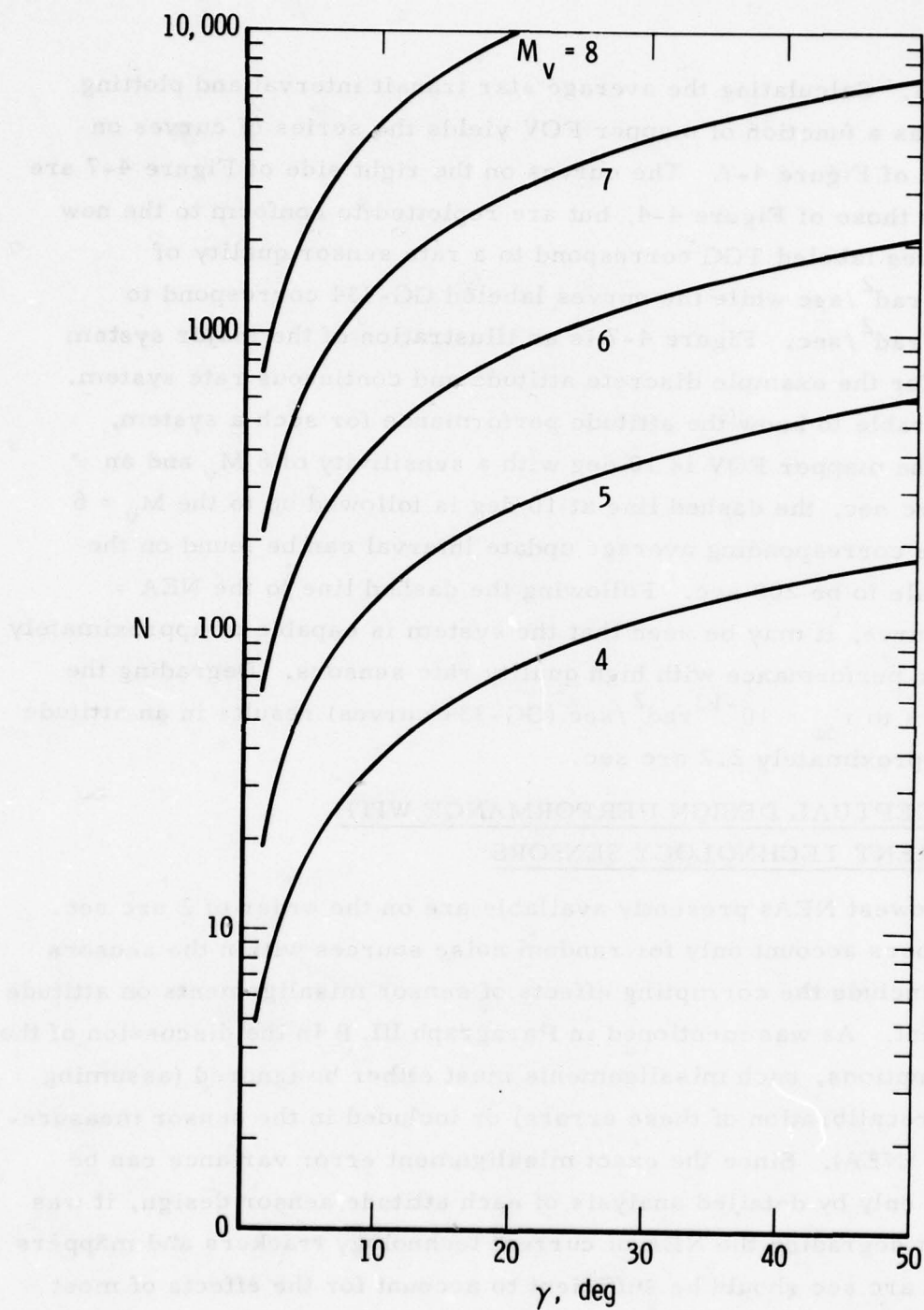


Figure 4-6. Number of Stars per Revolution versus Sensor Field of View

sensitivities. Calculating the average star transit interval and plotting the results as a function of mapper FOV yields the series of curves on the left side of Figure 4-7. The curves on the right side of Figure 4-7 are the same as those of Figure 4-4, but are replotted to conform to the new axes. Curves labeled TGG correspond to a rate sensor quality of $r_{\delta\omega} = 10^{-16} \text{ rad}^2/\text{sec}$ while the curves labeled GG-334 correspond to $r_{\delta\omega} = 10^{-13} \text{ rad}^2/\text{sec}$. Figure 4-7 is an illustration of the major system trade-offs for the example discrete attitude and continuous rate system. If it is desirable to know the attitude performance for such a system, given that the mapper FOV is 10 deg with a sensitivity of $6 M_v$ and an NEA of 5 arc sec, the dashed line at 10 deg is followed up to the $M_v = 6$ curve. The corresponding average update interval can be found on the vertical scale to be 200 sec. Following the dashed line to the NEA = 5 arc-sec curve, it may be seen that the system is capable of approximately 0.4 arc-sec performance with high quality rate sensors. Degrading the rate sensors to $r_{\delta\omega} = 10^{-13} \text{ rad}^2/\text{sec}$ (GG-334 curves) results in an attitude error of approximately 2.2 arc sec.

B. CONCEPTUAL DESIGN PERFORMANCE WITH CURRENT TECHNOLOGY SENSORS

The lowest NEAs presently available are on the order of 2 arc sec. These numbers account only for random noise sources within the sensors and do not include the corrupting effects of sensor misalignments on attitude measurement. As was mentioned in Paragraph III. B in the discussion of the study assumptions, such misalignments must either be ignored (assuming complete precalibration of these errors) or included in the sensor measurement error (NEA). Since the exact misalignment error variance can be determined only by detailed analysis of each attitude sensor design, it was decided that degrading the NEA of current technology trackers and mappers from 2 to 5 arc sec should be sufficient to account for the effects of most sensor misalignments in this study. Additional parameters assumed for

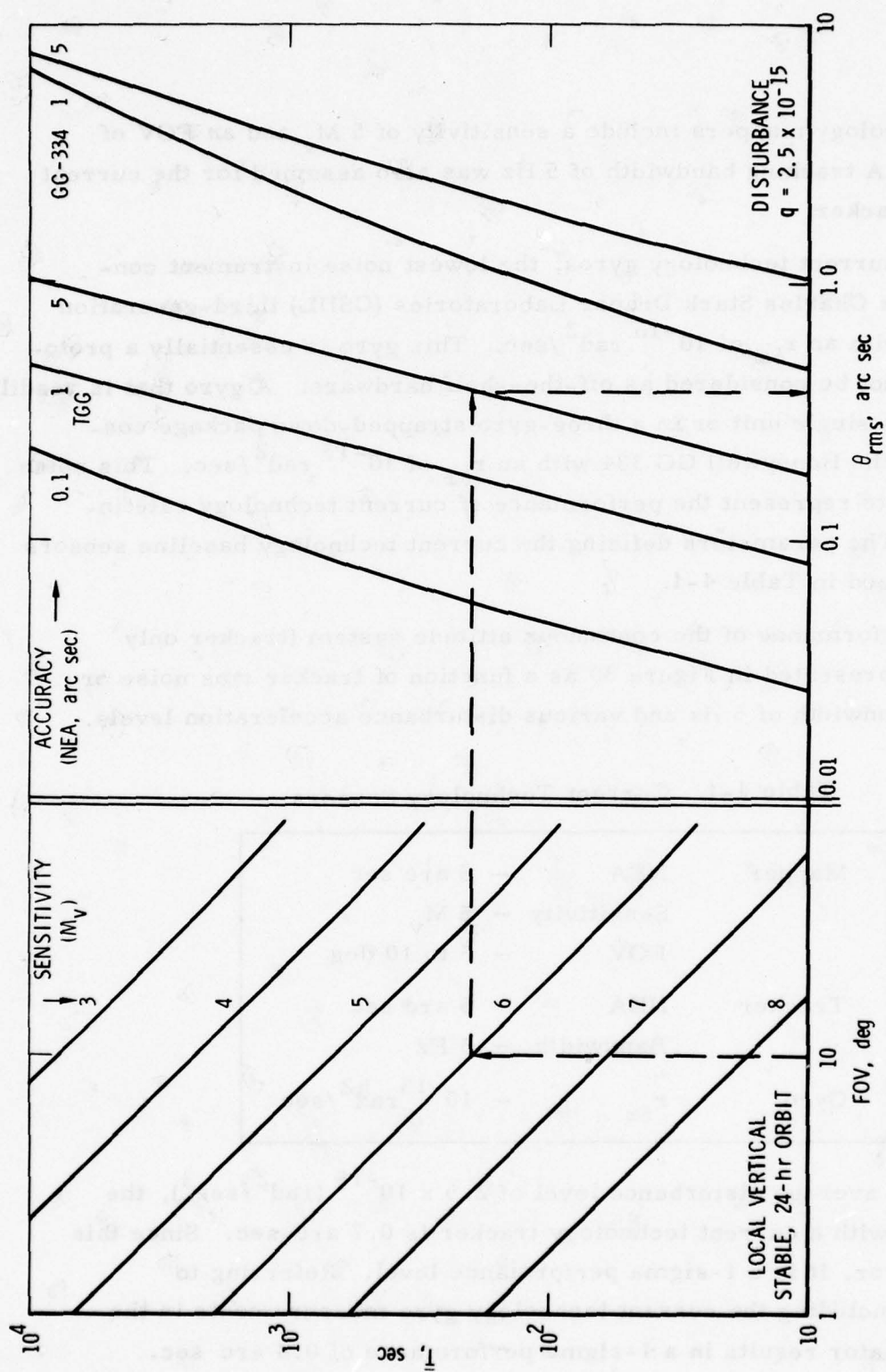


Figure 4-7. System Performance versus Sensor Parameters for Discrete Attitude Continuous Rate System

current technology mappers include a sensitivity of $5 M_v$ and an FOV of 5 to 10 deg. A tracking bandwidth of 5 Hz was also assumed for the current technology tracker.

Of the current technology gyros, the lowest noise instrument considered is the Charles Stark Draper Laboratories (CSDL) third-generation gyro (TGG) with an $r_{\delta\omega}$ of $10^{-16} \text{ rad}^2/\text{sec}$. This gyro is essentially a prototype and cannot be considered as off-the-shelf hardware. A gyro that is readily available as a single unit or in a three-gyro strapped-down package configuration is the Honeywell GG 334 with an $r_{\delta\omega}$ of $10^{-13} \text{ rad}^2/\text{sec}$. This noise level is used to represent the performance of current technology rate instruments. The parameters defining the current technology baseline sensors are summarized in Table 4-1.

The performance of the continuous attitude system (tracker only system) was presented in Figure 30 as a function of tracker rms noise or NEA for a bandwidth of 5 Hz and various disturbance acceleration levels.

Table 4-1. Current Technology Sensors

Mapper	NEA	- 5 arc sec
	Sensitivity	- $5 M_v$
	FOV	- 5 to 10 deg
Tracker	NEA	- 5 arc sec
	Bandwidth	- 5 Hz
Gyro	$r_{\delta\omega}$	- $10^{-13} \text{ rad}^2/\text{sec}$

Assuming the average disturbance level of $2.5 \times 10^{-15} (\text{rad}^2/\text{sec}^3)$, the performance with a current technology tracker is 0.7 arc sec. Since this is an rms error, it is a 1-sigma performance level. Referring to Figure 4-2, including the current technology gyro measurements in the attitude estimator results in a 1-sigma performance of 0.4 arc sec.

The performance of the discrete attitude system (mapper only system) depends on the update interval as well as the mapper NEA. Assuming that the mapper only system is on a spinning vehicle of some kind (spinner, dual-spinner, or yaw-spinner), the update interval would be a function of the sensitivity of the mapper and the spin rate of the vehicle. For the purpose of defining a baseline performance, it is assumed that the mapper sensitivity is sufficient to obtain one sighting per revolution of the vehicle and that the spin rate is 20 revolutions per min (rpm). The resulting update interval for this example is 3 sec. Using Figure 4-3, the 1-sigma performance for the current technology discrete attitude system is 2 arc sec.

As an alternate example, it is assumed that the discrete attitude system is mounted on a local vertical stable vehicle in a 24-hr orbit. The scan rate in this case is equal to the orbital rate. It is also assumed that the FOV is 10 deg and the sensitivity is $5 M_v$ as indicated in Table 4-1. Then, using the left side of Figure 4-7, a 700-sec update interval results in a 1-sigma performance much greater than 10 arc sec for the current technology discrete attitude system. It can be seen from this figure that the update interval must be reduced by at least an order of magnitude down to 70 sec before the current technology system can deliver a performance of less than 10 arc sec. For a single-slit sensor, the trade-off between FOV and sensitivity to obtain this reduction in update interval is illustrated on the left side of Figure 4-7. Thus, the sensitivity must be increased to $7 M_v$ for a 10-deg FOV to obtain an order of magnitude reduction in update interval. Alternately, allowing the FOV to increase to 30 deg permits a reduction in sensitivity to $6 M_v$ for an update interval on the order of 70 sec.

These demands on the mapper sensitivity and FOV may be alleviated by the addition of rate information. Referring again to Figure 4-7, a discrete attitude and continuous rate system operating at an update interval

of 700 sec with current technology gyro information ($r_{\delta\omega} = 10^{-13} \text{ rad}^2/\text{sec}$) results in a 1-sigma performance of 3.2 arc sec. Thus, the addition of rate information has reduced the attitude error below 10 arc sec without having to reduce the update interval.

In summary, within the limitations imposed by the study assumptions and constraints, the 1-sigma performance capabilities of the various conceptual designs with current technology instruments are estimated to be:

- a. The continuous attitude system is capable of 0.7 arc sec for the average disturbance environment.
- b. The continuous attitude and rate system is capable of 0.4 arc sec.
- c. The discrete attitude system for the 20-rpm spinner is capable of 2 arc sec, assuming one sighting per revolution.
- d. The discrete attitude system on the local vertical 24-hr orbit vehicle delivers a performance worse than 10 arc sec for a 10-deg FOV, 5-M_v sensitivity mapper.
- e. The discrete attitude and continuous rate system for the same vehicle and mapper as that in case d above is capable of 3.2 arc sec.

C. ATTITUDE REFERENCE TECHNOLOGY DEVELOPMENT

The attitude reference system performance sensitivities vary with the type of system, i.e., discrete or continuous, as well as the operating point about which the system is designed, e.g., the $\Omega'T$ value for a discrete system or the $r_{\delta\omega}$ value for a continuous system with gyros. Hence, the technology development necessary to improve future system performance varies to some extent depending on the system type.

Discrete systems without gyros will probably be used to provide the attitude reference on spinning or dual-spin configurations. The attitude sensors for these configurations will be mappers to take advantage of the body spin to scan the sensor LOS. The bandwidth and update interval ($\Omega'T$) product, defined in Paragraph IV.A for the discrete system, will probably

be less than 1 due to high spin rates. As long as the mapper sensitivity is sufficient to obtain at least one or two sightings per spin revolution, the technology development effort should concentrate on improving the mapper NEA. Such improvement involves the reduction and/or precalibration of mapper misalignments with respect to the vehicle reference frame as well as the minimization of signal processing and detector noise contributions to timing error. Assuming that the current technology mapper is capable of a 5 arc-sec NEA, a reasonable technology improvement goal would be an NEA of 1 arc sec.

Discrete systems with gyro information will probably be used on local vertical, earth-oriented satellite configurations. Gyro information is necessary in these configurations to inhibit the growth of the estimation errors between discrete mapper updates. The performance sensitivities indicate that improvements can be realized by advancing gyro technology and/or mapper technology.

Gyro technology improvement refers to the reduction of the rate measurement noise or uncertainty parameter $r_{\delta\omega}$. Present off-the-shelf hardware in gyros is capable of $r_{\delta\omega} = 10^{-13} \text{ rad}^2/\text{sec}$. Development programs to improve this figure to at least $10^{-16} \text{ rad}^2/\text{sec}$ should be conducted.

Mapper technology advancement efforts for discrete systems with gyros should be concerned with decreasing the time interval between discrete updates. This may be accomplished by increasing the FOV, adding more detector slits, or increasing the mapper sensitivity. An area that was not explored but which has a major impact on system performance (especially convergence time) is the false update problem. Since the analysis of this problem is highly dependent on sensor design, it was not included in this study. Mapper parameters such as sensitivity have a major influence on this problem since the probability of a false update is, in many cases, a function of the signal-to-noise ratio. Thus, improvements in performance due to increasing mapper sensitivity (decreasing update interval) may be offset by the increase in the false update probability. Such a trade-off must be explored as part of the technology advancement effort.

Continuous systems with or without gyros are necessary on all inertially stable configurations. They may also be employed on earth-oriented, local vertical satellites as well as on the despun platform of a dual-spin configuration. The sensitivities for the continuous system are such that the greatest improvement in system performance is obtained by reducing the tracker NEA. This reduction must include minimization of misalignments such as gimbal runout errors for gimballed trackers as well as reduction of detector and signal processing electronics noise. Assuming an NEA of 5 arc sec as representative of current tracker technology, a reasonable technology goal would be a reduction of the NEA to 1 arc sec.

APPENDIX A. ATTITUDE ESTIMATOR EQUATIONS

This appendix is devoted to the derivation of the equations that define the attitude estimation filter implemented in the conceptual designs investigated by the HAADS effort. The mathematical development of the satellite dynamics follows the derivation presented by Beard¹ and is contained in Paragraph 1. A brief discussion of the structure of the Kalman filter used to estimate the satellite attitude and rate is presented in Paragraph 2. Paragraph 3 is a discussion of the sensor measurement geometries.

1. ATTITUDE DYNAMICS

The rigid body rotational dynamics of a satellite under the influence of external disturbance torques $\underline{\tau}$ can be written as

$$\dot{\underline{h}} + (\underline{\omega} \times) \underline{h} = \underline{\tau} \quad (\text{A-1})$$

where \underline{h} is the total satellite angular momentum, $\dot{\underline{h}}$ is its time derivative, $\underline{\omega}$ is the satellite angular velocity with respect to inertial space, and $(\underline{\omega} \times)$ is represented by the matrix

$$(\underline{\omega} \times) = \begin{pmatrix} 0 & -\omega_z & \omega_y \\ \omega_z & 0 & -\omega_x \\ -\omega_y & \omega_x & 0 \end{pmatrix} \quad (\text{A-2})$$

Assuming that the spacecraft contains a momentum wheel, the total angular momentum in Eq. (A-1) can be written as

$$\underline{h} = J \underline{\omega} + \underline{h}_w \quad (\text{A-3})$$

¹R. V. Beard, Unobservability in Attitude Estimation, TOR-0059(6472)-35, The Aerospace Corporation, El Segundo, California (16 March 1971).

where J is the satellite moment-of-inertia matrix and \underline{h}_w is the onboard wheel angular momentum. Substituting Eq. (A-3) into (A-1) and assuming that the wheel angular momentum is constant result in the expression

$$\dot{\underline{\omega}} = -J^{-1} \underline{\omega} \times (J \underline{\omega} + \underline{h}_w) + \underline{a} \quad (\text{A-4})$$

where \underline{a} is the external disturbance angular acceleration ($\underline{a} = J^{-1} \underline{\tau}$). Equation (III-4) is the nonlinear vector differential equation describing the satellite's angular velocity.

Representing the vehicle angular velocity as

$$\underline{\omega} = \underline{\omega}_0 + \delta \underline{\omega} \quad (\text{A-5})$$

where $\underline{\omega}_0$ is the nominal angular velocity of the undisturbed satellite defined by the equation

$$\dot{\underline{\omega}}_0 = -J^{-1} \underline{\omega}_0 \times (J \underline{\omega}_0 + \underline{h}_w) + \underline{a}_0 \quad (\text{A-6})$$

and $\delta \underline{\omega}$ represents the perturbation due to the presence of external disturbance angular accelerations \underline{a} in Eq. (A-4), the desired linearized description can be obtained by substitution of Eqs. (A-5) and (A-6) into (A-4) and neglecting higher order terms. It will be assumed in this study that the nominal angular acceleration \underline{a}_0 in Eq. (A-7) is zero. Hence, any external angular accelerations act to perturb the satellite from the nominal attitude. The result is

$$\delta \dot{\underline{\omega}} = F(\underline{\omega}_0, \underline{h}_w) \delta \underline{\omega} + \delta \underline{a} \quad (\text{A-7})$$

where

$$F(\underline{\omega}_0, \underline{h}_w) = J^{-1} [-(\underline{\omega}_0 \times) J + (J \underline{\omega}_0 + \underline{h}_w) \times] \quad (\text{A-8})$$

with the cross-products defined as

$$(\underline{\omega}_0 \times) = \begin{pmatrix} 0 & -\omega_{0z} & \omega_{0y} \\ \omega_{0z} & 0 & -\omega_{0x} \\ -\omega_{0y} & \omega_{0x} & 0 \end{pmatrix} \quad (\text{A-9})$$

and, letting $J\underline{\omega}_0 + \underline{h}_\omega \equiv \underline{v}$,

$$[(J\underline{\omega}_0 + \underline{h}_\omega) \times] = \begin{pmatrix} 0 & -v_z & v_y \\ v_z & 0 & -v_x \\ -v_y & v_x & 0 \end{pmatrix}$$

The satellite's attitude may be represented in various ways including Euler angles, quaternions, or direction cosines. Regardless of the particular representation chosen, the attitude time history may be obtained from a nominal attitude history and a set of infinitesimal rotations $\underline{\theta}$, between the nominal and actual body attitudes, which are driven by the perturbed angular velocity $\delta\underline{\omega}$. This may be seen from the following derivation (obtained from Ref. 1) for a direction cosine representation.

Define the following orthogonal coordinate frames:

B - body-fixed frame

B_0 - nominal body reference frame

I - inertial reference frame

Let $C_{F_2}^{F_1}$ denote the direction cosine matrix from coordinate frame F_2 to coordinate frame F_1 . Further, let $\underline{\theta}$ be a small angle rotation vector from B_0 to B expressed in the B_0 frame. It is a three-component vector whose direction is the axis about which the rotation is to be made, with magnitude

equal to the angle of rotation in radians. Now for small $\underline{\theta}$ the direction cosine matrix from B_0 to B is

$$C_{B_0}^B = I + [\underline{\theta} \times]$$

where

$$(\underline{\theta} \times) = \begin{pmatrix} 0 & -\theta_z & \theta_y \\ \theta_z & 0 & -\theta_x \\ -\theta_y & \theta_x & 0 \end{pmatrix}$$

Then the attitude of the satellite with respect to inertial space can be represented by

$$C_I^B = C_{B_0}^B C_I^{B_0} = [I + (\underline{\theta} \times)] C_I^{B_0} \quad (A-10)$$

where $C_I^{B_0}$ represents the nominal attitude of the body (satellite). If $C_I^{B_0}$ is known, the actual attitude C_I^B may be estimated by estimating $\underline{\theta}$. Let $\underline{\omega}_0$ be the inertial angular velocity of the nominal body (B_0 -frame) expressed in the B_0 -frame and $\underline{\omega}$ be the inertial angular velocity of the B -frame expressed in the B_0 -frame. Then, the nominal body attitude may be obtained by integrating the equation

$$\dot{C}_I^{B_0} = -(\underline{\omega}_0 \times) C_I^{B_0} \quad (A-11)$$

where the cross-product is defined by Eq. (A-9). In general, $\underline{\theta}$ is not a true vector quantity since it does not obey the commutative law, but if $\underline{\theta}$ is small it may be treated as a vector quantity. For any arbitrary vector v ,

$$\left(\frac{dv}{dt}\right)_{\text{inertial}} = \left(\frac{dv}{dt}\right)_{\text{relative to } B_0} + (\underline{\omega}_0 \times) \underline{v} \quad (\text{A-12})$$

Then for $\underline{\theta}$,

$$\left(\frac{d\theta}{dt}\right)_{\text{inertial}} = \underline{\omega} - \underline{\omega}_0 = \delta \underline{\omega} \quad (\text{A-13})$$

from Eq. (A-5) and

$$\left(\frac{d\theta}{dt}\right)_{\text{relative to } B_0} = \dot{\theta} \quad (\text{A-14})$$

Substitution of Eqs. (A-13) and (A-14) into the form of Eq. (A-12) and rearranging the result produce the desired differential equation for $\underline{\theta}$,

$$\dot{\underline{\theta}} = -(\underline{\omega}_0 \times) \underline{\theta} + \delta \underline{\omega} \quad (\text{A-15})$$

An equivalent derivation of Eq. (A-15) starting with Euler angle representation of the satellite attitude is supplied by Dixon.² Equations (A-8) and (A-15) together represent the desired linear description of the satellite's attitude dynamics. These two equations may be combined into a single linear vector differential equation by defining the state vector $\underline{x} = (\underline{\theta}, \delta \underline{\omega})$. The state equation is then

$$\dot{\underline{x}} = \underline{A} \underline{x} + \underline{w} \quad (\text{A-16})$$

²M. V. Dixon, Spacecraft Attitude Estimation with Motion Perturbation Equations, TOR-0066(5763)-13, The Aerospace Corporation, El Segundo, California (22 May 1970).

where the dynamics matrix A and the disturbance vector w are defined by

$$A = \left(\begin{array}{c|c} -(\underline{w}_0^x) & I \\ \hline 0 & F(\underline{w}_0, \underline{h}_w) \end{array} \right) ; \quad \underline{w} = \begin{pmatrix} \underline{0} \\ \underline{a} \end{pmatrix} \quad (A-17)$$

with I , which is the identity matrix, and $F(\underline{w}, \underline{h})$ defined by Eq. (A-18).

Since the state \underline{x} represents only the perturbations in satellite attitude and angular rate from the nominal attitude and rate of an undisturbed satellite, the actual satellite behavior must be determined from the equations

$$\underline{\omega} = \underline{\omega}_0 + \delta \underline{\omega} \quad (\text{A-18})$$

$$C_I^B = [I + (\underline{\theta} \mathbf{x})] C_I^{B_0} \quad (A-19)$$

which combine the nominal and perturbed states of the satellite. The nominal rate and attitude ($\underline{\omega}_0$ and $C_I^{B_0}$), in turn, satisfy the equations

$$\dot{\underline{\omega}}_0 = -J^{-1}[\underline{\omega}_0 \mathbf{x} (J \underline{\omega}_0 + \underline{h}_0)] \quad (\text{A-20})$$

$$\dot{C}_I^{B_0} = -(\frac{\omega_0}{x}) C_I^{B_0} \quad (A-21)$$

The attitude estimation filter implemented in all conceptual designs of this study will estimate the perturbed state \underline{x} of the actual satellite. These estimates must then be combined with the nominal attitude and angular rate states, in the manner of Eqs. (A-18) and (A-19), to obtain the total estimated attitude and rate. The nominal attitude and rate of the satellite are the solutions to Eqs. (A-20) and (A-21), which may be solved analytically or precomputed, thus requiring only integration of the linearized perturbation

equations in the form of Eq. (A-16) by the estimation filter. This approach can result in considerable computational advantages as discussed in Reference 2.

2. ESTIMATION FILTER

The structure of the continuous Kalman filter, which generates a minimum variance estimate of the actual state \underline{x} , is illustrated in Figure A-1. Referring to the block diagram shown in Figure A-1, the measurement vector $\underline{z} = (\underline{z}_\theta, \underline{z}_{\delta\omega})$ is generated from measurements of the actual body attitude and rate obtained by the onboard sensors. The nominal attitude and rate obtained from Eqs. (A-20) and A-21) and transformed into the sensor frames are subtracted from the attitude and rate sensor outputs to produce \underline{z} . These measurements are not perfect in that they are corrupted by sensor noise $\underline{n} = (\underline{n}_\theta, \underline{n}_{\delta\omega})$ and may be affected by the sensor measurement geometry matrix H . These imperfect measurements are inputs to the Kalman filter that generates an estimate $\hat{\underline{x}}$ of the actual state. The portion of the filter enclosed in the dashed outline in Figure A-1 is the dynamic model of the actual system. The output $\hat{\underline{x}}$ is used to generate an expected measurement $\hat{\underline{z}}$. The difference between the actual measurement \underline{z} and the expected measurement is multiplied by a time-varying gain K . The resultant is used to drive the dynamic model to follow the actual system. The matrix K is the Kalman gain and is a function of the observation noise covariance matrix, measurement geometry, disturbance acceleration statistics, and the system state error covariance matrix.

The sensor noise and disturbance acceleration can be characterized by their autocorrelation functions. Assuming that the sensor noise and disturbance acceleration are white gaussian processes, their autocorrelation functions are impulses and they can be represented by

$$\mathcal{E}[\underline{n}(t) \underline{n}^T(t + \tau)] = R\delta(\tau) \quad (\text{A-22})$$

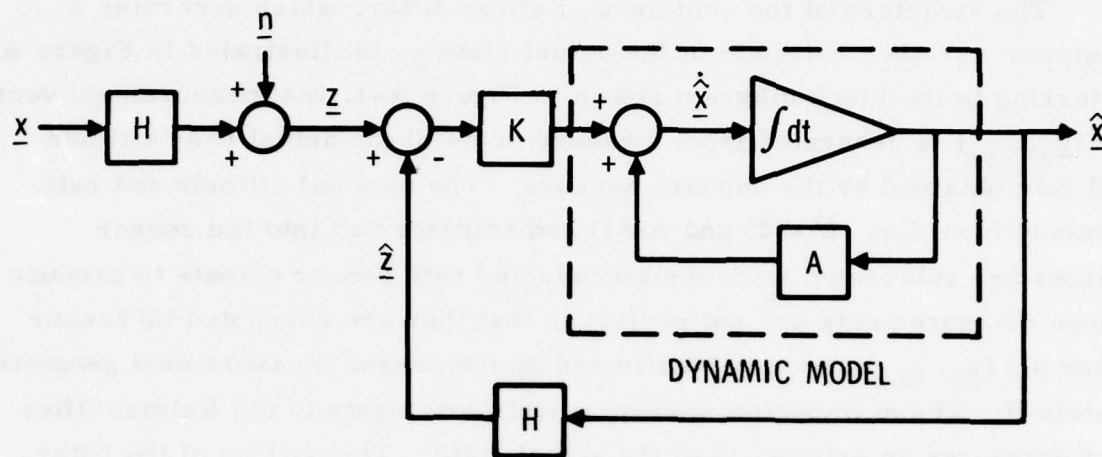


Figure A-1. Minimum Variance Estimator

and

$$\mathcal{E}[\underline{w}(t) \underline{w}^T(t + \tau)] = Q\delta(\tau) \quad (\text{A-23})$$

where \mathcal{E} implies the expected value of the bracketed quantity, δ is the Dirac delta function, and the matrices R and Q determine the areas of the sensor noise and disturbance acceleration impulsive autocorrelation functions respectively. In actuality, the sensor noise and disturbance acceleration are not perfectly white, with the result that their autocorrelation functions are curves rather than impulses. In most cases, however, they can be adequately approximated by the band-limited white noise assumption. In such cases, their autocorrelation functions are approximated by impulses of area equal to the areas under the actual sensor noise and disturbance acceleration autocorrelation functions. Let the area under the attitude sensor autocorrelation be represented by the parameter r_θ with dimensions $[\text{rad}^2 \cdot \text{sec}]$ and the area under the rate sensor autocorrelation function be represented by the parameter $r_{\delta\omega}$ with dimensions $[\text{rad}^2/\text{sec}]$. Then, under the white noise approximation, the R matrix in Eq. (A-22) can be written as

$$R = \begin{pmatrix} r_\theta I & \begin{array}{c} | \\ \hline \end{array} & \begin{array}{c} 0 \\ \hline \end{array} \\ \begin{array}{c} \hline \\ 0 \end{array} & \begin{array}{c} | \\ \hline \end{array} & \begin{array}{c} \hline \\ r_{\delta\omega} I \end{array} \end{pmatrix} \quad (\text{A-24})$$

where I is the identity matrix. This form for the R matrix assumes that the attitude measurements as well as the rate measurements are corrupted by the same noise level on each axis (i. e., all attitude sensors are of equal quality and all rate sensors are of equal quality). Assuming that the statistics of the disturbance accelerations affecting each vehicle axis are equal and using the white noise approximation results in the Q matrix of Eq. (A-23) expressed as

$$Q = \begin{pmatrix} 0 & \begin{array}{c} | \\ \hline \end{array} & \begin{array}{c} 0 \\ \hline \end{array} \\ \begin{array}{c} \hline \\ 0 \end{array} & \begin{array}{c} | \\ \hline \end{array} & \begin{array}{c} \hline \\ qI \end{array} \end{pmatrix} \quad (\text{A-25})$$

the parameter q represents the area under the actual autocorrelation function of the disturbance acceleration with dimension ($\text{rad}^2/\text{sec}^3$).

Note that, although Eqs. (A-24) and (A-25) assume equal quality sensors and equal accelerations on each axis, the performance analysis results presented in the later sections of this volume are not constrained by these assumptions. It will be shown that the individual axis performance for most attitude reference systems envisioned for future missions is unaffected by the performances of the other axes, i.e., there is little or no cross-axis coupling. Under such conditions, each axis can be treated independently. Hence, the equal-quality assumption is used only as a convenience in deriving the filter equations and should not be considered as a constraint on this study.

In addition to the R and Q matrices, the system covariance matrix P must be calculated to determine the Kalman gain matrix K for the filter in the block diagram of Figure A-1. The system covariance matrix is defined as

$$P(t) = \mathcal{E}[\underline{e}(t)\underline{e}^T(t)] \quad (\text{A-26})$$

where \mathcal{E} defines the expected value and $\underline{e}(t)$ is the estimation error defined by

$$\underline{e}(t) = \underline{x}(t) - \underline{\hat{x}}(t) \quad (\text{A-27})$$

The trace elements of the P matrix defined by Eq. (A-26) are the mean-squared estimation errors about each axis of the satellite, and the square root of each trace element gives the root mean square (rms) estimation error about each axis. Assuming the estimation error to be zero mean and gaussian, the rms error is equivalent to the 1-sigma estimation error about each axis.

If the measurements \underline{z} coming into the filter are continuous, the system covariance matrix P satisfies the Riccati equation

$$\dot{P} = AP + PA^T - PH^TR^{-1}HP + Q \quad (\text{A-28})$$

where the initial value $P(t = 0)$ is determined by the a priori uncertainties in the system states \underline{x} . The A matrix in Eq. (A-28) is the dynamics matrix defined by Eq. (A-17). Equation (A-28) must be integrated to determine $P(t)$. The Kalman gain matrix is then calculated for the continuous measurement system using the equation

$$K(t) = P(t) H^T R^{-1} \quad (A-29)$$

It is this gain that weights the input to the estimation filter dynamic model as shown in Figure A-1.

When processing both continuous and discrete measurements, as is the case when the attitude sensors are mappers and the rate sensors are continuous rate gyros, the continuous filter illustrated in Figure A-1 is used between discrete measurements. The information gained from the discrete measurement at time t_i and the estimate of \underline{x} immediately before the measurement $\underline{x}(t_i^-)$ is used to obtain an improved estimate:

$$\hat{\underline{x}}(t_i^+) = \hat{\underline{x}}(t_i^-) + K_i' (\underline{z}_i' - H' \hat{\underline{x}}(t_i^-)) \quad (A-30)$$

where

$$\underline{z}_i' = H' \underline{x}(t_i) + \underline{n}_i' \quad (A-31)$$

represents the discrete measurement at t_i , and \underline{n}_i' is the gaussian noise sequence associated with this discrete measurement. The measurement noise matrix R' is defined by

$$E \left[\underline{n}_i' \underline{n}_j'^T \right] = R' \delta_{ij} \quad (A-32)$$

where δ_{ij} is the discrete Kronecker delta function. The Kalman gain matrix satisfies

$$K_i' = P_i H'^T R'^{-1} \quad (A-33)$$

where the covariance matrix after the discrete measurement P_i is related to the covariance matrix before the measurement M_i by

$$P_i = M_i - M_i H'^T (H' M_i H' + R')^{-1} H' M_i \quad (A-34)$$

Between discrete measurements, the covariance matrix is propagated using the Riccati differential equation (A-28). This differential equation is initialized from M_i to P_i after each discrete measurement.

3. SENSOR MEASUREMENT GEOMETRIES

The H matrix in the Riccati equation (A-28) as well as the H' matrix in the discrete covariance update equation (A-34) represents the continuous and discrete sensor measurement geometry matrices respectively. Mathematically, the measurement matrix is a sensitivity matrix evaluated about the nominal measurement that relates the changes in the system states $\underline{\theta}$ and $\delta \underline{\omega}$ to changes in the attitude and rate measurements \underline{z}_θ and $\underline{z}_{\delta \omega}$ by the relation

$$\underline{z} = \begin{pmatrix} \underline{z}_\theta \\ \underline{z}_{\delta \omega} \end{pmatrix} = H \underline{x} + \underline{n} \quad (A-35)$$

where $\underline{n} = (\underline{n}_\theta, \underline{n}_\omega)$ is the measurement noise and $\underline{x} = (\underline{\theta}, \delta \underline{\omega})$ is the system state vector. The H matrix can be partitioned to represent the attitude sensor measurement matrix H_θ and the rate sensor measurement matrix H_ω by the equation

$$H = \left(\begin{array}{c|c} H_{\theta} & 0 \\ \hline 0 & H_w \end{array} \right) \quad (A-36)$$

For a system with continuous attitude and rate measurements (i.e., trackers and rate gyro information), both H_{θ} and H_w are nonzero matrices. If only continuous attitude measurements are available, H_w is the zero matrix. For a system with discrete attitude measurements (mappers) and continuous rate measurements (rate gyros), the continuous and discrete measurement matrices used in Eqs. (A-28) and (A-34) become

$$H = \left(\begin{array}{c|c} 0 & 0 \\ \hline 0 & H_w \end{array} \right) ; \quad H' = \left(\begin{array}{c|c} H_{\theta} & 0 \\ \hline 0 & 0 \end{array} \right) \quad (A-37)$$

with nonzero values for H_{θ} and H_w . If only discrete attitude measurements are available, then H_w is the zero matrix and the H' matrix above is used to update the covariance through Eq. (A-34). Between updates, the system covariance is propagated using a linear form of Eq. (A-28) obtained by dropping the negative term on the right side of this equation due to the fact that H_w and, hence, H are equal to zero matrices.

The actual form of the H_{θ} and H_w matrices depends upon the number of degrees of measurement freedom for each sensor and the sensor orientations with respect to the vehicle reference coordinate system. Looking at the rate sensor measurement matrix H_w , it may be written in the form

$$H_w = \left(\begin{array}{c} \leftarrow h_1^T \rightarrow \\ \leftarrow h_2^T \rightarrow \\ \vdots \\ \leftarrow h_m^T \rightarrow \end{array} \right) \quad (A-38)$$

where the vectors \underline{h}_i are unit vectors defining the measurement axes of the rate sensors and m is the number of measurement degrees of freedom. For example, an H_w equal to the 3×3 identity matrix is indicative of a package of three single-degree-of-freedom rate gyros with measurement axes aligned along the body reference axes.

To illustrate the derivation of the attitude sensor measurement matrix H_θ , consider a star tracker example. The actual measurement defined by the tracker is

$$\underline{z}_a = \underline{u}^s + \underline{n}_\theta \quad (\text{A-39})$$

where \underline{u}^s is the unit vector to the star in the sensor coordinate frame (s-frame) and \underline{n}_θ is the tracker measurement noise. Since the attitude information desired by the Kalman filter is a measurement of the perturbation in satellite attitude from nominal (where nominal implies the attitude of an undisturbed satellite), the actual measurement (Eq. (A-39)) must be compared to a nominal measurement defined by

$$\underline{z}_n = \underline{u}^{s_0} \quad (\text{A-40})$$

where \underline{u}^{s_0} is the unit vector along the star LOS in nominal sensor coordinates (s_0 -frame). Equation (A-40) represents a perfect (noiseless) star tracker measurement from a nominal (undisturbed) satellite. The desired attitude information is then contained in the difference equation

$$\underline{z} = \underline{z}_a - \underline{z}_n = (\underline{u}^s - \underline{u}^{s_0}) + \underline{n}_\theta \quad (\text{A-41})$$

Defining the actual satellite reference coordinate system as the B-frame and the nominal satellite reference coordinate system as the B_0 -frame, the LOS vectors in Eq. (A-41) may be written as

$$\underline{u}^s = C_{B\underline{u}}^s{}^B \quad (A-42)$$

and

$$\underline{u}^{s_0} = C_{B_0\underline{u}}^{s_0}{}^{B_0} = C_{B\underline{u}}^s{}^{B_0} \quad (A-43)$$

where C_B^s is the direction cosine matrix transforming a vector in the B-frame to one in the sensor or s-frame. It is assumed that no misalignments exist between the body and sensor frames, i.e., $C_{B_0}^{s_0} = C_B^s$. Substitution of Eqs. (A-42) and (A-43) into Eq. (A-41) results in

$$\underline{z} = C_{B\underline{u}}^s{}^B (\underline{u}^B - \underline{u}^{B_0}) + \underline{n}_\theta \quad (A-44)$$

The actual body reference frame is related to the nominal by the direction cosine matrix $C_{B_0}^B$. Then \underline{u}^B may be rewritten as

$$\underline{u}^B = C_{B_0\underline{u}}^B{}^{B_0} \underline{u}^{B_0} \quad (A-45)$$

It is the $C_{B_0}^B$ matrix that contains the attitude perturbation information in the form

$$C_{B_0}^B = I + (\underline{\theta} \times) \quad (A-46)$$

where θ is the vector of infinitesimal angular rotations about the body reference axes. Substituting Eqs. (A-46) and (A-45) into Eq. (A-49), collecting terms, and reversing the order of the cross-product result in

$$\underline{z} = -C_B^s(\underline{u}^{B_0} \times) \underline{\theta} + \underline{n}_\theta \quad (A-47)$$

where \underline{u}^{B_0} is the unit vector of the star LOS in nominal body coordinates, and the cross-product is written as

$$(\underline{u}^{B_0} \times) = \begin{pmatrix} 0 & -u_z & u_y \\ u_z & 0 & -u_x \\ -u_y & u_x & 0 \end{pmatrix} \quad (A-48)$$

Thus, the star tracker measurement geometry matrix takes the form

$$H_\theta = -C_B^s(\underline{u}^{B_0} \times) \quad (A-49)$$

To give some physical interpretation to the cross-product relationship in Eq. (A-49), consider the two-axes star sensor example illustrated in Figure A-2. Here the sensor frame, defined by the unit vectors $(\underline{i}_s, \underline{j}_s, \underline{k}_s)$, is aligned with the body reference frame, defined by the unit vectors $(\underline{i}_B, \underline{j}_B, \underline{k}_B)$, so that C_B^s is the identity matrix. Let the sensor optical axis be along \underline{k}_s so that the attitude measurements are taken along the \underline{i}_s and \underline{j}_s axes. It can be seen from Figure 2 that a small rotation θ_y about the \underline{j}_B axis will produce an output measurement z_x along the \underline{i}_s axis and a small rotation θ_x about \underline{i}_B produces a signal z_y along the \underline{j}_s axis. Since these rotations are in terms of infinitesimal rotations, they may be treated as vectors and the cross-product of the unit LOS vector with the rotation vector produces the desired result.

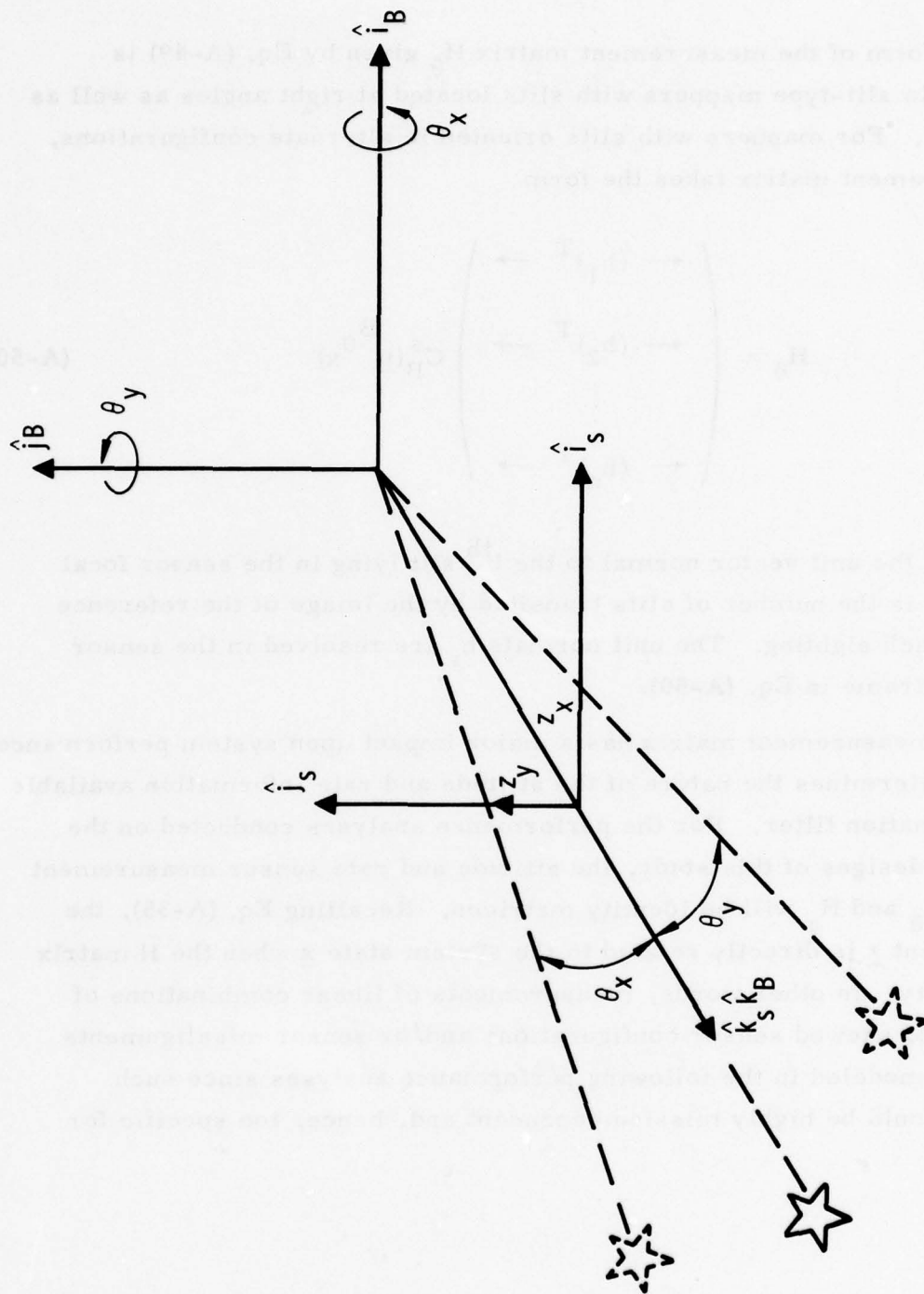


Figure A-2. Star Sensor Measurement Geometry

The form of the measurement matrix H_θ given by Eq. (A-49) is applicable to slit-type mappers with slits located at right angles as well as to trackers. For mappers with slits oriented in alternate configurations, the measurement matrix takes the form

$$H_\theta = \begin{pmatrix} \leftarrow (h_1)^T \rightarrow \\ \leftarrow (h_2)^T \rightarrow \\ \vdots \\ \leftarrow (h_n)^T \rightarrow \end{pmatrix} C_B^s(\underline{u}^B \quad \underline{0} \quad \underline{x}) \quad (A-50)$$

where h_i is the unit vector normal to the i^{th} slit lying in the sensor focal plane and n is the number of slits transited by the image of the reference object on each sighting. The unit normals h_i are resolved in the sensor coordinate frame in Eq. (A-50).

The measurement matrix has a major impact upon system performance in that it determines the nature of the attitude and rate information available to the estimation filter. For the performance analyses conducted on the conceptual designs of this study, the attitude and rate sensor measurement matrices H_θ and H_ω will be identity matrices. Recalling Eq. (A-35), the measurement \underline{z} is directly related to the system state \underline{x} when the H matrix is an identity. In other words, measurements of linear combinations of states due to skewed sensor configurations and/or sensor misalignments will not be modeled in the following performance analyses since such modeling would be highly mission dependent and, hence, too specific for this study.

APPENDIX B. NORMALIZATION OF EQUATIONS

The normalization procedure involves a transformation of the covariance matrix P of the form

$$E = SPS^T \quad (B-1)$$

where the scaling matrix S is of the general form

$$S = \frac{1}{\sqrt{r'_\theta}} \begin{pmatrix} R(\phi) & 0 \\ 0 & \frac{1}{\Omega_0} R(\phi) \end{pmatrix} \quad (B-2)$$

The parameter r'_θ is the discrete attitude sensor measurement noise parameter with units (rad^2), and the Ω_0 parameter is a scaling frequency with units of (1/sec). The $R(\phi)$ matrix is an orthogonal transformation matrix resulting from a rotation, ϕ , about one of the satellite body reference axes. Thus,

$$[R(\phi)]^{-1} = [R(\phi)]^T \quad (B-3)$$

The normalization proceeds by differentiating Eq. (B-1), substituting Eq. (B-28) for \dot{P} , and employing the definition of E from Eq. (B-1) in the result. Collecting terms and simplifying using the property of Eq. (B-3) results in the expression

$$\begin{aligned} \dot{E} = & [\dot{S}S^{-1} + SAS^{-1}] E + E[\dot{S}S^{-1} + SAS^{-1}]^T \\ & - E(HS^{-1})^T R^{-1} (HS^{-1}) E + SQS^T \end{aligned} \quad (B-4)$$

Defining the normalized time by

$$\tau = \Omega_0 t \quad (B-5)$$

it is easily shown that

$$\dot{E} = \Omega_0 \frac{dE}{d\tau} \quad (B-6)$$

Substitution of Eq. (B-6) into Eq. (B-4) yields

$$\frac{dE}{d\tau} = \tilde{A}E + E\tilde{A}^T - \frac{1}{\Omega_0} E\tilde{H}^T R^{-1} \tilde{H}E + \frac{1}{\Omega_0} SQS^T \quad (B-7)$$

where the normalized dynamics matrix \tilde{A} is defined by

$$\tilde{A} \equiv \frac{1}{\Omega_0} [\dot{S}S^{-1} + SAS^{-1}] \quad (B-8)$$

and the normalized measurement geometry matrix \tilde{H} is defined by

$$\tilde{H} \equiv HS^{-1} \quad (B-9)$$

Let the measurement noise, measurement geometry, and disturbance acceleration matrices take the form

$$R = \begin{pmatrix} r_\theta I & 0 \\ 0 & r_{\delta\omega} I \end{pmatrix}, \quad H = \begin{pmatrix} 0 & 1 & 0 \\ 0 & 0 & 1 \end{pmatrix}, \quad Q = \begin{pmatrix} 0 & 1 & 0 \\ 0 & 0 & qI \end{pmatrix} \quad (B-10)$$

where I is a 3×3 identity matrix. This particular H matrix, when substituted into the Riccati equation, represents a continuous rate measurement system. The baseline system configuration mechanized in the covariance analysis program is a mixed system with continuous rate measurement and discrete attitude measurements. Using this baseline system, the performance of a totally continuous system may be approached by increasing the discrete measurement rate, while the performance of a totally discrete attitude measurement system may be analyzed by setting the rate measurement uncer-

tainty $r_{\delta\omega}$ to a very large value. Thus, the measurement geometry matrix defined above will be used in this derivation of the normalized Riccati equation implemented in the covariance analysis program.

Using the definitions of Eqs. (B-2), (B-9), and (B-10) to simplify Eq. (B-7), the desired normalized form of the Riccati equation is

$$\frac{dE}{d\tau} = \tilde{A}E + E\tilde{A}^T - \frac{1}{r'_\omega} EI_{22} E + \alpha I_{22} \quad (B-11)$$

where

$$I_{22} \equiv \begin{pmatrix} 0 & 0 \\ 0 & I \end{pmatrix}$$

and the normalized dynamics matrix \tilde{A} was defined by Eq. (B-8). The parameters τ , r'_ω , and α are dimensionless variables defined as

$$r'_\omega \equiv \frac{r_{\delta\omega}}{r'_\theta \Omega_0} \quad (B-12)$$

$$\tau \equiv \Omega_0 t \quad (B-13)$$

with

$$\Omega_0 \equiv \left(\frac{q}{r'_\theta \alpha} \right)^{1/3} \quad (B-14)$$

and α , an arbitrary scaling constant introduced to improve the numerical stability of the Riccati equation. Adjustment of α simply rescales the normalized Eq. (B-11) so that numerical instabilities encountered in integration over initial transients may be avoided.

The normalization of the discrete covariance update equation proceeds by pre-multiplying and post-multiplying both sides of Eq. (B-14) with S and S^T respectively. Using the definition of E in Eq. (B-1) and defining the normalized covariance prior to the update by

$$N \equiv SMS^T \quad (B-15)$$

the resulting normalized update equation can be written as

$$E_i = N_i + N_i \tilde{H}'^T [\tilde{H}' N_i \tilde{H}'^T + R']^{-1} \tilde{H}' N_i \quad (B-16)$$

where the normalized discrete sensor measurement geometry matrix is

$$\tilde{H}' \equiv \tilde{H}' S^{-1} \quad (B-17)$$

Equations (B-11) and (B-17) are the relations used to propagate the normalized covariance matrix E in the covariance analysis program. The major parameters varied during the covariance analysis are r'_ω and the discrete update interval in terms of the normalized time τ as defined by Eqs. (B-12) and (B-13). De-normalization of the results may be accomplished by solving Eq. (B-1) for the covariance matrix P . For scaling matrices of the form defined by Eq. (B-2), the result is

$$P = S' E S'^T \quad (B-18)$$

with

$$S' = S^{-1} = \sqrt{r'_\theta} \begin{pmatrix} R(\phi)^T & 0 \\ 0 & \Omega_0 R(\phi)^T \end{pmatrix} \quad (B-19)$$

APPENDIX C. NORMALIZED CONCEPTUAL DESIGN DYNAMICS

1. SYSTEM A DYNAMICS

This system is designed for a three-axis stabilized, local-vertical oriented satellite. As illustrated in Figure C-1, the satellite body axes remain aligned with the local vertical axes throughout the orbit. Hence, a pitch rate equal to the orbital angular velocity and acting about the j_B axis is required to maintain the desired orientation. This rate is identified as Ω_y in the figure. It was shown in Appendix A that, in general, the linearized satellite attitude dynamics can be described by the A matrix of Eq. (A-17). For this system,

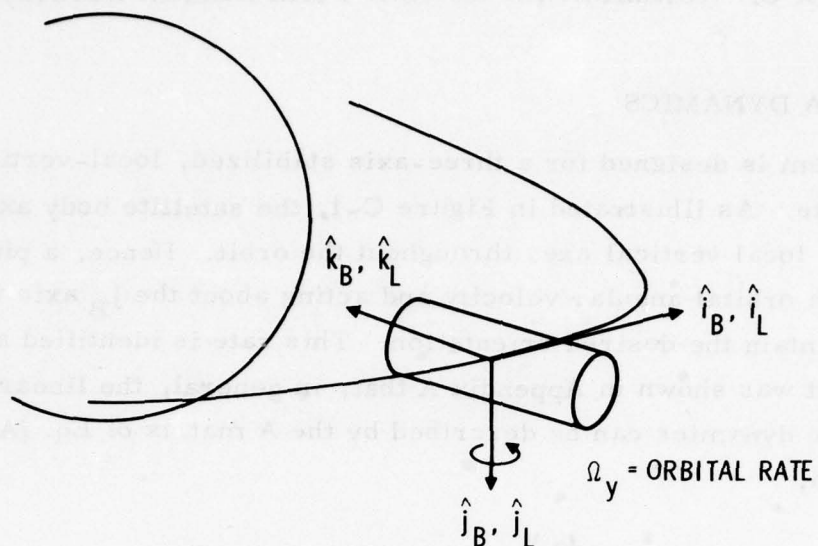
$$\underline{\omega}_0 = \begin{pmatrix} 0 \\ \Omega_y \\ 0 \end{pmatrix}, \quad \underline{h}_w = \underline{0}$$

as a result of the presence of pitch rate and the absence of momentum bias. Substituting these relations

$$S = \frac{1}{\sqrt{r\dot{\theta}}} \begin{pmatrix} I & | & 0 \\ 0 & | & I \\ \hline 0 & | & \Omega_0 I \end{pmatrix} \quad (C-1)$$

the normalized dynamics matrix, from Eq. (B-8), for this system is

$$\tilde{A} = \left(\begin{array}{ccc|ccc} 0 & 0 & -\rho & 1 & & \\ 0 & 0 & 0 & & I & \\ \hline \rho & 0 & 0 & & 0 & 0 & k\rho \\ & 0 & & & 0 & 0 & 0 \\ & & & & 0 & 0 & 0 \end{array} \right) \quad (C-2)$$



DYNAMIC CHARACTERISTICS:

1. BODY REFERENCE AXES ALIGNED WITH LOCAL VERTICAL AXES
2. ORBIT RATE Ω_y ABOUT PITCH AXIS

SCALING MATRIX:

$$S = \frac{1}{\sqrt{r'}\theta} \left(\begin{array}{c|c} 1 & 0 \\ \hline 0 & \frac{1}{\Omega_0} \end{array} \right)$$

NORMALIZED DYNAMICS:

$$\tilde{A} = \left(\begin{array}{ccc|ccc} 0 & 0 & -\rho & & & \\ 0 & 0 & 0 & & 1 & \\ \hline \rho & 0 & 0 & & & \\ \hline & & & 0 & 0 & k\rho \\ & & & 0 & 0 & 0 \\ & & & 0 & 0 & 0 \end{array} \right)$$

DYNAMIC PARAMETERS:

$$k = 1 - J_z/J_x$$

$$\rho = \Omega_y/\Omega_0$$

Figure C-1. System A Dynamics (Local Vertical, Three-Axis Stable Configuration)

where the normalized dynamic parameters k and p are defined by

$$k = 1 - J_z/J_x \quad (C-3)$$

$$p = \Omega_y/\Omega_0 \quad (C-4)$$

and it is assumed that the pitch and roll moments of inertia are equal ($J_x = J_y$) or nearly so.

2. SYSTEM B DYNAMICS

This system is characterised by a spin about the yaw axis, indicated by Ω_z in Figure C-2. The yaw axis is maintained pointing toward the center of the earth by a pitch rate Ω_y . A momentum wheel is aligned with the yaw axis and operated to cancel the spacecraft's spin momentum. For this system,

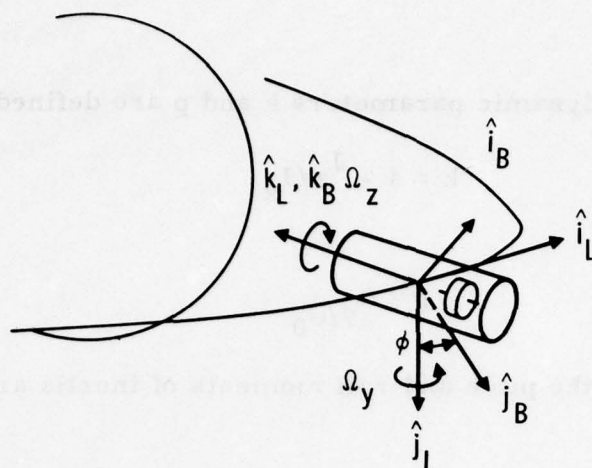
$$\underline{\omega}_0^L = \begin{pmatrix} 0 \\ \Omega_y \\ \Omega_z \end{pmatrix}, \quad \underline{h}_w^L = \begin{pmatrix} 0 \\ 0 \\ -J_z \Omega_z \end{pmatrix}$$

where the superscript L indicates that the vectors are resolved in the local vertical coordinate frame. Defining the spin angle ϕ by

$$\phi = \Omega_z t$$

the transformation between the local vertical and the body reference coordinate system (B-frame) is given by the rotation matrix

$$Z^T(\phi) = \begin{pmatrix} \cos \phi & \sin \phi & 0 \\ -\sin \phi & \cos \phi & 0 \\ 0 & 0 & 1 \end{pmatrix}$$



DYNAMIC CHARACTERISTICS:

1. ORBITAL RATE Ω_y ABOUT \hat{j}_L - AXIS
2. BODY SPIN Ω_z ABOUT YAW AXIS
3. MOMENTUM WHEEL ALONG YAW TO CANCEL SPIN MOMENTUM

SCALING MATRIX:

$$S = \frac{1}{\sqrt{r'_\theta}} \begin{pmatrix} z(\phi) & 0 \\ 0 & \frac{1}{\Omega_0} z(\phi) \end{pmatrix}$$

WHERE

$$z(\phi) = \begin{pmatrix} \cos \phi & -\sin \phi & 0 \\ \sin \phi & \cos \phi & 0 \\ 0 & 0 & 1 \end{pmatrix}, \quad \phi = \Omega_z t$$

NORMALIZED DYNAMICS:

$$\tilde{A} = \left(\begin{array}{ccc|ccc} 0 & 0 & -\rho & & & \\ 0 & 0 & 0 & & & \\ \hline \rho & 0 & 0 & 0 & 0 & k\rho \\ & & & 0 & 0 & 0 \\ & & & 0 & 0 & 0 \end{array} \right)$$

DYNAMIC PARAMETERS:

$$k = 1 - J_z/J_x$$

$$\rho = \Omega_y/\Omega_0$$

Figure C-2. System B Dynamics (Local Vertical, Yaw-Spin Configuration)

Thus, the nominal angular velocity and the wheel angular momentum may be resolved in the body axes as

$$\underline{\omega}_0^B = Z^T(\phi) \underline{\omega}_0^L, \quad \underline{h}_w^B = Z^T(\phi) \underline{h}_w^L$$

Substitution of these equations into Eq. (A-9) results in the dynamics matrix

$$A = \left(\begin{array}{c|c} -Z^T(\phi) (\underline{\omega}_0^L \times) Z(\phi) & I \\ \hline 0 & Z^T(\phi) F(\underline{\omega}_0^L, \underline{h}_w^L) Z(\phi) \end{array} \right) \quad (C-5)$$

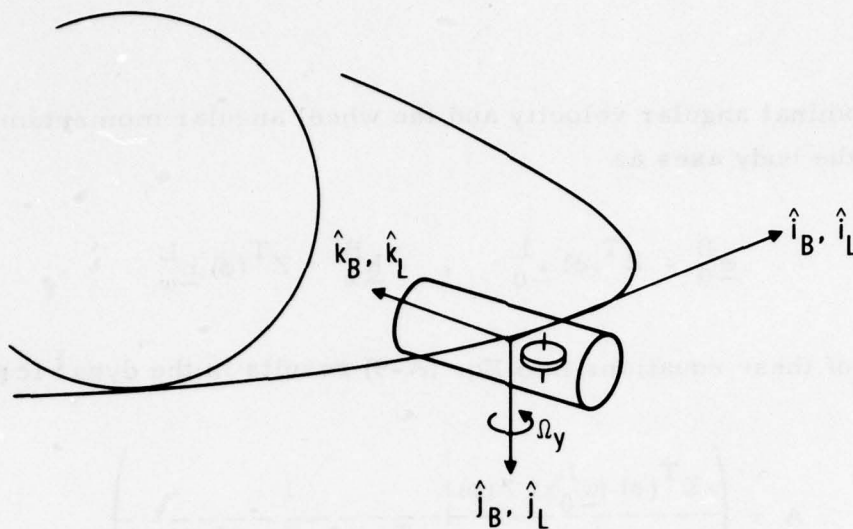
The scaling matrix used in normalizing the dynamics for System B will be defined by

$$S = \frac{1}{\sqrt{r_\theta}} \left(\begin{array}{c|c} Z(\phi) & 1 \\ \hline 0 & \frac{1}{\tilde{\omega}_0} Z(\phi) \end{array} \right) \quad (C-6)$$

Use of this matrix in Eq. (B-8) eliminates the dependence of the dynamics upon the rotation angle ϕ , which is a function of time. The resultant normalized dynamics matrix represents the effective rigid body dynamics in the local vertical frame and is time invariant. The expression for \tilde{A} is identical to the normalized dynamics of System A (Eq. [C-2]) when it is assumed that the pitch and roll inertias are nearly equal, as in the previous case.

3. SYSTEM C DYNAMICS

The orbital configuration of System C is similar to that of System A with the addition of a momentum wheel on the pitch axis to provide gyroscopic stability in roll and yaw. The configuration is illustrated in Figure C-3. The nominal angular velocity and wheel momentum resolved in the body reference frame are



DYNAMIC CHARACTERISTICS:

1. BODY REFERENCE AXES ALIGNED WITH LOCAL VERTICAL AXES
2. ORBIT RATE Ω_y ABOUT PITCH AXIS
3. MOMENTUM WHEEL ALONG PITCH AXIS WITH BIAS h_w

SCALING MATRIX:

$$S = \frac{1}{\sqrt{r'_\theta}} \left(\begin{array}{c|c} 1 & 0 \\ \hline 0 & \frac{1}{\Omega_0} \end{array} \right)$$

NORMALIZED DYNAMICS:

$$\tilde{A} = \left(\begin{array}{ccc|ccc} 0 & 0 & -\rho & & & \\ 0 & 0 & 0 & & 1 & \\ \rho & 0 & 0 & & & \\ \hline & & & 0 & 0 & \rho b \\ & & & 0 & 0 & 0 \\ & & & -\rho a & 0 & 0 \end{array} \right)$$

DYNAMIC PARAMETERS:

$$\rho = \Omega_y / \Omega_0$$

$$a = h_w / (J_z \Omega_y)$$

$$b = k + h_w / (J_x \Omega_y)$$

$$k = 1 - J_z / J_x$$

Figure C-3. System C Dynamics (Local Vertical, Momentum-Biased Configuration)

$$\underline{\omega}_0 = \begin{pmatrix} 0 \\ \Omega_y \\ 0 \end{pmatrix}, \quad \underline{h}_\omega = \begin{pmatrix} 0 \\ h_W \\ 0 \end{pmatrix}$$

Using these relations to form the dynamics matrix (Eq. [4-17]) substituting the result along with the same scaling matrix as System A (Eq. [C-1] into Eq. [B-8]) yields for the normalized dynamics

$$\tilde{A} = \begin{pmatrix} 0 & 0 & -p & 1 & & \\ 0 & 0 & 0 & 1 & I & \\ 0 & 0 & 0 & 1 & & \\ \hline & & & 0 & 0 & \rho b \\ & 0 & & 1 & 0 & 0 \\ & & & -pa & 0 & 0 \end{pmatrix} \quad (C-7)$$

with the normalized parameters

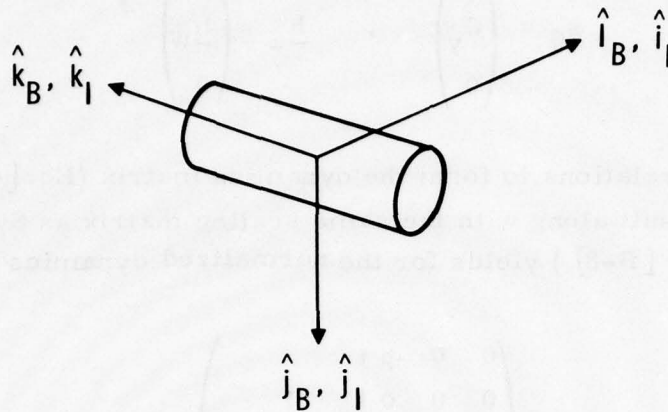
$$a = h_W / (J_z \Omega_y)$$

$$b = k + h_W / (J_x \Omega_y)$$

The parameters k and ρ are defined by Eqs. (C-3) and (C-4), respectively. The assumption is again made that the roll and pitch moments are nearly equal.

4. SYSTEM D DYNAMICS

Referring to Figure C-4, System D maintains a fixed orientation with respect to inertial space and has no momentum bias. Hence, both the nominal angular velocity and wheel momentum in Eq. (C-9) are zero vectors. The scaling used to normalize this system is



DYNAMIC CHARACTERISTICS:

1. BODY REFERENCE AXES ALIGNED WITH INERTIAL AXES
2. ZERO NOMINAL ANGULAR VELOCITY

SCALING MATRIX:

$$S = \frac{1}{\sqrt{r_\theta} \Omega_0} \left(\begin{array}{c|cc} 1 & & 0 \\ \hline 0 & 1 & 1 \end{array} \right)$$

NORMALIZED DYNAMICS:

$$\tilde{A} = \left(\begin{array}{c|c} 0 & 1 \\ \hline 0 & 0 \end{array} \right)$$

Figure C-4. System D Dynamics (Inertially Stable Configuration)

$$S = \frac{1}{\sqrt{r_\theta} \Omega_0} \begin{pmatrix} I & 1 & 0 \\ 0 & 1 & 0 \\ 0 & 0 & I \end{pmatrix} \quad (C-8)$$

The resulting normalized dynamics matrix becomes

$$\tilde{A} = \begin{pmatrix} 0 & 1 \\ 0 & 0 \end{pmatrix} \quad (C-9)$$

5. SYSTEM E DYNAMICS

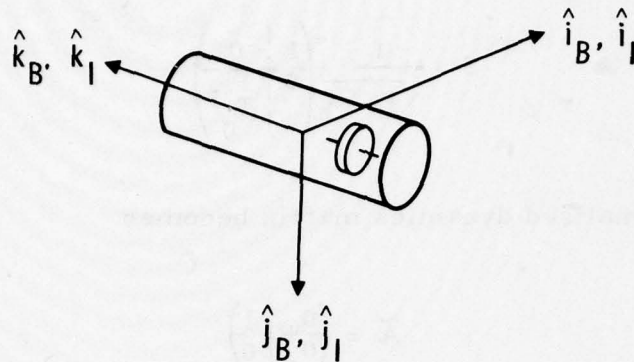
System E is designed for an inertially stable vehicle with an onboard momentum wheel. Hence, the nominal angular velocity is zero, but the momentum bias may be oriented along one of the three body axes. Referring to Figure C-5, let

$$\underline{h}_w = \begin{pmatrix} 0 \\ h_w \\ 0 \end{pmatrix}$$

Then, from Eq. (C-9),

$$F(\underline{\omega}_0, \underline{h}_w) = \begin{pmatrix} 0 & 0 & \frac{h_w}{J_x} \\ 0 & 0 & 0 \\ -\frac{h_w}{J_z} & 0 & 0 \end{pmatrix}$$

Using the scaling matrix defined by Eq. (C-8), the normalized dynamics matrix is



DYNAMIC CHARACTERISTICS:

1. BODY REFERENCE AXES ALIGNED WITH INERTIAL AXES
2. ZERO NOMINAL ANGULAR VELOCITY
3. MOMENTUM WHEEL ALONG ROLL WITH BIAS h_w

SCALING MATRIX:

$$S = \frac{1}{\sqrt{r_\theta} \Omega_0} \left(\begin{array}{c|c} 1 & 0 \\ \hline 0 & \frac{1}{\Omega_0} \end{array} \right)$$

NORMALIZED DYNAMICS:

$$\tilde{A} = \left(\begin{array}{c|cc} 0 & & 1 \\ \hline & 0 & 0 & c \\ 0 & 0 & 0 & 0 \\ \hline & -d & 0 & 0 \end{array} \right)$$

DYNAMIC PARAMETERS:

$$c = h_w / (J_x \Omega_0)$$

$$d = h_w / (J_z \Omega_0)$$

Figure C-5. System E Dynamics (Inertially Stable Momentum-Biased Configuration)

$$\tilde{A} = \begin{pmatrix} 0 & -\frac{I}{c} & 0 & 0 \\ 0 & 0 & 0 & 0 \\ 0 & 0 & 0 & 0 \\ -d & 0 & 0 & 0 \end{pmatrix} \quad (C-10)$$

with the normalized parameters

$$c = h_W / (J_x \Omega_0) \quad (C-11)$$

$$d = h_W / (J_z \Omega_0) \quad (C-12)$$

If an axis of inertial symmetry were chosen along the j_B -axis, these parameters would be the same, resulting in symmetric cross-coupling between the i_B and k_B axes.

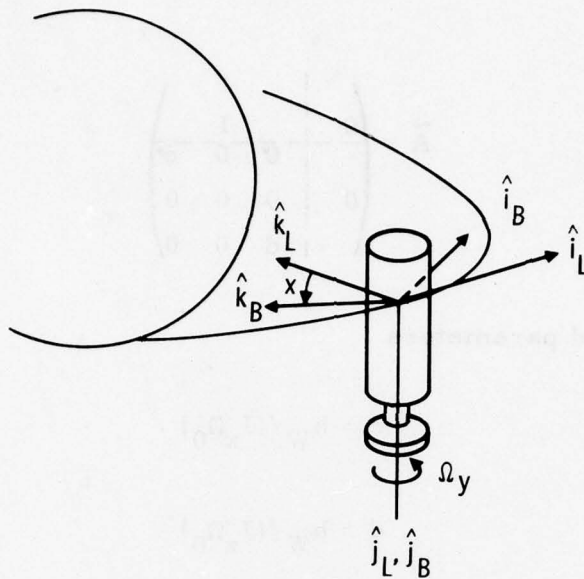
6. SYSTEM F DYNAMICS

System F is applicable to either a spinning or a dual-spin configuration. Referring to Figure C-6, the spacecraft is assumed to be spinning about the pitch axis (j_B - axis). Written in the local vertical frame, the nominal angular velocity is the sum of the spin and orbital angular velocities so that

$$\underline{\omega}_0^L = \underline{\omega}_{\text{spin}} + \underline{\omega}_{\text{orbit}} = \begin{pmatrix} 0 \\ \Omega_y \\ 0 \end{pmatrix} \quad (C-13)$$

Defining the body spin angle γ about the j_B -axis by the expression

$$\gamma = (\omega_{\text{spin}})t$$



DYNAMIC CHARACTERISTICS:

1. ORBIT RATE ABOUT PITCH AXIS
2. BODY SPIN ABOUT PITCH AXIS
3. TOTAL PITCH RATE IS Ω_y

SCALING MATRIX:

$$S = \frac{1}{\sqrt{r'_\theta}} \begin{pmatrix} Y(\gamma) & 0 \\ 0 & \frac{1}{\Omega_0} Y(\gamma) \end{pmatrix}$$

WHERE

$$Y(\gamma) = \begin{pmatrix} \cos \gamma & 0 & \sin \gamma \\ 0 & 1 & 0 \\ -\sin \gamma & 0 & \cos \gamma \end{pmatrix}; \gamma = \Omega_y t$$

NORMALIZED DYNAMICS:

$$\tilde{A} = \begin{pmatrix} 0 & 1 & 0 & 0 \\ 0 & 0 & 0 & 0 \\ 0 & 0 & 0 & 0 \\ -\rho(1-k) & 0 & 0 & 0 \end{pmatrix}$$

DYNAMIC PARAMETERS:

$$\rho = \Omega_y / \Omega_0$$

$$k = 1 - J_y / J_x$$

Figure C-6. System F Dynamics (Dual-Spin or Spinner Configuration)

then the transformation between the local vertical (L-frame) and the body reference (B-frame) coordinate systems is the rotation matrix

$$Y^T(\gamma) = \begin{pmatrix} \cos \gamma & 0 & -\sin \gamma \\ 0 & 1 & 0 \\ \sin \gamma & 0 & \cos \gamma \end{pmatrix}$$

Hence, the nominal angular velocity is the same expression in both the body and local vertical frames; that is,

$$\underline{\omega}_0^B = Y^T(\gamma) \underline{\omega}_0^L = \underline{\omega}_0^L$$

The resulting dynamics matrix, with no wheel momentum, becomes

$$A = \left(\begin{array}{ccc|ccc} 0 & 0 & -\Omega_y & & & \\ 0 & 0 & 0 & & I & \\ \Omega_y & 0 & 0 & & & \\ \hline & & & 0 & 0 & -k\Omega_y \\ & 0 & & 0 & 0 & 0 \\ & & & k\Omega_y & 0 & 0 \end{array} \right)$$

The kinematic cross coupling due to the $-(\underline{\omega}_0 \times)$ matrix can be eliminated by transforming the dynamics from the body to the local vertical frame in a manner similar to that used in the derivation for System B. With the scaling matrix defined as

$$S = \frac{1}{\sqrt{r'_\theta}} \left(\begin{array}{c|c} Y(\gamma) & 0 \\ \hline 0 & \frac{1}{\Omega_0} Y(\gamma) \end{array} \right)$$

the normalized dynamics for System F is

$$\tilde{A} = \begin{pmatrix} 0 & 0 & 1 & \rho(1-k) \\ 0 & 0 & 0 & 0 \\ -\rho(1-k) & 0 & 0 & 0 \end{pmatrix} \quad (C-14)$$

where the parameters k and ρ are defined by Eqs. (C-3) and (C-4), respectively.

APPENDIX D. POWER SPECTRAL DENSITY ESTIMATES

A. INTRODUCTION

The various power spectral density (PSD) estimates that were utilized to establish present day state-of-the-art rate sensor performance are documented in this Appendix. For this program, the rate sensors were assumed to be high performance gyros of the single-degree-of-freedom, rate integrating type equipped with hydrodynamic gas spin bearings. Data were collected for the following five gyro designs of this type:

<u>Gyro Model</u>	<u>Gyro Designer/Manufacturer</u>
TGG 25-IRIG Mod 3 }	CSDL
GI-T1-B GI-K7G }	Northrop
GG 334	Honeywell

Most of the data were obtained from Reference 1. However, some additional information was obtained from other sources and is presented for comparison in the following discussion.

B. DISCUSSION

Data for all of the units are contained in Reference 1. These data were obtained by CSDL in support of the Orbiting Astronomical Observatory (OAO) program for the National Aeronautics and Space Administration (NASA) Goddard Space Flight Center. In this effort, the data were generated by caging each gyro in a very low-gain loop so that, for frequencies above the loop break frequency, the pickoff output represented angular position sensed about the gyro input axis desired for the OAO program. The loop gain between pick-off and torquer was selected to provide a 40-sec time constant or equivalent

Reference 1. A. Truncale, W. Koenigsberg, and R. Harris, Spectral Density Measurements of Gyro Noise, Report No. E-2641, Charles Stark Draper Laboratories, Cambridge, Massachusetts (February 1972).

to a break frequency of 0.004 Hz. The demodulated pickoff signal was passed through a second-order 200-Hz filter to reduce high frequency folding in the PSD extraction. The gain in the pickoff signal channel was adjusted to provide a sensitivity of 1 V/arc sec at the recorder input. This signal was recorded on a frequency-modulated (FM) magnetic tape recorder at the test site, and the recorded data were subsequently digitized and processed by a computer to PSD form.

The resulting spectra were simplified by linearizing the computer-generated plots, and the results are presented in Reference 1. Since these spectra were plotted in power density units involving angle, i.e., (arc sec)²/Hz, but gyro noise expressed in units of angular rate was desired for the HAADS study, it was necessary to convert the data from one form to the other. This was accomplished by multiplying the ordinates of the positional PSD by ω^2 where ω is the frequency associated with each ordinate. To do this, the ordinate for the lowest value of frequency was multiplied by ω^2 expressed in (rad/sec)², and all other values were corrected by increasing the linearized slopes by +2 decades/decade proceeding from left to right. The power density units are then

$$\left(\frac{\text{arc sec}}{\text{s}}\right)^2 / \text{Hz}$$

or, equivalently,

$$\left(\frac{\text{deg}}{\text{h}}\right)^2 / \text{Hz}$$

The curves shown in Reference 1 begin at a frequency of 0.01 Hz and, for the purposes of the HAADS study, are terminated at 50 Hz. Where possible, the total area under each curve over the frequency region from 0.01 to 50 Hz was computed and converted to an rms noise value. The equations used to compute these areas are summarized in paragraph D.E..

Data from a low noise version of the GG 334, taken in The Aerospace Corporation Guidance and Control Laboratory, are also presented. The Low Noise GG 334 A6 is the same unit as that described in the CSDL report and has been undergoing evaluation testing there for some time. A typical PSD result is plotted. A PSD for the "standard" GG 334 (as opposed to low noise), based on some data taken on a Honeywell GG 2200 attitude reference package, is also included. This package has an orthogonal set of GG 334 A6 gyros that are the attitude sensors. Some low frequency data taken on a standard GG 334 for the SPARS Program are also included for purposes of comparison.

The rms noise amplitude for each gyro and test situation over the frequency range of 0.01 to 50 Hz is listed in Table D-1. A figure of merit was also computed for each gyro. This figure of merit is the rms noise amplitude for 0.01 to 1 Hz and gives a relative indication of the performance of an attitude determination system that utilizes the gyro in question. The frequency range was selected on the basis that a suitable Kalman filter would remove noise components below 0.01 Hz and the spacecraft inertia would remove frequencies above 1 Hz. Note that these numbers do not, in general, correlate with the rms noise values taken to 50 Hz. This is because all of the PSDs exhibit relatively high power densities at the higher frequencies (above 1 Hz), and these values heavily influence the rms value over the 50-Hz range but obviously have no influence on the rms value for the lower range. Thus, for example, the 25-IRIG had one of the higher rms noise values over a 50-Hz range but also exhibited one of the lowest figures of merit.

It should be noted that these figures of merit are based on very limited data samples taken under different test conditions. Hence, conclusions based on such data concerning the performance of one gyro in relation to another are probably erroneous. An example of this is the almost 1-order-of-magnitude spread between the results for the two TGG gyros. The associated linearized PSDs are presented in Figures D-1 through D-5.

Table D-1. Summary of the rms Noise Levels for the Gyros

Gyro	rms Noise 0.01 to 50 Hz (deg/hr)	Figure of Merit rms Noise 0.01 to 1 Hz (deg/hr)	Test Location and Comment	PSD Fig. No.
TGG	0.84	0.003	CSDL, Prototype S/N 212, IA Down	A-1
TGG	1.3	0.019	CSDL, Preprototype S/N 204, OA Up	A-1
25-IRIG Mod 3	5.4	0.019	CSDL, OA Up	A-2
GI-T1-B	6.2	0.037	Northrop, Norwood, MA, OA Up	A-3
GI-K7G	0.48	0.004	Northrop, Norwood, MA, OA Up	A-4
GG 334	0.18	0.002	Honeywell, Minneapolis, IA Up, Low Noise Gyro	A-5
GG 334	0.30	-- ^a	Aerospace Corp., OA Down, Low Noise Gyro, 25-Hz Loop	A-5
GG 334	--	0.007	Honeywell, Minneapolis, Standard Gyro	A-5
GG 334	1.3	0.032	Honeywell, Florida, Package Test, Standard Gyro	A-5

^aResult considered erroneous. See text for discussion.

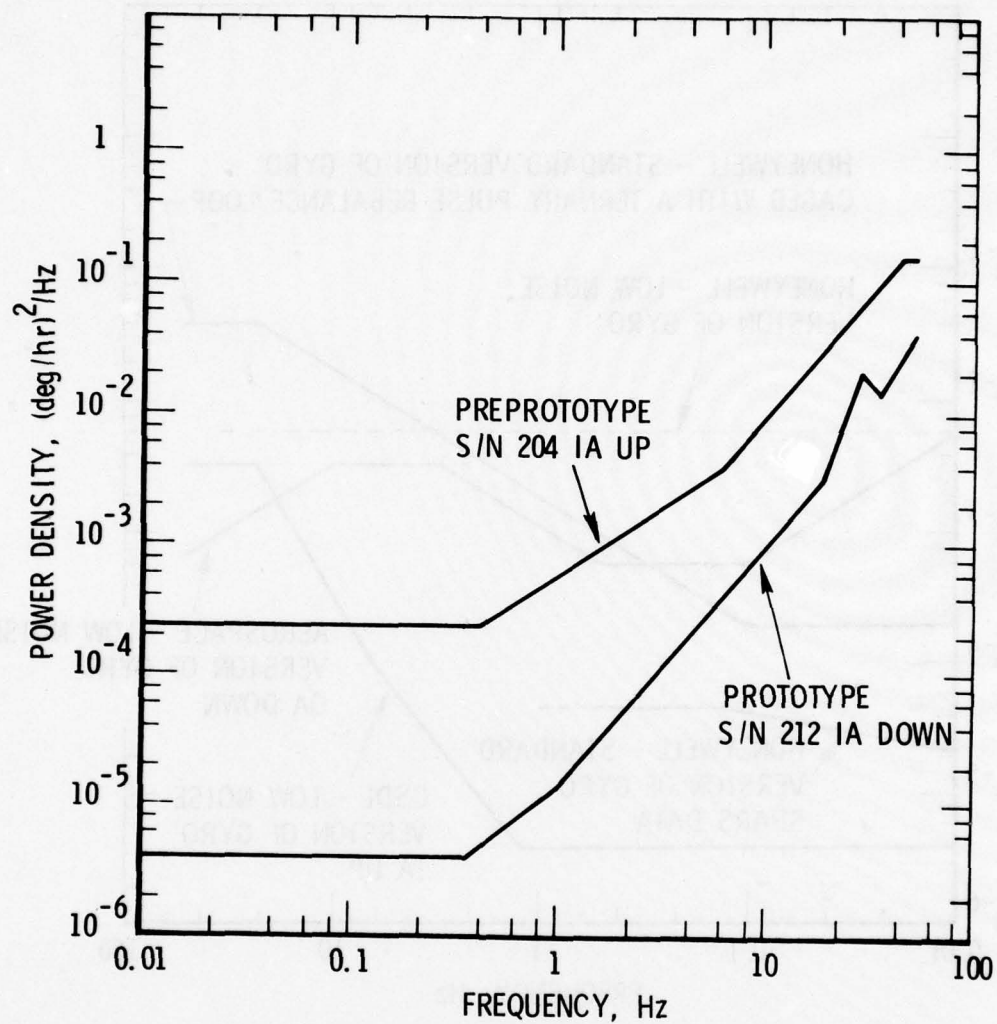


Figure D-1. Linearized Power Spectral Densities for Preprototype and Prototype Versions of the TGG Developed by CSDL

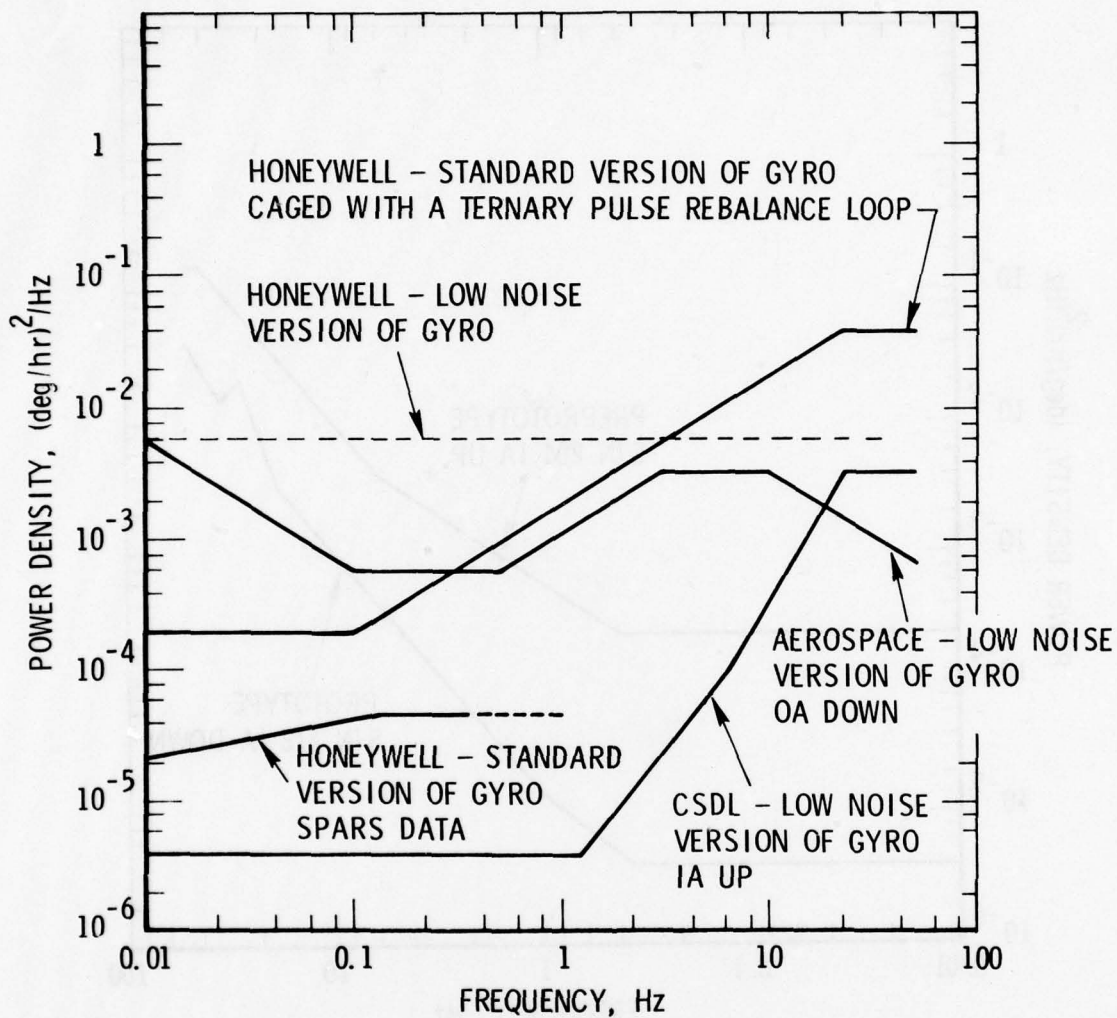


Figure D-2. Linearized Power Spectral Densities for the Honeywell GG 334 (Data were derived by Honeywell, CSDL, and The Aerospace Corporation.)

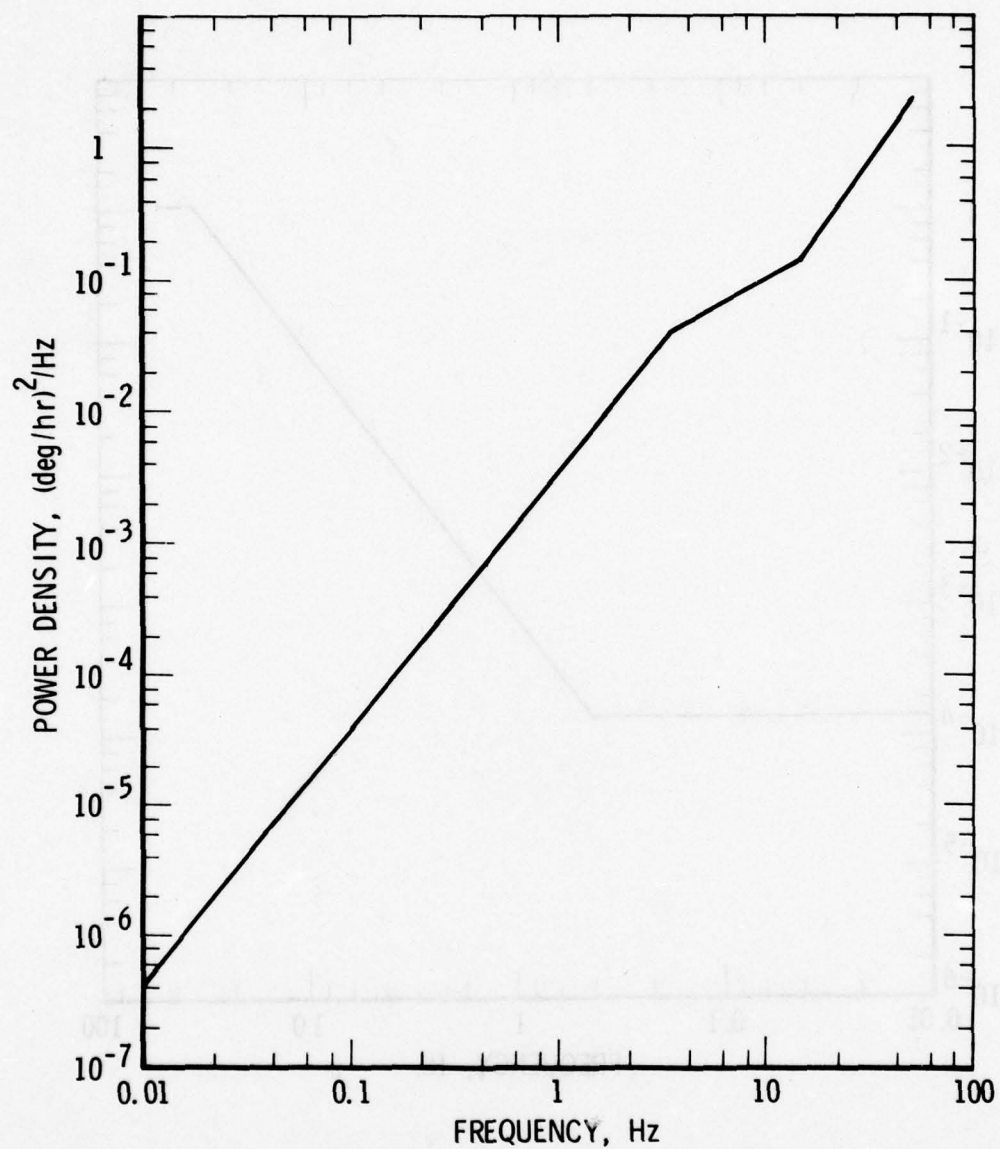


Figure D-3. Linearized Power Spectral Density for the Northrop GI-T1-B Gyro (The data were taken with the gyro OA Up)

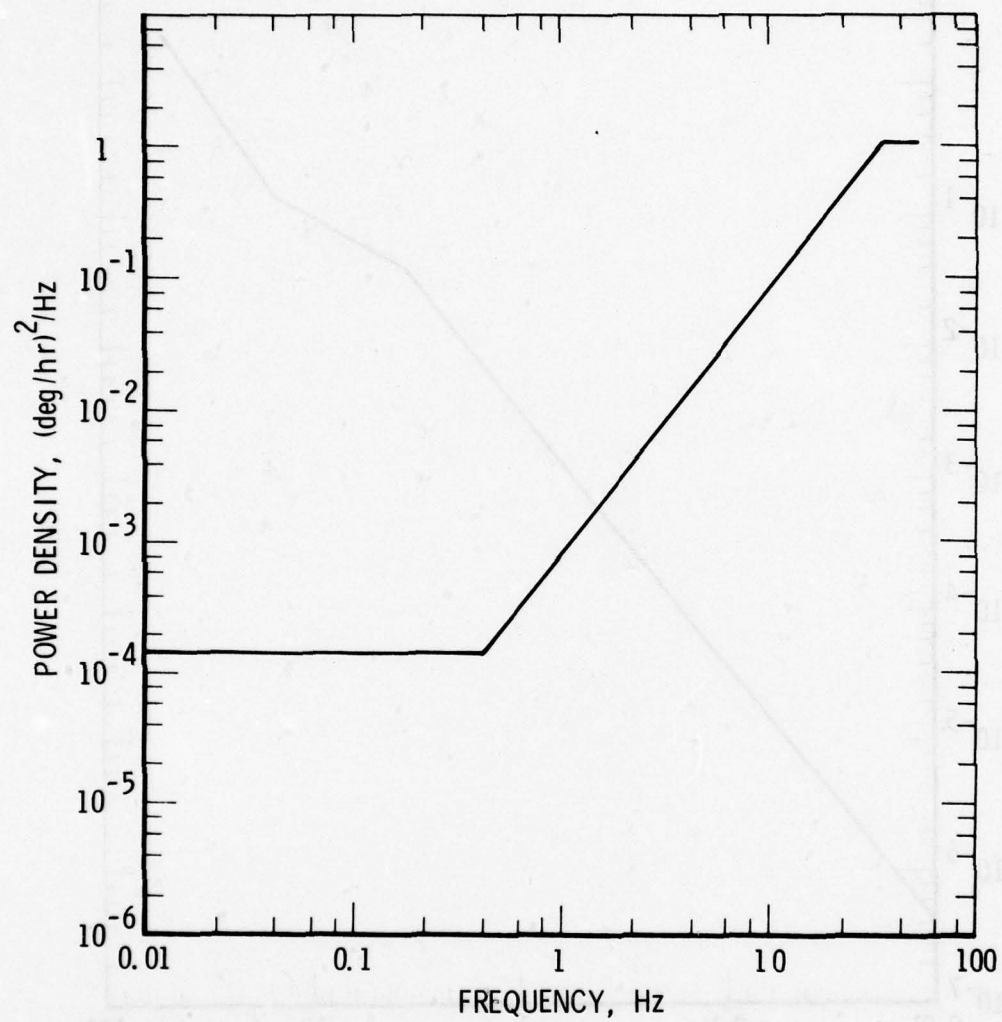


Figure D-4. Linearized Power Spectral Density for the 25 IRIG Mod 3 Gyro. (The data were taken with the gyro OA Up.)

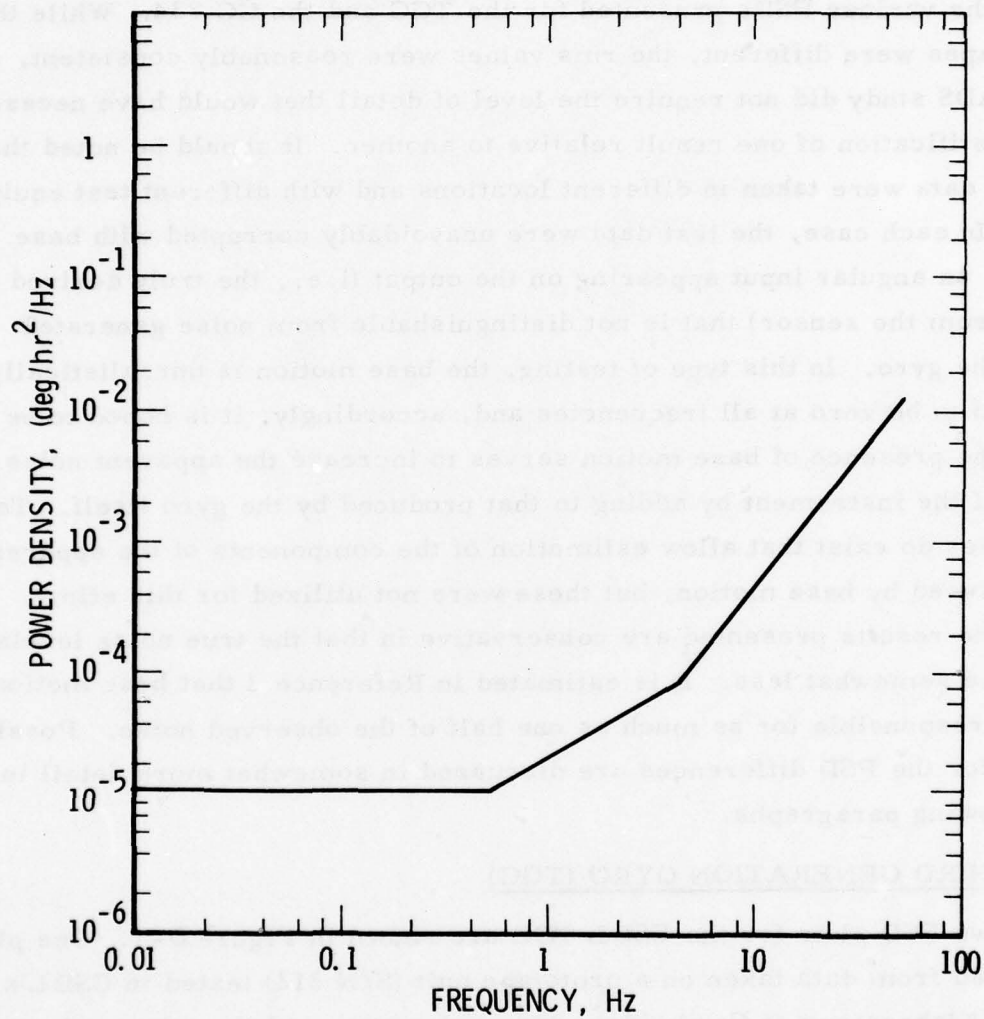


Figure D-5. Linearized Power Spectral Density for the Northrop GI-K7G Gyro. (The data were taken with the gyro OA Up.)

Little effort has been expended in attempting to reconcile differences among the various PSDs presented for the TGG and the GG 334. While the PSD shapes were different, the rms values were reasonably consistent, and the HAADS study did not require the level of detail that would have necessitated justification of one result relative to another. It should be noted that the test data were taken in different locations and with different test equipment. In each case, the test data were unavoidably corrupted with base motion, an angular input appearing on the output (i.e., the truly desired output from the sensor) that is not distinguishable from noise generated within the gyro. In this type of testing, the base motion is unrealistically assumed to be zero at all frequencies and, accordingly, it is hoped to be low. The presence of base motion serves to increase the apparent noise output of the instrument by adding to that produced by the gyro itself. Test techniques do exist that allow estimation of the components of the apparent noise caused by base motion, but these were not utilized for this effort. Thus, the results presented are conservative in that the true noise levels should be somewhat less. It is estimated in Reference 1 that base motion may be responsible for as much as one half of the observed noise. Possible causes for the PSD differences are discussed in somewhat more detail in the following paragraphs.

C. THIRD GENERATION GYRO (TGG)

Two PSD plots for the CSDL TGG are shown in Figure D-1. One plot is derived from data taken on a prototype unit (S/N 212) tested in CSDL's gyro test laboratory at Cambridge, Massachusetts, and the other is based on data obtained from a preprototype unit tested at CSDL's test facility in Bedford, Massachusetts. While the PSD shapes are quite similar, the levels differ on the average by about 1 order of magnitude where the preprototype data are noisier, and the rms values differ by a factor of 1.5. While the causes for this discrepancy can only be conjectural, one can cite the differences in the gyros, test locations, and, possibly, in the test equipment.

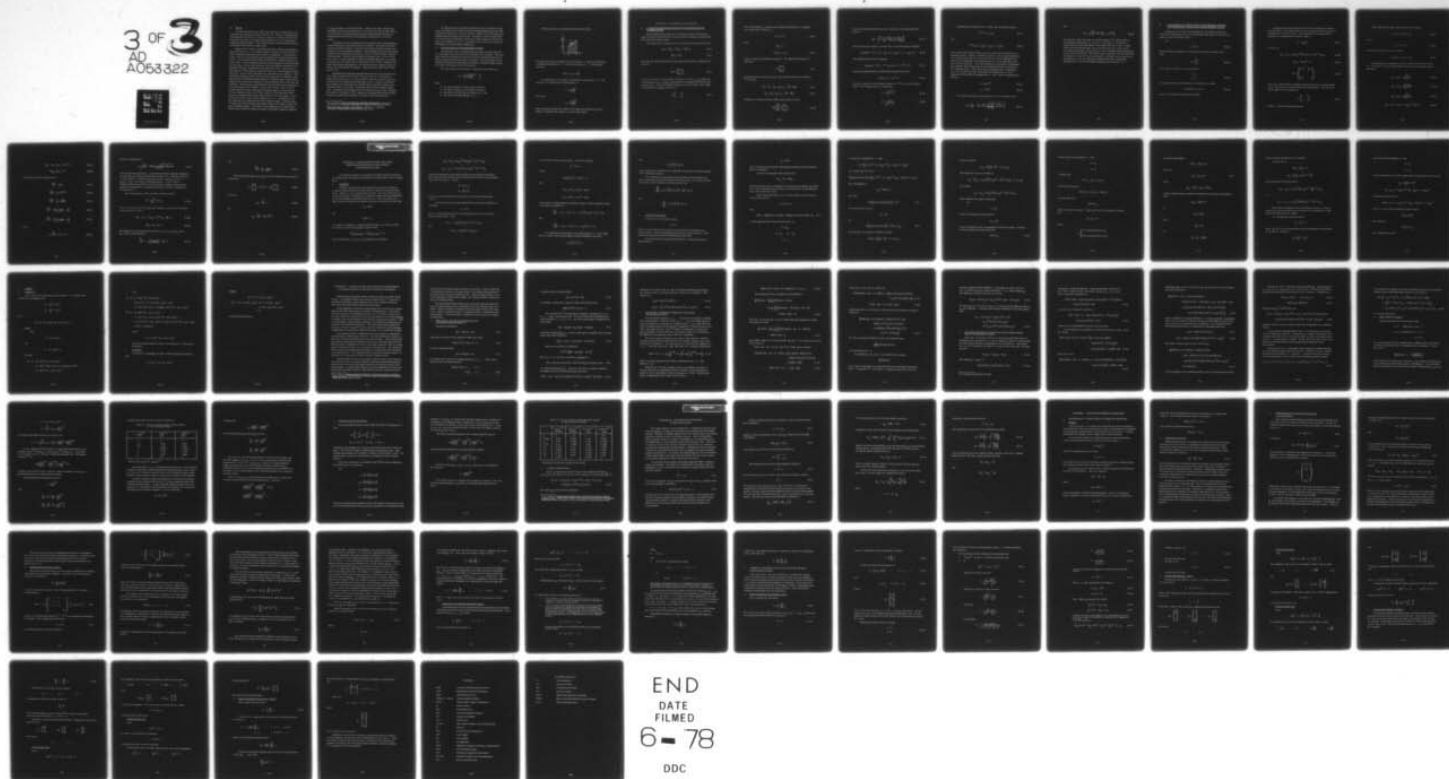
AD-A053 322

AEROSPACE CORP EL SEGUNDO CALIF ENGINEERING SCIENCE --ETC F/G 22/3
HIGH ALTITUDE ATTITUDE DETERMINATION STUDY.(U)

UNCLASSIFIED

MAR 78 R T UYEMINAMI, M V DIXON, T A FUHRMAN F04701-77-C-0078
TR-0078(3526)-1 SAMSO-TR-78-70 NL

3 OF 3
AD
A053322



D. GG 334

The data presented from CSDL and Aerospace in Figure D-2 were obtained from low noise versions of the GG 334. This unit, designated the Low Noise GG 334 A6 unit, is similar to the other versions of the GG 334 except that the wheel is shrouded with beryllium covers to minimize gas turbulence inside the float. This modification has demonstrated improved performance with regard to output noise.

While the rms values for the PSDs obtained by CSDL and Aerospace agree quite well, i.e., 0.2 compared with 0.3 deg/hr, the noise levels at lower frequencies differ by several orders of magnitude. As noted previously, one can cite ground noise and test equipment to explain the discrepancies. The Aerospace data exhibit a 20-dB/decade rolloff at frequencies above 10 Hz. This is probably caused by the loop dynamics associated with the test setup. In this case, the gain of the loop rebalance electronics was adjusted to provide a bandwidth of approximately 25 Hz. Therefore, the loop dynamics would attenuate noise from any source with frequencies above this value. In this respect the CSDL test method was quite different. They adjusted the loop gain to have the first break frequency at 0.004 Hz so that the gyro/loop combination would respond as a position sensor from this frequency on up to the break frequency of the demodulator filter, which was set at 200 Hz. (The frequency associated with the gyro gimbal time constant is not involved because it is higher, in this case, 350 Hz.) Thus, the frequency response of their setup when measuring angular position was flat over the frequency range from 0.004 to 200 Hz, and the positional PSD obtained was unaffected by sensor/loop dynamics over this range. In converting their PSD to one involving angular rate (i.e., multiplying by ω^2), the result was also unaffected over this frequency region. This may help to explain why the Aerospace data droops relative to the CSDL result in the upper frequency region. This effect is also suggested in the other PSDs derived from CSDL data where the slopes in the upper frequency region all

are approximately +2 decades/decade. Coupled with their sensor/loop bandwidth, this situation would occur if the noise were white in this region. A conventional rate sensing implementation would attenuate the noise at frequencies above the first break frequency (usually in the 1 to 50-Hz region).

The figure of merit computed from the Aerospace GG 334 data seemed unreasonably high (0.028 deg/hr) and was rejected. The cause for the difficulty is unknown; however, it may have been associated with seismic disturbances or test equipment problems. Some additional data from the SPARS Program were obtained from Jackson^a in order to provide another estimate of this quantity. The data were limited in frequency from 0.01 to 0.35 Hz and, hence, it was not possible to show the complete spectrum or to obtain a value for the rms noise over the range from 0.01 to 50 Hz. However, the power density was extrapolated to 1 Hz and was used to compute a figure of merit, the result being 0.007 deg/hr. These data were taken from a standard GG 334.

Honeywell has presented some PSD data that were also obtained from a low noise version of the GG 334.^b Since the data were presented as a linear plot on both axes, it was not possible to develop a log-log form accurately for direct comparison with the other results. However, the dotted line in Figure D-2 represents the average value of the PSD obtained over a frequency range of 0 to 25 Hz. Agreement with the other results is quite good. If the plot is extrapolated to 50 Hz and the rms noise value computed, the result is 0.54 deg/hr, which compares reasonably well with the similar results from CSDL and Aerospace (0.18 and 0.30 deg respectively).

^a D. B. Jackson, Gyro Test Results and Model Verification, Report No. TM-20959-4, Honeywell, Minneapolis, Minnesota (26 January 1968).

^b Low-Noise Gyro Testing, Final Report, Report No. 21594-FR, Honeywell, Minneapolis, Minnesota (31 July 1971).

An additional curve is plotted in Figure D-2 that is based on data from one channel of an attitude reference package designated the GG 2200 produced by Honeywell. This unit contains standard GG 334 A6 gyros and exhibits generally higher noise levels. Each gyro is held at pickoff null by a ternary pulse rebalance loop that has a pulse weight of 0.06 arc sec/pulse and a bandwidth of 10 Hz. The output of the unit was not filtered in obtaining the data presented in Figure D-2.

E. CALCULATION OF THE RMS NOISE VALUES

The equations used to compute the areas under the linearized PSD curves plotted on log-log scales are listed below for reference. The area under the PSD represents the statistical variance associated with the frequency range over which the area is computed. The total variance is obtained by summing the areas under each region of constant slope, and the rms value is the square root of this quantity.

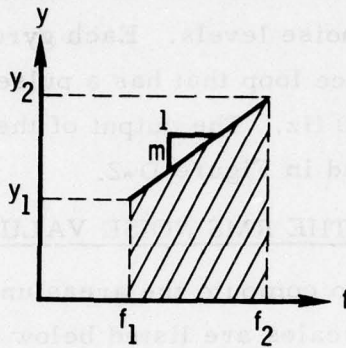
On a log-log plot the area under a straight line with slope m is:

$$\text{Area} = \frac{y_1 f_1}{m+1} \left[\left(\frac{f_2}{f_1} \right)^{m+1} - 1 \right]$$

where

- f_1 = the lower frequency of the region of interest,
- f_2 = the upper frequency of the region of interest,
- y_1 = the abscissa of the line associated with f_1 , and
- m = the slope in decades/decade, $m \neq -1$.

These parameters are illustrated in the sketch below



Note that this equation computes the area down to $y = 0$ and that the equation is indeterminate when $m = -1$. For the case where $m = -1$, the equation becomes:

$$\text{Area} = y_1 f_1 \ln \frac{f_2}{f_1}$$

As noted before, this equation computes the area down to $y = 0$. The equation of a straight line on log-log paper is:

$$y = y_1 \left(\frac{f}{f_1} \right)^m$$

and, hence,

$$y_2 = y_1 \left(\frac{f_2}{f_1} \right)^m$$

Note that these equations are valid for all values of m and that y_2 for one region of constant slope becomes y_1 for the next region.

APPENDIX E. KALMAN FILTER METHODS

1. Z-TRANSFORM INTERPRETATION OF THE STEADY-STATE KALMAN FILTER

In the following discussion, the Z-transform model of the discrete angle measurement Kalman filter is derived and its response characterized by a continuous system model.

The Kalman filter equations for a discrete measurement process are:

$$\hat{\underline{x}}_{i+1} = \hat{\underline{x}}'_{i+1} + K(z_{i+1} - H\hat{\underline{x}}'_{i+1}) \quad (E-1)$$

$$\hat{\underline{x}}'_{i+1} = \Phi \hat{\underline{x}}_i \quad (E-2)$$

where the two-dimensional state $\hat{\underline{x}}$ represents the estimates of attitude and rate and

$$\hat{\underline{x}}_{i+1} = \begin{pmatrix} \hat{\theta}_{i+1} \\ \hat{\omega}_{i+1} \end{pmatrix} \quad (E-3)$$

are the best estimates of the angle θ and rate ω at time t_{i+1} just after the measurement at t_{i+1} , and $\hat{\underline{x}}'_{i+1}$ denotes the best estimate just prior to this measurement. The state transition matrix Φ for this system, where angle θ represents the integral of rate ω , is

$$\Phi = \begin{pmatrix} 1 & T \\ 0 & 1 \end{pmatrix} \quad (E-4)$$

The measurements z_i consist only of angle measurements θ corrupted by a random noise sequence n_i

$$z_i = \theta_i + n_i \quad (\text{E-5})$$

where

$$E(n_i) = 0$$

$$E(n_i n_j) = r' \delta_{ij} \quad (\text{E-6})$$

and $E(\cdot)$ denotes the expectation operator. The Kalman filter gains are denoted by

$$K = \begin{pmatrix} K_\theta \\ K_w \end{pmatrix} \quad (\text{E-7})$$

Substituting these equations into Eq. (E-1) produces difference equations for $\hat{\theta}_i$ and \hat{w}_i .

$$\hat{\theta}_{i+1} = \hat{\theta}_i + T\hat{w}_i + K_\theta [z_{i+1} - (\hat{\theta}_i + T\hat{w}_i)] \quad (\text{E-8})$$

$$\hat{w}_{i+1} = \hat{w}_i + K_w [z_{i+1} - (\hat{\theta}_i + T\hat{w}_i)] \quad (\text{E-9})$$

Taking the Z-transform of these differential equations yields

$$A(Z) \begin{pmatrix} \hat{\theta} \\ \hat{w} \end{pmatrix} = \begin{pmatrix} K_\theta \\ K_w \end{pmatrix} z \quad (\text{E-10})$$

where zero initial conditions have been assumed, and the matrix $A(Z)$ is given by

$$A(Z) = \left(\begin{array}{c|c} Z - (1 - K_\theta) & - (1 - K_\theta) T \\ \hline K_w & Z - (1 - K_w T) \end{array} \right) \quad (E-11)$$

The characteristic equation of matrix $A(Z)$ is its determinant $\det[A(Z)]$.

$$\det[A(Z)] = Z^2 \left\{ 1 - [(1 - K_\theta) + (1 - K_w)] Z^{-1} + (1 - K_\theta) Z^{-2} \right\} \quad (E-12)$$

The standard form for this equation is

$$\det[A(Z)] = Z^2 (1 - e^{-aT} \cos bT Z^{-1} + e^{-2aT} Z^{-2}) \quad (E-13)$$

where the continuous filter characteristic equation is given by

$$\det[A(s)] = (s + a)^2 + b^2 \quad (E-14)$$

The time response of the continuous system is $e^{-at} \cos bt$, and its bandwidth Ω' and damping ratio ζ' are given by

$$\Omega' = \sqrt{a^2 + b^2} \quad (E-15)$$

$$\zeta' = \frac{a}{\sqrt{a^2 + b^2}} \quad (E-16)$$

Comparing the coefficients of Z in Eqs. (E-12) and (E-13) gives

$$e^{-2aT} = (1 - K_{\theta}) \quad (\text{E-17})$$

and

$$e^{-aT} \cos bT = \frac{1}{2} [(1 - K_{\theta}) + (1 - K_{\omega} T)] \quad (\text{E-18})$$

Once steady-state Kalman gains K_{θ} and K_{ω} have been determined and a sampling period T chosen, coefficients a and b of the sampled-data filter can be determined from Eqs. (E-17) and (E-18), and the equivalent continuous filter bandwidth Ω' and damping ratio ζ' can be calculated from Eqs. (E-15) and (E-16). The prime notation has been added to distinguish the bandwidth and damping ratio of the sampled-data filter from those of the continuous filter. In the limit as the sampling period T approaches zero, the sampled-data filter bandwidth and damping ratio Ω' and ζ' approach the bandwidth and damping ratio Ω and ζ of the continuous filter given by:

$$\Omega = (q/r)^{1/4} \quad (\text{E-19})$$

$$\zeta = 1/\sqrt{2} \quad (\text{E-20})$$

The steady-state Kalman gains K_{θ} and K_{ω} can be calculated from

$$y^2 \equiv \frac{T^3 q}{r'} = \frac{2(2 - K_{\theta}) - \sqrt{3 K_{\theta}^2 - 36 K_{\theta} + 36}}{\sqrt{1 - K_{\theta}}} \quad (\text{E-21})$$

and

$$TK_{\omega} = \sqrt{\frac{T^3 q}{r}} \sqrt{1 - K_{\theta}} = y \sqrt{1 - K_{\theta}} \quad (E-22)$$

Note that the steady-state gain K_{θ} and the product TK_{ω} depend only on the grouping of parameters T , q , and r' denoted by y . Parameter q represents the (white) disturbance acceleration PSD level, and r' represents the mean-squared angle sensor measurement error in Eq. (A-6). The steady-state values of K_{θ} and $K_{\omega}T$ can be calculated using parameter y in Eqs. (E-21) and (E-22). With these values, using Eqs. (E-17) and (E-18), the products aT and bT can be determined. From Eqs. (E-15) and (E-16) the products aT and bT specify the sampled-data filter steady-state damping ratio ζ' and the bandwidth sampling-period product $\Omega'T$.

2. CALCULATION OF STEADY-STATE PERFORMANCE FOR THE TWO-DIMENSIONAL STATE ANGLE MEASUREMENT FILTER

Equations are derived in this appendix for calculating the expected steady-state attitude and rate errors and Kalman filter gains for the discrete angle measurement Kalman filter.

Let

$$\underline{e} = \hat{\underline{x}} - \underline{x} \quad (\text{E-23})$$

denote the filter estimation error where $\hat{\underline{x}}$ is the filter estimate of the state

$$\underline{x} = \begin{pmatrix} \theta \\ \omega \end{pmatrix} \quad (\text{E-24})$$

where angle θ and rate ω are governed by:

$$\begin{aligned} \dot{\theta} &= \omega \\ \dot{\omega} &= a \end{aligned} \quad (\text{E-25})$$

and random (white noise) disturbance accelerations a satisfy

$$E [a(t) a(\tau)] = q \delta(t - \tau) \quad (\text{E-26})$$

where $E(\cdot)$ denotes the expectation operator.

Assuming that measurements of the state are available at constant time intervals T , the Kalman filter for the continuous system above can be formulated in the discrete form. The standard discrete Kalman filter equations for computing the covariance matrix

$$P = E(\underline{e}\underline{e}^T) \quad (E-27)$$

are given by

$$P_{i+1} = M_{i+1} - M_{i+1} H^T (H^T M_{i+1} H + R)^{-1} H M_{i+1} \quad (E-28)$$

$$M_{i+1} = \Phi P_i \Phi^T + W \quad (E-29)$$

$$W = q \begin{pmatrix} \frac{1}{3} T^3 & \frac{1}{2} T^2 \\ \frac{1}{2} T^2 & T \end{pmatrix} \quad (E-30)$$

where M_i represents the covariance matrix just prior to a measurement and P_i represents its value just after the measurement. The state transition matrix Φ for the system is

$$\Phi = \begin{pmatrix} 1 & T \\ 0 & 1 \end{pmatrix} \quad (E-31)$$

where T is the measurement interval.

When only discrete angle measurements z_i are taken,

$$z_i = \theta_i + n_i = H \underline{x}_i + \underline{n}_i \quad (\text{E-32})$$

where

$$H = (1 \quad | \quad 0) \quad (\text{E-33})$$

and the measurement errors n_i satisfy

$$E(n_i n_j) = R \delta_{ij} \equiv r' \delta_{ij} \quad (\text{E-34})$$

Substituting these equations into Eqs. (E-28) and (E-29) and setting $P_i = P$ and $M_i = M$ for the steady-state values gives the following scalar equations:

$$P_{11} = M_{11} - \frac{M_{11}^2}{M_{11} + r'} \quad (\text{E-35})$$

$$P_{12} = M_{12} - \frac{M_{11} M_{12}}{M_{11} + r'} \quad (\text{E-36})$$

$$P_{22} = M_{22} - \frac{M_{12}^2}{M_{11} + r'} \quad (\text{E-37})$$

$$M_{11} = P_{11} + 2 P_{12} T + P_{22} T^2 + \frac{q}{3} T^3 \quad (\text{E-38})$$

$$M_{12} = P_{12} + P_{22} T + \frac{1}{2} T^2 q \quad (\text{E-39})$$

$$M_{22} = P_{22} + q T \quad (\text{E-40})$$

The solutions to these equations are:

$$\frac{M_{11}}{r'} = \frac{v}{1-v} \quad (\text{E-41})$$

$$\frac{P_{12}}{r'} = \frac{y}{T} \sqrt{1-v} \quad (\text{E-42})$$

$$\frac{M_{12}}{r'} = \frac{y}{T} \sqrt{\frac{1}{1-v}} \quad (\text{E-43})$$

$$\frac{P_{22}}{r'} = \frac{y}{T^2} \left[\sqrt{\frac{v}{1-v}} - \frac{y}{2} \right] \quad (\text{E-44})$$

$$\frac{M_{22}}{r'} = \frac{y}{T^2} \left[\sqrt{\frac{v}{1-v}} + \frac{y}{2} \right] \quad (\text{E-45})$$

where

$$v \equiv \frac{P_{11}}{r'} ; 0 \leq v \leq 1 \quad (\text{E-46})$$

must be computed from

$$y \equiv \sqrt{\frac{T^3 q}{r'}} = \frac{3(2 - v) - \sqrt{3v^2 - 36v + 36}}{\sqrt{1 - v}} \quad (E-47)$$

The dimensionless parameter v represents the ratio of attitude estimation accuracy (P_{11}) to sensor measurement accuracy (r'). Note that a value of v can be chosen, y calculated from Eq. (B-25), and M_{11}/r' , P_{12}/r' , M_{12}/r' , P_{22}/r' , and M_{22}/r' determined from $v = P_{11}/r'$ and y . Equation (B-25) represents the trade-off between system accuracy represented by the parameter v and the measurement rate that is contained in the parameter y .

The average values of the covariance matrix elements,

$$\bar{P} = \frac{1}{T} \int_0^T P(t) dt \quad (E-48)$$

where T is used due to the steady-state condition, can also be determined from parameters y and v .

$$\bar{P}_{11} = P_{11} + T P_{12} + \frac{1}{3} T^2 P_{22} + \frac{q}{12} T^3 \quad (E-49)$$

$$\bar{P}_{22} = P_{22} + \frac{q}{2} T \quad (E-50)$$

Substituting the previously derived values for P_{11} , P_{12} , and P_{22} into Eqs. (E-49) and (E-50) gives

$$\frac{\bar{P}_{11}}{r'} = v + \left(\frac{3 - 2v}{3\sqrt{1 - v}} \right) y - \frac{1}{12} y^2 \quad (E-51)$$

and

$$\frac{\bar{P}_{22}}{r'} = \frac{y}{T^2} \frac{v}{\sqrt{1-v}} \quad (\text{E-52})$$

The Kalman filter gains K_θ and K_ω are also related to the covariance elements by

$$K = \begin{pmatrix} K_\theta \\ K_\omega \end{pmatrix} = P H^T R^{-1} = \frac{1}{r'} \begin{pmatrix} P_{11} \\ P_{12} \end{pmatrix} \quad (\text{E-53})$$

Therefore,

$$K_\theta = \frac{P_{11}}{r'} = v \quad (\text{E-54})$$

and

$$K_\omega = \frac{P_{12}}{r'} = \frac{y}{T} \sqrt{1-v} \quad (\text{E-55})$$

APPENDIX F. DERIVATION OF UPPER AND LOWER PERFORMANCE BOUNDS FOR THE RANDOM MEASUREMENT FILTER

This appendix contains a derivation of an upper and lower bound for the Kalman filter covariance matrix when the measurements occur at random times.

1. THEOREM

Consider a Kalman filter with fixed initial covariance matrix P_0 in which measurements may be taken only at a sequence of fixed decision times. Whether or not a measurement is made, such a decision time is a random event with a probability p of making a measurement and probability $(1 - p)$ of not making a measurement ($0 \leq p \leq 1$). Then, P_u and P_L are upper and lower bounds on the expected covariance matrix in the sense that

$$P_u - E[P]$$

and

$$E[P] - P_L$$

are positive semidefinite. Except at decision times, P_u and P_L satisfy the normal covariance propagation equations with

$$P_u|_{\text{initial time}} = P_L|_{\text{initial time}} = P_0$$

At a decision time, P_u and P_L are updated by the formulas

$$P_{ua} = P_{ub} - p P_{ub} H^T (H P_{ub} H^T + R)^{-1} H P_{ub}$$

$$P_{La} = P_{Lb} - p P_{Lb} H^T (p H P_{Lb} H^T + R)^{-1} H P_{Lb}$$

where the subscripts a and b denote values after and before the decision time respectively, H denotes the observation matrix, and R is the measurement noise covariance. That is,

$$\underline{m} = H \underline{x} + \underline{r}$$

$$R = E[\underline{r} \underline{r}^T]$$

where \underline{m} is the measurement vector and \underline{r} is the measurement noise vector.

Taking the limit as the interval between decision times that goes to zero gives

$$p = \nu dt$$

where ν is the expected number of measurements per sec of a Poisson measurement process. Then,

$$d P_u = -\nu P_u H^T (H P_u H^T + R)^{-1} H P_u dt$$

and

$$d P_L = -\nu P_L H^T R^{-1} H P_L dt$$

for the effects of the measurements. If the state satisfies

$$\dot{\underline{x}} = F \underline{x} + \underline{n}$$

where

$$E[\underline{n}(t) \underline{n}^T(s)] = N(t) \delta(t - s)$$

then

$$d P_u = (F P_u + P_u F^T + N) dt$$

$$d P_L = (F P_L + P_L F^T + N) dt$$

for the effects of plant dynamics and process noise, and the continuous limit of the discrete equations is

$$\frac{dP_u}{dt} = F P_u + P_u F^T + N - v P_u H^T (H P_u H^T + R)^{-1} H P_u$$

and

$$\frac{dP_L}{dt} = F P_L + P_L F^T + N - v P_L H^T R^{-1} H P_L$$

If a continuous measurement is also being made (i.e., if star sightings are random and rate gyro data are always available), the terms

$$-P_u H_d^T R_d^{-1} H_d P_u$$

and

$$-P_L H_d^T R_d^{-1} H_d P_L$$

where H_d and R_d correspond to the continuous measurement, should be added to the continuous equations.

If m different measurements are being made with observation and noise matrices H_k and R_k and measurement mean rates v_k , then the measurement terms in the continuous equations take the form

$$- \sum_{k=1}^m v_k P_u H_k^T (H_k P_u H_k^T + R_k)^{-1} H_k P_u$$

and

$$- \sum_{k=1}^m v_k P_L H_k^T R_k^{-1} H_k P_L$$

2. PROOF OF THEOREM

In the proof, the inequality notation

$$A \geq B$$

will be used to denote the fact that $(A - B)$ is a positive semidefinite symmetric matrix. Two matrix inequality lemmas are used in the proof. Their statements and proofs are given following this main proof.

The proof will be by mathematical induction. Assume that before a filtering phase

$$P_u \geq E[P]$$

Then it will be proved that this relationship still holds after the filtering phase is completed.

The desired inequality holds initially since

$$P_{u_0} = P_0 = E[P_0]$$

Between decision times, everything is deterministic and linear and, therefore, if the inequality holds just after one decision time, it will hold just before the next decision time.

Now, let the subscripts b and a denote values before and after a decision time and let

$$J = H^T R^{-1} H$$

Then,

$$E[P_a] = E[P_a | \text{measurement}] p + E[P_a | \text{no measurement}] (1 - p) \quad (F-1)$$

For the expected value with a measurement, let

$$A = P_{ub}$$

$$B = P_b \quad B' = P_a$$

$$C = J$$

in Lemma (1), Paragraph F.3. Then

$$P_a \leq (P_{ub}^{-1} + J)^{-1} + (I + P_{ub} J)^{-1} (P_b - P_{ub}) (I + J P_{ub})^{-1}$$

and, taking expected values,

$$E[P_a | \text{measurement}] \leq (P_{ub}^{-1} + J)^{-1} + (I + P_{ub} J)^{-1} (P_{ub} - E[P_b]) (I + J P_{ub})^{-1}$$

But, by hypothesis,

$$P_{ub} - E[P_b] \geq 0$$

and, thus,

$$E[P_a | \text{measurement}] \leq (P_{ub}^{-1} + J)^{-1} \quad (F-2)$$

If no measurement occurs,

$$P_a = P_b$$

and

$$E[P_a | \text{no measurement}] = E[P_b] \leq P_{ub} \quad (F-3)$$

Inserting Eqs. (F-2) and (F-3) into (F-1) yields

$$E[P_a] \leq p (P_{ub}^{-1} + J)^{-1} + (1 - p) P_{ub}$$

Thus we will take

$$P_{ua} = p \left(P_{ub}^{-1} + J \right)^{-1} + (1 - p) P_{ub}$$

This expression may be rewritten as

$$P_{ua} = p \left\{ P_{ub} - P_{ub} H^T \left(H P_{ub} H^T + R \right)^{-1} H P_{ub} \right\} + (1 - p) P_{ub}$$

and, finally,

$$P_{ua} = P_{ub} - p P_{ub} H^T \left(H P_{ub} H^T + R \right)^{-1} H P_{ub}$$

which completes the upper bound proof.

Let

$$S = p^{-1}$$

be the true information matrix and let

$$S_L = P_L^{-1}$$

be the information matrix corresponding to the lower bound. It will be proved by mathematical induction that

$$E[S] \leq S_L \tag{F-4}$$

Using Lemma (2), Paragraph F.3, with

$$A = S_L$$

$$B = S$$

it follows that

$$P \geq P_L - P_L (S - S_L) P_L$$

and taking expectations

$$E[P] \geq P_L + P_L (S_L - E[S]) P_L$$

and using Eq. (F-4),

$$E[P] \geq P_L$$

which is the desired result. To prove Eq. (F-4), note that at a decision time

$$S_a = S_b + \theta J$$

where

$$\theta = \begin{cases} 1 & \text{if a measurement occurs} \\ 0 & \text{if no measurement occurs} \end{cases}$$

and taking expectations,

$$E[S_a] = E[S_b] + p J$$

Now, let

$$S_{La} = S_{Lb} + p J \quad (F-5)$$

Then,

$$S_{La} - E[S_a] = S_{Lb} - E[S_b]$$

and the right-hand side is positive semidefinite by the induction hypothesis.

Thus,

$$S_{La} - E[S_a] \geq 0$$

or

$$S_{La} \geq E[S_a]$$

Also,

$$P_{L0} = P_0$$

so

$$S_{L0} = S_0 = E[S_0]$$

and the induction hypothesis is true initially.

Using Eq. (F-5),

$$P_{La}^{-1} = P_{Lb}^{-1} + p J$$

$$P_{La} = (P_{Lb}^{-1} + p H^T R^{-1} H)^{-1}$$

and by the matrix inversion lemma,

$$P_{La} = P_{Lb} - P_{Lb} H^T \left(H P_{Lb} H^T + \frac{R}{p} \right)^{-1} H P_{La}$$

or

$$P_{La} = P_{Lb} - p P_{Lb} H^T (p H P_{Lb} H^T + R)^{-1} H P_{La}$$

State update (multiplication by the transition matrix) is a linear operation on the information matrix so that Eq. (F-4) holds after a state update if it holds before the update.

For incorporation of process noise,

$$P_a = P'_b + N'$$

where P'_b and N' are generated from linear nonsingular transformations of P_b and N . Therefore,

$$S_a = (S'^{-1}_b + N')^{-1}$$

By Lemma (1), Paragraph F.3, with

$$A = S_L$$

$$B = S$$

we have (note that S_L uses the regular Kalman formula for process noise)

$$S_{La} = (S'_{Lb}{}^{-1} + N')^{-1}$$

$$S_a \leq S_{La} + (I + S'_{Lb} N')^{-1} (S'_b - S'_{Lb}) (I + N' S'_{Lb})^{-1}$$

and taking expected values,

$$E[S_a] \leq S_{La} - (I + S'_{Lb} N')^{-1} (S'_{Lb} - E[S'_b]) (I + N' S'_{Lb})^{-1}$$

However, by the induction hypothesis and linearity,

$$S'_{Lb} \geq E[S'_b]$$

and, therefore,

$$E[S_a] \leq S_{La}$$

This completes the proof.

3. LEMMA

a. Lemma (1)

If A, B, and C are symmetric positive definite $n \times n$ matrices and A and B are nonsingular and

$$A' = \{A^{-1} + C\}^{-1}$$

$$B' = \{B^{-1} + C\}^{-1}$$

then,

$$B' \leq A' + (I + AC)^{-1} (B - A) (I + CA)^{-1}$$

Proof

Now,

$$A' = A(I + CA)^{-1}$$

and

$$B' = (I + BC)^{-1} B$$

and thus

$$\begin{aligned} B' - A' &= (I + BC)^{-1} B - A(I + CA)^{-1} \\ &= (I + BC)^{-1} \{B(I + CA) - (I + BC)A\} (I + CA)^{-1} \\ &= (I + BC)^{-1} (B - A) (I + CA)^{-1} \end{aligned}$$

and

$$\begin{aligned}
 B' - A' &= (I + AC)^{-1} (B - A) (I + CA)^{-1} \\
 &= \left\{ (I + BC)^{-1} - (I + AC)^{-1} \right\} (B - A) (I + CA)^{-1} \\
 &= (I + AC)^{-1} \left\{ (I + AC) - (I + BC) \right\} (I + BC)^{-1} (B - A) (I + CA)^{-1}
 \end{aligned}$$

$$\begin{aligned}
 B' - A' &= (I + AC)^{-1} (B - A) (I + CA)^{-1} \\
 &= (I + AC)^{-1} (A - B) C (I + BC)^{-1} (B - A) (I + CA)^{-1} \\
 &= -(I + AC)^{-1} (B - A) (I + CB)^{-1} (I + CB) C (I + BC)^{-1} (B - A) (I + CA)^{-1} \\
 &= -M^T (C + CBC) M \leq 0
 \end{aligned}$$

where

$$M = (I + BC)^{-1} (B - A) (I + CA)^{-1}$$

and the inequality follows because $C \geq 0$ and $CBC \geq 0$. This proves the lemma.

b. Lemma (2)

If A and B are nonsingular, positive, definite symmetric matrices, then

$$B^{-1} \geq A^{-1} - A^{-1} (B - A) A^{-1}$$

Proof

$$B^{-1} - A^{-1} = B^{-1}(A - B)A^{-1}$$

$$\begin{aligned} B^{-1} - A^{-1} + A^{-1}(B - A)A^{-1} &= (A^{-1} - B^{-1})(B - A)A^{-1} \\ &= A^{-1}(B - A)B^{-1}(B - A)A^{-1} \\ &\geq 0 \end{aligned}$$

which proves the lemma.

APPENDIX G. KALMAN FILTER EQUATIONS FOR MEASUREMENTS AT RANDOM POINTS IN TIME AND NUMERICAL EXAMPLES

Measurements for Kalman filters sometimes arrive at random points in time. An example would be star sensor measurements.¹ A measure of the filter performance in this situation is the error covariance expected value taken over all possible random-point sequences.

In this appendix, a discussion is presented of the case where the random points in time are determined by a Poisson counting process. The matrix differential equation for propagation of the error covariance expected value is found. Since the arrival times of the measurements are not known a priori, the Kalman filter gains depend on the particular random-point sequence. That is, they depend on the particular realization of the Poisson counting process in the set of all possible realizations. The matrix differential equation for the error covariance expected value requires at every time-point knowledge of additional error covariance statistics; therefore, it is not directly solvable.

If a suboptimal filter is implemented where the gains are independent of the particular random-point sequence, the matrix differential equation for the error covariance expected value is directly solvable. This is because the only statistic entering in the equation is the error covariance expected value. Since the filter is suboptimal, its error covariance expected value is an upper bound on the Kalman filter error covariance expected value. The suboptimal filter is worthy of consideration and study as a possible practical alternative to the Kalman filter. The suboptimal filter realization independent gains are chosen so as to minimize the error covariance expected value.

A lower bound to the error covariance expected value is found directly from the exact error covariance expected value matrix differential equation, and turns out to be close to the upper bound for low intensity Poisson counting processes. A second lower bound is derived in Appendix F and turns out to be close to the upper bound for high intensity Poisson counting processes.

¹S. M. Melzer, Satellite Attitude Estimation with Measurements at Random Points in Time, TR-0076(6111)-6, The Aerospace Corporation, El Segundo, California (10 December 1975).

Intensity is the average number of points per unit time. Thus, at both ends of the intensity spectrum, the upper bound is an excellent approximation to the actual error covariance expected value. When the upper bound is close to the maximum of the two lower bounds, the suboptimal filter is almost as good as the Kalman filter.

By simulating the upper bound error covariance expected value transient, an approximation of the convergence time of the Kalman filter is obtained. Again, it should be noted that the derived upper bound is the exact error covariance expected value for a suboptimal filter of realization independent gains. The Kalman filter is different in that its gains are realization dependent.

1. THE KALMAN FILTER WITH DISCRETE AND CONTINUOUS MEASUREMENTS

The plant is modeled by

$$\dot{\underline{x}}(t) = A(t) \underline{x}(t) + \underline{w}(t) \quad (G-1)$$

where $\underline{x}(t)$ is the state vector and $\underline{w}(t)$ is white state noise

$$E[\underline{w}(t) \underline{w}^T(t')] = Q(t) \delta(t - t') \quad (G-2)$$

A vector of measurements

$$\underline{y}(t) = H(t) \underline{x}(t) + \underline{v}(t) \quad (G-3)$$

is available only at discrete sampling instants $t_1 < t_2 \dots$. Here, $\underline{v}(t)$ is finite variance measurement noise

$$\begin{aligned} E[\underline{v}(t) \underline{v}^T(t')] &= 0 & t \neq t' \\ &= R_v(t) & t = t' \end{aligned} \quad (G-4)$$

A second vector of measurements

$$\underline{z}(t) = G(t) \underline{x}(t) + \underline{u}(t) \quad (G-5)$$

is available continuously, and $\underline{u}(t)$ is white measurement noise

$$E[\underline{u}(t) \underline{u}^T(t')] = R_u \delta(t - t') \quad (G-6)$$

Let t_i denote the i^{th} time that $\underline{y}(t)$ is available, and define $t_i^+ = t_i + \epsilon$, $t_i^- = t_i - \epsilon$ with ϵ arbitrarily small. For the time period during which $\underline{y}(t)$ is not available, i.e., $t_{i-1}^+ \leq t \leq t_i^-$, the state estimate $\hat{\underline{x}}(t)$ is updated by the linear filter

$$\dot{\hat{\underline{x}}}(t) = A(t) \hat{\underline{x}}(t) + K_u(t) [\underline{z}(t) - G(t) \hat{\underline{x}}(t)] \quad (G-7)$$

with initial condition $\hat{\underline{x}}(t_{i-1}^+)$. At time t_i when $\underline{y}(t)$ is available, the correction made to the state estimate is

$$\hat{\underline{x}}(t_{i+1}^+) = \hat{\underline{x}}(t_i^-) + K_v(t_i^-) [\underline{y}(t_i) - H(t_i) \hat{\underline{x}}(t_i^-)] \quad (G-8)$$

The error covariance is defined by

$$P(t) \triangleq E[(\hat{\underline{x}}(t) - \underline{x}(t)) (\hat{\underline{x}}(t) - \underline{x}(t))^T]$$

For $t_{i-1}^+ \leq t \leq t_i^-$, the error covariance propagates by

$$\dot{P}(t) = A(t) P(t) + P(t) A^T(t) - P(t) G^T(t) R_u^{-1}(t) G(t) P(t) + Q(t) \quad (G-9)$$

with initial condition $P(t_{i-1}^+)$. At time t_i , the error covariance reduction resulting from the new information $\underline{y}(t_i)$ is given by

$$P(t_i^+) = P(t_i^-) - P(t_i^-) H^T(t_i) [H(t_i) P(t_i^-) H^T(t_i) + R_v(t_i)]^{-1} H(t_i) P(t_i^-) \quad (G-10)$$

Equations (G-9) and (G-10) are only true when the gains $K_u(t)$ and $K_v(t_i^-)$ are chosen in order to minimize the trace of the error covariance. The choices are

$$K_u(t) = P(t) G^T(t) R_u^{-1}(t) \quad (G-11)$$

$$K_v(t_i^-) = P(t_i^-) H^T(t_i) [H(t_i) P(t_i^-) H^T(t_i) + R_v(t_i)]^{-1} \quad (G-12)$$

2. THE ERROR COVARIANCE EXPECTED VALUE FOR THE KALMAN FILTER

For the specific sequence $t_1, t_2 \dots$ of points at which $y(t)$ is available, $P(t)$ is deterministic. However, if the $t_1, t_2 \dots$ occur at random points in time, then the error covariance is a random process. Let ζ index elements of the probability space S of all possible realizations of random points in time. Thus, $t_i(\zeta)$ means the time of the i^{th} instant of realization ζ at which $y(t) = y(t_i)$ is available. $P(t; \zeta)$ is the error covariance at time t for realization ζ , and $E[P(t; \zeta)]$ is the expected value of the error covariance.

We assume that the sequence $t_1(\zeta), t_2(\zeta)$ is determined by a Poisson counting process $N(0; t; \zeta)$ where $N(0; t; \zeta)$ is the number of points on the interval $(0, t)$ for realization ζ . The point $t_i(\zeta)$ occurs when $N(0; t; \zeta)$ changes from $i-1$ to i . Given the interval $(t, t+\Delta]$, then (with the ζ argument understood)

$$P[N(t, t+\Delta) = k] = \frac{1}{k!} \left(\int_t^{t+\Delta} \lambda(n) dn \right)^k \exp \left(- \int_t^{t+\Delta} \lambda(n) dn \right) \quad (G-13)$$

where $\lambda(t)$ is the intensity of the Poisson counting process, i.e., d/dt
 $E[N(0, t)] = \lambda(t)$.

With $N(0, t; \zeta)$ a Poisson counting process, the numbers of points on disjoint intervals are independent random variables, and the placement of points on $(0, t]$ is independent of their placement on $(t, t+\Delta]$. It follows that $P(t; \zeta)$ is independent of $N(t, t+\Delta; \zeta)$ and, therefore,

$$E[P(t, \zeta) | N(t, t+\Delta; \zeta) = k] = E[P(t; \zeta)], \quad k = 0, 1, 2, \dots \quad (G-14)$$

We proceed to derive an equation for $d/dt E[P(t; \zeta)]$.

$$\begin{aligned} \frac{d}{dt} E[P(t; \zeta)] &= \lim_{\Delta \rightarrow 0} \frac{1}{\Delta} E[P(t+\Delta; \zeta) - P(t; \zeta)] \\ &= \lim_{\Delta \rightarrow 0} \frac{1}{\Delta} \sum_{k=0}^{\infty} \left[E[P(t+\Delta; \zeta) - P(t; \zeta) | N(t, t+\Delta) = k] \right] \\ &\quad \times P[N(t, t+\Delta; \zeta) = k] \end{aligned} \quad (G-15)$$

From Eq. (G-14) and Eq. (G-15) it follows that (the argument ζ is understood when not used)

$$\begin{aligned} \frac{d}{dt} E[P(t)] &= \lim_{\Delta \rightarrow 0} \frac{1}{\Delta} \sum_{k=0}^{\infty} \left[E[P(t+\Delta) | N(t, t+\Delta) = k] - E[P(t)] \right] \\ &\quad \times P[N(t, t+\Delta) = k] \end{aligned} \quad (G-16)$$

Since $P[N(t, t+\Delta) = k]$ is of the order Δ^k , only the $k = 0, 1$ terms of Eq. (G-16) affect the limit.

From Eqs. (G-9), (G-14), and (G-15), [$0(\Delta)$ means order Δ]

$$\begin{aligned} E[P(t+\Delta) | N(t, t+\Delta) = 0] - E[P(t)] &= \left[A(t) E[P(t)] + E[P(t)] A^T(t) \right. \\ &\quad \left. - E[P(t) G^T(t) R_u^{-1}(t) G(t) P(t)] \right. \\ &\quad \left. + Q(t) \right] \Delta + 0(\Delta^2) \end{aligned} \quad (G-17)$$

$$P[N(t, t+\Delta) = 0] = 1 - \lambda(t)\Delta + 0(\Delta^2) \quad (G-18)$$

From Eqs. (G-10), (G-13), and (G-14),

$$E[P(t+\Delta) | N(t, t+\Delta) = 1] - E[P(t)] = -E\left[P(t) H^T(t) [H(t) P(t) H^T(t) + R_v(t)]^{-1} H(t) P(t)\right] + o(\Delta) \quad (G-19)$$

$$P[N(t, t+\Delta) = 1] = \lambda(t) \Delta + o(\Delta^2) \quad (G-20)$$

Substituting Eqs. (G-17) through (G-20) into (G-16) and taking the indicated limit gives

$$\begin{aligned} \frac{d}{dt} E[P(t; \zeta)] &= A(t) E[P(t; \zeta)] + E[P(t; \zeta)] A^T(t) + Q(t) \\ &\quad - E[P(t; \zeta) G^T(t) R_u^{-1}(t) G(t) P(t; \zeta)] \\ &\quad - \lambda(t) E\left[P(t; \zeta) H^T(t) [H(t) P(t; \zeta) H^T(t) + R_v(t)]^{-1} H(t) P(t; \zeta)\right] \end{aligned} \quad (G-21)$$

We note in passing that $E[d/dt P(t; \zeta)]$ is not defined because

$$\frac{\partial^2}{\partial t \partial \Delta} E[P(t+\Delta; \zeta) P(t; \zeta)]$$

is discontinuous at $\Delta = 0$.

Given $E[P(t; \zeta)]$, Eq. (G-21) is not sufficient to compute

$$\frac{d}{dt} E[P(t; \zeta)]$$

as we require knowledge of the expected value of two nonlinear functions of $P(t; \zeta)$. In Appendix G.3 we propose a suboptimal linear filter that will

provide an upper bound for $E[P(t;\zeta)]$. A solvable case of Eq. (G-21) is $G(t) = 0$, $H(t)$ of the same rank as $P(t)$ and $R_v(t) = 0$. Then, letting $P_{L1} = d/dt E[P(t;\zeta)]$, it follows from Eq. (G-21) that

$$\dot{P}_{L1}(t) = A(t) P_{L1}(t) + P_{L1}(t) A^T(t) + Q(t) - \lambda(t) P_{L1}(t) \quad (G-22)$$

For the case $G(t) = 0$, $R_v(t) \neq 0$ $P_{L1}(t)$ is a lower bound for $E[P(t;\zeta)]$; that is, $P_{L1}(t) < E[P(t;\zeta)]$.^{*} A second lower bound for $E[P(t;\zeta)]$ is derived in Appendix D.

$$\begin{aligned} \dot{P}_{L2} = & A(t) P_{L2}(t) + P_{L2}(t) A^T(t) + Q(t) \\ & - P_{L2} G^T(t) R_u^{-1}(t) G(t) P_{L2}(t) \\ & - \lambda(t) P_{L2}(t) H^T(t) R_v^{-1}(t) H(t) P_{L2}(t) \end{aligned} \quad (G-23)$$

3. AN ERROR COVARIANCE EXPECTED VALUE UPPER BOUND USING A SUBOPTIMAL FILTER

From Eqs. (G-11) and (G-12) we see that the Kalman filter gains are dependent on the realization ζ . A class of suboptimal filters is characterized by choosing $K_u(t)$ and $K_v(t_i^-)$ independent of the realization ζ . This means that, for each realization, the gains are functions only of the time t that they are used.

$$K_u(t; \zeta_1) = K_u(t; \zeta_2) = K_u(t) \quad (G-24)$$

and, when $t_i(\zeta_1) = t_j(\zeta_2) = t$,

$$K_v(t_i^-(\zeta_1); \zeta_1) = K_v(t_j^-(\zeta_2); \zeta_2) = K_v(t) \quad (G-25)$$

^{*} $A \gtrless B$ means $\text{trace } [A] \gtrless \text{trace } [B]$.

with $K_v(t)$ a continuous function. Assuming the filter structure of Eqs. (G-7), (G-8), (G-24), and (G-25), then for $t_{i-1}^+ \leq t \leq t_i^-$, the error covariance propagates by

$$\begin{aligned} \dot{P}(t; \zeta) = & [A(t) - K_u(t) G(t)] P(t; \zeta) + P(t; \zeta) [A^T(t) - G^T(t) K_u^T(t)] \\ & + K_u(t) R_u(t) K_u^T(t) + Q(t) \end{aligned} \quad (G-26)$$

At t_i the error covariance reduction is

$$\begin{aligned} P(t_i^+) = & P(t_i^-) + [1 - K_v(t_i) H(t_i)] P(t_i^-) [1 - H^T(t_i) K_v^T(t_i)] \\ & + K_v(t_i) R_v(t_i) K_v^T(t_i) - P(t_i^-) \end{aligned} \quad (G-27)$$

where $P(t_i^-)$ means $P(t_i^-(\zeta); \zeta)$ and $K_v(t_i)$ means $K_v(t_i(\zeta))$.

As in Paragraph 2 of Appendix G, consider the interval $(t, t+\Delta)$. From Eq. (G-26),

$$\begin{aligned} E[P(t+\Delta) | N(t, t+\Delta) = 0] - E[P(t)] = & \left[[A(t) - K_u(t) G(t)] E[P(t)] \right. \\ & + E[P(t)] [A^T(t) - G^T(t) K_u^T(t)] \\ & \left. + K_u(t) R_u(t) K_u^T(t) + Q(t) \right] \Delta + o(\Delta) \end{aligned} \quad (G-28)$$

From Eq. (G-27),

$$\begin{aligned} E[P(t+\Delta) | N(t, t+\Delta) = 1] - E[P(t)] = & [1 - K_v(t) H(t)] E[P(t)] [1 - H^T(t) K_v^T(t)] \\ & + K_v(t) R_v(t) K_v^T(t) - E[P(t)] + o(\Delta) \end{aligned} \quad (G-29)$$

Substituting Eqs. (G-28), (G-29), (G-18), and (G-20) into (G-16) and taking the limit as $\Delta \rightarrow 0$ gives

$$\begin{aligned} \frac{d}{dt} E[P(t;\zeta)] = & [A(t) - K_u(t) G(t)] E[P(t;\zeta)] \\ & + E[P(t;\zeta)] [A^T(t) - G^T(t) K_u^T(t)] + K_u(t) R_u(t) K_u^T(t) + Q(t) \\ & + \lambda(t) \left[-K_v(t) H(t) E[P(t;\zeta)] - E[P(t;\zeta)] H^T(t) K_v^T(t) \right. \\ & \left. + K_v(t) [H(t) E[P(t;\zeta)] H^T(t) + R_v(t)] K_v^T(t) \right] \end{aligned} \quad (G-30)$$

which is sufficient to propagate $E[P(t;\zeta)]$. To utilize realization independent gains, they are chosen to minimize the trace of $d/dt E[P(t;\zeta)]$, which minimizes at every time point the trace of $E[P(t;\zeta)]$. It is straightforward to show that the best choices of realization (ζ) independent gains are

$$K_u(t) = E[P(t;\zeta)] G^T(t) R_u^{-1}(t) \quad (G-31)$$

$$K_v(t) = E[P(t;\zeta)] H^T(t) [H(t) E[P(t;\zeta)] H^T(t) + R_v(t)]^{-1} \quad (G-32)$$

Substitution of these gains into Eq. (VI-53) gives

$$\begin{aligned} \frac{d}{dt} E[P(t;\zeta)] = & A(t) E[P(t;\zeta)] + E[P(t;\zeta)] A^T(t) \\ & + Q(t) - E[P(t;\zeta)] G^T(t) R_u^{-1}(t) G(t) E[P(t;\zeta)] \\ & - \lambda(t) E[P(t;\zeta)] H^T(t) [H(t) E[P(t;\zeta)] H^T(t) + R_v(t)]^{-1} \\ & \times H(t) E[P(t;\zeta)] \end{aligned} \quad (G-33)$$

as the propagation of the suboptimal filter error covariance expected value.

Equation (G-33) is sufficient to propagate $E[P(t;\zeta)]$. Denote the error covariance for the suboptimal filter of this section as $P^s(t;\zeta)$ and let $P^0(t, \zeta)$ denote the optimal filter (Kalman filter) error covariance. It follows that

$$P^s(t;\zeta) \geq P^0(t;\zeta) \quad \text{for every } \zeta \in S \quad (G-34)$$

$$E[P^s(t;\zeta)] \geq E[P^0(t;\zeta)] \quad (G-35)$$

Abbreviating $P_s(t) \triangleq E[P^s(t;\zeta)]$, then

$$\begin{aligned} \dot{P}_s(t) = & A(t) P_s(t) + P_s(t) A^T(t) + Q(t) - P_s(t) G^T(t) R_u^{-1}(t) G(t) P_s(t) \\ & - \lambda(t) P_s(t) H^T(t) [H(t) P_s(t) H^T(t) + R_v(t)]^{-1} H(t) P_s(t) \end{aligned} \quad (G-36)$$

Equation (VI-59) is the same upper bound found in Appendix D by a different method.

Concerning the suboptimal filter, Eqs. (G-31) through (G-33) provide the filter gains $K_u(t)$ and $K_v(t)$. The gain $K_u(t)$ is applied continuously to the continuous $\underline{z}(t)$ information, while the gain $K_v(t)$ is used at the random points in time $t = t_i$ at which $\underline{y}(t)$ is available. If $A(t)$, $Q(t)$, $G(t)$, $H(t)$, $R_u(t)$, $R_v(t)$, and $\lambda(t)$ are all deterministic, then the gains $K_u(t)$ and $K_v(t)$ can be precomputed.

Equation (G-36) is a nonstandard matrix differential equation that has yet to be studied for global and local behavior. However, for now, consider the linear time-invariant, i.e., ($A(t)$ etc ... all time-invariant) case and examine the behavior of Eq. (G-39) about the stationary point P_s where

$$A P_s + P_s A^T + Q - P_s G^T R_u^{-1} G P_s - \lambda P_s H^T [H P_s H^T + R_v]^{-1} H P_s = 0 \quad (G-37)$$

The requirement needed in order for the stationary point P_s to be stable is that the linear matrix differential equation in δP , given by

$$\begin{aligned} \dot{\delta P} = & \left[A - P_s G^T R_u^{-1} G - \lambda P_s H^T [H P_s H^T + R_v]^{-1} H \right] \delta P \\ & + \delta P \left[A^T - G^T R_u^{-1} G P_s - \lambda H^T [H P_s H^T + R_v]^{-1} H P_s \right] \\ & + \lambda P_s H^T [H P_u H^T + R_v]^{-1} H \delta P H^T [H P_s H^T + R_v]^{-1} H P_s \quad (G-38) \end{aligned}$$

be asymptotically stable.

4. FIRST-ORDER EXAMPLE

Consider the plant and measurement models

$$\dot{x} = w \quad ; \quad E[w(t)w(t')] = q\delta(t - t')$$

$$y = x + v; \quad E[v(t)v(t')] = r, \quad t = t'$$

$$= 0, \quad t \neq t'$$

The measurements $y(t)$ are available only at random points in time determined by a stationary Poisson counting process of intensity λ . From Eq. (G-21),

$$\frac{d}{dt} E[p(t;\zeta)] = q - \lambda E\left[\frac{p^2(t;\zeta)}{p(t;\zeta) + r}\right]$$

where $p(t;\zeta)$ is the scalar error covariance. Let p denote the steady-state error covariance expected value, then $p = \lim_{t \rightarrow \infty} E[p(t;\zeta)]$. The two steady-state lower bounds on p are from (G-22) and (G-23) [abbreviate P_{L1} by P_1]

$$q - \lambda p_1 = 0; p_1 = q/\lambda$$

$$q = \lambda \frac{p_2^2}{r} = 0; p_2 = \left(\frac{qr}{\lambda}\right)^{1/2}$$

The steady-state upper bound on p is from (G-36)

$$0 = q - \lambda \frac{p_s^2}{p_s + r}; p_s = \frac{1}{2} \frac{q}{\lambda} + \frac{1}{2} \left[\left(\frac{q}{\lambda}\right)^2 + 4\left(\frac{qr}{\lambda}\right) \right]^{1/2}$$

A test, which demonstrates that p_s is a good approximation to p , is to compute $(p_1/p_s)^{1/2}$ when $p_1 \geq p_2$ and $(p_2/p_s)^{1/2}$ when $p_2 \geq p_1$. If in either case the ratio is near 1, then p_s is a good approximation to p . The bounds on $(p/p_s)^{1/2}$ are

$$\max \left[\left(\frac{p_2}{p_s}\right)^{1/2}, \left(\frac{p_1}{p_s}\right)^{1/2} \right] < \left(\frac{p}{p_s}\right)^{1/2} < 1$$

If neither of the ratios is near 1, then we cannot say whether or not p_s is a good approximation to p without further analysis.

To parameterize the numerical work, let

$$\alpha = \left(\frac{q}{\lambda r}\right)^{1/2}$$

Then

$$\frac{p_s}{p_1} = \frac{1}{2} + \frac{1}{2} \left(1 + \frac{4}{\alpha^2}\right)^{1/2}$$

$$\frac{p_s}{p_2} = \frac{\alpha}{2} \left[1 + \left(1 + \frac{4}{\alpha^2}\right)^{1/2}\right]$$

A listing of the ratios versus α is given in Table G-1.

Table G-1. Error Covariance Expected Value Bounds for the First-Order Filter

$\alpha = \left(\frac{q}{\lambda r}\right)^{1/2}$	$\left(\frac{p_1}{p_s}\right)^{1/2}$	$\left(\frac{p_2}{p_s}\right)^{1/2}$
0	0	1 ^a
0.2	0.425	0.96 ^a
0.5	0.625	0.88 ^a
1	0.785 ^a	0.785 ^a
2	0.91 ^a	0.645
4	0.97 ^a	0.485
∞	1 ^a	0

^aNext to $\max (p_1/p_s)^{1/2}, (p_2/p_s)^{1/2}$

For this problem, p_s is a reasonable approximation to p over the whole parameter range and is especially good for small and large α . Also, since p_s is the error covariance expected value for the suboptimal filter, implementation of the suboptimal filter is a practical alternative in this example.

A point of interest is how the average error covariance of a uniform sampled system compares with the error covariance expected value of the randomly sampled system. Let the uniformly sampled system have a sampling rate of λ samples/sec and let p_d denote its average error covariance (including the time between samples). It can be shown that

$$p_d = p_s - \frac{1}{2} \frac{q}{\lambda}$$

It follows that

$$p_d = \frac{1}{2} \left(\left(\frac{q}{\lambda} \right)^2 + 4 \left(\frac{qr}{\lambda} \right) \right)^{1/2}$$

Forming the ratios p_d/p_1 and p_d/p_2 , we have

$$\frac{p_d}{p_1} = \frac{1}{2} \left(1 + \frac{4}{\alpha^2} \right)^{1/2}$$

$$\frac{p_d}{p_2} = \frac{\alpha}{2} \left(1 + \frac{4}{\alpha^2} \right)^{1/2}$$

For $0 < \alpha < 1$, p_2 is the greater (better) of the two lower bounds, and over this range $p_2 < p_d < p_s$. For $\alpha > 1$, p_1 is the greater of the two lower bounds and for $1 < \alpha < 1.15$, $p_1 < p_d < p_s$. Since p is for both parameter ranges just discussed (also nested between the lower bound and p_s), it follows that for $0 < \alpha < 1.15$ the uniformly sampled error covariance average value is a fair representation of the randomly sampled error covariance expected value p .

For $\alpha > 1.15$, $p_d < p_1$ and the uniformly sampled filter average error covariance drops below our best lower bound for p . Note that

$$\lim_{\alpha \rightarrow \infty} \left(\frac{p_d}{p} \right)^{1/2} = \lim_{\alpha \rightarrow \infty} \left(\frac{p_d}{p_1} \right)^{1/2} = 0.707$$

$$\lim_{\alpha \rightarrow 0} \left(\frac{p_d}{p} \right)^{1/2} = \lim_{\alpha \rightarrow 0} \left(\frac{p_d}{p_2} \right)^{1/2} = 1$$

5. A SECOND-ORDER EXAMPLE

Given the plant and measurement model described in Paragraph G. 1 with

$$A = \begin{bmatrix} 0 & 1 \\ 0 & 0 \end{bmatrix}, \quad Q = \begin{bmatrix} 0 & 0 \\ 0 & q \end{bmatrix}, \quad G = 0$$

$$R_u = 0, \quad H = [1 \quad 0], \quad R_v = r, \quad \lambda(t) = \lambda$$

The plant can be thought of as a vehicle with attitude and rate as state variables. The vehicle is subject to white angular acceleration noise. Only attitude measurements are available at random discrete points in time. The random points in time are determined by a stationary Poisson counting process.

The error covariance of the Kalman filter $P^0(t; \zeta)$ and the suboptimal filter $P^s(t; \zeta)$ are 2×2 matrices.

Let

$$p = \lim_{t \rightarrow \infty} E[P_{11}^0(t; \zeta)]$$

$$p_s = \lim_{t \rightarrow \infty} E[P_{11}^s(t; \zeta)]$$

$$m = \lim_{t \rightarrow \infty} E[P_{22}^0(t; \zeta)]$$

$$m_s = \lim_{t \rightarrow \infty} E[P_{22}^s(t; \zeta)]$$

Thus p is the steady-state expected value of the attitude estimate error variance of the Kalman filter and p_s is the same quantity for the suboptimal filter.

Similarly, m and m_s are steady-state velocity estimate error variances for the Kalman and suboptimal filters respectively. Let p_1 and p_2 be our two lower bounds for p and let m_1 and m_2 be the two lower bounds for m . Then, p_1 , p_2 , m_1 , and m_2 are found from Eqs. (G-22) and (G-23) while p_s and m_s are found from Eq. (G-36).

The bound on position estimate error variance expected value is

$$\max \left[\left(\frac{p_1}{p_s} \right)^{1/2}, \left(\frac{p_2}{p_s} \right)^{1/2} \right] < \left(\frac{p}{p_s} \right)^{1/2} < 1$$

and the velocity estimate error variance expected value is

$$\max \left[\left(\frac{m_1}{m_s} \right)^{1/2}, \left(\frac{m_2}{m_s} \right)^{1/2} \right] < \frac{m}{m_s} < 1$$

It turns out that p_1/p_s , p_2/p_s , m_1/m_s , and m_2/m_s are all fixed by the parameter

$$\alpha = \frac{1}{\lambda} \left(\frac{q\lambda}{r} \right)^{1/4}$$

The relevant ratios as a function of α are listed in Table G-2. Note that, for both small and large α , p_s and m_s are excellent approximations to p and m .

Table G-2. Error Covariance Expected Value Bounds
for the Second-Order Filter

α	$(p_1/p_s)^{1/2}$ Attitude	$(p_2/p_s)^{1/2}$ Attitude	$(m_1/m_s)^{1/2}$ Rate	$(m_2/m_s)^{1/2}$ Rate
0	0	1.0 ^a	0	1.0 ^a
0.0316	0.004	0.983 ^a	0.148	0.995 ^a
0.1	0.035	0.946 ^a	0.261	0.981 ^a
0.316	0.175	0.828 ^a	0.445	0.938 ^a
1.0	0.565 ^a	0.475	0.656	0.780 ^a
2.0	0.692 ^a	0.205	0.702 ^a	0.590
4.0	0.707 ^a	0.074	0.707 ^a	0.420
8.0	0.707 ^a	0.026	0.707 ^a	0.297
∞	0.707 ^a	0	0.707 ^a	0

^aOperable ratio with the greatest lower bound.

6. A THIRD LOWER BOUND

There is a third lower bound¹ which is better (higher) than both P_{L1} and P_{L2} but only applies for the case of no continuous measurements ($G(t) = 0$).

$$\begin{aligned} \dot{P}_{L3}(t) = & A(t) P_{L3}(t) + P_{L3}(t) A^T(t) + Q(t) - \lambda(t) P_{L3}(t) \\ & + \lambda(t) [P_{L2}^{-1}(t) + H^T(t) R_V^{-1}(t) H(t)]^{-1} \end{aligned} \quad (G-39)$$

Note that $P_{L2}(t)$ must first be computed.

¹S. M. Melzer, Kalman Filter Performance with Measurements at Random Points in Time, ATM-75(7433-07)-1, The Aerospace Corporation, El Segundo, California, dated 29 January 1975 (not available for external distribution).

APPENDIX H. EQUATIONS FOR THE SINGLE INTEGRATOR SYSTEM

The single integrator may be thought of as a suboptimal estimator that directly integrates continuous rate measurements between discrete attitude updates. Whenever an attitude update occurs, the measurement is processed optimally to obtain an improved attitude estimate. The rate integration between attitude updates is usually accomplished by rate integrating gyros. The SPARS filter is representative of the single integrator type. This filter is suboptimal in the sense that only attitude measurements are optimally processed in obtaining the attitude estimate. Although the rate is measured, it is directly integrated without filtering to propagate the estimate between attitude measurements. In contrast, the double integrator can be considered a fully optimal filter in the sense that both attitude and rate measurements are processed optimally to obtain estimates of both states.

To illustrate the derivation of the single integrator filter, consider a single axis example. The output of a single-degree-of-freedom rate integrating gyro may be considered as the continuous attitude estimate $\hat{\theta}$ satisfying the equation

$$\dot{\hat{\theta}} = \omega + n_{\omega} \quad (\text{H-1})$$

where ω is the angular velocity measured by the gyro and n_{ω} is additive white noise with strength r_{ω} defined by

$$\mathcal{E}\{n_{\omega}(t) n_{\omega}(\tau)\} = r_{\omega} \delta(t - \tau) \quad (\text{H-2})$$

Equation (H-1) is a model of the rate integrating gyro, which assumes that the only corrupting influence on the output of the gyro is an additive white rate noise that results in a random walk-type attitude estimation error. Other error sources such as bias and scale factor are assumed to be precalibrated.

Attitude measurements will be assumed to occur on a discrete time basis modeled by

$$z_i = \theta_i + n_{\theta_i} \quad (\text{H-3})$$

where θ_i is the true attitude at time t_i and n_{θ_i} is white noise of strength r'_θ defined by

$$\mathcal{E}\{n_{\theta_i} n_{\theta_j}\} = r'_\theta \delta_{ij} \quad (\text{H-4})$$

The symbol δ_{ij} is the discrete delta function defined by

$$\delta_{ij} = \begin{cases} 1, & i = j \\ 0, & i \neq j \end{cases}$$

The estimation error for the single integrator system is

$$\epsilon = \hat{\theta} - \theta \quad (\text{H-5})$$

where $\hat{\theta}$ satisfies Eq. (H-1) and θ , which is the true attitude, satisfies

$$\dot{\theta} = \omega \quad (\text{H-6})$$

The behavior of the estimation error (Eq. [H-5]) may be determined analytically by deriving the expressions for the system covariance in two regions, namely, between discrete updates and at a discrete attitude update. Let t_0 be the time of the last update and t_1 be the time just prior to the next update. Then the covariance at the last update is defined by

$$p_{\theta_0} = \mathcal{E}\{\epsilon_0^2\} = \{(\hat{\theta}_0 - \theta_0)^2\} \quad (\text{H-7})$$

The covariance just prior to the next update is given by

$$m_{\theta_1} = \mathcal{E}\{(\hat{\theta}_1 - \theta_1)^2\} \quad (\text{H-8})$$

Integration of Eqs. (H-1) and (H-2) and substitution into (H-8) yields

$$m_{\theta_1} = \mathcal{E}\{(\hat{\theta}_0 - \theta_0)^2\} + \int_{t_0}^{t_1} \int_{t_0}^{t_1} \mathcal{E}\{n_w(\tau) n_w(\alpha)\} d\tau d\alpha \quad (\text{H-9})$$

where it has been assumed that n_w over the interval $[t_0, t_1]$ is uncorrelated with $\hat{\theta}_0$ and θ_0 . Substituting Eqs. (H-2) and (H-7) into (H-9) and performing the double integral results in

$$m_{\theta_1} = p_{\theta_0} + r_w(t_1 - t_0) \quad (\text{H-10})$$

Thus, the single integrator filter covariance grows linearly with time between discrete attitude updates.

At the time of the next discrete update (t_1), the covariance obeys Eq. (A-34). For this single axis example the result is

$$p_{\theta_1} = m_{\theta_1} - \frac{m_{\theta_1}^2}{m_{\theta_1} + r_{\theta}'} = \frac{m_{\theta_1} r_{\theta}'}{m_{\theta_1} + r_{\theta}'} \quad (\text{H-11})$$

where

$$H = 1, R = r_{\theta}'$$

Assuming a constant update interval

$$T = (t_1 - t_0)$$

and solving Eqs. (H-10) and (H-11) simultaneously yields

$$p_{\theta} = \frac{r_{\omega} T}{2} \left(-1 + \sqrt{1 + \frac{4r_{\theta}}{r_{\omega} T}} \right) \quad (H-12)$$

$$m_{\theta} = \frac{r_{\omega} T}{2} \left(1 + \sqrt{1 + \frac{4r_{\theta}}{r_{\omega} T}} \right) \quad (H-13)$$

The time subscript has been dropped in these equations since, for a constant update interval, the filter reaches steady state when

$$p_{\theta_i} = p_{\theta_{i+1}} = p_{\theta}$$

and

$$m_{\theta_i} = m_{\theta_{i+1}} = m_{\theta}$$

APPENDIX I. METHODS FOR SENSOR OPTIMIZATION

1. MATHEMATICAL FORMULATION OF SENSOR OPTIMIZATION

a. Notation

In this subsection, the problem of determining the sensor orientations to minimize the worst case measurement errors is mathematically formulated, and the optimal configurations and their performances are given. A simple derivation of the optimal sensor configuration is also presented.

To convert the problem of minimizing the worst case measurement errors into mathematical terms, define a covariance matrix

$$P = E(\underline{e} \underline{e}^T)$$

where the n -dimensional error vector

$$\underline{e} = \underline{x} - \hat{\underline{x}}$$

is the difference between the true state variables \underline{x} and their estimates $\hat{\underline{x}}$ and $E(y)$ denotes the expectation of the random variable y .

Let P_b and P_a be the values of the covariance matrix P just before and just after a measurement. They are related by

$$P_a^{-1} = P_b^{-1} + M$$

where

$$M = H^T R^{-1} H$$

is the "information" matrix of the measurement. The $(m \times n)$ matrix H linearly relates the m sensor measurements \underline{z} to the n state variables \underline{x} by

$$\underline{z} = H \underline{x} + \underline{n}$$

where the sensor measurement errors \underline{n} are assumed to be a white noise sequence. For continuous measurements, they satisfy

$$E(\underline{n}(t) \underline{n}(\tau)^T) = R \delta(t-\tau)$$

For a discrete measurement process,

$$E(\underline{n}_i \underline{n}_j^T) = R \delta_{ij}$$

b. Optimization Criterion

Mathematically stated, the problem is to choose the sensor directions (represented by the H matrix) to maximize the measurement information matrix M for prescribed sensor accuracies (denoted by matrix R). Since the sequential change in the inverse of the covariance matrix and the information matrix M is related by

$$P_a^{-1} = P_b^{-1} + M \quad (I-1)$$

as the elements of the information matrix M increase, the covariance matrix after the measurement P_a decreases for a given value of the covariance matrix before the measurement P_b . Therefore, maximizing (in some sense) the measurement information matrix M minimizes (in the same sense) the covariance matrix after the measurement P_a for a given initial condition before the measurement P_b .

In order to determine a reasonable criterion for maximizing the information matrix M, first diagonalize M. Then the diagonal elements of the diagonalized M matrix, i.e., the eigenvalues of M, represent the measurement information provided on each axis. Therefore, a reasonable criterion for maximizing M is to maximize the smallest eigenvalue of M. This is equivalent to minimizing the measurement errors in the worst case direction. When it is possible to make all eigenvalues of M nonzero, this policy also maximizes the determinant of M, which minimizes the volume of the measurement error ellipsoid.

c. Relationship between Sensor Orientations and Information Matrix

This criterion of maximizing the smallest (nonzero) eigenvalue of M will now be used to calculate the optimal sensor directions. In order to relate the information matrix to the sensor orientations, rewrite the equation for M , i.e.,

$$M = H^T R^{-1} H \quad (I-2)$$

in the form

$$M = H^T R^{-1} H = \sum_{i=1}^m \frac{1}{r_i} \underline{h}_i \underline{h}_i^T \quad (I-3)$$

where matrix R is assumed to be diagonal with elements r_i . (If it is not diagonal, it may be diagonalized.) Here the rows of $(m \times n)$ matrix H are formed by the m n -dimensional vectors \underline{h}_i .

$$H = \begin{pmatrix} \underline{h}_1^T \\ \underline{h}_2^T \\ \vdots \\ \underline{h}_m^T \end{pmatrix}$$

Physically, the \underline{h}_i vectors represent the sensor axis directions. For example, if the sensor is a rate gyro, the \underline{h}_i vector would correspond to the unit vector along the input axis. In a slit-type star sensor, \underline{h}_i is a unit vector perpendicular to the slit direction, lying in the focal plane.

In sensors that measure in more than one direction simultaneously, such as star trackers, all of the \underline{h}_i vectors are not independent. For example, let \underline{h}_1 and \underline{h}_2 be the sensor directions associated with a star tracker. Then, \underline{h}_1

and \underline{h}_2 are perpendicular and lie in a plane normal to the star sensor LOS vector \underline{u} . Let

$$M_1 = \frac{1}{r_1} \underline{h}_1 \underline{h}_1^T$$

and

$$M_2 = \frac{1}{r_2} \underline{h}_2 \underline{h}_2^T$$

be the measurement information provided from sensor axes \underline{h}_1 and \underline{h}_2 respectively. Then, from Eq. (I-3) the total information provided by the star tracker is

$$M = M_1 + M_2 = \frac{1}{r} (\underline{h}_1 \underline{h}_1^T + \underline{h}_2 \underline{h}_2^T) \quad (I-4)$$

where the axes of the sensor have been assumed to be of equal quality so $r_1 = r_2 = r$. Multiplying Eq. (I-4) by orthogonal unit vectors \underline{h}_1 , \underline{h}_2 , and \underline{u} gives

$$M \underline{h}_1 = \frac{1}{r} \underline{h}_1 = \lambda_1 \underline{h}_1 \quad M \underline{h}_2 = \frac{1}{r} \underline{h}_2 = \lambda_2 \underline{h}_2 \quad M \underline{u} = \underline{0} = \lambda_3 \underline{u}$$

Therefore, \underline{h}_1 , \underline{h}_2 , and \underline{u} are eigenvectors of M with eigenvalues $\lambda_1 = \lambda_2 = \frac{1}{r}$ and $\lambda_3 = 0$. Since matrix

$$M = \frac{1}{r} (I - \underline{u} \underline{u}^T) \quad (I-5)$$

(where I is the identity matrix) has the same eigenvectors and eigenvalues as matrix M in Eq. (I-4), the two matrices are equivalent. Equation (I-5) is the expression for the information matrix of a two-dimensional sensor whose LOS is along \underline{u} . These vectors \underline{u} are to be chosen to maximize the smallest eigenvalue of the total information matrix, which is comprised of the sum of all individual sensor information matrices.

The first term in Eq. (I-5) is independent of the sensor orientations and, hence, does not enter into the optimization procedure. The second term in Eq. (I-5) is of the same form as the expression for M in Eq. (I-3). Therefore, the following analysis will consider only the expression for M given by Eq. (I-3).

d. Optimizing the Information Matrix

The sensor axis directions \underline{h}_i are now chosen to maximize the smallest eigenvalue of the information matrix M. From Eq. (I-3), vectors \underline{h}_i and matrix M are related by

$$M = \sum_{i=1} \frac{1}{r_i} \underline{h}_i \underline{h}_i^T$$

Since M is a symmetric matrix, it can be diagonalized by a similarity transformation.

$$T_1 M T^T = \Lambda = \begin{pmatrix} \lambda_1 & 0 & 0 & \dots \\ 0 & \lambda_2 & 0 & \\ 0 & 0 & \lambda_3 & \\ \vdots & & & \ddots \\ \vdots & & & & \lambda_m \end{pmatrix} = \frac{1}{r_i} (T \underline{h}_i) (T \underline{h}_i)^T \quad (I-6)$$

where λ_i is the eigenvalue of M and $T^T = T^{-1}$ is an orthonormal transformation matrix. Now, defining new unit vectors

$$\underline{v}_i = T \underline{h}_i \quad (I-7)$$

and substituting them into Eq. (I-6) gives

$$\Lambda = \begin{pmatrix} \lambda_1 & 0 & \dots & 0 \\ 0 & \lambda_2 & & \\ \vdots & & \ddots & \\ 0 & & & \lambda_m \end{pmatrix} = \sum_{i=1}^m \frac{1}{r_i} \underline{v}_i \underline{v}_i^T \quad (\text{I-8})$$

Taking the trace (the sum of the diagonal elements of a matrix) of both sides of Eq. (I-8) gives

$$\sum_{i=1}^m \lambda_i = \sum_{i=1}^m \frac{1}{r_i} \quad (\text{I-9})$$

where the trace of a sum of matrices equals the sum of the traces and, since the \underline{v}_i are unit vectors, the trace of $\underline{v}_i \underline{v}_i^T$ is unity. Equation (I-9) indicates that the sum of the eigenvalues of the information matrix M must always be the same regardless of the orientations of the sensor vectors \underline{h}_i .

The volume of the measurement error ellipsoid is inversely proportional to the determinant of the information matrix $\det(M)$, which equals the product of its eigenvalues

$$\det(M) = \lambda_1 \cdot \lambda_2 \cdot \dots \cdot \lambda_n \quad (\text{I-10})$$

Choosing the sensor directions to minimize the volume of the measurement error ellipsoid or, equivalently, maximize the determinant of M , subject to the constraint that the sum of the eigenvalues is fixed, results in all the eigenvalues of M being equal.

$$\lambda_i = \lambda = \frac{1}{n} \sum_{i=1}^m \frac{1}{r_i} \quad (\text{I-11})$$

Similarly, maximizing the smallest eigenvalue of M would give the same result.

This relationship is true providing the sensor axis \underline{h}_i can be chosen so that none of the eigenvalues is zero. This is always possible when there are at least as many sensors as there are directions to measure ($m \geq n$), since each sensor can be oriented along a different axis. However, when there are fewer sensors than directions to measure ($m < n$), there must be at least $(n - m)$ zero eigenvalues of M because there are insufficient sensors to measure all axes.

Even if there are more sensors than axes to measure ($m \geq n$), it still may not be possible to make all eigenvalues of M equal. To derive this additional condition, which the sensor accuracies $1/\sqrt{r_j}$ must satisfy in order for the eigenvalues λ_i of M to be equal, assume the eigenvalues are equal and calculate $\underline{h}_k^T M \underline{h}_k$.

$$\underline{h}_k^T M \underline{h}_k = \lambda \underline{h}_k^T \underline{h}_k = \sum_{i=1}^m \frac{1}{r_i} (\underline{h}_k^T \underline{h}_i)^2$$

Noting that \underline{h}_k is a unit vector and expanding the right-hand side of this equation gives

$$\lambda = \frac{1}{r_k} + \sum_{\substack{i=1 \\ i \neq k}}^m \frac{1}{r_i} (\underline{h}_k^T \underline{h}_i)^2 \geq \frac{1}{r_k} \quad (\text{I-12})$$

The equality in Eq. (I-12) occurs when all the remaining instrument axes \underline{h}_i ($i \neq k$) are orthogonal to \underline{h}_k . Using Eq. (I-11) as a substitute for λ in Eq. (I-12) gives

$$\frac{1}{r_k} \leq \frac{1}{n} \sum_{i=1}^m \frac{1}{r_i} \quad (\text{I-13})$$

This condition must be satisfied in addition to there being more sensors than axes ($m \geq n$) before all the eigenvalues of the information matrix

can be made equal. Actually, the inequality in Eq. (I-13) can only be satisfied if $m \geq n$, and when $m = n$ it can only be satisfied when all the r_i are equal. Physically, when this inequality is satisfied, any one instrument is not superior to all the remaining instruments combined. This situation for $n = 2$ and $m = 3$ can be illustrated by the case where two colinear sensors along the axes \underline{j}_2 and \underline{j}_3 are perpendicular to a third sensor along \underline{j}_1 . Let us assume that the sensors along \underline{j}_2 and \underline{j}_3 have the same accuracy so $1/r_2 = 1/r_3 = 1/r$ while the sensor along \underline{j}_1 is more accurate, so $1/r_1 = b/r$ where b is greater than unity. If b equals 2, the inequality in Eq. (I-13) is just reached, and the sensors along \underline{j}_2 and \underline{j}_3 combined have the same accuracy as the sensor along \underline{j}_1 , so the eigenvalues of M are equal. However, if parameter b exceeds 2, then the combined accuracy of the sensors along \underline{j}_2 and \underline{j}_3 cannot achieve the accuracy of the sensor along \underline{j}_1 so the eigenvalues of M , which represent the measurement accuracies in the different directions, cannot be equal. These arguments show that the inequality in Eq. (I-13) is a necessary condition for all the eigenvalues of M (and, hence, the measurement accuracies in each direction) to be equal. It may also be shown that this condition is sufficient. The numerical techniques for calculating the sensor axis orientations are presented in Paragraph I. 2.

When the inequality in Eq. (I-13) is not satisfied and $m < n$, then all the sensor axes \underline{h}_i are orthogonal.

When the inequality in Eq. (I-13) is not satisfied and $m \geq n$, then the sensors are ordered so that

$$J_1 \geq J_2 \geq J_3 \geq \dots \geq J_m \quad (\text{I-14})$$

where

$$J_i \equiv 1/r_i$$

This ordering implies that the most accurate sensor is along \underline{h}_1 , the second best along \underline{h}_2 , etc. Then, find the smallest integer k so that

$$J_k \leq \frac{1}{n-k+1} \sum_{i=k}^m J_i \quad (I-15)$$

The first $(k-1)$ instruments (the superior instruments) with axes along $\underline{h}_1, \underline{h}_2 \dots \underline{h}_{k-1}$ are mounted orthogonally to each other and all the remaining sensors. The $(k-1)$ eigenvalues of M associated with these instruments, i.e., $\lambda_n, \lambda_{n-1} \dots \lambda_{(n-k+2)}$, equal $J_1, J_2 \dots J_{(k-1)}$ respectively. The remaining $n-k+1$ instruments are mounted orthogonally to the $(k-1)$ superior sensors so that the remaining $n-k+1$ eigenvalues of M are all equal and satisfy

$$\lambda_j = \lambda = \frac{1}{n-k+1} \sum_{i=k}^m J_i \quad ; \quad j = 1, 2 \dots (n-k+1) \quad (I-16)$$

When $k = 1$, this case reduces to the case where all eigenvalues of M are equal.

e. Properties of the Optimal Information Matrix

In this subsection the previously described characteristics of the optimal information matrix are summarized and additional properties presented. First, define vectors $\underline{j}_1, \underline{j}_2 \dots \underline{j}_m$ so that

$$\underline{j}_i = \frac{1}{\sqrt{r_i}} \underline{h}_i \quad ; \quad i = 1, 2 \dots m$$

where \underline{h}_i represents unit vectors, so

$$|\underline{j}_i|^2 = \frac{1}{r_i} = J_i \quad ; \quad i = 1, 2 \dots m$$

Order the vectors \underline{j}_i so that

$$J_1 \geq J_2 \geq J_3 \geq \dots \geq J_m$$

Also order the n eigenvalues of M , i.e., λ_i , so that

$$\lambda_1 \geq \lambda_2 \geq \lambda_3 \geq \dots \geq \lambda_n$$

Substituting the \underline{j}_i vectors for the \underline{h}_i vectors in Eq. (I-3) for M gives

$$M = \sum_{i=1}^m \underline{j}_i \underline{j}_i^T \quad (I-17)$$

The optimal M matrix has the following properties:

- a. The smallest eigenvalue of the optimal M matrix, namely, λ_1 , equals or is larger than the smallest eigenvalue of any other matrix M in the form of Eq. (I-17).
- b. If the k smallest eigenvalues of a nonoptimal matrix satisfying Eq. (I-17) equal the k smallest eigenvalues of the optimal M matrix, then the remaining $(n-k)$ eigenvalues of M must equal or be greater than the corresponding $(n-k)$ eigenvalues of the nonoptimal M matrix. Mathematically stated, if the eigenvalues of the nonoptimal matrix μ_i satisfying Eq. (I-17) are ordered so that

$$\mu_1 \leq \mu_2 \leq \mu_3 \leq \dots \leq \mu_m$$

and the eigenvalues of the optimal M matrix λ_i are similarly ordered, then

$$\lambda_1 \leq \lambda_2 \leq \lambda_3 \leq \dots \leq \lambda_n$$

Then,

a. $\lambda_1 \geq \mu_1$

and

b. If the first k eigenvalues are equal,

$$\lambda_i = \mu_i \quad ; \quad i = 1, 2 \dots k$$

so

$$\lambda_i \geq \mu_i \quad ; \quad i = k+1, \dots n$$

Physically, this implies that, if an information matrix is as good as the optimal information matrix on the k^{th} worst axes, it must be poorer than the optimal matrix on one or more of the remaining axes.

The optimal M matrix has the property that all the vectors $\underline{j}_1, \underline{j}_2 \dots \underline{j}_m$ are eigenvectors of M and the eigenvalue corresponding to \underline{j}_i is greater than or equal to J_i . Note that if $m > n$, there will be more eigenvectors of M than eigenvalues (M always has n eigenvalues) so several \underline{j}_i vectors will correspond to the same eigenvalue. A similar situation occurs in the case of the identity matrix where any vector is an eigenvector with a unity eigenvalue.

If $m \leq n$, then the vectors \underline{j}_i of the optimal M matrix are all orthogonal to each other and the eigenvalue of M corresponding to \underline{j}_i equals J_i .

The optimal M matrix is a scalar multiple of the identity matrix if, and only if,

$$J_1 \leq \frac{1}{n} \sum_{i=1}^m J_i$$

In this case, the optimal M is unique, except for a rotation or relabeling of axes, and is given by

$$M = \left(\frac{1}{n} \sum_{i=1}^m J_i \right) I$$

2. NUMERICAL METHODS FOR CALCULATING THE OPTIMAL SENSOR ORIENTATIONS

In this subsection, numerical methods for calculating the optimal sensor orientations are presented along with simple numerical examples. These numerical methods and their proofs have been provided by Professor J. E. Potter of Massachusetts Institute of Technology. These numerical techniques have been generalized to calculate the sensor configurations that will produce assigned accuracies along each axis. These generalized techniques and examples are also illustrated.

a. Sensor Orientation Construction: Case I

First, consider the case where

$$J_1 \leq \frac{1}{n} \sum_{k=1}^m J_k \quad (I-18)$$

where the J_i have been ordered so that $J_1 \geq J_2 \geq J_3 \geq \dots \geq J_m$. In this case, the optimal information matrix M is given by

$$M = \lambda I \quad (I-19)$$

where I is the identity matrix and scalar λ satisfies

$$\lambda = \frac{1}{n} \sum_{i=1}^m J_i \quad (I-20)$$

To start the numerical procedure, let

$$\underline{j}_i = \frac{1}{r_i} \underline{h}_i = \sqrt{\lambda_i} \underline{e}_i, \quad i = 1, 2, \dots, n \quad (I-21)$$

and

$$\underline{j}_i = \underline{0} \quad i = n+1, \dots, m \quad (I-22)$$

where

$$\underline{e}_i = \begin{bmatrix} \delta_{1i} \\ \delta_{2i} \\ \vdots \\ \delta_{ni} \end{bmatrix} \quad (I-23)$$

and δ_{ij} is the delta function ($\delta_{ij} = 1$ for $i = j$ and zero otherwise). Set the values of λ_i in Eq. (I-21) equal to the desired eigenvalues of M . For the optimal M matrix given by Eq. (I-19), all the λ_i are equal and are given by Eq. (I-20).

Initialize the indices l and u by setting

$$\begin{aligned} l &= 1 \\ u &= m \end{aligned} \quad (I-24)$$

The procedure increases ℓ and decreases u until $u = \ell$, which terminates the procedure.

The iteration procedure consists of the following steps:

- a. If $|\underline{j}_\ell|^2 = J_\ell$, set $\ell = \ell+1$ and exit from the step.
- b. If

$$|\underline{j}_\ell|^2 - J_\ell \geq J_u - |\underline{j}_u|^2 \quad (\text{I-25})$$

denote this as Case a and set

$$\mu = \frac{J_u - |\underline{j}_u|^2}{|\underline{j}_\ell|^2 - |\underline{j}_u|^2} \quad (\text{I-26})$$

Otherwise, denote it as Case b and set

$$\mu = \frac{|\underline{j}_\ell|^2 - J_\ell}{|\underline{j}_\ell|^2 - |\underline{j}_u|^2} \quad (\text{I-27})$$

Now define

$$\gamma = \frac{\underline{j}_\ell \cdot \underline{j}_u}{|\underline{j}_\ell|^2 - |\underline{j}_u|^2} \quad (\text{I-28})$$

and calculate

$$x = \frac{-2\gamma - (2\mu-1)}{1 + \sqrt{1 + 4\gamma^2 - (2\mu-1)^2}} \quad (\text{I-29})$$

$$C = \frac{1 + x}{\sqrt{2(1+x^2)}} \quad (\text{I-30})$$

$$S = \frac{1 - x}{\sqrt{2(1+x^2)}} \quad (\text{I-31})$$

Note that C and S are analogous to cosine and sine functions in that

$$C^2 + S^2 = 1 \quad (\text{I-32})$$

When $\gamma = 0$, Eqs. (I-30) and (I-31) reduce to

$$C(\gamma=0) = \sqrt{1-\mu} \quad (\text{I-33})$$

$$S(\gamma=0) = \sqrt{\mu} \quad (\text{I-34})$$

Now, replace \underline{j}_ℓ and \underline{j}_u by new values:

$$(\underline{j}_\ell)_{\text{new}} = C \underline{j}_\ell + S \underline{j}_u \quad (\text{I-35})$$

$$(\underline{j}_u)_{\text{new}} = -S \underline{j}_\ell + C \underline{j}_u \quad (\text{I-36})$$

Note that the sum of the squares of the magnitudes of the new \underline{j}_ℓ and \underline{j}_u is equal to the sum of the squares of the magnitudes of the old \underline{j}_ℓ and \underline{j}_u .

$$|(\underline{j}_\ell)_{\text{new}}|^2 + |(\underline{j}_u)_{\text{new}}|^2 = |\underline{j}_\ell|^2 + |\underline{j}_u|^2 = J_\ell + J_u \quad (\text{I-37})$$

Finally, in Case a, set

$$u = u - 1 \quad (I-38)$$

and exit from the step.

In Case b, set

$$l = l + 1 \quad (I-39)$$

and exit from the step.

b. Construction Example: Case I

Consider the case where $n = 2$ and $m = 3$ and the J_i satisfy the inequality in Eq. (I-15):

$$J_1 = 4; J_2 = 3; J_3 = 2$$

Then, in the optimal M matrix, all the eigenvalues are equal and are given by Eq. (I-20).

$$\lambda_i = \lambda = \frac{9}{2}$$

From Eqs. (I-21), (I-22), and (I-23), initialize the procedure with

$$j_1 = \begin{bmatrix} \frac{3}{\sqrt{2}} \\ 0 \end{bmatrix} ; \quad j_2 = \begin{bmatrix} 0 \\ \frac{3}{\sqrt{2}} \end{bmatrix} ; \quad j_3 = \begin{bmatrix} 0 \\ 0 \end{bmatrix}$$

and indices

$$l = 1 ; \quad u = 3$$

First Iteration Step

Since

$$(|j_1|^2 - J_1 = \frac{1}{2}) < (J_3 - |j_3|^2 = 2)$$

the inequality in Eq. (I-25) is not satisfied, so this is Case b where

$$\mu = \frac{1}{9} \quad ; \quad \gamma = 0 \quad ; \quad C = \frac{2\sqrt{2}}{3} \quad ; \quad S = \frac{1}{3}$$

and

$$(j_1)_{\text{new}} = \begin{bmatrix} 2 \\ 0 \end{bmatrix} \quad ; \quad (j_3)_{\text{new}} = \begin{bmatrix} -\frac{1}{\sqrt{2}} \\ 0 \end{bmatrix}$$

Vector j_2 is unchanged. Since this is Case b, the l index is augmented as

$$l = 2 \text{ and } u = 3$$

completing the iteration step.

Second Iteration Step

Since

$$(|j_2|^2 - J_2 = \frac{3}{2}) \geq (J_3 - |j_3|^2 = \frac{3}{2})$$

the inequality in Eq. (I-25) is satisfied, so this is Case a where

$$\mu = \frac{3}{8} \quad ; \quad \gamma = 0 \quad , \quad C = \sqrt{\frac{5}{8}} \quad ; \quad S = \sqrt{\frac{3}{8}}$$

and

$$(\underline{j}_2)_{\text{new}} = \begin{bmatrix} -\frac{\sqrt{3}}{4} \\ +\frac{3\sqrt{5}}{4} \end{bmatrix} ; \quad (\underline{j}_3)_{\text{new}} = \begin{bmatrix} -\frac{\sqrt{5}}{4} \\ -\frac{3\sqrt{3}}{4} \end{bmatrix}$$

Vector \underline{j}_1 is unchanged. Since this is Case a, the u index is decremented and

$$l = 2 , \quad u = 2$$

Since $l = 2$, this completes the iteration.

Checking the results, the final values of \underline{j}_i have the correct magnitudes

$$|\underline{j}_1|^2 = 4 = J_1 ; \quad |\underline{j}_2|^2 = 3 = J_2 ; \quad |\underline{j}_3|^2 = 2 = J_3$$

and the matrix M is correct.

$$M = \sum_{i=1}^3 \underline{j}_i \underline{j}_i^T = \frac{9}{2} \begin{bmatrix} 1 & 0 \\ 0 & 1 \end{bmatrix}$$

c. Construction Example: Unequal λ_i

The following example will illustrate the construction when unequal measurement accuracies are desired on each axis. The procedure is exactly the same as that described before even when the inequality in Eq. (I-18) is not satisfied, except that the procedure is initialized with the desired eigenvalues in Eq. (I-21). These desired eigenvalues, i.e., λ_i , must satisfy the constraint

$$\sum_{i=1}^n \lambda_i = \sum_{i=1}^m J_i \quad (\text{I-40})$$

Consider the J_i from the previous example

$$J_1 = 4 \quad ; \quad J_2 = 3 \quad ; \quad J_3 = 2$$

and suppose the desired accuracy ratios are

$$\frac{\lambda_1}{\lambda_2} = \frac{2}{1}$$

Since the eigenvalues λ_1 and λ_2 must satisfy Eq. (I-40), the desired eigenvalues of matrix M are $\lambda_1 = 6$ and $\lambda_2 = 3$.

Therefore, to start the numerical procedure, using Eqs. (I-21), (I-22), and (I-23), set

$$\underline{j}_1 = \begin{bmatrix} \sqrt{6} \\ 0 \end{bmatrix} \quad ; \quad \underline{j}_2 = \begin{bmatrix} 0 \\ \sqrt{3} \end{bmatrix} \quad ; \quad \underline{j}_3 = \begin{bmatrix} 0 \\ 0 \end{bmatrix}$$

and indices

$$l = 1 \quad ; \quad u = 3$$

First Iteration Step

Since

$$(|\underline{j}_1|^2 - J_1 = 2) \geq (J_3 - |\underline{j}_3|^2 = 2)$$

the inequality in Eq. (I-25) is just satisfied, so this is Case a where

$$\mu = \sqrt{1/3} \quad ; \quad \gamma = 0 \quad ; \quad C = \sqrt{2/3} \quad ; \quad S = \sqrt{1/3}$$

and

$$(\underline{j}_1)_{\text{new}} = \begin{bmatrix} 2 \\ 0 \end{bmatrix} \quad ; \quad (\underline{j}_3)_{\text{new}} = \begin{bmatrix} -\sqrt{2} \\ 0 \end{bmatrix}$$

Vector \underline{j}_2 is unchanged. Since this is Case a, decrement the u index

$$\ell = 1 \text{ and } u = 2$$

completing the iteration step.

Second Iteration Step

Since

$$(|\underline{j}_1|^2 - J_1) = 0$$

the index ℓ is immediately increased so

$$\ell = 2 \text{ and } u = 2$$

completing the entire iteration procedure.

Checking the results, the final values of \underline{j}_i have the correct magnitudes

$$|\underline{j}_1|^2 = 4 \quad ; \quad |\underline{j}_2|^2 = 3 \quad ; \quad |\underline{j}_3|^2 = 2$$

and the matrix M

$$M = \sum_{i=1}^3 \mathbf{j}_i \mathbf{j}_i^T = \begin{bmatrix} 6 & 0 \\ 0 & 3 \end{bmatrix}$$

also has the desired eigenvalues.

d. Sensor Orientation Construction: Case II

Now, consider the case where

$$J_1 > \frac{1}{n} \sum_{k=1}^m J_i \quad (I-41)$$

In this case, the eigenvalues of the optimal information matrix M are given by

$$\lambda_j = \lambda = \frac{1}{n-k+1} \sum_{i=k}^m J_i \quad ; \quad j = 1, 2, \dots, (n-k+1)$$

$$\lambda_j = J_i \quad ; \quad j = (n-k+2), \dots, n$$

where k is the smallest integer so that

$$J_k \leq \frac{1}{n-k+1} \sum_{i=k}^m J_i$$

Using the construction outlined, find a set of (n-k+1) dimensional vectors $\mathbf{j}'_k, \dots, \mathbf{j}'_n$ so that

$$\sum_{i=k}^m \mathbf{j}'_i \mathbf{j}'_i^T = \lambda I$$

and convert these to n -dimensional vectors \underline{j}_i by adding $(k-1)$ zeros at the top.

$$\underline{j}_i = \begin{bmatrix} 0_{(k-1)} \\ \underline{j}_i \end{bmatrix} \quad i = k, k+1, \dots, m$$

Then, set

$$\underline{j}_i = J_i \underline{e}_i \quad i = 1, 2, \dots, (k-1)$$

where

$$\underline{e}_i = \begin{bmatrix} \delta_{1i} \\ \delta_{2i} \\ \vdots \\ \delta_{ni} \end{bmatrix}$$

This completes the construction.

Physically, the first $(k-1)$ vectors \underline{j}_i (orienting the superior sensors) are all orthogonal to each other and the remaining $(n-k+1)$ \underline{j}_i vectors. These remaining vectors are distributed over the remaining $(n-k+1)$ dimensional subspace according to the numerical procedure outlined so that the smallest $n-k+1$ eigenvalues of M are all equal.

GLOSSARY

AIRS	Advanced Inertial Reference System
BLIP	Background Limited Performance
CMG	control moment gyro
COMSAT, comsat	communications satellite
CSDL	Charles Stark Draper Laboratories
dc	direct current
ESG	electrostatic gyro
ESP	Eclectic Simulation Program
FM	frequency modulated
FOV	field of view
HAADS	High Altitude Attitude Determination Study
IR	infrared
IRIG	inertial rate integrating gyro
LOS	line of sight
NA	not available
N. A.	not applicable
NASA	National Aeronautics and Space Administration
NEA	noise equivalent angle
OAQ	Orbiting Astronomical Observatory
PM-RIG	permanent magnet rate integrating gyro
PSD	power spectral density

GLOSSARY (Continued)

rf	radio frequency
rms	root mean square
rpm	revolutions per minute
rss	root sum square
SARA	Single-Axis Reference Assembly
SPARS	Space Precision Attitude Reference System
TGG	Third Generation Gyro